Reconfigurable Varactor-Based Microwave Components for Low-Cost Antenna Array Design: Phase Shifters, Attenuators and Diplexers

by

Yuan YUAN

B. Eng. (Electronic and Information Engineering),
Xidian University, China, 2004
M. Eng. (Electronic Science and Technology),
Xidian University, China, 2007

Thesis submitted for the degree of

Doctor of Philosophy

in

School of Electrical and Mechanical Engineering
Faculty of Engineering, Sciences and Techonology
The University of Adelaide

2023

Supervisors:
Prof. Christophe Fumeaux
School of Electrical & Mechanical Engineering, The University of Adelaide
Dr. Shengjian Jammy Chen
College of Science and Engineering, Flinders University
School of Electrical & Mechanical Engineering, The University of Adelaide

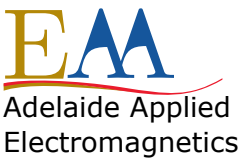

To my dearest parents,
my considerate husband, Zhi
my gorgeous daughter Zien
and my parents-in-law
with all my love.

Contents

Abstract

PHASED array antennas are important for advanced wireless communications, providing high directivity and beam steering capabilities. However, conventional phased arrays are expensive, bulky, heavy and power-hungry due to their complex architecture and electronic controls. For systems demanding low cost, light weight, compact size, and low power consumption, reconfigurable antenna arrays can be a practical alternative to traditional phased arrays. Electronically controlled reconfigurable antennas offer the ability to adjust their operating frequency, radiation pattern, polarization, or any combinations of these aspects by using tunable electronic components such as PIN diodes, switches, varactors and/or micro-electromechanical systems (MEMS). One way to realize reconfigurable antenna array is to start by designing a reconfigurable feeding network and then co-designing corresponding antenna elements, before combining these two structures to form the whole array based on the system requirements. However, when designing low-cost and compact reconfigurable antenna arrays, several critical aspects should be taken into consideration. Firstly, the reconfigurable feeding network may result in a large number of components and a complex structure, leading to a higher insertion loss and a possible degradation in antenna performance through reduced efficiency. Secondly, if the feeding network is not designed properly, integrating it into the system can lead to a high demand in space, consequently enlarging the overall size, manufacture complexity and cost.

In this context, compact, seamlessly-integrable, low-power, low-cost and tunable microwave components are needed to build reconfigurable feeding networks. Through using these feeding networks, low-cost and compact reconfigurable antenna arrays can be realized as alternatives to conventional phased arrays. Varactor-based phase shifters to control the signal phase, reconfigurable attenuators to control the signal magnitude and reconfigurable diplexers to control the signal frequency are essential components to construct these so-called reconfigurable feeding networks. This is in line with the goal of this thesis, which comprises three coherent objectives. Firstly, the dissertation presents a concept of low-cost varactor-based phase shifters, which are operating in differential mode. A phase shifter pair based on this concept is able to supply full-360° phase difference tuning range between its two output ports. The devices can be

directly integrated with 50 Ω feed transmission lines, which results in a compact, low-cost and lightweight design of the feeding network and saves space which would be required by conventional phase shifter blocks. Based on such differential phase shifter pairs, a 1×4 linear dielectric resonator antenna array is designed, which is excited by a feeding network comprising 3 phase shifter pairs to control the array scanning sum-pattern continuously from -45° to 45° and the null of a difference pattern from -30° to 30°. A dedicated procedure for accurately calibrating these beam-steerable antennas is also proposed, aiming to provide a general approach to enhance the performance of the reconfigurable feeding network. Secondly, a tunable transmission-type attenuator with easily-extendable and tunable attenuation level, small initial insertion loss, and satisfactorily low reflection coefficient is presented, which is integrated onto a 50 Ω microstrip transmission lines with several side-loaded shorted-end varactor-based stubs. This arrangement allows a compact and low-loss structure, as well as seamless integration with planar transmission lines in microwave circuits, which also makes them suitable for applications with limited real estate. It is proven that a 3-stub attenuator can offer tunable attenuation from 1.0 to 13.5 dB with reflection coefficient lower than -11.4 dB, and that by cascading them a larger attenuation range can be obtained. Thirdly, a frequency-switchable varactor-based diplexer concept is proposed for a low-cost and compact pattern- and frequency-switchable microstrip antenna array. This diplexer concept, which represents an extension in functionality of the differential phase shifter pair, is able to supply different responses to different frequencies in a wide-band range, instead of utilizing the phase difference performance in a narrow operation band. Seamless integration with the feeding network enables a dual-band antenna pair to become a pattern- and frequency-switchable array with unique functionality.

All the results presented in this thesis are derived from varactor-based microwave components that offer a range of benefits, including low cost, lightweight construction, low power consumption, and a seamless integration topology. All these proposed reconfigurable devices allow construction of reconfigurable feeding networks with phase and magnitude tuning abilities, as well as frequency reconfigurability. This means that antenna arrays fed by this type of feeding networks can achieve versatile and competitive reconfigurability in their radiation performance, while maintaining a compact size, low weight, low power consumption and affordability.

Originality Declaration

I certify that this work contains no material which has been accepted for the award of any other degree or diploma in my name, in any university or other tertiary institution and, to the best of my knowledge and belief, contains no material previously published or written by another person, except where due reference has been made in the text. In addition, I certify that no part of this work will, in the future, be used in a submission in my name, for any other degree or diploma in any university or other tertiary institution without the prior approval of the University of Adelaide and where applicable, any partner institution responsible for the joint award of this degree.

The author acknowledges that copyright of published works contained within the thesis resides with the copyright holder(s) of those works.

I give permission for the digital version of my thesis to be made available on the web, via the University's digital research repository, the Library Search and also through web search engines, unless permission has been granted by the University to restrict access for a period of time.

I acknowledge the support I have received for my research through the provision of an Australian Government Research Training Program Scholarship.

01/08/2023

Signed

Date

Acknowledgments

I sincerely would like to express my deep gratitude to my supervisors Prof. Christophe Fumeaux, and Dr. Shengjian Jammy Chen. In August 2019, I began my Ph.D. research journey under their guidance. Since then, they have been patiently guiding me into the research of microwave devices and antenna array designs, and always analyze complex problems, and inspire me to explore deeper into finding solutions and explore new potential direction of my research. I always remember a word that Christophe told me, "There must be an answer to the question, and I feel that you will find it soon." This sentence strongly inspired me to solve the problem one after another. Prof. Fumeaux is a very supportive, approachable and responsible supervisor for my Ph.D. study. His profound and comprehensive knowledge, and solid theoretical foundation of electromagnetics and antennas always inspire me. Extremely, one of the brightest aspects of his image, is his high standard and rigorous scientific attitudes towards research. His high degree of self-discipline, and serious and responsible spirit deeply affects me as well. He always has a weekly one-hour meeting with his Ph.D students individually to discuss the research progress and new ideas and solve research problems. His response to emails, feedbacks on academic manuscript to his students are very timely and highly pertinent even during nights and weekends. In my opinion, Prof. Christophe Fumeaux is a ***SUPERMAN*** supervisor. I would like to express my deepest acknowledgement for your enthusiastic supervision, encouraging and patient guidance, technical and financial support and being a role model for me as a scholar. Dr. Chen is my another ***OUTSTANDING*** supervisor with broad and profound knowledge in electromagnetics and antennas. He always points out the critical points in our discussions and encourages me to solve problems from the fundamentals. When I encountered some complicated but crucial situations in my research, he always patiently discussed and analyzed with me and gave me confidence. His thoughtful and rigorous scientific attitudes always inspire me as well. My two respectful supervisors always patiently revise my manuscripts with critical and rigorous comments. These comments are pretty valuable for me and enable me to enhance many capabilities, including my critical thinking and logical writing skills. These all priceless treasures during my Ph.D. study and will have a profound impact on my future life and work.

I also wish to express my gratitude for the support and advices from my friends and colleagues in our Applied Electromagnetics Group at the University of Adelaide, Dr. Nghia Nguyen Trong, Dr. Quoc Hung Dang, Dr. Sree Pramod Pinapati, Dr. Siti Nailah Mastura Zainarry, Dr. Xiaolong You, Mr. Xiaoyang Yin, Mr. Purna Samal, Mr. Baoqi Zhu, Mr. Junyi Chen, Mr. Tianchang Ma and Mr. Patrick Joseph Bartley. Additionally, I would like to express my appreciation towards my colleagues and friends from our sister group, i.e., Terahertz Engineering Laboratory, Prof. Withawat Withayachumnankul, Dr. Weijie Gao, Dr. Wendy Suk Ling Lee, Dr. Xiaojing Lv, Ms. Panisa Dechwechprasit, Mr. Harrison Noel Lees, Mr. Mingxiang Stephen Li, Mr. Bryce Chung, Ms. Linxi Chen, Mr. Sakib Quader and Mr. Chun Yin Tam. I enjoyed very much the time of our group meetings and our group parties. They are all precious memories in my life. I also would like to acknowledge the kindness and assistance from the professional technical staff and friends in the School of Electrical and Mechanical Engineering: Mr. Danny Di Giacomo, Mr. Alban O'Brien, Mr. Norio Itsumi, Mr. Brandon Pullen, Mr. David Bowler, Mr. Hayden Westell, Mr. Aubrey Benjamin Slater, Dr. Bing Yan, Dr. Xin Yuan (Vernon), Mr. Qiang Gao, and Ms. Hua Ma. In particular, I would like to specially acknowledge technical support from Mr. Danny Di Giacomo and Dr. Bing Yan with sincere thanks, since I have received important help from them on numerous occasions.

I sincerely acknowledge the generous financial support from the University of Adelaide with a "Research Training Program Stipend", which supports me through my three and a half years Ph.D study, particularly during the challenging times under the influence of the epidemic. Additionally, I would like to express my gratitude to the Applied EM Group for a short term scholarship, which gives me a solid support during the last period of my Ph.D. journey.

To my beloved family, the most important part of my life, I would like to express my deepest thankfulness and love to my parents, who always unconditionally love, understand, support and offer me the best they can. I love you so much! I also wish to express my sincere appreciation to my parents-in-law who give me plenty of understanding, love and support. My precious daughter, **Enya**, is the source of my dedication and serves as a constant inspiration in my pursuit of both her well-being and my dreams. She truly is the light of my life, constantly radiating her love and understanding towards me, which serves as an strong support during my study.

Finally, I would like to extend my deepest and most sincere gratitude to my husband, **Simon (Dr. Zhi Xu)**, my most solid spiritual pillar. He is always by my side, offering unwavering support and unwavering belief in me, without any conditions. I LOVE YOU, MY DARLING!

Yuan Yuan
July 2023
Adelaide, Australia

Abbreviation

BST	Barium Strontium Titanate
CMOS	Complementary Metal-Oxide-Semiconductor
CPW	Coplanar Waveguide
DMR	Dual-Mode Resonator
DMS	Defected Microstrip Structure
DR	Dielectric Resonator
DRA	Dielectric Resonator Antenna
DSP	Digital Signal Processing
FET	Field-Effect Transistor
FPGA	Field Programmable Gate Array
GA	Genetic Algorithm
GCPW	Grounded Coplanar Waveguide
GHz	Gigahertz
GSS	Graphene Sandwich Structure
IoT	Internet of Things
IP3	Third-order Intercept Point
ISM	Industrial, Scientific, and Medical
LTCC	Low-Temperature Co-fired Ceramic
MEMS	Micro-Electromechanical Systems
MIMO	Multiple-Input Multiple-Output
NRI-TL	Negative-Refractive-Index Transmission Line
PCB	Printed Circuit Board
Py	Permalloy
PZT	Integrating Lead Zirconate Titanate
QE-BPF	Quasi-Elliptic Band-Pass Filter
RF	Radio Frequency
RMS	Root Mean Square
SIR	Stepped-Impedance Resonator
SIW	Substrate-Integrated Waveguide
SSIR	Shorted Stepped-Impedance Resonator
SW-BPF	Switchable Band-Pass Filters

UWB	Ultra-Wideband
WLAN	Wireless Local Area Network

Awards and Scholarships

2019

- Research Training Program Stipend, The University of Adelaide

2023

- Best Student Paper Award (2nd), IEEE RADIO international conference (RADIO 2023)
- Applied EM Group short term scholarship, The University of Adelaide

Publications

Journal Articles

Published

Y. Yuan, S. J. Chen, and C. Fumeaux, "Varactor-Based Phase Shifters Operating in Differential Pairs for Beam-Steerable Antennas," *IEEE Transactions on Antennas and Propagation*, vol. 70, no. 9, pp. 7670–7682, 2022.

In preparation

Y. Yuan, S. J. Chen, and C. Fumeaux, "Transmission-type Varactor-based Tunable Attenuator," *IEEE Transactions on Microwave Theory and Techniques*, 2023.

Y. Yuan, S. J. Chen, and C. Fumeaux, "Pattern- and Frequency-reconfigurable Antenna Array Fed by Varactor-based Frequency-switchable Diplexer," journal to be determined, 2023.

Conference Articles

Y. Yuan, S. J. Chen, and C. Fumeaux,"A 3d-printed hybrid dielectric resonator antenna with low cross-polarization," in *2022 International Symposium on Antennas and Propagation (ISAP)*, 2022, pp. 79–80.

Y. Yuan, S. J. Chen, and C. Fumeaux, "Varactor-based 360° differential phase shifter pair," in *5th Australian Microwave Symposium (AMS)*, 2023, pp. 29-30.

Y. Yuan, S. J. Chen, and C. Fumeaux, "Calibrated design of beam-steerable antennas fed by varactor-based phase shifter," *the 17th European Conference on Antennas and Propagation (EuCAP)*, March 2023. **(Convened paper)**

Y. Yuan, S. J. Chen, and C. Fumeaux, "Pattern optimization of beam-reconfigurable antenna fed by varactor-based phase shifters," *The 8th edition of the IEEE RADIO International Conference (RADIO)*, May, 2023. **[Best Student Paper Award (2nd), IEEE RADIO International Conference (RADIO 2023)]**

List of Figures

List of Tables

Chapter 1

Introduction

IN this introduction, a brief overview is provided on reconfigurable antennas that rely on electronic tuning components. Additionally, the significance and difficulties related to designing such reconfigurable microwave devices are discussed. The chapter outlines the aims and motivations behind the thesis, emphasizing the unique novel contributions made in this dissertation. The conclusion of the chapter details the structural arrangement of the thesis.

1.1 Introduction and Motivation

PLANAR reconfigurable antenna systems have gathered significant attention in recent years due to the rapid growth of modern wireless communications systems [1,2]. These antennas offer the capability to adjust their characteristics in terms of resonance frequency [3], radiation pattern [4], polarization [5], or any combinations of these three [6–8], which enables multi-functionality in a single antenna or array. Beside the multi-functionality, low cost, low weight and low power consumption are also essential requirements for reconfigurable antenna array in modern communications systems. Reconfigurability in antennas can be implemented using different techniques [9], such as electrical [10, 11], optical [12, 13], and physical actuation [14,15], or with smart materials [16–18]. The most commonly employed technique for reconfiguration is electrical reconfiguration, which involves utilizing active components like PIN diodes [19, 20], varactors [21, 22], and RF-MEMS (Micro-Electromechanical Systems) switches [23,24]. These components provide effective means of satisfying the aforementioned requirements.

To design antennas exhibiting the aforementioned characteristics, there has been a significant interest in developing planar microwave devices that utilize tunable devices such as phase shifters [25,26], attenuators [27,28], and diplexers [29], which could be integrated into a planar antenna or array to practically realize reconfigurability. This has led to the creation of numerous novel devices with suitable properties in microwave technology. Regarding phase shifters, characteristics such as a large phase tuning span, low insertion loss level, compact size, and/or simple control circuit are highly desired. For attenuators, required characteristics include a large adjustable attenuation range, minimized loss, satisfactory impedance match, and/or a compact structure. As for diplexers, it is a common practice to combine two filters operating at different frequencies with good impedance matching and high inter-port isolation. Due to the challenges of achieving concurrent satisfaction of these desired properties for reconfigurable microwave devices, dedicated and coherent device topologies, design strategies and microwave engineering technologies for the fabrication, connections and integration into antenna systems are critical. Consequently, research on these particular aspects of novel microwave devices is of significant interest for reconfigurable antenna system designs.

This dissertation investigates the design, fabrication and system integration of tunable microwave devices, such as phase shifters, attenuators and diplexers, for reconfigurable antenna systems with emphasis placed on achieving low cost, compact size, easy-integration, low power consumption, and unique multi-functional capabilities.

1.2 Objectives of the Thesis

There are four main objectives of the thesis which are described in details in the following.

1. **Development of full-360°, compact size, low-cost, low insertion loss phase shifters with seamless integration to planar transmission lines**

   Compared to PIN-diode and RF MEMS switches, varactors offer the advantage of small current flow and continuous tuning characteristics, making them a valuable foundation for achieving low power consumption in phase shifters. Although varactor-based phase shifters with large phase tuning span, small insertion loss, compact structure, and simple control circuits are major design objectives in engineering research, achieving all of these merits in a single design remains an ongoing challenge, that has not to be fully addressed. Most designs have only covered a subset of these desirable characteristics. For instance, an amplitude-variable phase shifter utilizing 13 varactors controlled by 13 voltages was proposed in [30], which achieved a phase shift of full-360° but with a relatively high insertion loss of 5.27 dB. In contrast, a phase shifter based on nonuniform transmission lines comprising only 3 end-shorted varactors was proposed in [31], which exhibited a small insertion loss of less than 1.3 dB but only a limited phase tuning range of 90°. These examples illustrate that the most critical challenge for this type of phase shifters is to achieve a maximum phase shift with compact and simple structures, while maintaining a low insertion loss level. To address this challenge, this dissertation aims to develop a brand new topology, along with its equivalent circuit model, that can simultaneously achieve these characteristics. The proposed approaches include a novel differential topology, designed using fast optimization algorithms based on equivalent circuit models, which result in a compact and low-cost phase shifter that delivers full-360° tuning span and low insertion loss.

2. **Development of a pattern reconfigurable antenna array fed by a single port feeding network with seamless integration of varactor-based phase shifters**

A component-based planar pattern-reconfigurable antenna array is proposed, whose performance is directly determined by the performance of the phase shifter units that provide phase control. Due to the challenges in simultaneously achieving the expected performance measures mentioned before, the characteristics of the array antenna driven by varactor-based phase shifter units will also have limitations, such as a constrained scanning angular range or a relative large size. For instance, a 1×4 dielectric resonator antenna (DRA) array conceptualized in [32] and based on four continuously tunable phase shifters, could continuously scan within an angular range of $\pm 30^{\circ}$. The phase shifter utilized 11 Barium strontium titanate (BST) Metal-Insulator-Metal varactors to reach a phase shifting span of 260° with maximum bias voltages up to 50 V and an insertion loss 5.9 dB. In [33], another 1×4 substrate-integrated waveguide (SIW) phased array realized continuous scanning from -45° to 45° by employing reflective type phase shifters with smooth phase agility. Each phase shifter was based on only 2 varactors and produced a 290° continuously tunable phase shift with an insertion loss below 3.5 dB, but with a separate size of $1.24 \times 0.46\lambda_0$, which means that an extra space with a length of $1.24\lambda_0$ was required for the phase shifters to be added in front of the radiating elements. However, both large-angle scanning and miniaturization of the structure are important advantages of planar reconfigurable antenna arrays, and the lack of either will limit the application. Therefore, based on our aforementioned phase shifter design, it is possible to directly integrate the phase shifters on the 50 Ω transmission line of the feeding network, enabling large-angle scanning of the antenna array without significant additional space requirement. Meanwhile, a full-360° phase tuning range and small insertion loss allows the excited antenna array to scan in a relatively wide angular space. It is noted that, as a standard step for any phased array operation, a dedicated calibration method designed for this type of phase shifter has been developed in this dissertation, enabling precise beam control for the reconfigurable array.

3. **Development of compact size, low cost, low insertion loss reconfigurable attenuators series**

   Variable attenuators are essential components in RF and millimeter-wave applications, such as wireless communications and radar systems [34], where amplitude control is necessary for various purposes, including signal calibration and beam tapering. These attenuators typically have several specifications to satisfy, including attenuation range, tuning resolution, bandwidth, insertion loss, and amplitude/phase errors. In addition, they are required to consume low DC-power and have a small chip-area requirement, which is especially relevant when used in large-scale phased-array systems. For attenuators realized in planar technologies, there are two major categories found in the literature, namely of reflection and transmission types. While reflection-type attenuators are realized on multi-port devices [35,36], transmission-type attenuators allow the wave to pass through a transmission line, reducing signal amplitude in the process. However, limited attenuation range, high return loss and high insertion loss (defined as minimal possible attenuation level) are typical drawbacks of transmission-type variable attenuators [37]. To address these challenges, researchers have invested significant efforts in exploring novel materials, such as graphene, to exploit its tunable resistance under voltage control. Large attenuation levels could be obtained, but they were generally affected by high insertion and/or return losses. In addition, they mainly required external control through bias-tees, and were based on non-standard fabrication techniques and materials, which are still not mature enough before they can be applied in engineering design. Aiming to find a better solution, the third objective of this dissertation is to explore a varactor-based transmission-type tunable attenuator that combines advantageous characteristics such as large attenuation range, small minimum insertion loss, minimal phase shift, and low return loss while being based on a simple and compact planar structure with embedded DC-control circuit.

4. **Development of a pattern- and frequency-switchable microstrip antenna array using a frequency-switchable varactor-based diplexer**

   Diplexers are widely used in microwave circuits and systems as three-port devices that split input signals from a common input port into two channels with different operating frequencies [38]. They are a key component in many communications systems, allowing a single antenna to transmit and receive on different

frequencies simultaneously. Most commonly, a diplexer is realized by combining two or more dedicated filter branches to select the corresponding working frequency or band. Recent studies have employed various approaches for the high quality filters design, such as hairpin resonators [39], stepped-impedance resonators [40] [41], and square ring resonators [42], to satisfy the requirements in a diplexer application. Nevertheless, once these filter branches are designed, the operational frequency becomes fixed and cannot be altered thereafter. On another hand, pattern- or frequency- switchable antennas have been developed with the ability to vary their radiation patterns or operation frequency by using electronic components, including PIN diodes [43], varactors [44] [45] and RF MEMS [46]. In microwave systems, the inclusion of additional or complex structures can lead to increased loss and cost. To address this issue, a desired solution is the development of a compact and cost-effective tunable circuit that offers multiple functionalities within a single design [47]. In line with this design consideration, a significant potential for improvement lies in combining diplexer and antenna to obtain multi-reconfigurability based on a single and simple reconfigurable feeding network. This integration enables the antenna system to operate in multiple states, presenting a valuable advancement in antenna technology. Particularly in planar microwave systems, this approach reduces the requirement for extra components while ensuring efficient performance. To explore an enhanced solution, this dissertation focuses on a two-element pattern-reconfigurable antenna array that utilizes a varactor-based diplexer. This configuration enables the antenna to achieve three operation modes in two frequency bands, with bidirectional or two swappable directional radiation patterns.

1.3 Thesis Structure and the Original Contributions

This dissertation presents several original contributions to the field of reconfigurable, varactor-based microwave components for low-cost antenna array design. The contributions can be generally categorized into four major parts. The first part of the thesis introduces a low-cost, compact varactor-based phase shifter with a differential phase tuning range of 360°, which is used to control phase in feeding networks. The second part of the thesis focuses on the application of these phase shifters for beam-steerable antenna arrays. The third part discusses the design of a varactor-based

transmission-type attenuator that is low-cost, compact, and has an adjustable attenuation level, which is used to manipulate magnitude in feeding networks. Finally, the last part investigates the designs of frequency-switchable varactor-based diplexers that present a multiple functionality for designing reconfigurable antennas. A frequency- and pattern-reconfigurable antenna based on the diplexer is designed to validate the concept.

Based on the four major contributions, the thesis outline is illustrated in Fig. 1.1. This thesis starts with introduction and literature review in the first two chapters and ends up with a concluding discussion in the last chapter. The main chapters in between focus on the original contributions of the thesis, as described in detail in the following.

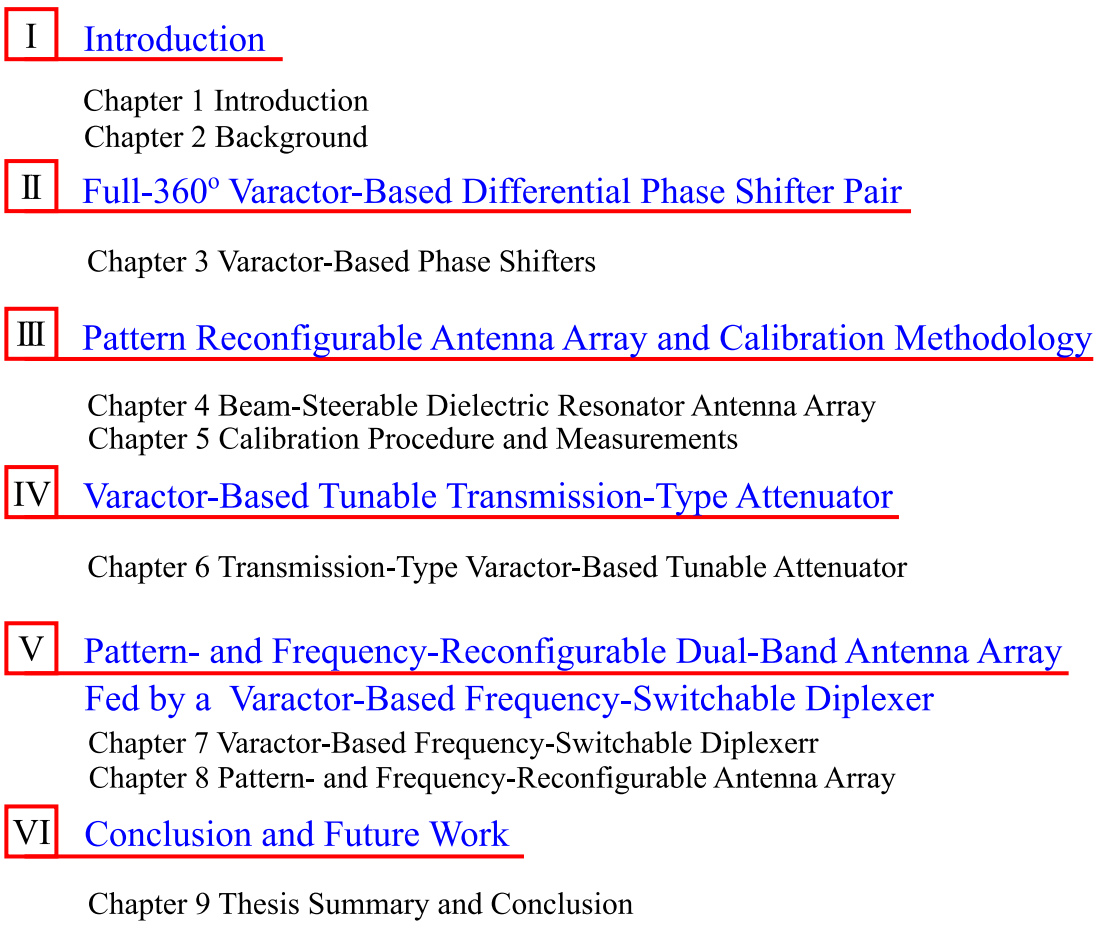

Figure 1.1. Thesis outline. The thesis comprises 9 chapters where the first two chapters are dedicated to the introduction and literature review and the last chapter concludes the dissertation. The chapters in between include the main contributions of the thesis.

Chapters 1 & 2 provide the necessary context and background information required for the rest of the thesis. The second chapter contains a review of microwave devices including phase shifters, attenuators and diplexers.

Chapter 3 describes the original contributions of a low-cost, compact varactor-based phase shifter pair, which operates in differential mode and provides a large relative phase tuning range with low insertion loss. The phase shifter pair's design incorporates a novel differential concept and a compact topology, which not only simplifies the design process but also improves the system's overall performance. The original contributions in Chapter 3 are listed as following.

1) A novel concept of varactor-based phase shifter pair operating in differential mode is presented. The phase shifter pair contains two branches with identical basic phase-tuning units which consists of a microstrip transmission line segment loaded with several shunt shorted-stub-terminated varactors. The differential phase shifter pair can achieve a nearly full 360° phase shift, which allows a low-loss and simple structure. An accurate equivalent circuit model for this phase shifter unit is developed to optimize the structure with a genetic algorithm (GA). A pair of phase-tuning units, each including three stub-loaded varactors, is identified as a processing solution to produce a continuously tunable phase difference nearly covering 0° to 360°. This design has been published in the flagship journal of the *IEEE Antennas and Propagation Society*, the *IEEE Transactions on Antennas and Propagation*, with the title "Varactor-based Phase Shifters Operating in Differential Pairs for Beam-steerable Antennas " [48].

2) An improved phase shifter is designed utilizing the same equivalent circuit model. The enhanced design is realized on a substrate with lower permittivity, which eases of fabrication. It realizes a complete 360° continuous relative phase tuning with small insertion loss, which makes this design highly competitive. The outcomes of this enhanced design were presented at the *5th Australian Microwave Symposium (AMS)* in 2023 under the title "Varactor-Based 360° Differential Phase Shifter Pair" [49].

Chapters 4 & 5 are dedicated to the original contributions of the pattern reconfigurable antenna array implementations. Chapter 4 outlines a four-element linear pattern reconfigurable antenna array excited by a feeding network, which contains three

phase shifter pairs described in [48] in differential mode. Due to the seamless integration of the phase shifter to a 50 Ω transmission line of the feed network, the beam control network structure is significantly simplified. Additionally, Chapter 5 presents a dedicated calibration procedure for this type of phase shifter pairs to ensure precise phase and amplitude distributions in accordance with specific requirements. As a result, the pattern reconfigurable antenna is capable of producing accurately steerable sum patterns and null patterns. There are four contributions in Chapter 4 and Chapter 5, which are listed below.

1) A 3D-printed DRA exhibits low cross-polarization is introduced as element for this array. To enhance polarization purity, an optimized T-shaped feeding structure is utilized instead of the conventional probe excitation. The T-shaped feeding structure effectively reduces the cross-polarization level, resulting in the highest cross-polarized components being around -15 dB over the entire operational bandwidth from 4.75 to 5.25 GHz. The design's outcomes were presented at *the 2022 International Symposium on Antennas and Propagation (ISAP)* under the title of "A 3D-Printed Hybrid Dielectric Resonator Antenna with Low Cross-Polarization " [50].

2) A 1 × 4 linear DRA array that utilizes the proposed differential phase shifter pairs fed by a single port network is designed. The differential phase shifter pair can be directly integrated onto a host transmission line building a corporate feed, resulting in a compact phased feeding network structure. The array enables simultaneous pattern and frequency reconfigurability. Measured results indicate that the array can accurately scan its beam from -45° to 45° continuously. This design has been published in the *IEEE Transactions on Antennas and Propagation*, the flagship journal of the *IEEE Antennas and Propagation Society*, under the title of "Varactor-based Phase Shifters Operating in Differential Pairs for Beam-steerable Antennas " [48].

3) An accurate calibration procedure for a single-feed beam-steerable antenna controlled by varactor-based phase shifters operating in differential pairs is presented. The calibration process is based on the performance curve of each phase shifter, which is measured at dedicated sampling points on the circuit. A fast selection algorithm is used to determine the control voltages for all differential phase shifter pairs based on the required phase differences. The final control voltages for a particular beam configuration are validated

and fine-tuned on-board at the sampling points. The accurate null-scanning from -30° to 30° demonstrates the effectiveness of this procedure. The outcomes of this research were showcased at the *17th European Conference on Antennas and Propagation (EuCAP)* in the convened session *CS17: Emerging Beam-Steering Antenna Solutions for Satellite and Terrestrial Communications including* 5G+, under the title "Calibrated Design of Beam-Steerable Antennas Fed by Varactor-Based Phase Shifters" [51].

4) A pattern optimization technique for the beam-steerable DRA array has been developed as the last and necessary step in the dedicated calibration procedure. By considering the four elements as two sub-group, the phase compensations can be evaluated for the three pairs of phase shifters in the two-stage feeding network. Unexpected pattern distortions caused by material and fabrication tolerances after the feeding network are identified and corrected. The calibration procedure is then completed with these corrections incorporated into all parts of the whole antenna array. The findings of this study were presented at the *8th IEEE RADIO International Conference* under the title "Pattern Optimization of Beam-Reconfigurable Antenna Fed by Varactor-based Phase Shifters " [52].

Chapter 6 presents a series of transmission-type tunable attenuators. Based on the literature review of transmission-type attenuators, designing a tunable attenuator in transmission mode poses a challenge, which consists in achieving combined advantageous characteristics such as large attenuation range, small minimum insertion loss, minimal phase shift, and low return loss, while being based on a simple and compact planar structure with embedded dc-control circuit. To solve this challenge, a novel transmission-type attenuator topology is proposed and the original contribution is shown below.

1) A tunable transmission-type attenuator is presented which consists in a 50 Ω host microstrip line with a series of side-loaded shorted-end varactor-based stubs. The shorted-end stubs are loaded with varactors, capacitors and resistors. These elements are added on one side of the host line without line interruption, which allows a compact and low-loss structure. An accurate equivalent circuit model for the generic attenuator topology is developed for fast optimization of the structure with a GA. A series of attenuators with

three to nine stubs are developed following the proposed method to investigate the achievable performance for different stub numbers. The designed attenuators can produce continuously tunable attenuation levels of 1 - 10 dB with 3 stubs, 2 - 20 dB with 6 stubs and 3 - 30 dB with 9 stubs at 5 GHz. These outcomes are being prepared for submission to the *IEEE Transactions on Microwave Theory and Techniques*, with the title "Transmission-type Varactor-based Tunable Attenuator".

Chapters 7 & 8 Chapter 7 describes a frequency-switchable diplexer concept which is then used to create two-element pattern- and frequency-reconfigurable antenna array in Chapter 8. The diplexer maintains the same topology as the phase shifter tuning unit discussed in Chapter 3 but utilizes the characteristic response to different frequency bands instead of using phase values within a frequency. By changing the bias voltages applied to the varactors, it becomes possible to enable or disable specific frequencies, thereby providing a frequency-switchable functionality. The varactor-based diplexer can be directly integrated on a straight-through 50 Ω microstrip line, which allows a compact size and reduces the complexity of the antenna system. In Chapter 8, combining the frequency-switchable diplexer with radiating structures, a dual-band array realizes pattern- and frequency- reconfigurabilities within three operation modes, producing bidirectional or directional radiation patterns. The contribution of this part is illustrated as following.

1) A frequency- and pattern-reconfigurable antenna array with two elements, driven by a frequency-switchable varactor-based diplexer, is proposed. The diplexer consists of a T-junction power divider with two identical frequency-selective units placed symmetrically on the output branches. The reconfigurable diplexer is realized by two varactor-based short-ended stubs standing on one side of a 50 Ω transmission line, which allows simple and compact structure. The reconfigurable diplexer provides not just two distinct frequencies but also allows to switch between them, and operates in dual-band frequencies. Furthermore, the array includes a metallic isolation plate, resulting in the array exhibiting two directional patterns as well as a bidirectional pattern. The outcomes of this design are in preparation for submission to the *IEEE Transactions on Antennas and Propagation*, or another journal of the *IEEE Antennas and Propagation Society* under the tentative tile of

"Pattern- and Frequency-reconfigurable Antenna array Fed by a Varactor-based Frequency-switchable Diplexer" .

Conclusion (Chapter 9) provides a summary of all the projects included in this thesis, as well as a prospective view about the further work.

Chapter 2

Background

RECONFIGURABLE antennas have been widely developed for wireless communications systems with increased flexibility, adaptability, and efficiency. They have the capability to dynamically adjust their electromagnetic characteristics, such as radiation pattern, polarization, or frequency, with the aim to adapt to varying operating conditions and communications requirements. Key components, such as phase shifters, attenuators, and diplexers, play an essential role to realize the desired reconfigurabilities and their characteristics define the antenna's performance. This chapter provides a comprehensive review of the types, advantages, and drawbacks of existing state-of-the-art phase shifters, attenuators, and diplexers. It also highlights the achievements made in their implementation and identifies the research gaps and challenges that still need to be addressed. This analysis serves as a foundation for further researches in reconfigurable antenna technology.

2.1 Introduction

RECONFIGURABLE antennas have attracted much attention in wireless communications systems because of their flexibility and adaptability. They are able to adjust their radiation characteristics, such as frequency, radiation pattern, polarization or any combinations of these three, to satisfy various requirements from wireless communications systems.

For modern communications, planar reconfigurable antennas have been developed widely with versatile arrangements involving electronic components, such as PIN diodes, varactors and RF switches. Several advantages of pattern-reconfigurable antennas have been demonstrated during their development, including compact structure, low cost, and low power consumption when compared to traditional phased arrays, which are generally highly desired in a wide variety of applications in wireless communications systems.

Importantly, planar reconfigurable antennas incorporate various reconfigurable components, including phase shifters, attenuators, and diplexers, which play essential roles in achieving the desired reconfiguration. By reconfiguring these components, the operating characteristics of the antenna can be controlled and adjusted effectively.

This chapter provides a concise literature review of phase shifters, attenuators, and diplexers in the context of reconfigurable antenna technology, with particular emphasis on the challenges involved in designing these components for compact and cost-effective planar reconfigurable antenna systems. Sections 2.2, 2.3, and 2.4 will discuss the advancements and drawbacks associated with phase shifters, attenuators, and diplexers, respectively. Additionally, Section 2.5 summarizes the relevant research gaps and design challenges encountered in application of phase shifting and diplexing components to reconfigurable antennas, followed by concluding remarks.

2.2 Phase Shifters

Phase shifters are electronic devices used to control the phase of a signal passing through them. They play an important role in various applications, including phased array antennas, wireless communications systems, radar systems, and beamforming systems. By controlling the phase of signals, phase shifters enable specific phase distribution in multi-element antennas to create beam-steering functionality, leading to improved pattern performances.

2.2.1 Types of Phase Shifters

Based on the technique used to implement the phase-shifting functionality, phase shifters can be classified into three major categories, namely digital phase shifters, optical phase shifters and analog phase shifters [53].

1. **Digital phase shifters:** Digital phase shifters discretize the phase into predetermined phase states, allowing to change among different states by digitally controlling each phase-shifter bit. The number of bits in a digital phase shifter determines the number of available phase states that the system can switch to. Achieving accurate switching between different states is a critical aspect of digital phase shifters. Several methods have been employed to implement digital phase shifters. In references [54] [55], microelectromechanical systems (MEMS) were utilized to realize the phase shifter's state switching, as illustrated in Fig. 2.1. In [56] [57], transistors were employed as switches and their lumped component equivalents, such as resistors or capacitors, were utilized to produce the phase-shifting function. Additionally, PIN diodes are widely utilized in digital phase shifters as switching elements to control the phase shift of a signal. In a digital phase shifter, the PIN diode is biased in either the forward or reverse direction to

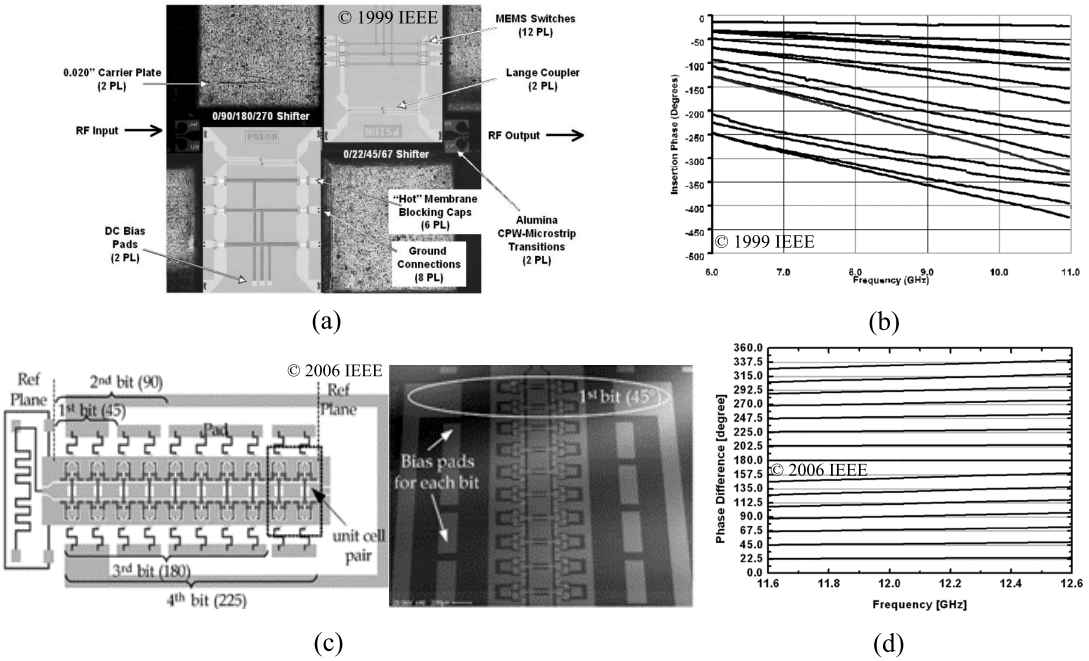

Figure 2.1. (a)Photograph of assembled 4-bit MEMS phase shifter circuit [54] and its (b) phase performance. (c) Schematic and photograph of a fabricated 4-bit phase shifter [55] and its (d) measured relative phase shifts for all 16 states.

control its conductivity. When the PIN diode is forward biased, it allows current to flow through it, and it behaves like a low-resistance switch. Conversely, when the diode is reverse-biased, it has a high impedance and acts as an open switch. To achieve discrete phase shifts, multiple PIN diodes are used in phase shifters. Each PIN diode is connected to a specific control signal that determines its biasing condition. By selecting enabled diodes, the phase shift can be controlled in discrete steps. For example, in the proposed design [58], which is shown in Fig. 2.2, the PIN diode was modeled as discrete components representing its forward and reverse states. Instead of requiring PIN diodes with high isolation, the loads were created using a single inductor connected in parallel with the PIN diodes. This approach simplified the design process. The resulting phase shifter configuration was a 4-bit type, allowing for 16 different states of phase shifts with the resolution of 22.5°.

Digital phase shifters offer precise phase control and fast switching speed, but they may have limitations in phase range and discrete phase resolution. Furthermore, they introduce losses and nonlinearity, involve system complexity and cost, and consume power. These factors should be considered when selecting a phase shifter for a specific application, especially for communications systems prioritizing accurate scanning and cost effectiveness.

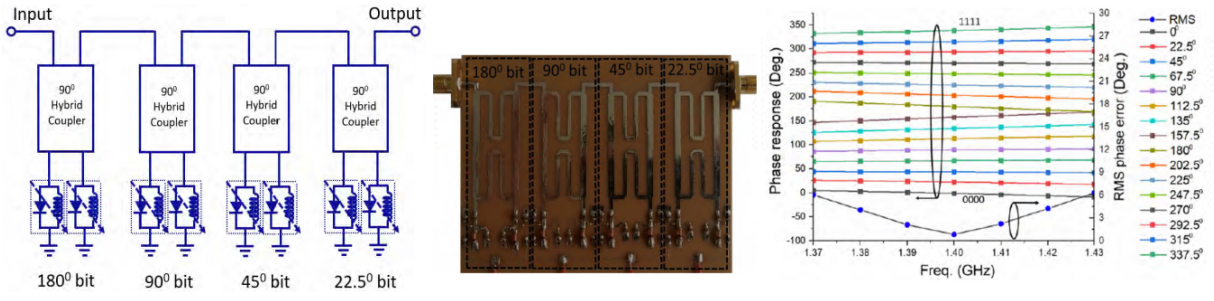

Figure 2.2. a) Configuration of 4-bit PIN diode reflection-type phase shifter [58], (b) photograph of the fabricated phase shifter [58], and (c) measured phase response of the phase shifter [58].

2. **Optical phase shifters:** Optical phase shifters play a crucial role in a wide range of RF-over-fiber applications. Applying optical phase shifters in microwave systems offers several advantages, including broad bandwidth, resilience to electromagnetic interference, superior isolation, and the ability to enable antenna remoting [59] [60]. Optical phase shifters are implemented using microwave optics methods, such as optical delay lines [61]. Nevertheless, optical phase shifters require a significant number of optical switches, leading to a considerable increase in the cost and complexity of the entire system [62]. Nevertheless, since optical phase shifters are not highly relevant to this thesis, no further review is given from here.

3. **Analog phase shifters:** Analog phase shifters represent another significant type of phase shifter, which operate by adjusting the phase of an input signal using analog circuits. Analog phase shifters can offer cost reduction by avoiding requirement for complex digital hardware in the network. The concept covers a wide variety of phase shifter types.

    1) **Ferrite phase shifters:** They are a type of traditional analog phase shifters that utilize the magnetic properties of ferrite materials to achieve phase shifting. The working principle of ferrite phase shifters is based on the Faraday effect and the interaction between the magnetic field and the microwave signal [63]. For over two decades, ferrite phase shifters have been employed in applications requiring precise phase control at moderate to high levels of microwave power. However, this type phase shifter is usually bulky and involves relatively large power consumption, which is excessive for compact and cost-effective microwave systems. Figure 2.3 shows a typical ferrite phase shifter, presented in [64].

    2) **Electronic components phase shifters:** These phase shifters rely on solid-state electronic components for phase modulation, which utilize the properties of the components to introduce a controlled phase shift in the signal path. They can function at a lower cost without the requirement for complex digital hardware in the network. Therefore, a significant amount of research and development has been dedicated to this type of phase shifters to facilitate low-cost and miniaturized microwave systems.

    By varying the voltage applied to the electronic components, such as PIN diodes [65] [66], varactors [67] [68], tunable inductors [69] and transistors or

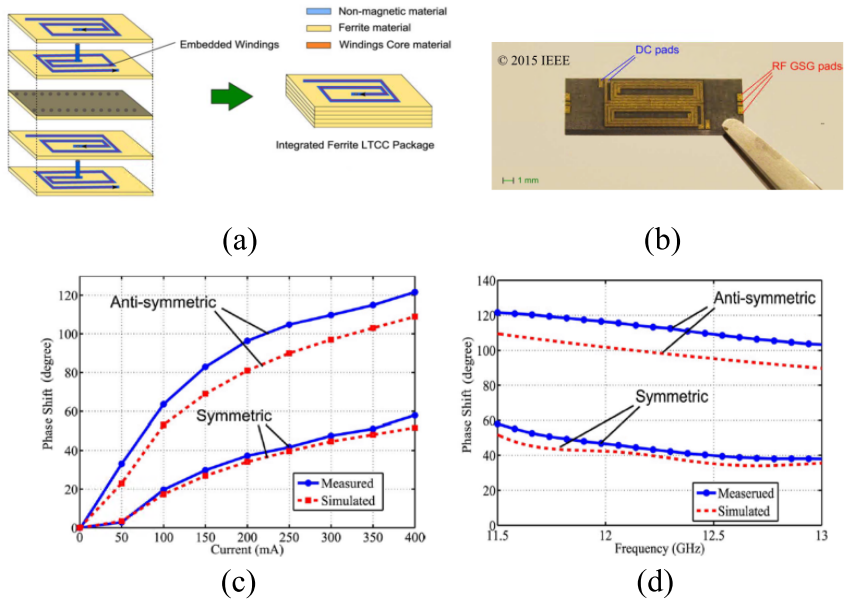

Figure 2.3. (a) The structure of a phase shifter based on substrate integrated waveguide (SIW) in ferrite low-temperature co-fired ceramic (LTCC) with embedded bias windings [64], (b) fabricated prototype of the phase shifter [64], (c) simulated and measured phase shift versus bias current at 11.5 GHz, and (d) phase shift versus frequency at 400 mA of bias current [64].

MEMS devices [70] [71], the phase shift can be adjusted within a specified range.

A) PIN diodes usually behave as switch maintaining two states, "ON" and "OFF," to generate a phase difference in between them. Therefore, in phase shifter units where only PIN diodes are involved in control, the phase shift values are typically discrete and fixed. For example, in [65], a phase shifter employed multiple cascaded reconfigurable defected microstrip structure (DMS) units, which was produced by adding a slot in a microstrip line and bridging it with PIN diodes. By controlling the PIN diodes between "ON" and "OFF" states, the DMS units generated phase shifts by altering the current paths. The performance of the phase shifter with varying numbers of DMS units was evaluated through simulations and experiments. In the case of a 9-DMS phase shifter, which is shown in Fig. 2.4, the highest measured insertion loss was 2.3 dB when all the PIN diodes were in the "OFF" state. Compared to the reference phase shift achieved when all the PIN diodes were in the "ON" state, the measured phase shifts at the other three states were 44°, 95°, and 143°, respectively.

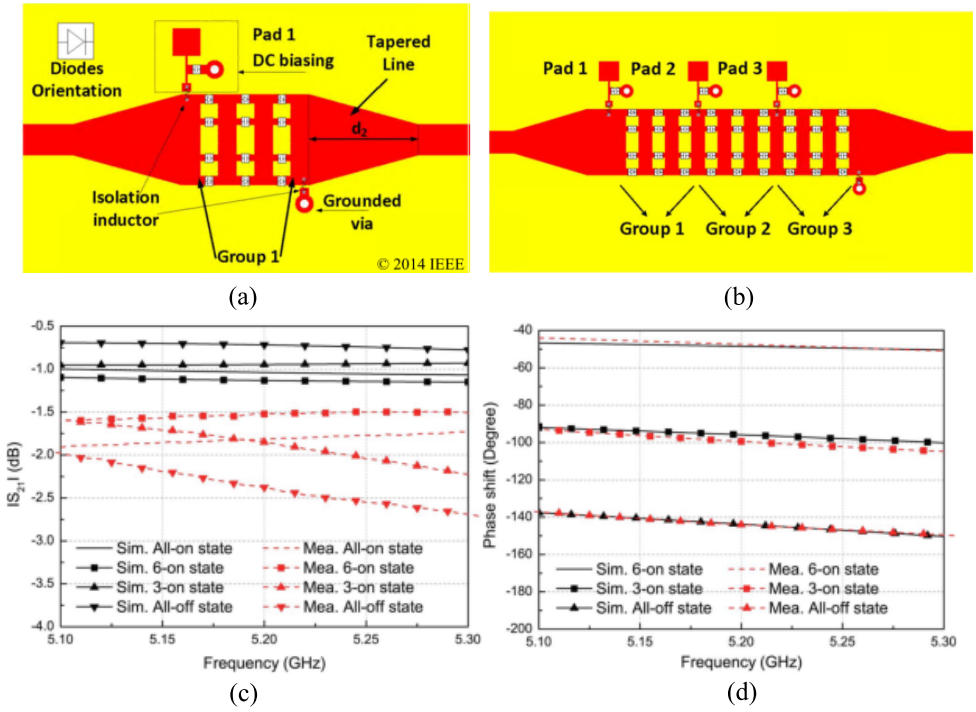

Figure 2.4. Prototypes of (a) the 3 units DMS phase shifter (1 group) [65], (b) the 9 units DMS phase shifter (3 groups) [65]. Simulated and measured results for the 9 units phase shifter [65], (c) the magnitude and (d) the phase shift of S_{21}.

B) Unlike the discrete and fixed phase shift values of phase shifters controlled by PIN diodes, varactor diodes offer the flexibility to continuously adjust the capacitance, enabling a continuous tuning of the phase shift. For example, a compact analog phase shifter based on varactor diodes and a coupled-line structure was employed to achieve continuous transmission phase ranging from 0° to 180° [68]. The structure of this compact analog phase shifter is displayed in Fig. 2.5. It consisted of two parallel coupling lines of equal length that were directly connected at one end and loaded with a varactor diode and a short-circuited stub. At the other end, two varactor diodes were connected in series between the parallel coupled lines, which were then linked to the ground through a microstrip line and a via hole. This phase shifter was tested to maintain its insertion loss between 0.95 and 1.35 dB at 5.6 GHz, and generally achieved less than 3 dB insertion loss from 5.35 to 6.32 GHz.

C) Tunable inductor-based phase shifters allow a wide range of phase tuning, involve low insertion loss, can provide good linearity, and enable high power levels. Additionally, they are relatively insensitive to temperature

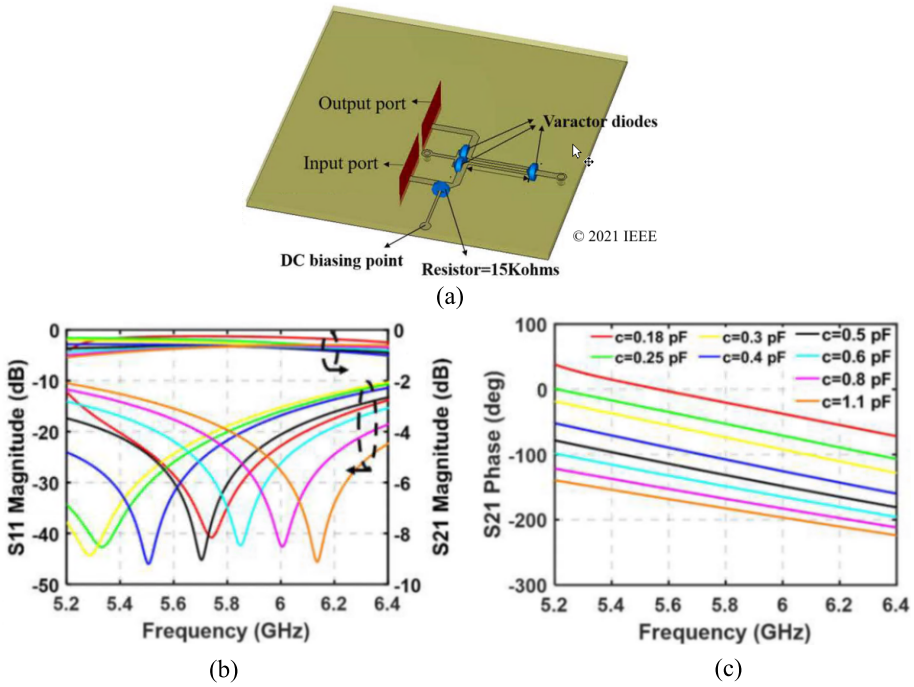

Figure 2.5. (a) Schematic of a compact 180° analog phase shifter, (b) simulated S-parameters of reflection and transmission magnitudes, and (c) transmission phases [68].

variations, providing more stable performance over temperature changes than their alternatives. In [69], a 3-D electrically tunable solenoid inductor was developed using a Permalloy (Py) thin film and surface micro-machining techniques. The unique magnetic core configuration allowed the inductor to operate over a wide frequency range. The inductance of the inductor was adjusted using DC current, achieving a tunability of over 10% with a 150 mA current. This tunable solenoid inductor was combined with a PZT-enabled metal-insulator-metal capacitor (Integrating lead zirconate titanate) to create a phase shifter with both inductive and capacitive tunability, which is shown in Fig. 2.6. Despite the merits mentioned above, tunable inductor-based phase shifters are typically larger and more complex compared to varactor-based phase shifters due to the inclusion of physical inductors and their tuning mechanisms. They may also require a higher DC power, which can be a limitation in low-power applications.

D) As for RF MEMS switches, they have gained wide popularity as a viable alternative to PIN diodes, field-effect transistors (FETs), and complementary metal-oxide-semiconductor (CMOS) transistors, due to their several advantages, such as low insertion loss, high linearity, wide bandwidth,

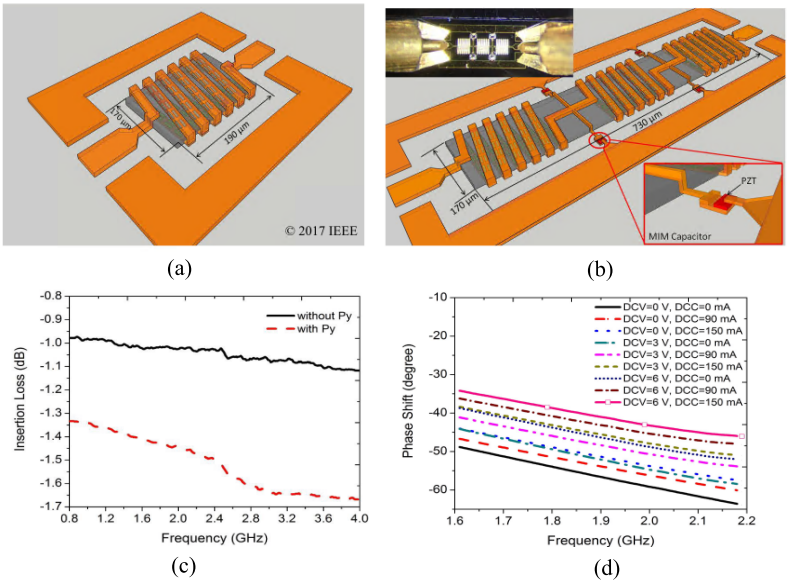

Figure 2.6. The schematic of (a) tunable inductor, and (b) tunable phase shifter with magnified view of capacitor. Measured (c) insertion loss of the inductor with or without Py thin film, and (d) phase shift of the device [69].

fast switching speed and high power handling abilities. For example, an RF MEMS-based phase shifter [71], which is shown in Fig. 2.7, was designed with high power handling capabilities, i.e., a measured third-order intercept point (IP3) exceeding 63 dBm. It also exhibited high phase and amplitude linearity, with a measured root mean square (RMS) deviation of less than $\pm 1.56^{\circ}$ and ± 0.16 dB, respectively. Furthermore, the measured insertion loss and return loss for the largest phase state were found to be 1.3 dB and 13 dB, respectively. However, compared to varactor-based phase shifters, RF MEMS phase shifters can be relatively expensive to manufacture, and may have a limited range of achievable phase shift with relatively high DC power consumption.

3) **Other type of analog phase shifters:** Other types of analog phase shifters include devices utilizing new materials such as graphene [72] or nanomaterial such as, $Ba_{0.7}Sr_{0.3}TiO_3$ [73]. Figure 2.8 shows a graphene-based phase shifter presented in [72], which was capable of achieving a maximum phase shift of 40° within the 5 to 6 GHz range, with an insertion loss of 3 dB.

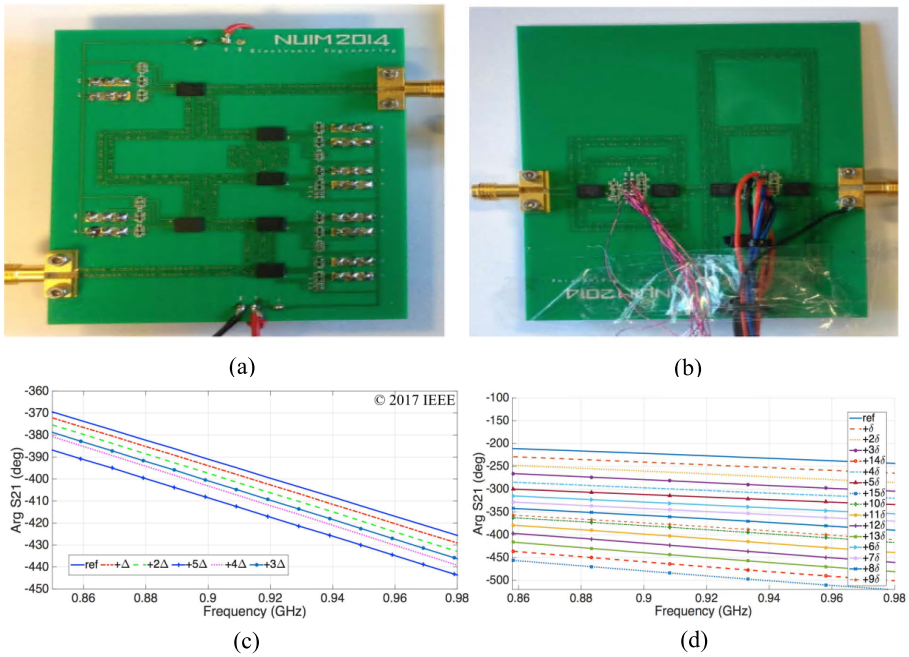

Figure 2.7. Prototypes of two-stage RF MEMS-based phase shifters with (a) small phase steps, (b) large phase steps, and measured phase states of (c) the small step phase shifter, and (d) large step phase shifter [71].

2.2.2 Summary

In summary, the choice of implementation method for a phase shifter depends on factors such as frequency range, desired phase resolution, insertion loss level, power consumption and geometry dimensions. Each approach offers its unique advantages and trade-offs in terms of performance, size, power consumption, and manufacturing complexity. The research work in this thesis majorly focuses on planar phase shifters suitable for compact, cost-effective, and reconfigurable microwave systems. Taking into account the advantages and disadvantages of the various options, varactor-based phase shifters are chosen as candidates and taken to in-depth research to address the challenges in their design. These findings will be analyzed in detail in Chapter 3.

2.3 Attenuators

Attenuators are widely used passive components in a variety of microwave applications. They serve multiple purposes, including limiting signal power levels, enhancing amplification stage matching, minimizing gain ripple, adjusting

power levels, and balancing power distribution among branches in power dividers [74].

Tunable attenuators have the capability to dynamically manipulate the signal strength within a system, making them highly versatile for various applications [75]. Planar tunable attenuators are characterized by their precise attenuation performance, power handling capability, impedance matching, compact size, and integration-friendly design. They are vital for achieving optimal signal management and performance in microwave systems.

2.3.1 Types of Planar Tunable Attenuators

Planar attenuators, commonly used in microwave systems, can be broadly classified into two categories based on their circuit structures: reflection-type attenuators and transmission-type attenuators. These two types employ different mechanisms to achieve signal attenuation. A more detailed explanation of each type is given in the following:

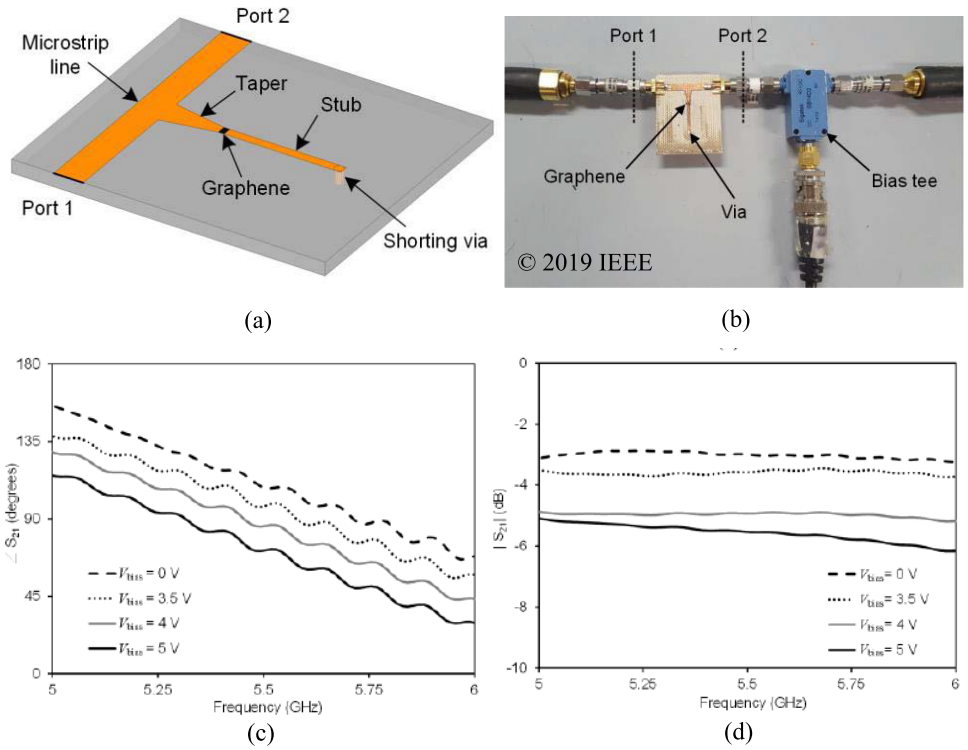

Figure 2.8. (a) Geometry of the graphene-based phase shifter, (b) prototype of the graphene-based phase shifter and the measurement setup [72]. Measured transmission characteristics of the phase shifter: (c) phase and (d) magnitude of S_{21} [72].

i) **Reflection-type attenuators:** These attenuators operate by controlling the reflection of the RF signal. Consequently, they need to employ dedicated structures that are designed to absorb the RF signal to be reflected, thereby achieving the desired attenuation level. Reflection-type attenuators are often implemented in multi-port devices such as 3-dB hybrid couplers [76] [77] [78], rat-race devices [35], and combined dividers [79] [80]. Figure 2.9 illustrates several typical reflection-type attenuators based on multi-port devices. A reflection variable attenuator in [77], which mainly consisted of a 3 dB quadrature coupler with 2 varactors to tune the attenuation from 2.2 to 17.0 dB in a bandwidth of 40% (2.8 to 4.2 GHz) is shown in Fig. 2.9(a). Another variable reflection-type attenuator is shown in Fig. 2.9(b) [78], which contained a 3-dB coupler, varactor diodes, and lumped components. By carefully manipulating the reflected signal, the attenuator could be effectively controlled, with an insertion loss of 1.3 dB and a minimum attenuation range of 36 dB from 2.3 to 2.7 GHz. The third example is a tunable attenuator illustrated in Fig. 2.9(c) [35], where the input signal was guided to enter a rat-race power splitter where two phase-opposite signals were generated. One signal then went through a common-gate FET biased in ON state, while the other signal passed through a second FET biased in the triode region. By tuning the gate voltage on the second FET, the amplitude of its signal was varied. After combining these two signals at the output, the variable attenuation was achieved from 6 to 30 dB with the operation band from 3.0 to 3.4 GHz. The advantage of reflection-type attenuators lies in their ability to control and manipulate the reflected signal. However, these attenuators typically require more complex circuits and may have larger physical size due to the additional structures involved in absorbing the reflected signals.

ii) **Transmission-type attenuators:** Unlike reflection-type attenuators, transmission-type attenuators allow the RF signal to pass through the attenuator without significant reflection. These attenuators employ a well-controlled signal absorbing mechanism that efficiently dissipates the desired amount of power, resulting in the expected attenuation level.

One of the key advantages of transmission-type attenuators is their compact structure and ease of circuit integration. This makes them particularly competitive in applications where space is limited or where seamless integration with other components is required.

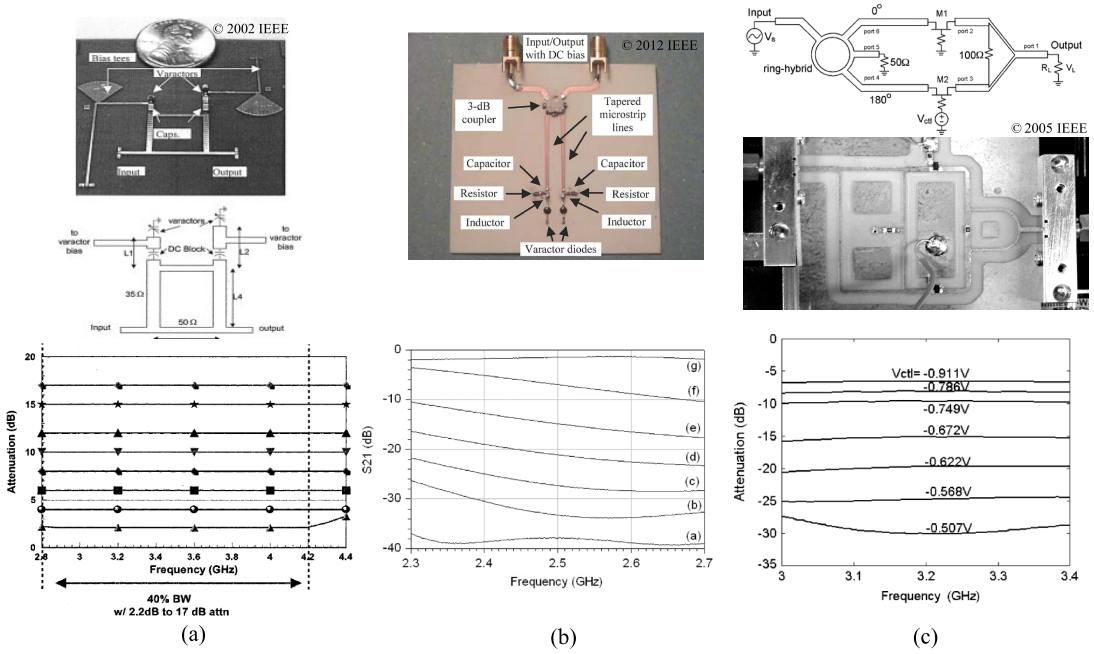

Figure 2.9. (a) Prototype and schematic diagram of a reflection-type attenuator and its measured tunable attenuation [77]. (b) Prototype of a 3 dB coupler-based impedance transformer attenuator and its measured tunable attenuation [78]. (c) Schematic diagram and prototype of an attenuator realized by a rat-race power splitter and a combiner and its measured tunable attenuation [35].

In summary, reflection-type attenuators manipulate the reflected RF signal to achieve attenuation, while transmission-type attenuators focus on controlling the signal absorption along a path for attenuation purposes. Each type has its own set of advantages and weaknesses to be considered, and the choice depends on specific application requirements, circuit design constraints, and the desired level of integration. This thesis mainly focuses on low-cost miniaturized planar microwave structures, which allow convenient circuit integration. Therefore, the focus of the research will be placed on transmission-type attenuators.

2.3.2 State-of-the-Art Transmission-Type Attenuators

Transmission-type attenuators enable the signals passing through while reducing their amplitude. However, they often suffer from a high return loss and from limitations in attenuation range [37]. To overcome these challenges, researchers have dedicated great efforts to investigate alternative materials like graphene, which offer tunable resistance under voltage control.

2.3.2 State-of-the-Art Transmission-Type Attenuators

While the literature on transmission-type attenuators is relatively limited, a notable development in recent years has been the emergence of graphene-based transmission-type attenuators. Before this, most transmission-type attenuators reported in the literature operated at fixed attenuation levels [81]. However, with the application of graphene as a new material, numerous transmission-type attenuators have been developed based on its unique characteristics. One of the most interesting features of graphene lies in its electronic conductivity which can be modified under proper bias voltage control, offering a wide range of values. This tunable conductivity characteristic enables the application of graphene in the development of tunable microwave attenuators [82]. Researchers have proposed utilizing this unique characteristic of graphene in various configurations of attenuators [83] [84] [85] [86]. In [83], a graphene-based attenuator with voltage-adjustable characteristics had been developed, which comprised a pair of LC bias circuits and microstrip lines. The attenuator operated within the frequency range of 0.1 to 5.0 GHz. The measured results demonstrated at 3 GHz an attenuation range from 7.0 to 17.9 dB by tuning a bias voltage from 0.0 to 5.5 V, as shown in Fig. 2.10. A flexible and stretchable attenuator was proposed in [84], which

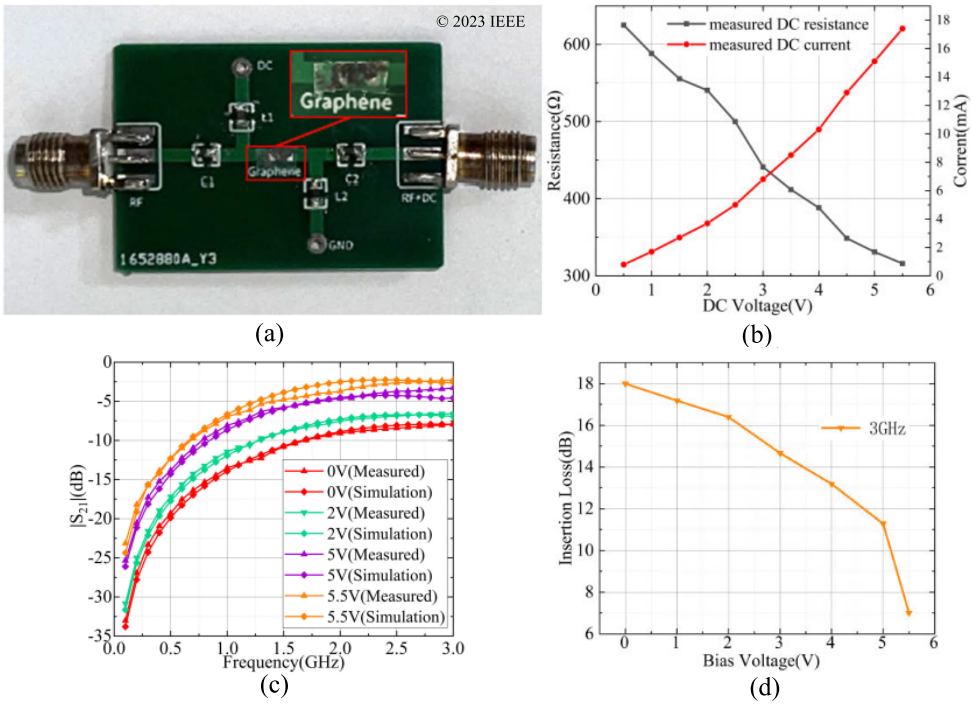

Figure 2.10. (a) Prototype of the graphene-based attenuator [83], (b) measured dc resistance and current versus bias voltage [83], (c) measurement and simulation results of attenuations at different voltages [83], and (d) insertion loss versus bias voltage at 3 GHz [83].

is shown in Fig. 2.11, utilizing coplanar waveguide (CPW) and graphene. The attenuator incorporated a graphene sandwich structure (GSS) on the CPW's upper surface which was made flexible and stretchable soft silicone elastomer and serpentine metal structures. By adjusting the surface impedance of the GSS with a bias voltage, the attenuation could be dynamically tuned within a range from 3 to 9 dB at 2.45 GHz, from 4 to 11 dB at 3.6 GHz, and from 5.4 to 13.0 dB at 5 GHz. with a reflection coefficient below -10 dB. Another tunable grounded

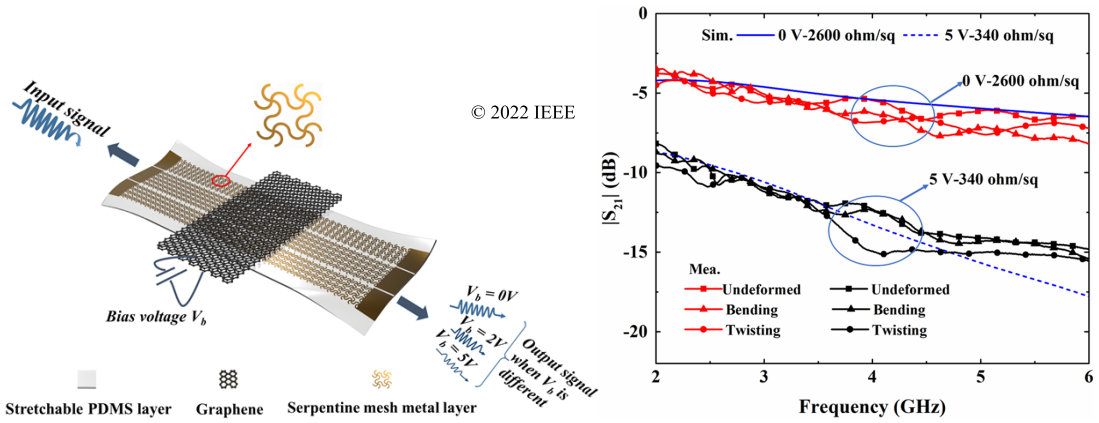

(a) (b)

Figure 2.11. (a) Structure and working principle of the tunable attenuator in [84] and (b) simulated and measured attenuations without GSS and with a 25 mm GSS in different surface impedances from 2 to 6 GHz [84].

coplanar waveguide (GCPW) attenuator based on graphene nanoplates was proposed in [86] and is shown in Fig. 2.12. It consisted of a 50 Ω GCPW transmission line with three pairs of graphene nanoplate pads embedded in the gaps between the signal line and upper metal ground. By tuning the bias voltages on the graphene, the resistance of graphene was controlled so as to obtain a tunable attenuation level. The attenuator supplied an attenuation from 2.5 to 14.0 dB with a reflection coefficient below -12 dB from 18 to 28 GHz. Large attenuation levels and broadband operation were demonstrated in this work, however at the cost of a large insertion loss level (minimum attenuation). The device also required a complex circuit for bias voltages or a bias-tee block for tunable operation. Additionally, these attenuators were based on non-standard fabrication techniques and materials, and thus might not be practically ready for mass production.

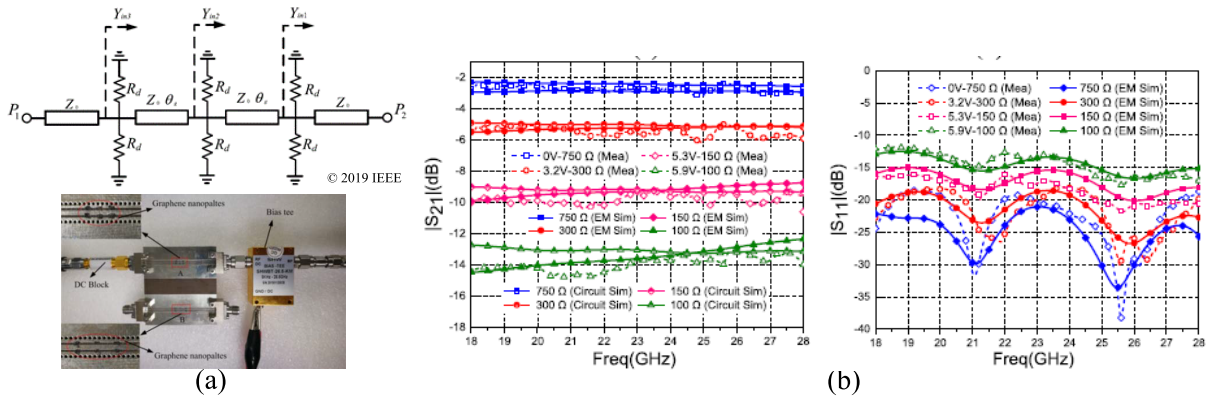

Figure 2.12. (a) Equivalent circuit and photographs of the GCPW attenuator [86], (b) transmission and reflection responses of the attenuator from 18 to 28 GHz as the distance between two graphene pads is 2 mm [86].

Besides graphene-based composites, different technologies have been employed to achieve tunability, such as PIN diodes [87] [88], RF-MEMS technology [89] [90], and FETs [91].

In [87], a filtering attenuator was designed based on a traditional microstrip line bandpass filter with PIN diodes, which were used as variable resistors to provide the selection of the operation band and the tunable attenuation, as shown in Fig. 2.13. The filtering attenuator obtained a tunable attenuation from 3.8 to 30.4 dB with a minimum return loss of 10 dB covering the operation band from 2.19 to 2.6 GHz.

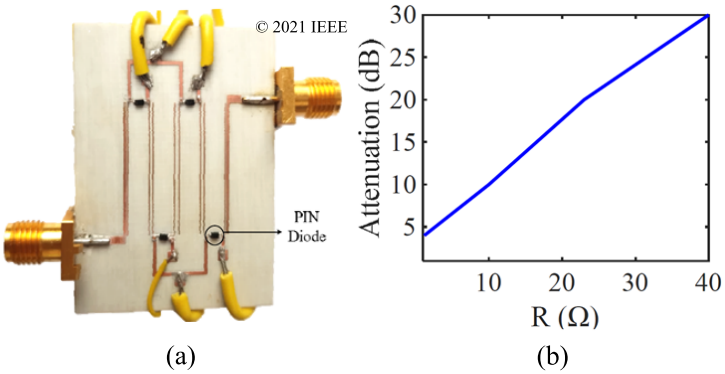

Figure 2.13. (a) Prototype of a filtering attenuator [87], and its (b) measured attenuation level when varying the forward bias resistance R of the PIN diode.

Figure 2.14 illustrates a planar RF MEMS-based attenuator, which was based on a meandered GCPW line with a low-resistivity silicon over it. A planar spiral coil

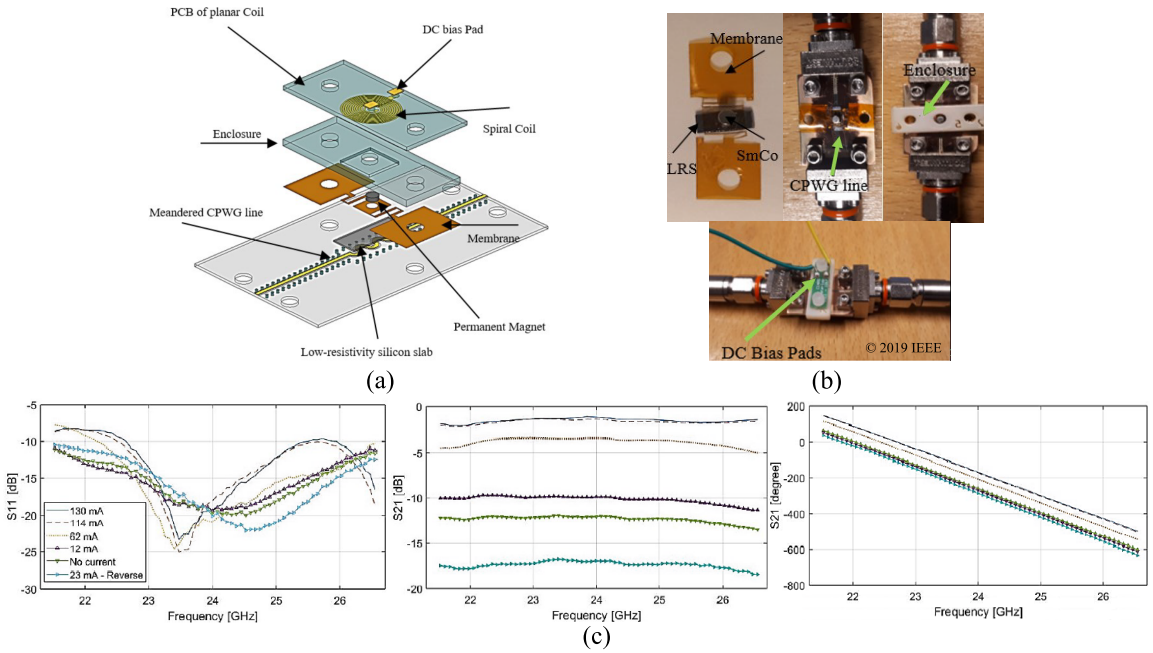

Figure 2.14. (a) 3D view of a planar RF MEMS-based attenuator [89], with (b) details of the assembly of the attenuator, c) measured results for 6 attenuation levels, from left to right: reflection coefficient, insertion loss and phase response of the attenuator [89].

and a magnetized permanent magnet were used to provide the magnetic force to produce the attenuation. The attenuator achieved an attenuation range of 16 dB with the insertion loss less than 1.2 dB from 21.5 to 26.5 GHz.

According to all the aforementioned examples , the tunability of a transmission-type attenuator is typically realized either through the use of new materials such as graphene, or various types of electronic components. It remains a research challenge to achieve an attenuator with specific characteristics, including large attenuation range, small minimum attenuation (i.e., insertion loss), small reflection and minimal phase shifting during adjustment of the attenuation level. Moreover, an ideal design should be compact, cost-effective, and controllable through simple and stable DC-control circuits (e.g., without the need of a bias-tee). It is a significant challenge to simultaneously obtain all these desired features, particularly for compact microwave systems operating within cost constraints and limited space scenarios.

2.3.3 Summary

To tackle the challenge of planar attenuators, the thesis has taken into account the advantages and disadvantages of the various methods reviewed in this section. Specifically, a varactor-based transmission-type attenuator has been chosen as a candidate for further in-depth research. In Chapter 6, the findings regarding a proposed novel configuration of attenuator will be thoroughly analyzed and discussed.

2.4 Diplexers

2.4.1 Diplexer Devices

A diplexer is a passive electronic device that combines or separates two or more different frequency bands on a shared transmission line. It enables simultaneous transmission and reception of signals in different frequency ranges sharing a single antenna or transmission line. This functionality makes diplexers essential components in various communications systems, including wireless networks, satellite systems, and radar systems.

In recent times, the concept of reconfigurable diplexers has become a viable solution for reconfigurable systems [92]. According to existing literature, based on the type of frequency tunability, reconfigurable diplexers can be generally classified in two categories, namely tunable diplexers and switchable diplexers.

i) **Tunable diplexers:** Tunable diplexers are usually realized by using two individually tunable filters [92] or resonators [93] [94], which are combined into one device. Three typical tunable diplexers are illustrated in Figs. 2.15 - 2.17. A tunable diplexer involving two tunable three-pole filters with high selectivity is shown in Fig. 2.15. One of these filters was optimized for high rejection at the lower frequency side, making it suitable as the higher channel branch of a diplexer. The other filter was optimized for high rejection at the higher frequency side, making it suitable for the lower channel branch of the diplexer. By combining these filters, a tunable three-pole diplexer with independent tuning of the lower and higher channel was created, where the insertion losses were 2.5 - 4.0 dB in the lower channel and 3.0 - 4.9 dB in the

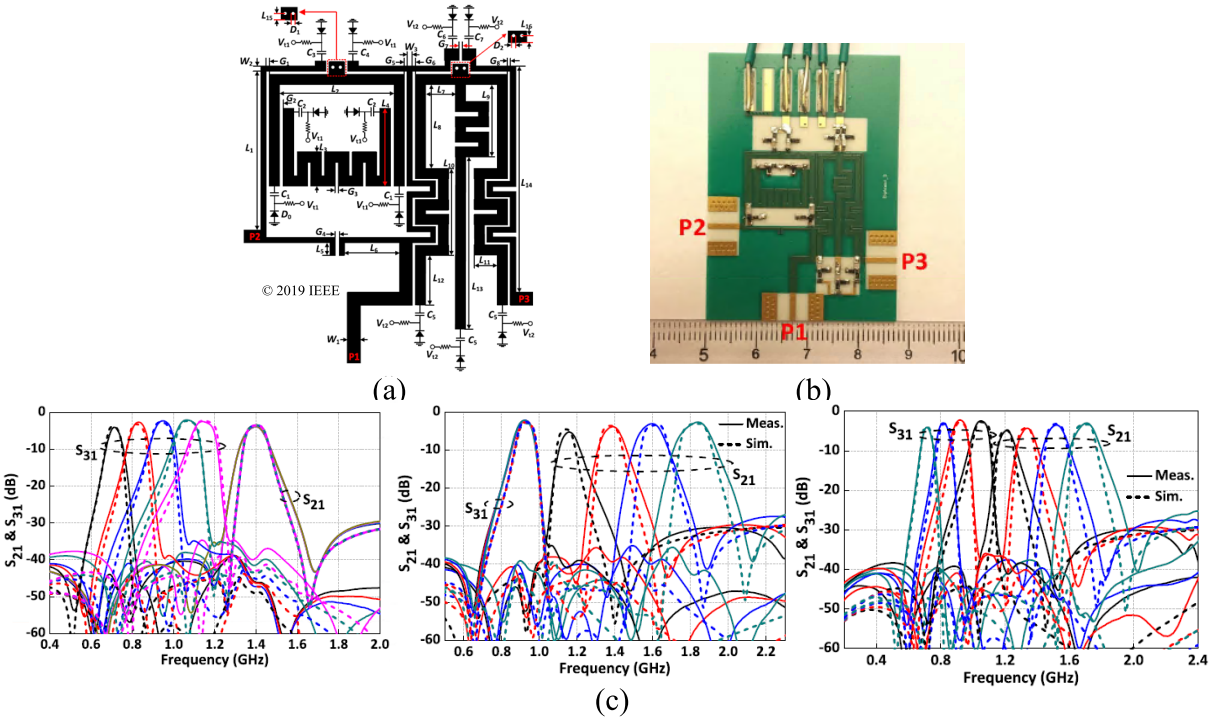

Figure 2.15. (a) Configurations of tunable diplexers with two tunable filters [92], (b) photograph of the fabricated tunable diplexer [92], and (c) measured and simulated S-parameters, from left to right: for the higher channel fixed, for the lower channel fixed and for both channels tuned [92].

higher channel. It covered the frequency range of 0.72 to 1.84 GHz with a high isolation of 39 dB. A compact microstrip diplexer was proposed with the ability to tune the center frequencies and reconfigure the filtering characteristics of both channels [94]. The diplexer consisted of two different dual-mode square loop resonators, as shown in Fig. 2.16. The center frequencies of both channels were adjusted independently by varactors. The reconfigurable filtering characteristics, namely transmission zeros, of both channels were created by selecting dedicated values for the perturbation and reference capacitances. As an example shown in Fig. 2.16(c), the centre frequency of the first channel was tuned for two filtering characteristics having left or right side transmission zero. Figure 2.17 illustrates a tunable diplexer, which had a compact structure obtained by combining two passband filters and a shared common resonator [93]. The diplexer was able to tune the desired frequencies in two channels either independently or simultaneously as displayed in Fig. 2.17(c). The tunable low channel was from 1.28 to 1.78 GHz with insertion loss between 2.0 dB and 2.5 dB, while the high channel was

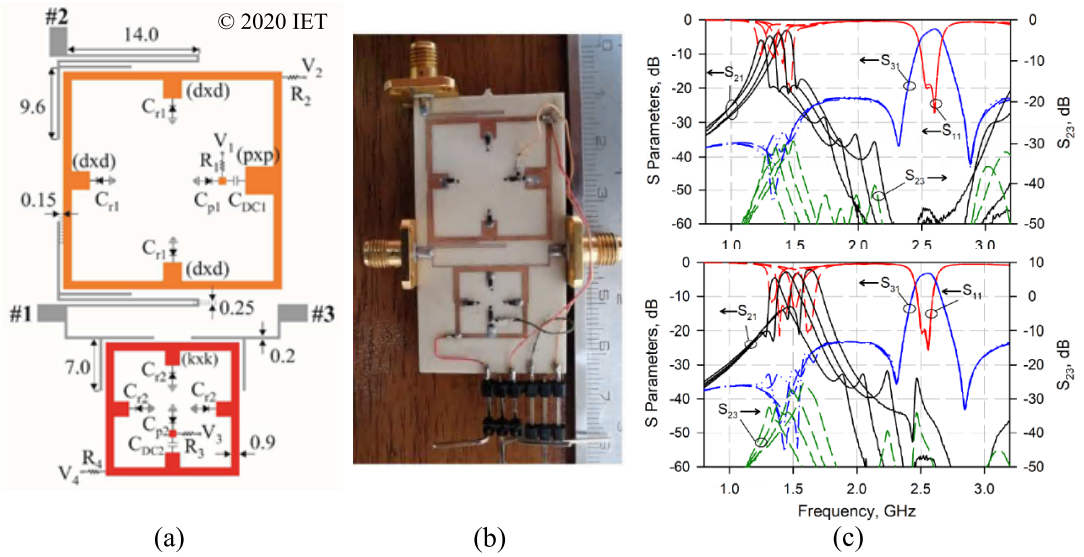

Figure 2.16. (a) Configurations of tunable diplexers with two dual-mode square loop resonators [94], (b) photograph of the prototype of the diplexer [94], and (c) first channel of the diplexer with right-side transmission zero and left-side transmission zero [94].

from 1.95 to 2.35 GHz with the insertion loss from 4.8 to 6.6 dB. The isolation between the two channels was larger than 35 dB. Generally, tunable diplex-

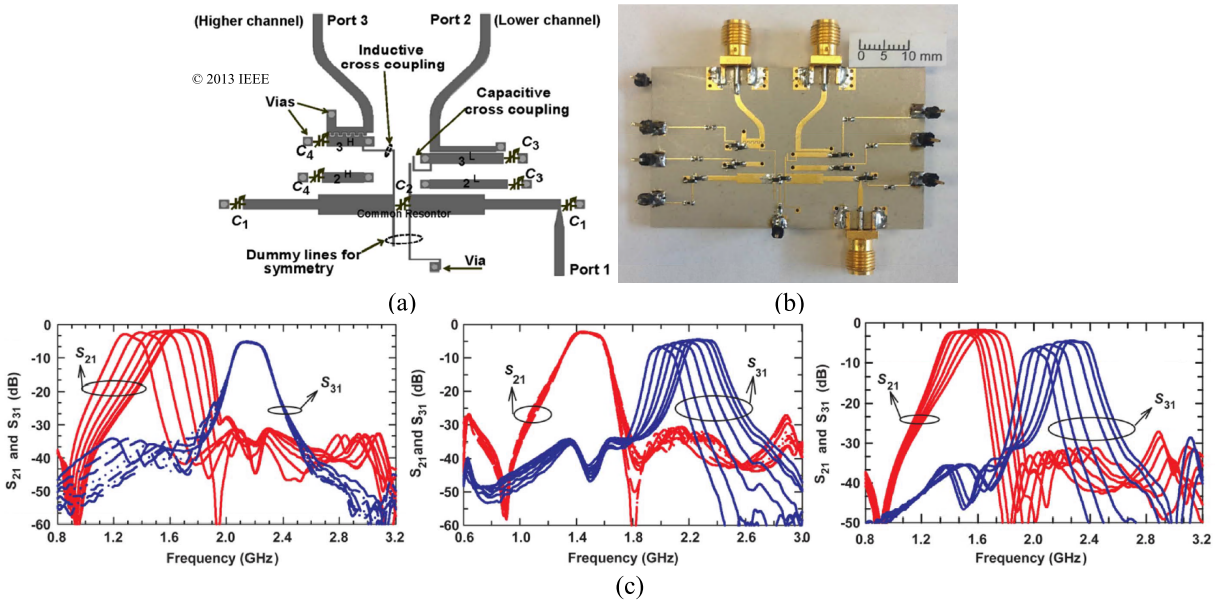

Figure 2.17. (a) Configurations of tunable diplexers with two passbands filters and a common resonator [93], (b) prototype of the diplexer [93], and (c) measured $|S_{21}|$, $|S_{31}|$, from left to right, tuning low channel with high channel fixed, tuning high channel with low channel fixed, and tuning both channels [93].

ers can produce a large frequency tuning range, but suffer from a relative high insertion loss level and require complex structures.

ii) **Switchable diplexers:** In contrast to tunable diplexers, switchable diplexers normally offer a lower insertion loss which is generally desired for most applications. A quasi-elliptic band-pass filter (QE-BPF), was proposed firstly in [95], with a combination of a shorted stepped-impedance resonator (SSIR) and a dual-mode resonator (DMR). Then, two switchable band-pass filters (SW-BPF) were employed at 900 and 1250 MHz respectively, by loading PIN diodes at two open ends of the DMR or SSIRs. Consequently, a switchable diplexer was created from a T-junction combined with the two 900 and 1250 MHz SW-BPFs. The fabricated QE-BPF, as shown in Fig. 2.18(a), offered four operation states with different on/off combinations of the used PIN diodes, which is illustrated in Fig. 2.18(b). The diplexer exhibited a low insertion loss of 1.92 dB at 900 MHz and 2.08 dB at 1250 MHz, and a high isolation of more than 51 dB. Another switchable diplexer proposed

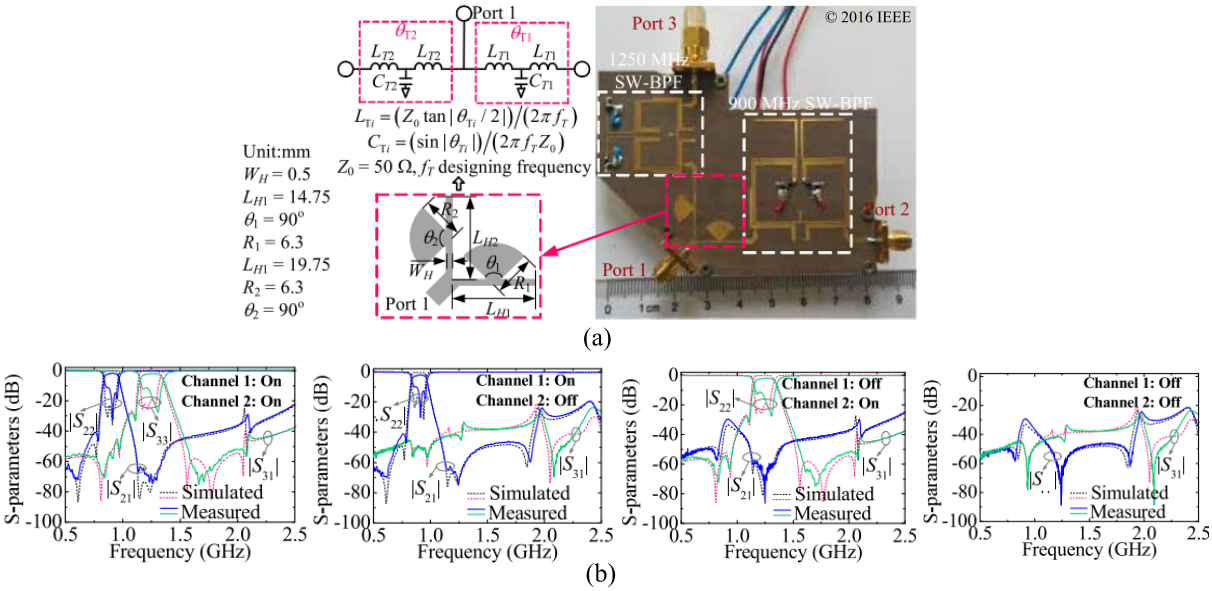

Figure 2.18. (a) Prototype of 900/1250 MHz switchable diplexer [95], and (b) simulated and measured results of the switchable diplexer with two channels operating in four states, namely from left to right, ON/ON, ON/OFF, OFF/ON, OFF/OFF [95].

in [96] was composed of four major parts, namely a stepped-impedance distributed coupling feeding line, four different quarter-wavelength stepped-impedance resonators (SIRs), two shunt open stubs and two PIN diodes

with their bias circuitry. The proposed diplexer, which is shown in Fig. 2.19, exhibited compactness, wide stopband, high selectivity, and independently controlled channels. The switchable diplexer enabled four operation states selected by PIN diodes utilized in two channels with center frequency of 1.2 GHz and 1.5 GHz respectively. When the PINs were all ON, the insertion losses were 2.10 dB at 1.2 GHz and 2.21 dB at 1.5 GHz, and the isolation between the two channels was up to 40 dB. As for the other states, the insertion losses at the stop channel were more than 30 dB.

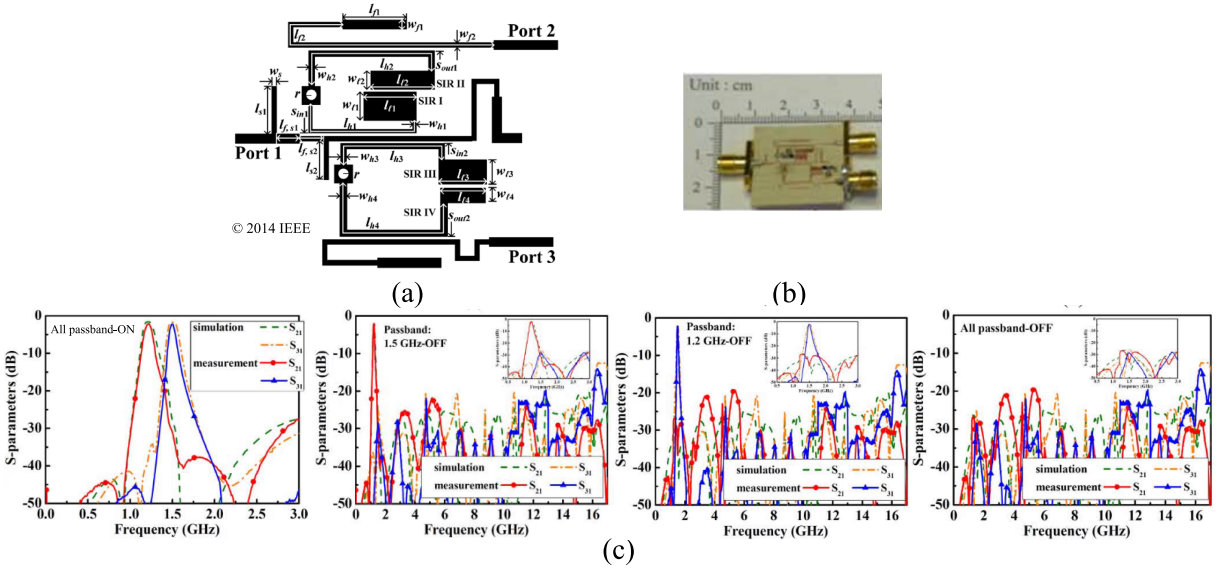

Figure 2.19. (a) Configurations of a high-isolation switchable diplexers with ultra-wide stopband [96], (b) photograph of the fabricated switchable diplexer [96], and (c) simulated and measured *S*-parameters of the switchable diplexer in four states, namely from left to right, ON/ON, ON/OFF, OFF/ON, OFF/OFF [96].

Although the switchable diplexer displays compact size and low insertion loss level, it only worked at one frequency channel at a time.

2.4.2 Summary

Based on the literature review, it is concluded that a tunable diplexer has typically the capability to allow a large dynamic frequency tuning span, but this feature is generally accompanied by a high insertion loss level, which is not desired in applications. Switchable diplexers offer much smaller insertion loss with compact

size but suffer from a relative complex structure and their operating frequencies or bands are fixed.

To address the challenges of the switchable diplexers, the research presented in this thesis has taken into account the advantages and disadvantages of various methods. A varactor-based frequency-switchable diplexer with simple topology has been identified as a desirable aim in this thesis. In Chapter 7, the findings on a novel topology of diplexer proposed in this work will be comprehensively analyzed and discussed.

2.5 Reconfigurable Antennas

2.5.1 Reconfigurable Antennas

In addition to the multifunctional demands of microwave devices, there is a growing need for multifunctional antennas in modern communications and radar systems. Reconfigurable antennas have emerged as an increasingly popular solution to fulfill these requirements.

In [97], a frequency- and pattern-reconfigurable two-element array was proposed, which is shown in Fig. 2.20. The radiators were implemented by two varactor-based open-end stubs which were controlled by two separate bias voltages. By tuning the bias voltages applied on the varactors, the resonances of the two patches were detuned slightly and a phase difference between them was created. The array operated in a frequency tuning range from 2.15 to 2.38 GHz with a pattern continuously scanning from -23° to +23° across broadside. Figure 2.21 illustrates a frequency- and pattern-reconfigurable antenna, which contained a rectangular patch connected with two slots by two pairs of PIN diodes [98]. Using different combinations of the four diodes states, the patch could be configured to operate at 4.5 and 4.8 GHz or 5.2 and 5.8 GHz with radiation pattern maxima switchable to 0°, +30° and -30°. Another frequency- and pattern-reconfigurable slot antenna [99] is shown in Fig. 2.22, which consisted of two switches allowing to select three frequency bands, i.e., 1.82 (F_1), 1.93 (F_2) and 2.10 GHz (F_3), and four slots at the edge of the ground loaded with three switches in each to allow beam steering to three angles, i.e., 0°, +15° and -15°. By utilizing 14 switches, the antenna offered 18 operation states, as shown in Fig. 2.22(c).

2.5.1 Reconfigurable Antennas

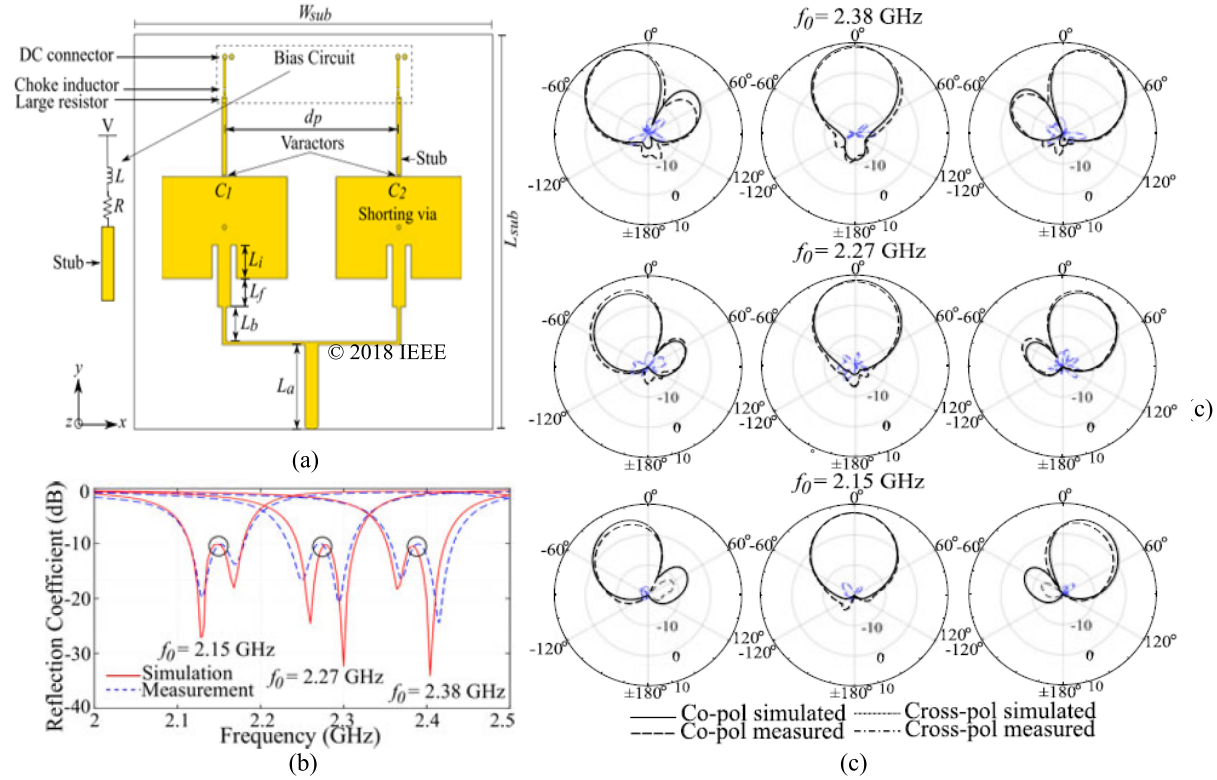

Figure 2.20. (a) Configurations of frequency- and pattern-reconfigurable antennas utilizing stub-loaded varactors and excited by a T-junction power divider [97], (b) reflection coefficient for different combinations of bias voltages for scanning operation [97], and (c) realized gain patterns at f_0 = 2.38, 2.27, and 2.15 GHz from top to bottom. [97].

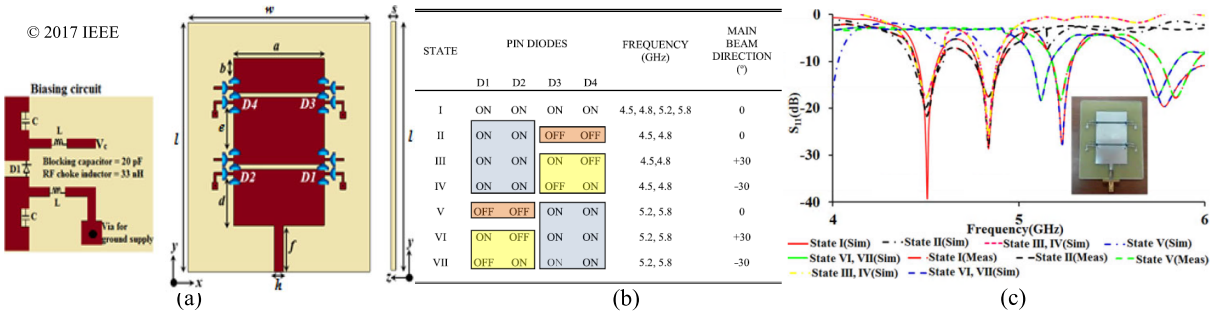

Figure 2.21. (a) Configurations of frequency- and pattern-reconfigurable antennas connected with two slots using a pair of PIN diodes on each slot [98], (b) operation states of the antenna [98] (Grey boxes: frequency reconfiguration, Yellow / orange boxes: pattern reconfiguration in frequency reconfigured states), and (c) simulated and measured S-parameters of the antenna [98], insert: the prototype of the antenna.

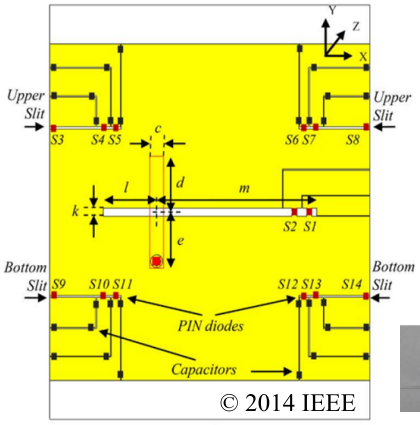

(a)

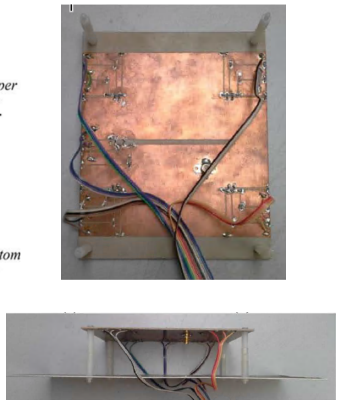

(b)

Freq	Beam angle	S1	S2	Switch - upper part slits					
				S3	S4	S5	S6	S7	S8
F1	0^0	0	0	0	0	0	0	0	0
	$+15^0$	0	0	1	1	1	1	1	1
	-15^0	0	0	0	0	0	0	0	0
F2	0^0	0	1	0	0	0	0	0	0
	$+15^0$	0	1	1	1	1	1	1	1
	-15^0	0	1	0	0	1	1	0	0
F3	0^0	1	1	0	0	0	0	0	0
	$+15^0$	1	1	1	1	1	1	1	1
	-15^0	1	1	0	1	1	1	1	0
Freq	Beam angle	S1	S2	Switch - bottom part slits					
				S9	S10	S11	S12	S13	S14
F1	0^0	0	0	0	0	0	0	0	0
	$+15^0$	0	0	0	0	0	0	0	0
	-15^0	0	0	1	1	1	1	1	1
F2	0^0	0	1	0	0	0	0	0	0
	$+15^0$	0	1	0	0	1	1	0	0
	-15^0	0	1	1	1	1	1	1	1
F3	0^0	1	1	0	0	0	0	0	0
	$+15^0$	1	1	0	1	1	1	1	0
	-15^0	1	1	1	1	1	1	1	1

* 1 = ON, * 0 = OFF

(c)

Figure 2.22. (a) Configurations of frequency- and pattern-reconfigurable antennas incorporating fourteen switches [99],(b) photographs of the fabricated antenna [99], and (c) switch configuration of the antenna [99].

These reconfigurable antennas mostly incorporate several electronic components to tune their operation bands and pattern directions. In general, the complexity of the antenna will increase with the number of tuning components required, and the corresponding loss will similarly increase and affect the overall performance of the antenna. Therefore, there is a need to implement pattern- and frequency-reconfigurable antennas with simple, compact and low loss tuning structures.

2.5.2 Summary

There are various ways to load electronic components on planar antennas to achieve changes in their electrical lengths and thus achieve reconfigurabilities. However, increasing the number of components loaded on the radiators generally leads to a relative bulky size, increased losses and costs. Therefore, there is a high potential in exploring reconfigurable antennas with simple structure and multiple reconfiguration modalities, as will be discussed in this thesis in Chapter 4 and Chapter 8, based on reconfigurable feeding networks using the tunable components proposed in the other chapters of the thesis.

2.6 Conclusion

This chapter has reviewed the research literature on phase shifters, attenuators and diplexers utilized in planar microwave applications. The major types of these devices, with their advantages and disadvantages, have been analyzed, which lead to selecting the aims of this thesis according to challenges that still need to be addressed. The literature review has also included typical frequency- and pattern-reconfigurable antennas, where complicated electronic components and control circuits are typically integrated with the radiators, which leads to antennas of high complexity and fabrication cost. As a result, it is highly desired to design multi-functional reconfigurable antennas with low complexity to minimize the manufacture costs. One promising approach is to design planar low-cost reconfigurable feeding networks to realize these antennas.

The research dedicated to reconfigurable devices presented in this thesis, i.e., phase shifters, attenuators and diplexers, is aiming to create the building blocks for a reconfigurable feeding network. The main goal is to provide a simple and multifunctional feeding topology, which is able to control the characteristics of the signals transmitted to the radiators, including phase, amplitude and frequency. Fed by such a feeding structure, a multi-element antenna or array can achieve reconfigurabilities without excessive structural complexity and with a relatively small number of lumped components on the radiators, with the aim of creating compact and low-cost devices for wireless communications applications.

To illustrate the benefits of the proposed tunable components, implementations of reconfigurable feeding networks embedded in antenna systems will be also proposed in the thesis. Chapter 4 will involve a beam-steerable antenna array with pattern- and frequency-reconfiguration fed by a reconfigurable feeding network, which is seamlessly integrated with three phase shifter pairs operating in differential mode. Chapter 8 will discuss a pattern- and frequency-reconfigurable antenna array without additional electronic components on the radiators. Exploiting the effect of a metallic isolation plate in between the two elements, a demonstration of both pattern and frequency reconfigurabilities will be presented.

Chapter 3

Varactor-Based Phase Shifters

PHASE shifters are fundamental and essential components for microwave and antenna engineering. In particular for phased arrays and pattern-reconfigurable antennas, the characteristics of the phase shifters critically determine the beam scanning capability. Focusing now on continuously tunable phase shifters, the most critical challenge remains achieving the maximum phase shift at the lowest complexity level, e.g., by using a topology that minimizes the number of cascaded unit structures. This objective is accompanied by the need to maintain a compact device size and minimize insertion loss.

To address this challenge, this chapter proposes a novel concept of varactor-based phase shifter operating in differential pair for beam-steerable antennas. Thanks to the differential pair configuration, the phase shifter element requires much less phase dynamic range compared to conventional phase shifters. The basic phase-tuning unit contains a 50 Ω host microstrip line, with several identical shorted-stub-loaded varactors mounted on its edge. A differential phase shifter pair with three identical stubs offers a full 360° phase difference span with a straightforward topology and relatively low insertion loss. Its design allows for seamless integration on a 50 Ω host microstrip line within microwave networks, ensuring compactness and reducing the need for additional space in the system to accommodate the phase shifter pairs.

Statement of Authorship

Title of Paper	Varactor-Based Phase Shifters Operating in Differential Pairs for Beam-Steerable Antennas
Publication Status	☑ Published ☐ Accepted for Publication ☐ Submitted for Publication ☐ Unpublished and Unsubmitted w ork w ritten in manuscript style
Publication Details	IEEE Transactions on Antennas and Propagation, vol. 70, no. 9, pp. 7670–7682, 2022

Principal Author

Name of Principal Author (Candidate)	Yuan YUAN		
Contribution to the Paper	Under the supervision of C. Fumeaux and S. J. Chen, I performed the design, simulation, prototype development, measurements and wrote the manuscript for submission.		
Overall percentage (%)	60%		
Certification:	This paper reports on original research I conducted during the period of my Higher Degree by Research candidature and is not subject to any obligations or contractual agreements with a third party that would constrain its inclusion in this thesis. I am the primary author of this paper.		
Signature		Date	26/07/2023

Co-Author Contributions

By signing the Statement of Authorship, each author certifies that:

i. the candidate's stated contribution to the publication is accurate (as detailed above);

ii. permission is granted for the candidate in include the publication in the thesis; and

iii. the sum of all co-author contributions is equal to 100% less the candidate's stated contribution.

Name of Co-Author	Christophe Fumeaux		
Contribution to the Paper	I acted as supervisor for the candidate, aided in design, development, and measurements, revising the manuscript, and evaluating the final version of the manuscript. I give consent for Yuan YUAN to present this paper for examination towards the Doctorate of Philosophy.		
Signature		Date	27/07/2023

Name of Co-Author	Shengjian Jammy Chen		
Contribution to the Paper	I acted as supervisor for the candidate, aided in design, development, and measurements, revising the manuscript, and evaluating the final version of the manuscript. I give consent for Yuan YUAN to present this paper for examination towards the Doctorate of Philosophy.		
Signature		Date	29/07/2023

Please cut and paste additional co-author panels here as required.

Statement of Authorship

Title of Paper	Varactor-Based 360° Differential Phase Shifter Pair
Publication Status	☑ Published ☐ Accepted for Publication ☐ Submitted for Publication ☐ Unpublished and Unsubmitted w ork w ritten in manuscript style
Publication Details	2023 5th Australian Microwave Symposium (AMS), Melbourne, Australia, 2023, pp. 29-30, doi: 10.1109/AMS57822.2023.10062325

Principal Author

Name of Principal Author (Candidate)	Yuan YUAN
Contribution to the Paper	Under the supervision of C. Fumeaux and S. J. Chen, I performed the design, simulation, prototype development, measurements and wrote the manuscript for submission.
Overall percentage (%)	60%
Certification:	This paper reports on original research I conducted during the period of my Higher Degree by Research candidature and is not subject to any obligations or contractual agreements with a third party that would constrain its inclusion in this thesis. I am the primary author of this paper.
Signature	Date 26/07/2023

Co-Author Contributions

By signing the Statement of Authorship, each author certifies that:

i. the candidate's stated contribution to the publication is accurate (as detailed above);

ii. permission is granted for the candidate in include the publication in the thesis; and

iii. the sum of all co-author contributions is equal to 100% less the candidate's stated contribution.

Name of Co-Author	Christophe Fumeaux
Contribution to the Paper	I acted as supervisor for the candidate, aided in design, development, and measurements, revising the manuscript, and evaluating the final version of the manuscript. I give consent for Yuan YUAN to present this paper for examination towards the Doctorate of Philosophy.
Signature	Date 27/07/2023

Name of Co-Author	Shengjian Jammy Chen
Contribution to the Paper	I acted as supervisor for the candidate, aided in design, development, and measurements, revising the manuscript, and evaluating the final version of the manuscript. I give consent for Yuan YUAN to present this paper for examination towards the Doctorate of Philosophy.
Signature	Date 29/07/2023

Please cut and paste additional co-author panels here as required.

3.1 Introduction

PHASE shifters enable precise control over the phase of RF signals. This control is essential for tasks such as beamforming, steering antenna arrays, controlling interference, and adjusting the phase relationship between different signals. For designs with emphasis on versatility, a continuously tunable phase shift is generally desirable.

Focusing on continuously tunable phase shifters, many attempts have been made to achieve a large phase tuning range, a low insertion loss, a low fabrication complexity and a reasonable cost [100–108]. For example, in [100], a phase shifter utilizing 11 Barium strontium titanate (BST) Metal-Insulator-Metal varactors was proposed, which reached a phase shift of 260° with maximum bias voltages up to 50 V and an insertion loss below 5.9 dB. In [102] a phase shifter was reported based on a reconfigurable impedance surface, and it contained 15 cascaded dipole-loaded varactors providing a phase shift of 464° with maximum insertion loss of 4.2 dB at 9.16 GHz. In [103], the authors proposed a metamaterial phase shifter that could supply 0° - 190° phase range at 7.2 GHz, containing 4 left-hand transmission-line units with 8 varactors and achieving an insertion loss below 3.5 dB from 7.2 to 8.7 GHz. A composite right/left-handed transmission line with 15 varactors achieved a continuously tunable phase-shift of approximately 360° at 2.4 GHz with an insertion loss below 2.5 dB [104]. In [105], a phase shifter featuring a 360° tunable phase variation and an insertion loss below 2.4 dB at 1 GHz was proposed, with 9 cascaded varactors. Usually, a larger number of cascaded structures will result in a larger phase shift span, however at the cost of a higher insertion loss, a larger size and a more complex control circuitry.

There exist other phase shifter types which use a small number of cascaded structures to realize a large phase tuning range, however with a large device geometry and a relatively high loss. A reflection-type phase shifter based on 2 varactors with a size of $1.24\lambda_0 \times 0.46\lambda_0$ was reported in [101]. It produced a 290° continuously tunable phase shift with an insertion loss below 3.5 dB. As demonstrated in [106], another reflection-type phase shifter containing only 2 varactors produced 0° - 190° phase difference with an insertion loss lower than 2.3 dB from 9 to 11 GHz. Similarly in [107], a device with 4 varactors resulted in a 0° - 360° phase range and 4.4 dB insertion loss at 2 GHz. In contrast, a phase shifter based on nonuniform transmission lines comprising 3 end-shorted varactors was proposed in [108] with an insertion loss of less than 1.3 dB. However, this phase shifter realized a relatively small phase tuning range

of 90°. Therefore, achieving a maximum phase shift with a minimum number of cascaded unit structures, while maintaining a small device size and low insertion loss is always the most critical challenge for this type of phase shifters.

In this chapter, a varactor-based phase shifter pair operating in differential mode to generate a 0° - 360° phase shift is proposed. The basic phase-tuning unit contains a shorted-stub-loaded varactor connected to the edge of a 50 Ω transmission line. The proposed geometry features low insertion loss and ease of integration to planar transmission lines. A design incorporating three cascaded phase-tuning stubs is identified as a practical solution to provide a nearly full 360° phase, with a maximum insertion loss of not higher than 1.74 dB at the center frequency of 5.00 GHz and 2.04 dB across the tunable operation range of 4.75 to 5.25 GHz. In addition, an accurate equivalent circuit model for the phase shifter is developed to implement a fast design and optimization process. Furthermore, a second enhanced design based on a similar phase shifter topology is presented in the second part of the chapter. It also consists of 3 shorted-stub-loaded varactors, however it can achieve a full 360° continuous phase tuning with a maximum insertion loss of 2.3 dB at 5.00 GHz and less than 2.5 dB from 4.75 GHz to 5.25 GHz, as validated in measurements.

The following sections are arranged as follows: Section 3.2 introduces the phase shifter working principles, and Section 3.3 shows the phase shifter analysis, design and optimization based on an equivalent circuit model. The concept of phase shifter is also experimentally validated in Section 3.4. Then Section 3.5 demonstrates an improved design of the phase shifter pair, followed by concluding remarks.

3.2 Working Principle of the Phase Shifter Pair

3.2.1 Differential Mode

Phase difference is the relevant factor in a beam steerable array to synthesize a pattern in a certain direction. The usual design of a phase shifter aims at supplying full 360° phase shift to achieve the desired beam scanning functionality. In contrast, a concept of phase shifter pair working in differential mode is proposed as shown in Fig. 3.1(a). The phase shifter pair consists of two phase-tuning units located symmetrically on the two output ports of a Wilkinson power divider, and these units are controlled individually by two separate voltages. The relative phase variation offered by this phase shifter

pair $\Delta\phi$ can be tuned continuously from 0° to 360°, if the phase difference between the two tuning units can be continuously adjusted from 0° to 180°. Two typical examples are given in Fig. 3.1(b) to illustrate the working principle. For instance, if the phase of P_1 is set to ϕ_1 while the phase of P_2 is tuned to ϕ_1 + 90°, then the phase difference $\Delta\phi$ from ϕ_1 to ϕ_2, namely $\Delta\phi = \phi_1$ - (ϕ_1 + 90°), is -90° (or 270°). When the phase of these two units are swapped by exchanging the two bias voltages, $\Delta\phi$ is then changed to 90° since $\Delta\phi$ = (ϕ_1 + 90°) - ϕ_1. Similarly, in the extreme case, one can also achieve -179° (or 181°) and 179° phase difference, if 179° is chosen as the phase difference between the tuning units. Due to the nature of phase swapping and subtraction, as well as operation in phase differences rather than absolute phases, this phase shifter pair is said to be working in a differential mode. In this operation modality, the phase tuning range requirement to realize a full 360° phase shift on the phase shifter pair can be halved, i.e., 0°-180°.

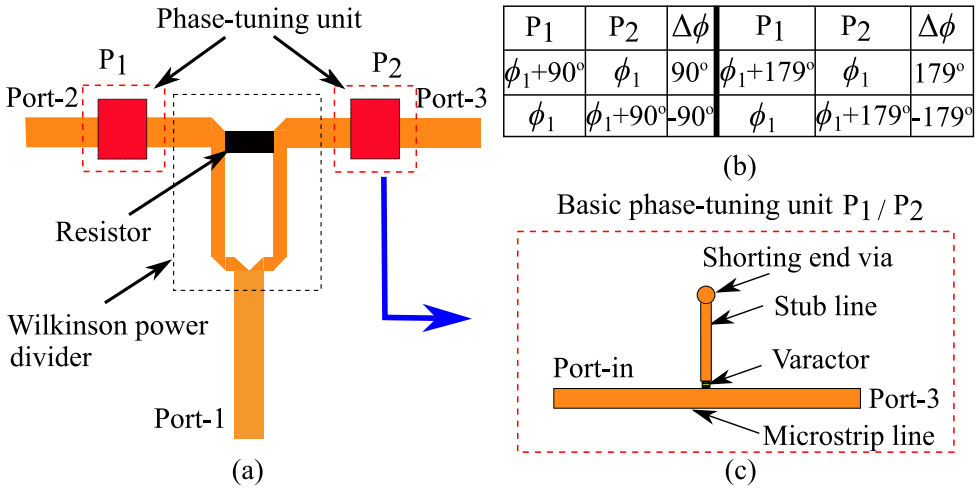

P_1	P_2	$\Delta\phi$	P_1	P_2	$\Delta\phi$
ϕ_1+90°	ϕ_1	90°	ϕ_1+179°	ϕ_1	179°
ϕ_1	ϕ_1+90°	-90°	ϕ_1	ϕ_1+179°	-179°

Figure 3.1. The proposed differential phase shifter pair: (a) General schematic diagram, (b) two typical phase tuning scenarios, and (c) general configuration of the basic phase-tuning unit.

3.2.2 Working Principle

To illustrate the work principle, a simplified phase-tuning unit loaded with a single stub (as shown in Fig. 3.1(c)) is investigated firstly. The most relevant phase-tuning part of the phase-tuning unit is a shorted-stub-loaded varactor. By adjusting the bias voltage to the varactor so that a different capacitance is obtained, the transmission characteristics of the main microstrip line will change due to the impedance variation at its junction to the varactor branch. As shown by the inset in Fig. 3.2(a), the varactor provides a capacitance value from 0.15 to 1.30 pF with a bias voltage from 18 to 0 V.

The simulated transmission coefficient and the corresponding phase of P_2 (or P_1) at the output Port-3 (or the output Port-2) with different varactor capacitances are shown in Fig. 3.2(a). Fig. 3.2(b) shows the phase ranges of the unit in a 360° circle according to the results shown in Fig. 3.2(a), i.e., the phase span in Reg-1 is covering the angular range between ϕ_1 (236° or -124°) and ϕ_2 (255° or -105°), and the one in Reg-2 between ϕ_3 (288° or -72°) and ϕ_4 (302° or -58°). The operational regions, marked as Reg-1 and Reg-2, are selected where the transmission coefficient is higher than -2 dB, i.e., the two highlighted green and blue areas. The magnitude of $|S_{21}|$ is mainly due to the

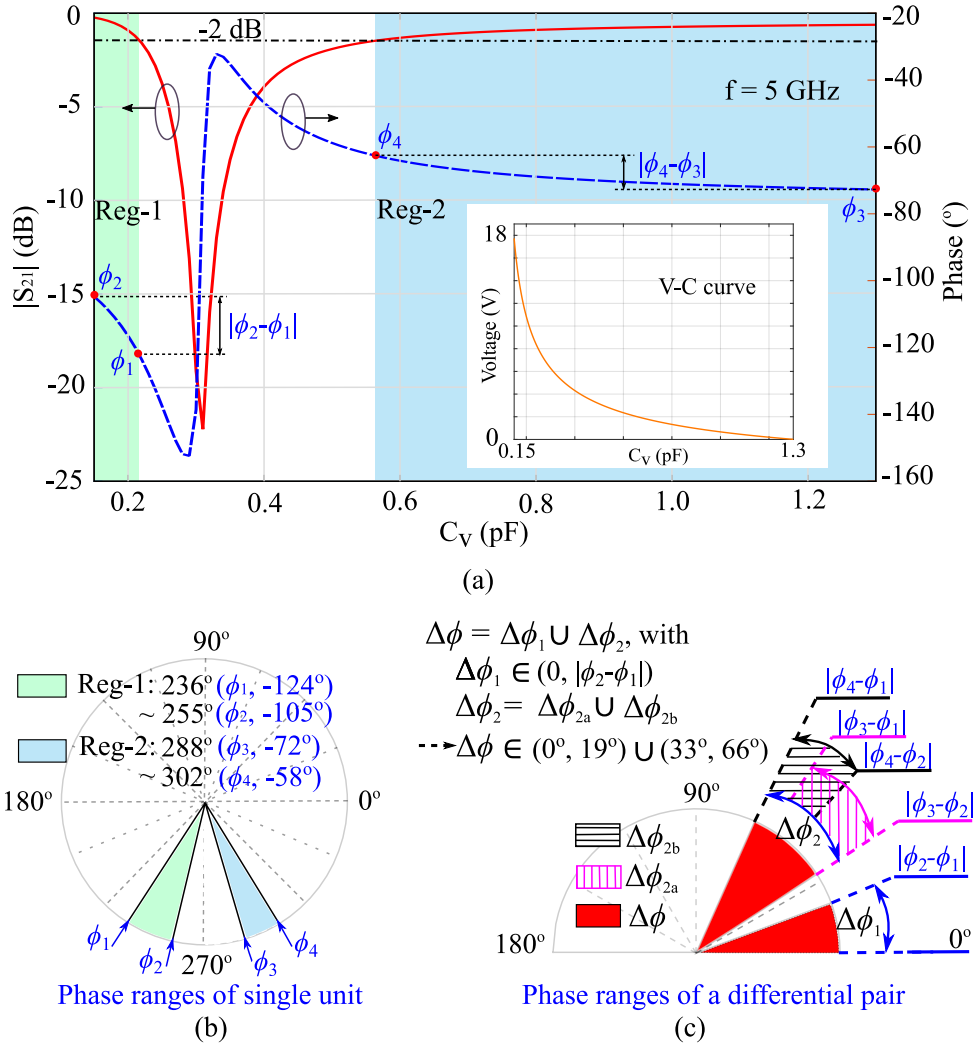

Figure 3.2. (a) Transmission characteristics of a single-stub phase-tuning unit (shown in Fig. 3.1(c)) at 5 GHz, in which the red line is the magnitude and the blue line is the phase, inset: reverse voltage-capacitance control curve of the varactor, (b) available phase regions provided by the basic phase-tuning unit corresponding to the values in Fig. 3.2(a), and (c) calculation of sub-phase-tuning areas $\Delta\phi_1$ and $\Delta\phi_2$ and the phase tuning range of a differential pair of phase-tuning units yielding in total an accessible phase difference $\Delta\phi$.

signal reflection (stop band) and the ohmic loss from the parasitic series resistance of the varactors (Reg-1 and Reg-2). Correspondingly, the available phases of the phase-tuning units can be selected individually in these two highlighted green (ϕ_1, ϕ_2) and blue (ϕ_3, ϕ_4) regions as shown in Fig. 3.2(b). The achievable phase difference, denoted as $\Delta\phi$, for a differential pair is the combination of the two sub-phase-tuning areas, namely the two red blocks $\Delta\phi_1$ and $\Delta\phi_2$ as shown in Fig. 3.2(c) which can be obtained by subtractions as

$$\Delta\phi \;=\; \Delta\phi_1 \cup \Delta\phi_2\,, \tag{3.1}$$

where

$$\Delta\phi_1 \;\in\; (0^\circ, |\phi_2 - \phi_1|)\,, \tag{3.2}$$

$$\Delta\phi_2 \;=\; \Delta\phi_{2a} \cup \Delta\phi_{2b}\,, \tag{3.3}$$

with

$$\Delta\phi_{2a} = (|\phi_3 - \phi_2|, |\phi_3 - \phi_1|)\,, \tag{3.4}$$

and

$$\Delta\phi_{2b} = (|\phi_4 - \phi_2|, |\phi_4 - \phi_1|)\,. \tag{3.5}$$

The resulting achievable phase ranges shown in Fig. 3.2(c) are normalized to ϕ_1 which corresponds to the reference of 0°. The first sub-phase-tuning range, $\Delta\phi_1$ as expressed in (3.2), is the same as the one from Reg-1 which always offers a wider phase difference compared to Reg-2. The second sub-phase-tuning range $\Delta\phi_2$ (expressed in (3.3)), is the overlapping area between the two subtracted phase ranges $\Delta\phi_{2a}$ (expressed in (3.4)) and $\Delta\phi_{2b}$ (expressed in (3.5)) highlighted as the pink and black regions in Fig. 3.2(c). It is worth mentioning that a stop band (with high insertion loss above 2 dB) exists between Reg-1 and Reg-2, whose position corresponds to the resonance of the structure. This resonance can therefore be controlled by the length of the stub after the varactor. Working precisely around the location of this stop band, allows to produce large continuous phase differences within two relative small sub-ranges Reg-1 and Reg-2. The optimization of the stop band allows to significantly control the phase tuning range. When the phase separation between the two operation ranges, namely $|\phi_3 - \phi_2|$, is equal or less than $|\phi_2 - \phi_1|$, $\Delta\phi_1$ and $\Delta\phi_2$ will merge in one single continuous phase-tuning range which maximizes the total phase span.

Importantly, this feature further relaxes the phase-tuning range requirement, as combining appropriately separated sub-ranges with sufficient angular span can allow to

cover 0° - 180° variation. Once the overall phase difference covered by these two sub-phase-tuning-areas fulfills the span of (0°, 180°), a phase shifter pair can realize full 360° phase tuning through swapping the bias voltages to the phase unit pair.

One also can observe that some of the phase difference $\Delta\phi$ can be obtained through different phase combinations which may have different levels of insertion loss. This offers additional possible combinations of signal phase and magnitude to each array element, which to some extent can allow to realize beam optimization.

3.2.3 Practical Configuration of the Phase-Tuning Unit

As cascading more phase-tuning stubs can lead to a wider phase-tuning span for a differential pair, configurations with up to four shorted-stub-loaded varactors are investigated in the following. The geometry and the simulated transmission characteristic curves of these four structures are illustrated in Fig. 3.3.

Their usable (varactor) capacitance ranges defined by the insertion loss less than 2 dB are shown in Fig. 3.3(a) with different colour bands, and the corresponding phase tuning ranges are summarized in Table 3.1.

Additionally, the available phase regions of a single phase shifter (full circle) and the phase-tuning spans of a phase shifter pair (half circle) are visually represented in Figs. 3.4(a), (b), (c) and (d) for the four designs respectively.

Table 3.1. Available phase regions of different cascaded phase-tuning units

Model	#Stub	Reg-1	Reg-2	Phase difference in pair
(i)	1	236° - 255°	288° - 302°	0° - 19°, 33° - 66°
(ii)	2	168° - 232°	295° - 314°	0° - 134°
(iii)	3	142° - 230°	336° - 41°	0° - 88°, 101° - 180°
(iv)	4	143° - 244°	27° - 98°	0° - 180°

In the first two cases with one or two stubs, the usable varactor capacitance range is wider but the phase dynamic range is lower than in the other two cases. The last case with four stubs is the best in terms of phase-tuning ability since it permits more than 0° - 180° continuous phase variation. Nevertheless, considering the insertion loss and complexity, the case with three stubs is found to be the most practical design with smooth phase-tuning ranges of (0°, 88°) and (101°, 180°), separated by a small phase

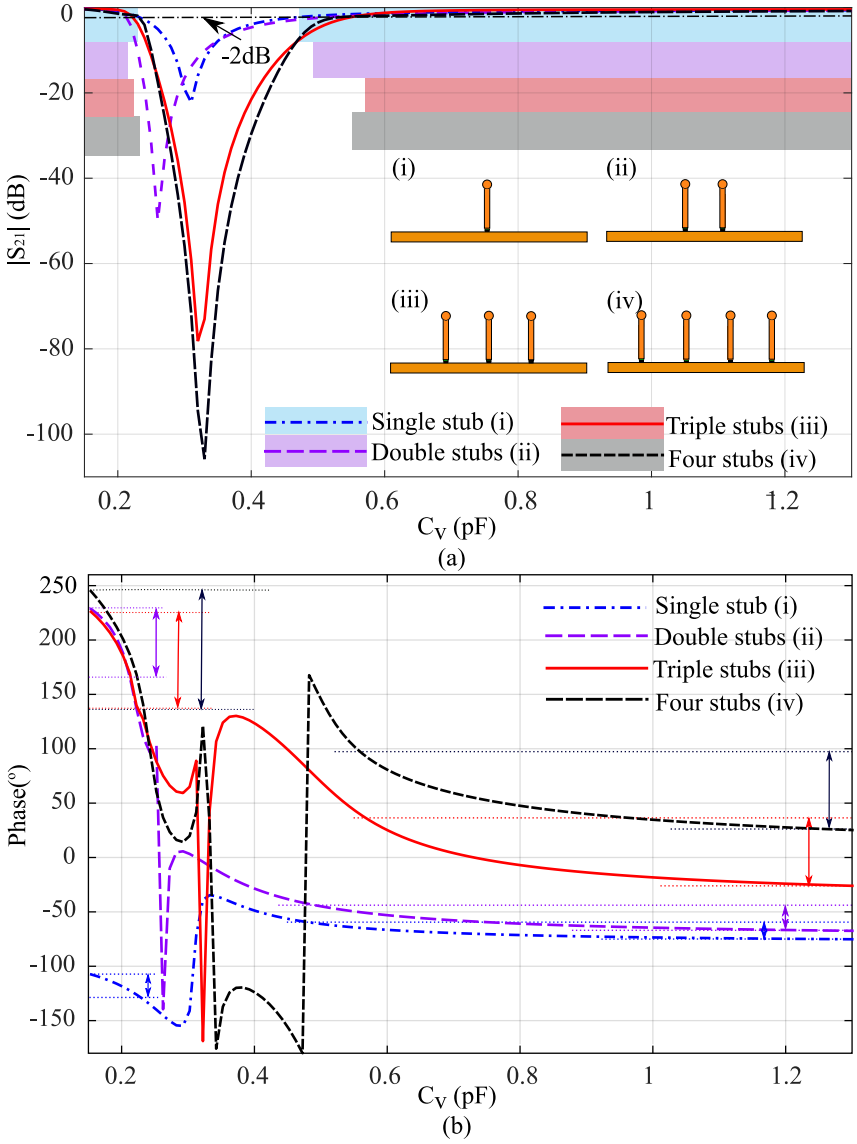

Figure 3.3. Transmission characteristics of the four considered phase-tuning unit models: (a) Magnitude and (b) phase. The vertical arrows illustrate the accessible phase tuning ranges in the two regions with $|S_{21}| >$ -2 dB.

gap of 13° which will be later optimized to less than 11°. This overall continuous phase-tuning range is sufficient for a general-purpose pattern-reconfigurable antennas, since such phase-tuning performance can be considered equivalent to a traditional 5-bit phase shifter which has a 11.25° phase-tuning resolution.

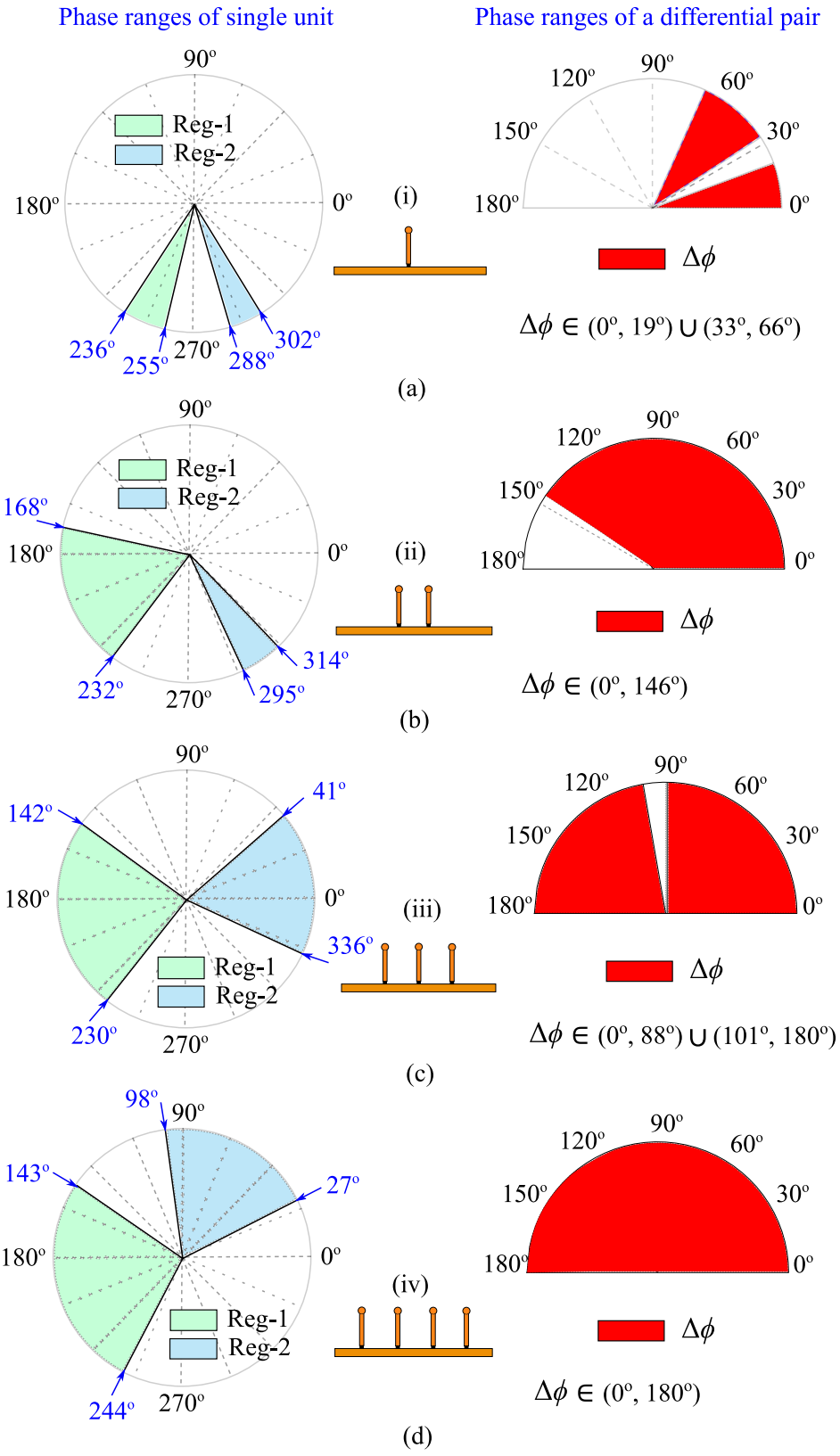

Figure 3.4. Phase-tuning capability of different cascaded single and paired phase shifters with (a) one stub, (b) two stubs, (c) three stubs and (d) four stubs.

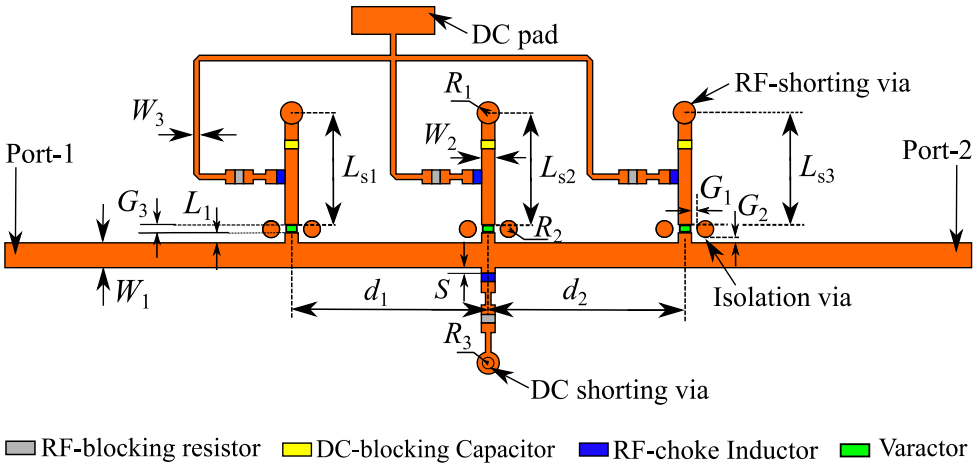

Figure 3.5. Geometry of the proposed phase-tuning unit with three varactor-loaded stubs. The dimensions are: $W_1 = 0.90$ mm, $W_2 = 0.48$ mm, $W_3 = 0.20$ mm, $L_1 = 0.36$ mm, $R_1 = 0.40$ mm, $R_2 = 0.30$ mm, $R_3 = 0.20$ mm, $G_1 = 0.30$ mm, $G_2 = 0.20$ mm $G_3 = 0.30$ mm, $S = 0.20$ mm, $L_{s1} = 4.05$ mm, $L_{s2} = 4.05$ mm, $L_{s3} = 4.05$ mm, $d_1 = 7.12$ mm, and $d_2 = 7.12$ mm.

3.3 Phase-Tuning Unit Design

Being chosen as the most advantageous building block for the proposed phase shifter pair, the 3-stub phase-tuning unit is discussed in detail in this section. As depicted in Fig. 3.5, it contains a microstrip transmission lines loaded with three varactors terminated with short-ended stubs. The phase-tuning unit is designed on a 0.635 mm thick Rogers RT6006 with relative permittivity of 6.15 and loss tangent of 0.0019 at 5 GHz. The varactors adopted in this design are MA46H120 which has a parasitic inductance of 0.05 nH and a resistance of 2 Ω [109]. As shown in Fig. 3.5, the bias network consists of an RF-choke inductor of 15 nH in series with an RF-blocking resistor of 1000 Ω. A 200 pF DC-blocking capacitor is inserted into the top section of the stub close to the RF-shorting via. The microstrip bias lines connected to the DC voltage are chosen to be 0.2 mm wide to increase their inductance and minimize radiation.

3.3.1 Equivalent Circuit Model

Aiming to achieve a fast design and optimization process for the phase shifter, an accurate equivalent circuit model of the 3-stub phase-tuning unit is developed. Since the bias network and the DC-blocking capacitor have very limited impact on the phase-tuning unit, they are neglected in the equivalent circuit model. For two-port networks in cascaded configuration, the [ABCD] matrix [110] (denoted with bold **A** in this thesis) provides a convenient way to compute the transmission characteristics of the overall

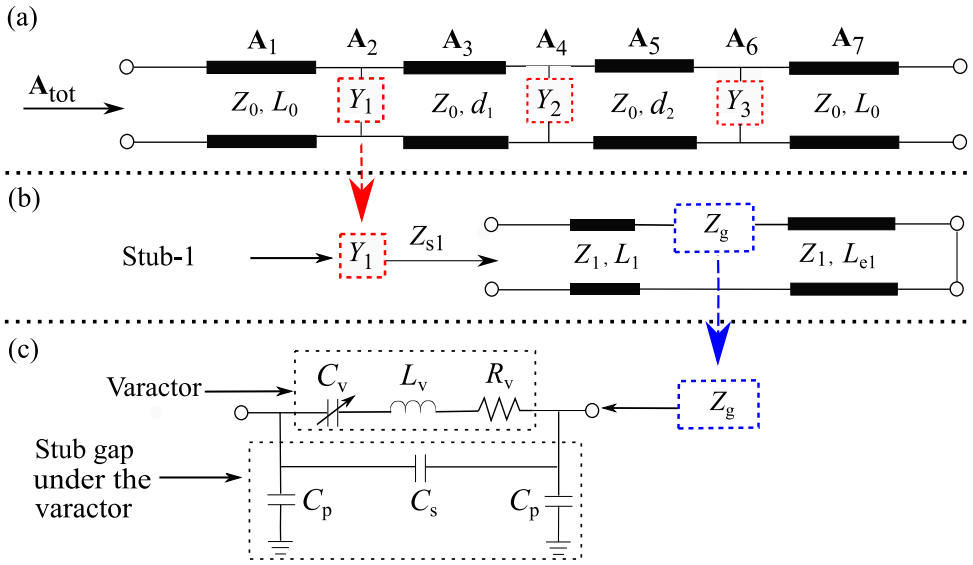

Figure 3.6. Equivalent circuit model: (a) The overall 3-stub phase-tuning unit, (b) the stub-loaded varactor and (c) the varactor and its connection to the stubs.

network by simple matrix multiplication, hence it is adopted in the circuit mode analysis.

The phase-tuning unit can be considered as four cascaded segments of microstrip transmission lines with three admittance branches in-between them. The equivalent circuit is illustrated in Fig. 3.6(a), and the matrix $\mathbf{A}_{tot}$ is obtained by multiplying $\mathbf{A}_1$ to $\mathbf{A}_7$ in order as

$$\mathbf{A}_{tot} = \prod_{i=1}^{7} \mathbf{A}_i = \mathbf{A}_1 \cdot \mathbf{A}_2 \cdot \mathbf{A}_3 \cdot \mathbf{A}_4 \cdot \mathbf{A}_5 \cdot \mathbf{A}_6 \cdot \mathbf{A}_7 \,. \tag{3.6}$$

The four transmission line networks $\mathbf{A}_1$, $\mathbf{A}_3$, $\mathbf{A}_5$ and $\mathbf{A}_7$, represent the microstrip line segments with physical lengths of L_0, d_1, d_2 and L_0 respectively, separated by three stub-loaded varactors which are approximated as the 3 admittances, described by $\mathbf{A}_2$, $\mathbf{A}_4$ and $\mathbf{A}_6$. The matrices $\mathbf{A}_1$ and $\mathbf{A}_7$, $\mathbf{A}_3$ and $\mathbf{A}_5$ are expressed as

$$\mathbf{A}_1 = \mathbf{A}_7 = \begin{bmatrix} \cos(\beta L_0) & j\sin(\beta L_0)\, Z_0 \\ j\sin(\beta L_0)/Z_0 & \cos(\beta L_0) \end{bmatrix} \tag{3.7}$$

$$\mathbf{A}_3 = \begin{bmatrix} \cos(\beta d_1) & j\sin(\beta d_1)\, Z_0 \\ j\sin(\beta d_1)/Z_0 & \cos(\beta d_1) \end{bmatrix} \tag{3.8}$$

$$\mathbf{A}_5 = \begin{bmatrix} \cos(\beta d_2) & j\sin(\beta d_2)\, Z_0 \\ j\sin(\beta d_2)/Z_0 & \cos(\beta d_2) \end{bmatrix} \tag{3.9}$$

where $\beta = 2\pi/\lambda_g$ and λ_g is the guided wavelength.

The admittances Y_1, Y_2 and Y_3 are composed of three parts including a stub with characteristic impedance of Z_1 and physical length of L_1 (the very short stub connected to the edge of the main microstrip line, as shown in Fig. 3.5), a varactor in series denoted as Z_g, and a short-ended stub with characteristic impedance Z_1 and effective physical length L_{en} (n = 1,2,3), which is shown in Fig. 3.6(b) for $n = 1$ (the first varactor branch). The corresponding matrices for the stubs can be expressed as

$$\begin{aligned}\mathbf{A}_{stub-n} = &\begin{bmatrix} \cos(\beta L_1) & j\sin(\beta L_1)\, Z_1 \\ j\sin(\beta L_1)/Z_1 & \cos(\beta L_1) \end{bmatrix} \begin{bmatrix} 1 & Z_g \\ 0 & 1 \end{bmatrix} \\ &\begin{bmatrix} \cos(\beta L_{en}) & j\sin(\beta L_{en})\, Z_1 \\ j\sin(\beta L_{en})/Z_1 & \cos(\beta L_{en}) \end{bmatrix} \\ &(n = 1, 2, 3).\end{aligned} \tag{3.10}$$

The equivalent circuit model of the connected varactor is shown in Fig. 3.6(c), which is comprised of a series RLC circuit representing the varactor in isolation, two shunt capacitors C_p approximating the parasitic capacitances between the stub edges and ground, in series with a capacitor C_s standing for the capacitance between the two stub edges. As a result, the impedance Z_g of the varactor on stub-n can be expressed as

$$Z_g \;=\; Z_{cp} // Z_m // Z_{cp}\,, \tag{3.11}$$

where Z_{cp} is the impedance of C_p while Z_m is the impedance of the varactor in parallel with C_s. Their expressions are given as:

$$Z_{cp} \;=\; 1/(j\omega C_p) \tag{3.12}$$

$$Z_m \;=\; 1/(j\omega C_s + (1/(R_v + j\omega L_v + 1/(j\omega C_v))))\,, \tag{3.13}$$

where $\omega = 2\pi f$ and f is the operating frequency.

In (3.13), C_v, L_v, R_v represent the series RLC circuit of the varactor in isolation. C_v is a tunable capacitance, L_v is a parasitic inductance and R_v stands for a parasitic resistance. The values of C_s and C_p are calculated according to [111]. Then, $\mathbf{A}_2$, $\mathbf{A}_4$ and $\mathbf{A}_6$ are obtained by

$$\mathbf{A}_2 = \mathbf{A}_4 = \mathbf{A}_6 = \begin{bmatrix} 1 & 0 \\ 1/Z_{sn} & 1 \end{bmatrix} \ (n = 1,2,3)\ , \tag{3.14}$$

where Z_{sn} is the input impedance when looking into each varactor branch from the main 50 Ω microstrip line, expressed as:

$$Z_{sn} = \frac{\mathbf{A}_{stub-n}(1,1)Z_l + \mathbf{A}_{stub-n}(1,2)}{\mathbf{A}_{stub-n}(2,1)Z_l + \mathbf{A}_{stub-n}(2,2)} \ (n = 1,2,3) \tag{3.15}$$

and Z_l is the load impedance which is zero from the shorted end of the stub. The $\mathbf{A}_{tot}$ for the overall structure is then obtained using (3.6), and the overall **S**-matrix can be finally computed from $\mathbf{A}_{tot}$ as discussed in [112].

Full-wave simulation with Ansys HFSS 2019 is deployed to validate the equivalent circuit model. The effective physical length of the shorted stub L_{en} in the circuit model depends on its physical length L_{sn} (n = 1,2,3), shorting via radius R_1, stub width W_2 and substrate thickness t. It is empirically found that the relation between them is

$$L_{en} = L_{sn} + t - l \ (n = 1,2,3)\ , \tag{3.16}$$

where l = 0.445 mm is an empirically found length compensating the additional inductance formed by the given via and stub width.

A second critical phenomenon observed in full-wave computation is the parasitic coupling between the main transmission line and the varactor-loaded stub. This coupling is not considered in the equivalent circuit model which causes a non-negligible discrepancy from simulation. Therefore, to suppress this coupling, isolation vias with radius R_2 are installed on both sides of the stub close to the varactor location (denoted as isolation via in Fig. 3.5). As a result of the addition of those vias, the coupling in this area is effectively mitigated.

As predicted by full-wave simulations, the solder layer for the varactors can slightly influence the phase-tuning unit performance, and therefore the solder layer effect needs to be empirically considered in the circuit model to achieve a higher accuracy. Based on the averaged values measured using a microscope, the solder layer dimensions are included in the HFSS simulation model with a bottom width of 0.35 mm, a length of 0.1 mm and a height of 0.1 mm. Correspondingly, this solder layer effectively changes the C_v range to 0.12 pF to 1.27 pF and increases the parasitic resistance of the varactor to 3 Ω in this equivalent circuit model.

3.3.2 Optimization

The phase-tuning unit has 6 key variables which significantly control the phase tuning range, i.e., the stub width W_2 (Z_1 in circuit model) and the 3 stub lengths L_{en} as well as the distances between the stubs d_1 and d_2, which are displayed in Fig. 3.5. These parameters are optimized using a genetic algorithm (GA) [113] based on the circuit model to maximize the phase tuning range while maintaining an acceptably low insertion loss. GA is utilized as a generic tool here since it is known to be very efficient for multi-objective optimization. The objective function for the GA considers the insertion loss and phase shift range simultaneously and it is based on the following 3 steps:

Step 1: Define the multi-objective merit function, which targets 180° continuous phase difference coverage between phase-tuning pairs while minimizing insertion loss (expressed in dB) over all phase combinations.

Step 2: Generate chromosomes which contain the values defining the length of the three stubs L_{e1}, L_{e2}, L_{e3}, the width of the stubs W_2, and the stub spacings d_1 and d_2. For each generated combination, calculate the phase-tuning unit performance based on the merit function, apply mating, mutation and selection rules of the GA.

Step 3: Repeat Step-2 until convergence to an optimal combination of these six parameters is reached using the GA algorithm.

When running the GA optimization algorithm multiple independent times, the obtained optimized results, which can satisfy the phase tuning span (0°-180°) while keeping a relatively low insertion loss below 2 dB (down to 1.5 dB), usually yield nearly equal stub lengths and stub spacings, i.e., $L_{e1} \cong L_{e2} \cong L_{e3}$ and $d_1 \cong d_2$. Therefore, a condition of equal stub length and spacing is enforced in the final optimization for the sake of design simplicity. The resulting critical geometrical parameters of the final design are given in Table 3.2.

As shown in Fig. 3.7(a), this design can produce 0° - 180° phase difference, with a small tuning gap between 80° and 91° at 5 GHz as listed in Table 3.3. The simulated and calculated transmission coefficient magnitude and phase obtained from the circuit method and full-wave simulation at 4.75 and 5.25 GHz are shown in Figs. 3.7(b) and (c) respectively. The results imply that the phase-tuning ability as listed in Table 3.3, is nearly identical across the frequency range from 4.75 to 5.25 GHz.

Table 3.2. Parameters of equivalent circuit method and full-wave method for the final designs.

Equivalent circuit variables		Full-wave variables	
Name	Value	Name	Value
L_{en}	4.24 mm	L_{sn}	4.05 mm
d_1	7.12 mm	d_1	7.12 mm
d_2	7.12 mm	d_2	7.12 mm
Z_1	69.52 Ω	W_2	0.48 mm

Table 3.3. Phase-tuning capability of the 3-stub phase-tuning unit at 5.00, 4.75 and 5.25 GHz

Frequency	Reg-1	Reg-2	Phase difference in pair
5.00 GHz	160° - 240°	331° - 21°	0° - 80°, 91° - 180°
4.75 GHz	179° - 275°	22° - 61°	0° - 96°, 107° - 180°
5.25 GHz	135° - 213°	299° - 2°	0° - 78°, 86° - 180°

3.4 Fabrication and Measurement

To verify the proposed analysis and design method, a stand-alone phase-tuning unit prototype is fabricated and measured, as displayed in Fig. 3.8. A reference 50 Ω microstrip transmission line is printed on the same substrate, and is used to calibrate the insertion loss purely due to the line. Two test pins soldered on the phase-tuning unit are used for the DC bias and ground connections, respectively. The measured performance of the prototype is compared with the results obtained from equivalent circuit model in Fig. 3.9, where a good agreement is observed, thus validating the design method.

The phase-tuning ability is measured with the appropriate varactor capacitance by applying the corresponding bias voltage. The resulting phase differences obtained in this test scheme are shown in Table 3.4, where the phase differences from 0° - 180° with 10° interval are successfully achieved within 5% tolerances based on calculated application of a pair of phase-tuning units. The measured insertion loss, after calibrating out the main transmission line loss of about 0.26 dB, is found to be not larger than 1.74 dB at 5 GHz. The same measured phase tuning range has been attained at 4.75 and 5.25 GHz with a slightly higher calibrated maximum insertion loss of 2.04 dB (not shown in this section for brevity).

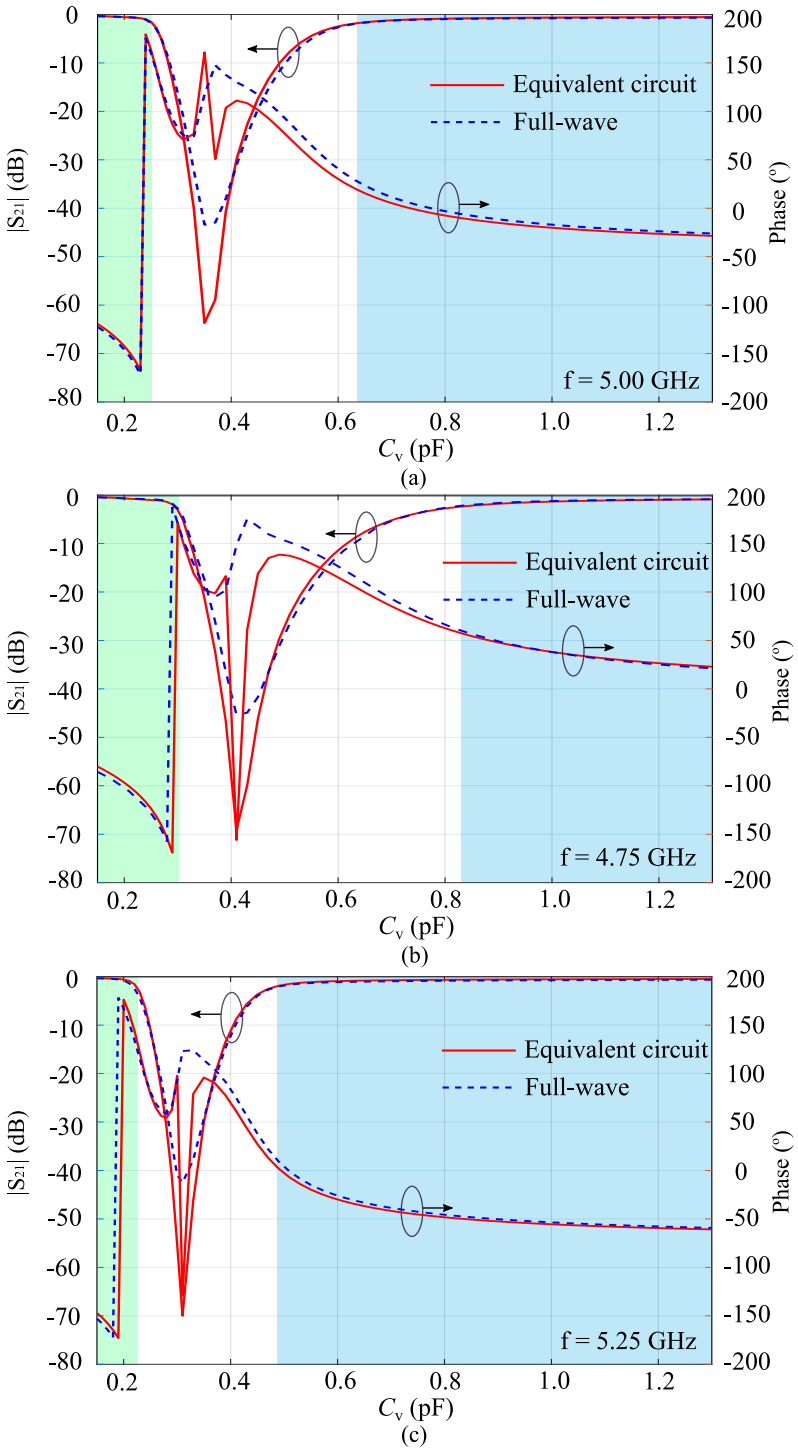

Figure 3.7. S_{21} magnitude and phase values of the final optimized design of 3-stub phase-tuning unit obtained from the equivalent circuit method and full-wave method at (a) 5.00 GHz, (b) 4.75 GHz and (c) 5.25 GHz.

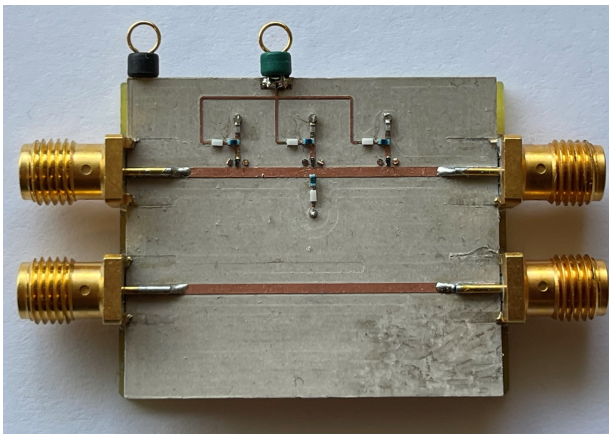

Figure 3.8. Photograph of the fabricated 3-stub phase-tuning unit. The dark green test pin is for DC bias circuit connection, and the black one is for the ground connection. A through 50 Ω transmission line is added on the same board as reference.

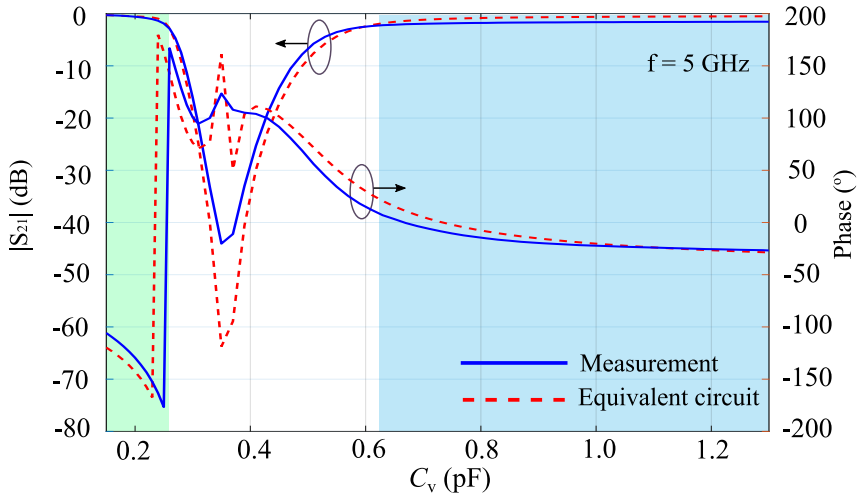

Figure 3.9. 3-stub phase-tuning unit prototype performance, showing the S_{21} magnitude and phase curves from the equivalent circuit method and measured results at 5 GHz.

3.5 Improved Design of the Phase Shifter

A further-improved design based on a similar phase-tuning unit topology is proposed in this part. The aim of this optimization is to improve the tuning ability of the differential phase shifter pair which consists of two 3-stub phase-tuning units. Additionally, the optimized phase-tuning unit is implemented on a more cost-effective substrate, thereby enhancing the processing potential of this design in compact and low-cost applications.

The differential phase shifter pair in Fig. 3.5 can reach a nearly full 360° phase-tuning span with two symmetrical gaps of 11°. To cover the gap, the optimized phase-tuning

Table 3.4. Measured phase reconfigurability of the phase-tuning unit prototype when used in pair at 5 GHz

C_1, C_2 (pF)	V_1, V_2 (V)	Meas. ϕ_1, ϕ_2 (°)	Meas. $IL_1{}^{\diamond}$ IL_2 (dB)	Meas. $\Delta\phi(°)^*$ ($\Delta\phi_{exp}(°)^{\triangle}$)
0.15, 0.15	17.8, 17.8	-105.7, -105.7	0.28, 0.28	0.0 (0)
0.17, 0.19	14.1, 11.8	-113.8, -123.5	0.35, 0.47	9.7 (10)
0.16, 0.20	15.7, 10.9	-109.6, -129.3	0.30, 0.57	19.7 (20)
0.15, 0.21	17.8, 10.1	-105.7, -135.9	0.28, 0.68	30.2 (30)
0.15, 0.22	17.8, 9.5	-105.7, -143.4	0.28, 0.84	37.7 (40)
0.17, 0.24	14.1, 8.4	-113.8, -163.2	0.35, 1.35	49.4 (50)
0.15, 0.24	17.8, 8.4	-105.7, -163.2	0.28, 1.35	57.5 (60)
0.15, 0.25	17.8, 8.0	-105.7, -176.5	0.28, 1.87	70.8 (70)
1.30, 0.15	0.0, 17.8	-26.7, -105.7	1.53, 0.28	79.0 (80)
1.30, 0.18	0.0, 12.8	-26.7, -1.0	1.53, 0.41	91.8 (90)
0.99, 0.19	0.7, 11.8	-22.0, -123.5	1.60, 0.47	101.5 (100)
1.17, 0.21	0.3, 10.1	-24.9, -135.9	1.56, 1.8	111.0 (110)
1.07, 0.22	0.5, 9.5	-23.7, -143.4	1.59, 0.84	119.7 (120)
0.99, 0.23	0.7, 8.9	-22.0, -152.4	1.60, 1.04	130.4 (130)
0.99, 0.24	0.7, 8.4	-22.0, -163.2	1.60, 1.35	141.2 (140)
1.30, 0.25	0.0, 8.0	-26.7, -176.5	1.53, 1.87	149.8 (150)
0.83, 0.25	1.2, 8.0	-16.4, -176.5	1.71, 1.87	160.1 (160)
0.71, 0.25	1.7, 8.0	-6.0, -176.5	1.90, 1.87	170.5 (170)
0.67, 0.25	1.9, 8.0	0.0, -176.5	2.00, 1.87	176.5 (180)

$^{\diamond}$ Phase-tuning unit insertion loss.

* Phase shifter pair tested phase difference.

$^{\triangle}$ Phase shifter pair expected phase difference.

unit is proposed and shown in Fig. 3.10. The enhanced design is realized on a 0.76 mm thick Rogers Diclad 880 with relative permittivity of 2.2. It also consists of three identical short-ended stubs loaded with varactors, however with two extra open-ended stubs introduced, located on the edge of a 50 Ω host microstrip line in between the stub-loaded varactors. The lower dielectric constant of the substrate results in a physically larger board and thus less mutual coupling between the varactors and the microstrip host line. As a consequence, the isolation via structures required in the original phase shifter design are no more needed in this present evolved design.

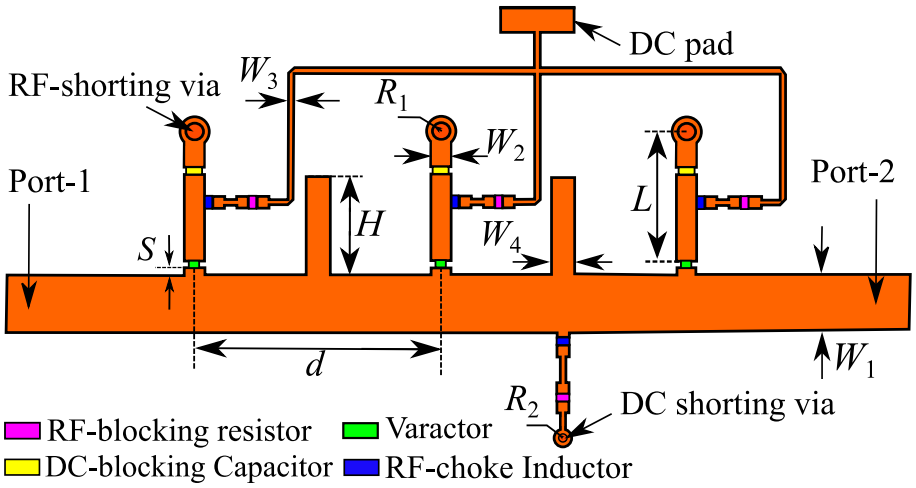

Figure 3.10. Geometry of the proposed phase-tuning unit of the differential pair with three varactor-loaded stubs. The major dimensions are: $W_1 = 2.32$ mm, $W_2 = 0.80$ mm, $W_3 = 0.20$ mm, $W_4 = 1.00$ mm, $L = 5.20$ mm, $R_1 = 0.40$ mm, $R_2 = 0.20$ mm, $S = 0.30$ mm, $H = 4.00$ mm, and $d = 10.00$ mm .

To eliminate the phase gap in the pair mode, the phase tuning unit needs to have a larger span of Reg-1 (as Reg-2 is usually smaller than Reg-1) and a smaller difference between ϕ_3 and ϕ_2 (see Fig. 3.11(b) and (c)), which can satisfy

$$|\phi_2 - \phi_1| \geq |\phi_3 - \phi_2|. \tag{3.17}$$

In order to achieve these requirements, two open-ended stubs are introduced to lengthen the path between two adjacent short-ended stubs. Due to this structure, the phase values in Reg-1 and Reg-2 are individually increased by a certain value. In particular, ϕ_3 becomes closer to ϕ_2, which reduces the phase difference between them and makes an important contribution to the elimination of the phase gap.

The phase tuning unit is simulated using Ansys HFSS 2021. It is predicted to cover a full 360° when operating in pair with a maximum insertion loss of 2 dB at 5 GHz, as shown in the red curves in Fig. 3.12(a). As shown in the polar phase plot in Fig. 3.12(b), a phase difference of (0°, 92°) can be achieved in Reg-1 while the phase gap between ϕ_3 and ϕ_2 is 91°. For the frequencies from 4.75 to 5.25 GHz, the device can almost fully cover 360° phase difference with a gap of 3° at 4.75 GHz and 25° at 5.25 GHz, when the insertion loss is less than 2 dB.

To verify the proposed design, a prototype of the optimized phase tuning unit has been fabricated, as shown in Fig. 3.13. The measured characteristic curves (in blue) are illustrated in Fig. 3.12(a). A very good agreement between simulation and measurement is

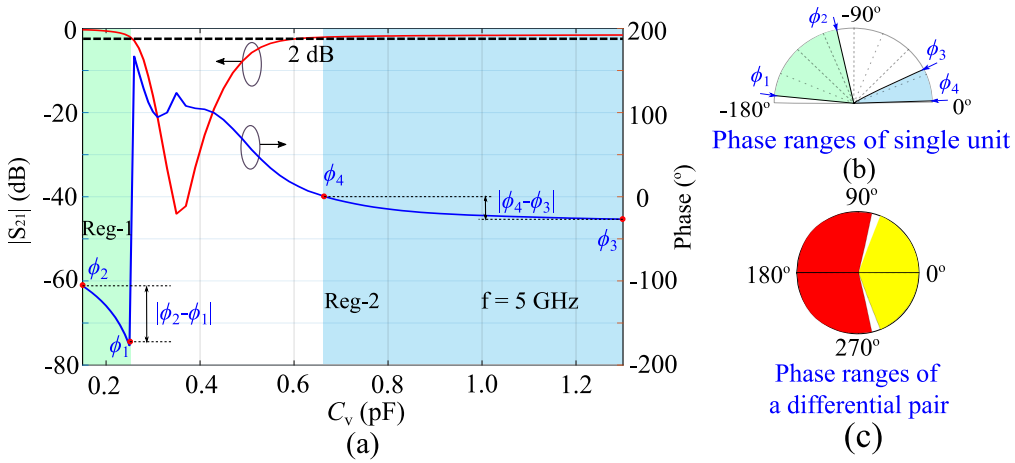

Figure 3.11. The differential phase shifter pair: (a) Transmission characteristics of the phase-tuning unit at 5 GHz, in which the red line is the magnitude and the blue line is the phase, (b) the available phase ranges of the phase-tuning unit corresponding to the values in Fig. 3.11(a), and (c) the phase range of the differential pair: the yellow region is achieved using Reg-1, the red region is achieved using the difference between Reg-1 and Reg-2, and the pink and orange regions are achieved by swapping the states of P_1 and P_2 in the differential pair structure shown in Fig. 3.1(a).

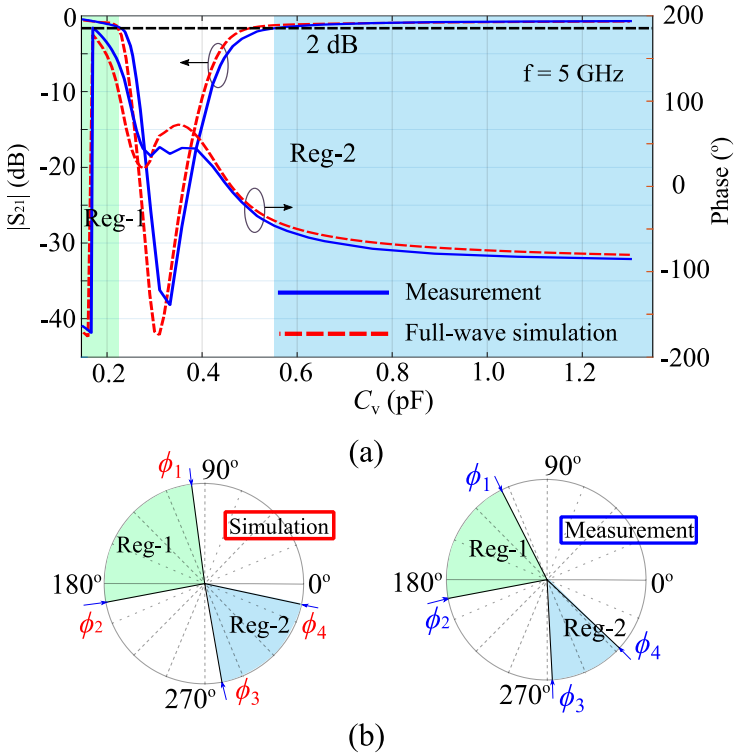

Figure 3.12. (a) Simulated and measured S_{21} parameters of the optimized phase-tuning unit at 5 GHz, and (b) the polar phase plot of the optimized phase-tuning unit corresponding to the values in Fig. 3.12(a).

observed, with a slightly smaller achievable phase range from 0° to 74° and the phase gap between ϕ_3 and ϕ_2 of 78° for an insertion loss smaller than 2 dB. This further optimized design is able to cover full 360° when the insertion loss is less than 2.3 dB at 5.00 GHz and less than 2.5 dB from 4.75 to 5.25 GHz. Although the insertion loss is slightly higher than that in simulations, the prototype still provides a very competitive performance which validates the proposed optimized concept.

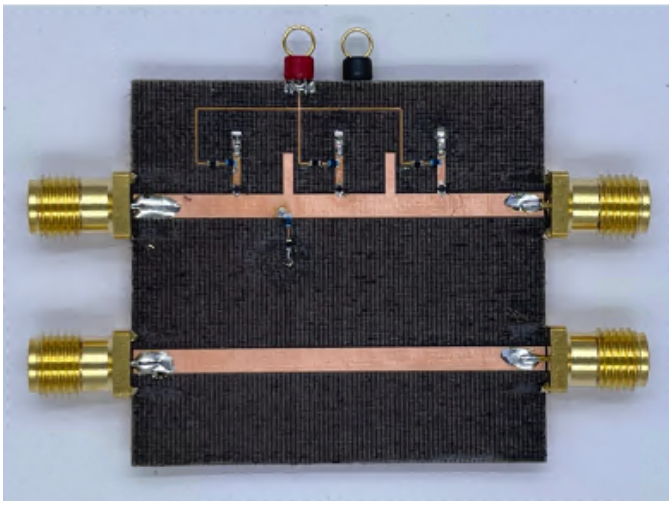

Figure 3.13. The optimized phase-tuning unit prototype.

3.6 Conclusion

A phase shifter concept based on a differential pair of varactor-loaded phase-tuning units has been proposed in this chapter. The differential pair configuration can halve the phase range requirement to achieve 0° to 360° phase tuning range, namely requiring only 0° to 180° tuning span for the pair. The general phase-tuning unit contains a main microstrip line and shorted-stub-loaded varactors on its lateral edge, which offers easy integration in planar technologies. It has been demonstrated that a 4-stub phase-tuning unit pair can generously cover the required 0° to 180° phase adjustment. However, a 3-stub design has been identified to be the most cost-effective option for common antenna designs, as it provides 0° - 180° phase tuning with only a 11° blind zone. The development of an equivalent circuit model computation allowing GA-based optimization has facilitated a fast design process for the 3-stub configuration. To validate the method, a 3-stub phase-tuning unit prototype is fabricated and measured. The measured results have shown the expected phase tuning range when operated in

a pair and a maximum insertion loss of 1.74 dB at 5.00 GHz and 2.04 dB from 4.75 to 5.25 GHz.

Based on the similar topology, an optimized phase-tuning unit operating in a differential pair configuration has been also proposed with the objective of enhancing both the phase-tuning capability to a full 360°, i.e., without gaps, and cost efficiency of the unit. By using a substrate with lower permittivity and adding two open-ended stubs to the original design, the optimized device no longer requires isolation vias, and importantly achieves a full 360° phase difference span with an insertion loss not higher than 2.3 dB at 5 GHz, which is competitive. All these results have implied that the enhanced phase shifter pair is a promising phase shifter solution for compact and low-cost microwave and antenna engineering.

Chapter 4

Beam-Steerable Dielectric Resonator Antenna Array

As an important type of pattern-reconfigurable antennas, beam-steerable antennas are in high demand for a wide variety of wireless communications applications. The phase control system plays an essential role in determining the beam steering angle. Traditionally, standalone phase shifters employed for this purpose have been able to provide a full 360° phase tuning span. However, they tend to be bulky, expensive, and require additional space to connect with the antenna system. On the other hand, planar phase tuning devices using lumped electronic components often results in a limited tuning range or higher insertion loss, limiting their applicability.

In order to achieve a compact and cost-effective beam-steerable antenna, three of those differential phase shifter pairs proposed in Chapter 3 are seamlessly integrated into a 1-to-4 equal power divider. This configuration creates a reconfigurable feeding network which can provide sufficient phase differences for a 4-element linear dielectric resonator antenna array, allowing the beam to be scanned from -45° to +45° with a tunable operating frequency band from 4.75 to 5.25 GHz.

Statement of Authorship

Title of Paper	A 3D-Printed Hybrid Dielectric Resonator Antenna with Low Cross-Polarization
Publication Status	☑ Published ☐ Accepted for Publication ☐ Submitted for Publication ☐ Unpublished and Unsubmitted w ork w ritten in manuscript style
Publication Details	2022 International Symposium on Antennas and Propagation (ISAP), Sydney, Australia, 2022, pp. 79-80, doi: 10.1109/ISAP53582.2022.9998813.

Principal Author

Name of Principal Author (Candidate)	Yuan YUAN
Contribution to the Paper	Under the supervision of C. Fumeaux and S. J. Chen, I performed the design, simulation, prototype development, measurements and wrote the manuscript for submission.
Overall percentage (%)	60%
Certification:	This paper reports on original research I conducted during the period of my Higher Degree by Research candidature and is not subject to any obligations or contractual agreements with a third party that would constrain its inclusion in this thesis. I am the primary author of this paper.
Signature	Date 26/07/2023

Co-Author Contributions

By signing the Statement of Authorship, each author certifies that:

i. the candidate's stated contribution to the publication is accurate (as detailed above);

ii. permission is granted for the candidate in include the publication in the thesis; and

iii. the sum of all co-author contributions is equal to 100% less the candidate's stated contribution.

Name of Co-Author	Christophe Fumeaux
Contribution to the Paper	I acted as supervisor for the candidate, aided in design, development, and measurements, revising the manuscript, and evaluating the final version of the manuscript. I give consent for Yuan YUAN to present this paper for examination towards the Doctorate of Philosophy.
Signature	Date 27/07/2023

Name of Co-Author	Shengjian Jammy Chen
Contribution to the Paper	I acted as supervisor for the candidate, aided in design, development, and measurements, revising the manuscript, and evaluating the final version of the manuscript. I give consent for Yuan YUAN to present this paper for examination towards the Doctorate of Philosophy.
Signature	Date 29/07/2023

Please cut and paste additional co-author panels here as required.

4.1 Introduction

RECONFIGURABLE antennas aim at producing tunable radiation characteristics for advanced wireless communications applications [114]. This ability is obtained by redistributing the electrical currents on their structure, which essentially can produce changes in operation frequency [115] [116] [117], radiation pattern [118] [119] [120], polarization [121] [122] [123] or any combination of these aspects [124] [125]. Particularly, as an important type of pattern-reconfigurable antennas, beam-steerable antennas are highly demanded for a wide variety of wireless communications applications such as 5G systems [126], wireless local area network (WLAN) [127] [128] and internet of things (IoT) systems [129] [130] [131].

For modern systems, planar beam-steerable antennas based on active electronic components such as PIN diodes [132] [133] [134], varactors [135] [136] and RF-switches [137] [138] [139] have been developed widely, promoting advantages of compact structure, low cost and low power consumption compared to traditional phased arrays. These antennas can be categorized into two types in terms of their beam steerability, namely beam-switching antennas which can switch their main beam to discrete angles [140–142] and beam-scanning antennas which can continuously scan their main beam in an angular range [100] [101].

A 2-D beam-switching 2-bit array was reported in [140] with three discrete pattern states, i.e., at angles (θ, ϕ): (0°, 0°), (0°, 28°) and (90°, 20°), which was based on 0°/90° phase shifters controlled by PIN-diodes. In [141], a microstrip patch array was proposed with the ability to switch its main beam to three discrete angles of -15°, 0° and 15°. A similar beam-switching microstrip patch array with a higher efficiency was then proposed in [142], and these two arrays both used PIN-diode-based discrete phase shifters. Due to the phase shifter's discrete tuning nature, these arrays possessed non-continuous beam steerability. However, continuous beam-scanning is generally preferable due to its flexibility in accurate beam control. Therefore, in order to equip antennas with continuous beam-scanning ability, phase shifters with continuous phase variation are needed. A 1 × 4 dielectric resonator antenna (DRA) array conceptualized in [100] could continuously scan within an angular range of ±30°, which was based on four continuously tunable phase shifters. As reported in [101], a 1 × 4 substrate-integrated waveguide (SIW) phased array realized continuous scanning from -45° to 45° by employing phase shifters with smooth phase agility. However, the phase shifter

in [100] was utilizing 11 Barium strontium titanate (BST) Metal-Insulator-Metal varactors, which reached a phase shift of 260° with maximum bias voltages up to 50 V and an insertion loss below 5.9 dB. In [101], a reflection-type phase shifter based on 2 varactors was utilized with a 290° continuously tunable phase shift and an insertion loss below 3.5 dB, while it was with a size of $1.24\lambda_0 \times 0.46\lambda_0$.

One can observe that the phase shifter configuration and performance critically determine the beam scanning, reconfiguration capability and the entire dimension of the antenna system. For designs with emphasis on compact size and low cost, continuously tunable phase shifters with full 360° phase shift are generally desirable, while maintaining a minimum number of cascaded unit structures, a small device size and a low insertion loss. The differential phase shifter pair concept proposed in Chapter 3 is a viable solution for these requirements. A compact reconfigurable feeding network is proposed in this chapter which incorporates 3 of differential phase shifter pairs. A 1×4 DRA array is excited by this feeding network, which can supply sufficient phase differences between elements to scan its beam from -45° to +45° with a tunable operating frequency band from 4.75 to 5.25 GHz. The chapter is arranged as follows: Section 4.2 focuses on the optimization of a low-cross-polarization DRA radiator element. In Section 4.3, the design of the feeding network and the integration of the array are presented. The scan ability of the array is demonstrated in Section 4.4, followed by concluding remarks.

4.2 Low-Cross-Polarization DRA Design

DRAs are good candidates for wireless communications systems due to their high design flexibility and versatility [143]. They can offer wide bandwidth, high radiation efficiency and ease of fabrication with diverse manufacturing technologies including 3D printing [144]. Therefore, significant research efforts have been invested in the development of DRAs. As an important aspect for antenna design, minimizing the cross-polarization level is also essential for DRAs. To achieve this goal, loading electromagnetic structures [145] and optimizing the feeding structures [146] are two major approaches. In [145], a series of metal rings and strips were introduced to reduce the cross-polarization of a DRA array by 20 dB. In [146], the cross-polarization level caused by the asymmetrical structure was reduced to -26 dB through involving a differential-fed structure with equal-amplitude and anti-phase signal.

4.2.1 Analysis, Design and Optimization

In this section, a 3D-printed DRA excited by a T-shaped feeding structure is proposed, which leads to improved cross-polarization compared to standard probe-feeding. A traditional rectangular DRA excited by a side probe is firstly designed as a reference, based on the method outlined in [143]. The DRA has a length of a, a width of a and a height of h, and it sits on a ground plane. The excitation is provided by a probe on the resonator side which is connected to a 50 Ω microstrip line on the backside of the substrate. The configuration and major dimensions of the probe-fed DRA are illustrated in Fig. 4.1(a). The dielectric resonator (DR) is 3D-printed using PREPERM 3-D ABS DK 10.0 from Premix Oy with 100% infill percentage, which yields the highest relative permittivity of 8.3 [147]. The substrate is a 0.635 mm thick substrate Rogers RT6006 laminate with a relative permittivity of 6.15 and a loss tangent of 0.0019 at 5 GHz. The exciting probe has a length of h_1 and a diameter of 1.0 mm. To affix and align the DR on the ground plane, a 3D-printed support frame is utilized (the red frame on the antenna prototypes), which has a negligible effect on the DRA performance due to its low relative permittivity of around 2.

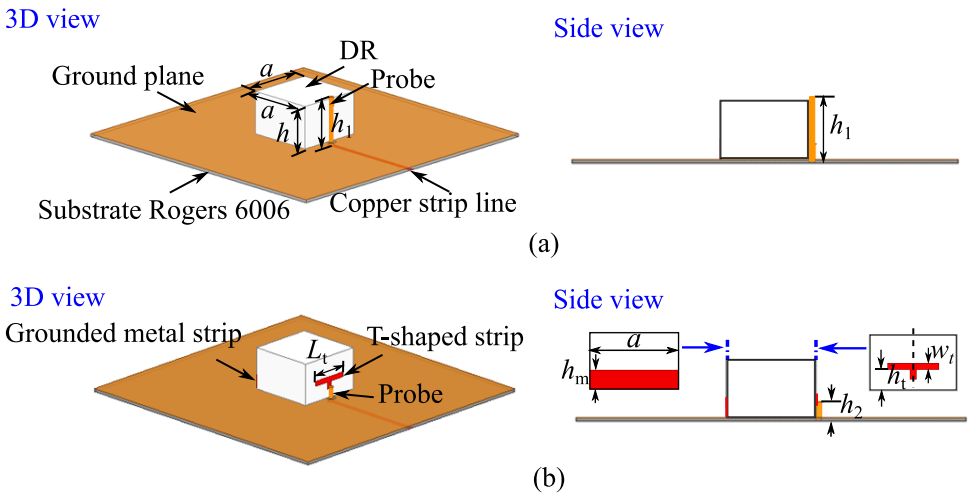

Figure 4.1. (a) Geometry of the reference probe-fed rectangular DRA and (b) geometry of the optimized DRA with T-shaped feeding structure. The major dimensions are: a =13.8 mm, h = 8.8 mm, h_1 = 10.0 mm, h_m = 3.0 mm, h_2 = 3.0 mm, h_t = 3.4 mm, w_t = 1.0 mm, and L_t = 8.0 mm.

The probe-fed DRA is predicted through simulations (performed using Ansys HFSS 2021) to work from 4.75 - 5.25 GHz with $|S_{11}|$ less than -10 dB, as shown in Fig. 4.2. Its simulated normalized H-plane patterns at 4.75, 5.00 and 5.25 GHz are plotted in

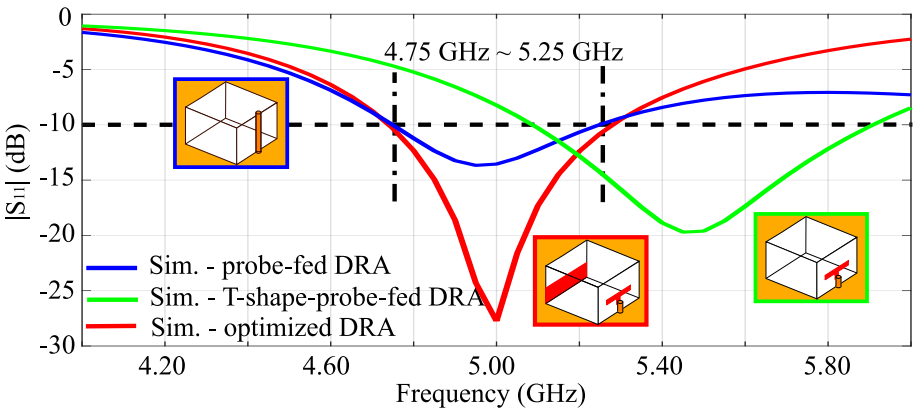

Figure 4.2. Simulated $|S_{11}|$ parameters of the probe-fed, T-shape-probe-fed and optimized T-shape-probe-fed DRAs.

Figs. 4.3(a) (b) and (c), respectively. Importantly, the simulated cross-polarization levels at these three frequencies are -11.2, -15.4 and -19.8 dB, respectively. It is emphasized that the H-plane contains the highest cross-polarization levels, and therefore the analysis is applied to this plane. The main source of the cross polarization component is the feeding probe, because a component of the currents on the probe will radiate in the cross-polarization except when $\theta = 0^\circ$ and 180°. It can be observed that the cross-polarization components are gradually increasing as the operation frequency decreases, and such a cross-polarization level of around -10 dB can be magnified significantly in an array design when scanning off broadside. Therefore, improving the polarization purity is very critical for DRA array applications.

Aiming to lower the cross-polarization level, a shorter feeding probe structure is intuitively adopted and a T-shaped strip is introduced to still provide a degree of freedom necessary to match the antenna. As shown in Fig. 4.1(b), the new feeding structure is applied on the same DRA configuration. More specifically, a T-shaped copper strip is soldered to a shortened probe and attached to the DR. The critical parameters of the T-shaped strip, including the length L_t, width w_t and relative height to the ground plane h_t are optimized using HFSS to achieve matching. It is noted that this new feed moves the operation frequency to a higher range from 5.09 to 5.91 GHz as shown in Fig. 4.2 as green line, and hence a grounded metal strip is introduced on the side of the DRA opposite to the feed. As a larger h_m leads to a lower resonance frequency, a value of 3 mm is chosen to bring the operation frequency range back to 4.75 to 5.25 GHz. In Fig. 4.3(a) (b) and (c), the simulated cross-polarization components in the H-plane are -19.2, -20.6

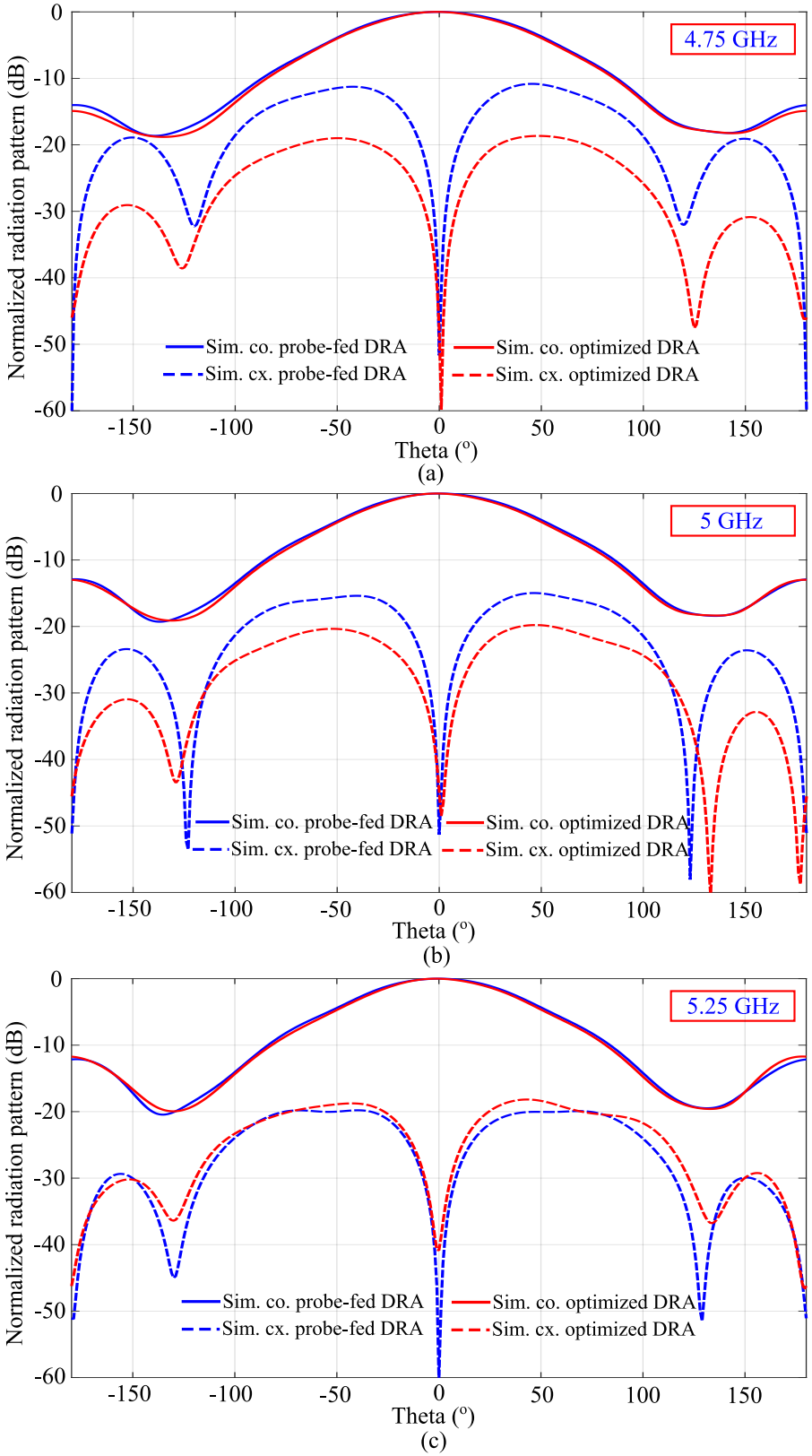

Figure 4.3. Simulated normalized radiation patterns in the H-plane at (a) 4.75 GHz, (b) 5.00 GHz and (c) 5.25 GHz.

and -18.7 dB at 4.75, 5.00 and 5.25 GHz respectively. As expected, with the new feeding structure, there is nearly a 8 dB reduction in the simulated cross-polarization at 4.75 GHz.

4.2.2 Fabrication and Measurement

To verify the proposed design, both DRA prototypes have been fabricated as shown in Fig. 4.4.

The measured reflection coefficient for the probe-fed DRA is from 4.74 to 5.45 GHz, whereas the value for the optimized DRA is from 4.7 to 5.4 GHz, as shown in Fig. 4.5. The measured normalized H-plane patterns of both prototypes are illustrated in Fig. 4.6. The highest measured cross-polarization levels are -8.2, -12.0 and -13.4 dB at 4.75, 5.00 and 5.25 GHz for the probe-fed DRA respectively, and for the T-strip-fed DRA the corresponding levels are -16.4, -15.0 and -13.7 dB at 4.75, 5 and 5.25 GHz respectively. The highest measured improvement in the cross-polarization at 4.75 GHz is 8.2 dB while the cross-polarization at 5.25 GHz is almost the same. The measured cross-polarization is a few dBs higher than predicted in simulations, which could be improved by a more accurate realization of the prototypes.

As a result of the cross-polarization component reduction, the experimentally obtained gains at 4.75 GHz are 3.9 and 6.4 dBi for the reference and the optimized DRAs respectively, and the gain increase is larger than 0.7 dB in the whole operation band as shown in Fig. 4.7. Using the new feeding, the performance of the H-plane patterns has been improved with lower measured cross-polarization levels, which remain consistent over the whole workband.

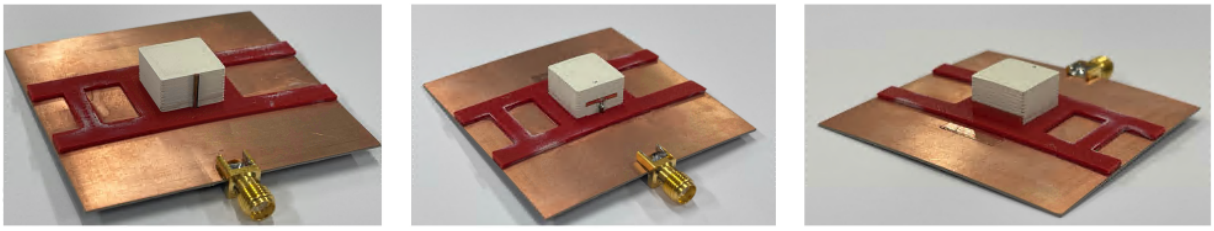

(a) (b) (c)

Figure 4.4. Prototypes of (a) the probe-fed rectangular DRA and the optimized DRA with T-shaped feeding structure: (b) Front view and (c) back view.

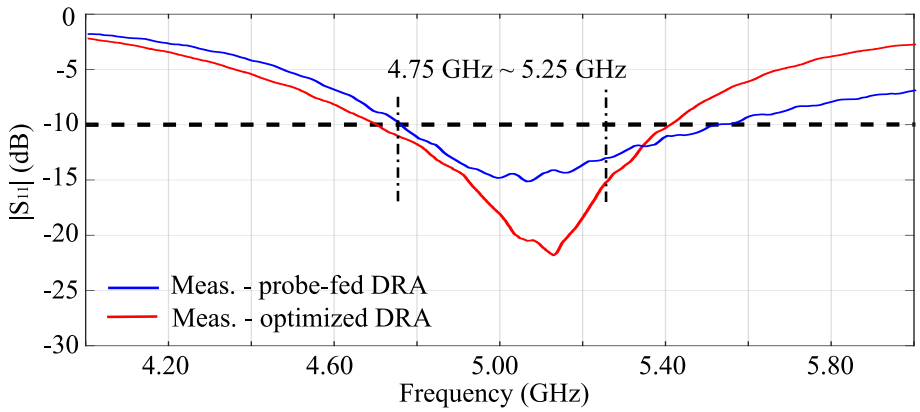

Figure 4.5. Measured $|S_{11}|$ parameters of the probe-feed, and optimized DRAs.

4.2.3 Summary

The optimized DRA antenna is a rectangular 3D-printed DR with a T-shaped-strip-loaded probe feed, a grounded metal strip and a ground plane. The T-shaped-strip-loaded feeding structure effectively reduces the cross-polarization by up to 8.2 dB, when compared to a counterpart antenna excited using a conventional SMA probe. Meanwhile, a grounded metal strip is introduced to compensate the shift to higher resonance frequency caused by the new feeding structure, so that the original operation frequency range is maintained. The utilization of the proposed feeding approach in the DRA array design presented in the next section results in a notable improvement of the cross-polarization level.

4.3 Array Structure

A 1 $\times$ 4 beam-steerable array with frequency reconfigurability is implemented. The configuration of the array consists of two major groups: four radiator antennas located on the top of the substrate and a reconfigurable feeding network positioned on the bottom, which can be described as follows:

Radiator elements: The DRA [148] is chosen as the radiating element, since such radiators can have wide bandwidth, low loss and can be conveniently fabricated with 3D printing technology [149]. The low-cross-polarization DRA optimized in Section 4.2 is utilized here as element, as shown in Fig. 4.8(a).

Feeding network: As shown in Fig. 4.8(b), the two-stage reconfigurable feeding network is comprised of three differential phase shifter pairs and their ground

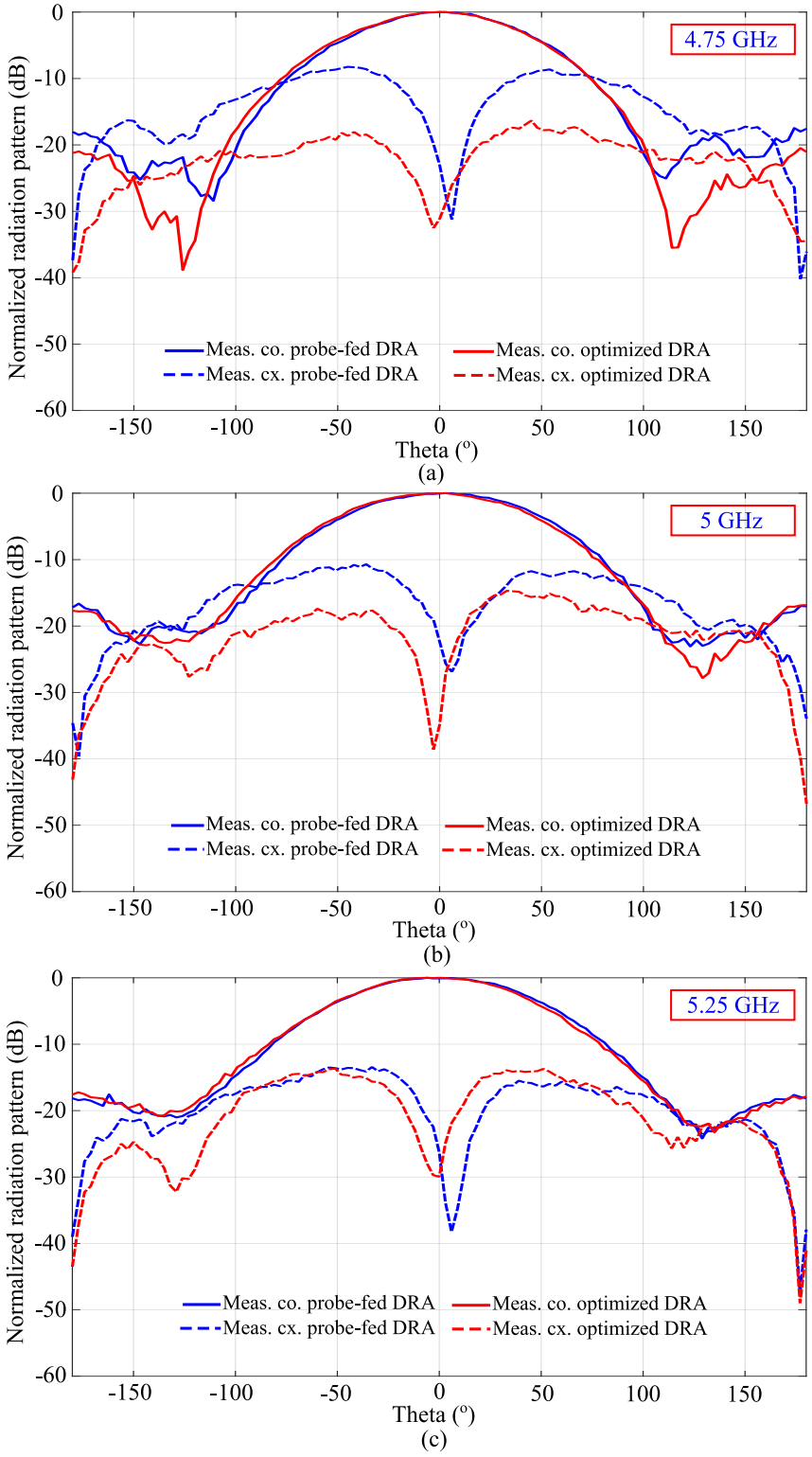

Figure 4.6. Measured normalized radiation patterns in the H-plane at (a) 4.75 GHz, (b) 5.00 GHz and (c) 5.25 GHz.

plane serves as the array ground as well. Each of these pairs is connected to a Wilkinson power divider to equally split the incoming power. The two units of

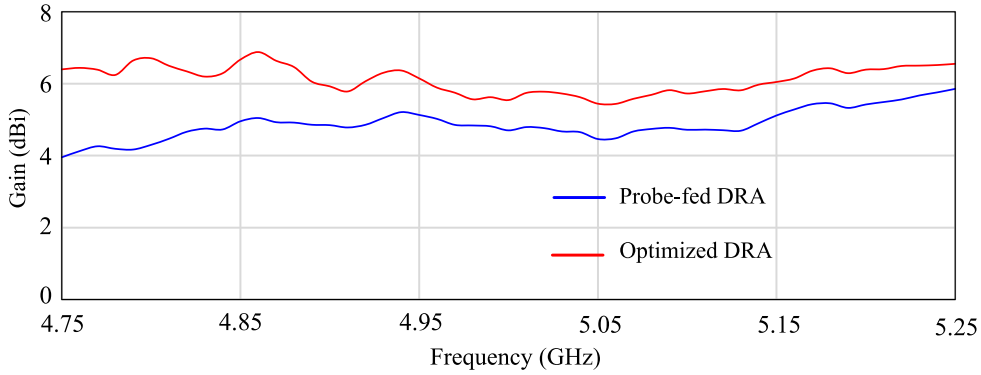

Figure 4.7. Realized gains in the H-plane of two DRAs.

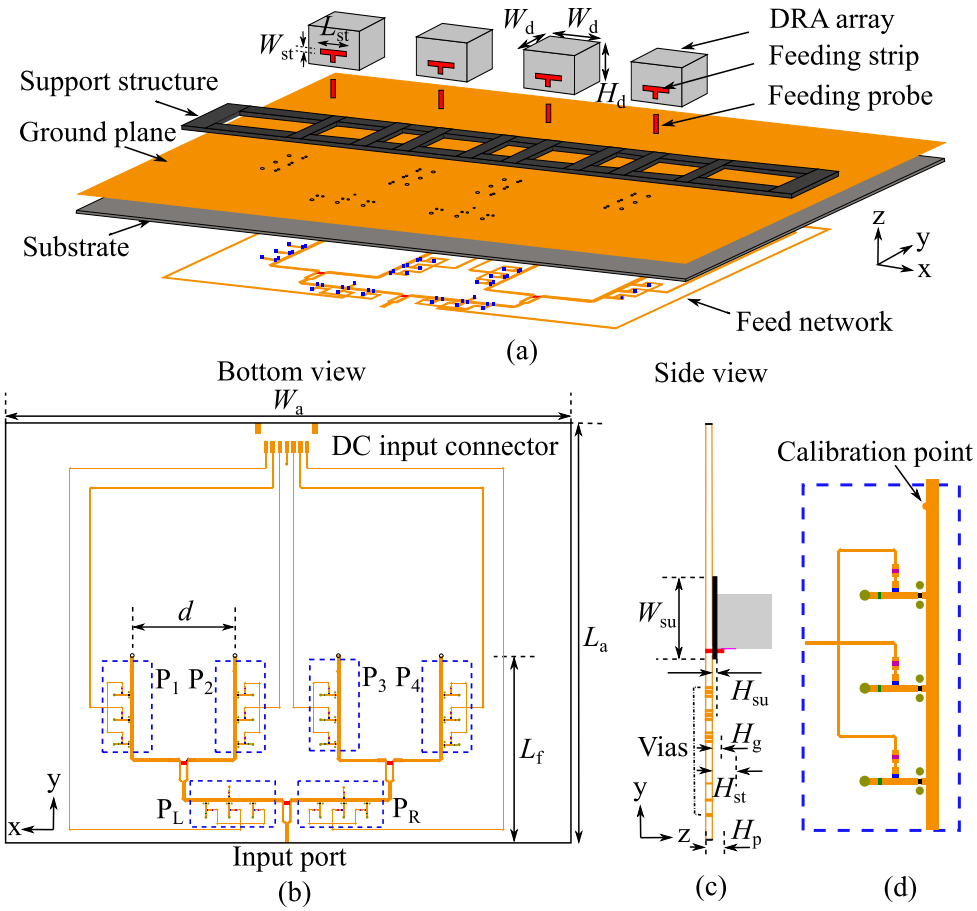

Figure 4.8. The configuration of the DRA array: (a) Exploded 3D perspective view of the whole array, (b) feeding network layout (bottom view of the array), (c) side-view of the array, and (d) zoomed-in view of the phase-shifting unit with calibration point. Critical dimensions are d = 30.00 mm, L_f = 60.60 mm, H_d = 12.00 mm, H_p = 3.00 mm, H_{su} = 1.00 mm, W_d = 13.76 mm, W_{su} = 24.00 mm, L_{st} = 9.00 mm, W_{st} = 1.00 mm,H_g = 1.40 mm, H_{st} = 4.40 mm, L_a = 136.00 mm, and W_a = 170.00 mm.

the first power division stage are denoted as P_L and P_R, whereas the four phase-tuning units in the second stage are denoted as P_1, P_2, P_3, P_4. Correspondingly, six separate DC voltages from three power supplies are used to manually control the phases of the three phase shifter pairs. All the DC bias controls are linked to a plug-in connector at the edge of the board.

It is worth to mention that there are six calibration points specifically designed at each end of the phase shifter unit. These points are magnified in Fig. 4.8(d). These simple points serve as dedicated structural designs used for on-board calibration, and the detailed description of the calibration procedure can be found in Chapter 5.

As displayed in Fig. 4.8, from bottom to top the array incorporates a reconfigurable feeding network, four probe-strip-fed 3D-printed DRA elements, and a 3D-printed structure supporting these DRAs. The whole structure is realized on a 0.635 mm thick substrate Rogers RT6006 laminate. Each DRA element with a square cross-section is excited by a T-shaped copper strip fed by a short copper probe which is connected to the phase-tuning unit on the other side of the substrate. The distance between these elements is 30 mm corresponding to a half wavelength in free space at 5 GHz. To precisely and securely accommodate the elements, a support structure 3D-printed with PLA (relative permittivity of 2) is utilized.

4.4 Beam-Steering Ability

The reconfigurable feeding network theoretically can supply phase variation from -180° to 180° to the four array elements, however, the scanning angle of the array is limited by the element radiation pattern. Therefore, the designed array aims to realize a continuous beam scanning from -45° to 45° in the H-plane (xz-plane) with frequency reconfigurability from 4.75 to 5.25 GHz.

The simulated radiation patterns of the proposed array at 5.00, 4.75 and 5.25 GHz are illustrated in Figs. 4.9 to 4.11. The simulated normalized 5.00 GHz radiation patterns scanning at angles of 0°, 10°, 20°, 30°, 40° and 45° in the H-plane are depicted in Fig. 4.9. The simulation predicts that the main beam can be scanned from 0° to 45° continuously with a gain drop of less than 2.42 dB. Similarly, the same beam steerability at 4.75 and 5.25 GHz can be observed in simulation as shown in Figs. 4.10 and 4.11

with a maximum gain drop of 2.95 and 3.34 dB respectively. The gain drops are mainly produced by the varactor losses which are generally not monotonously increasing with the scan angle. An optimal combination could be determined by a calibration process to improve performance to some extent. The technique to find the best combination of bias for low insertion loss for a beam towards a given direction, will be discussed in detail in Chapter 5. Due to the symmetry of the proposed array, only 0° to 45° beam scanning scenarios are demonstrated here. The simulated radiation patterns in the E-plane (as shown in Fig. 4.12) are mirror-symmetric with small fluctuations which are mainly caused by the finite ground plane size. The simulated cross-polarization levels in the E-plane are less than -50 dB and in H-plane are lower than -20 dB from 4.75 to 5.25 GHz. Experimental validation of the radiation patterns require a calibration procedure, which will be provided in the next chapter (Chapter 5).

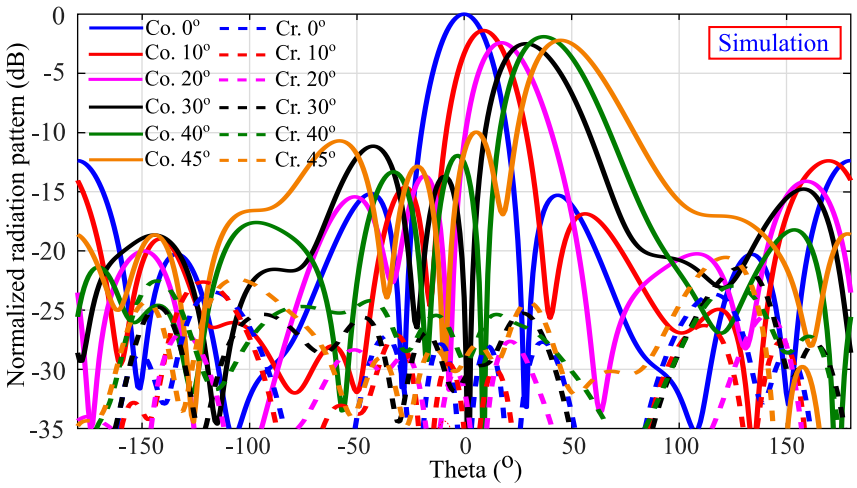

Figure 4.9. Simulated radiation patterns obtained when scanning from 0°, 10°, 20°, 30°, 40° to 45° in the H-plane at 5.00 GHz.

4.5 Conclusion

In order to achieve a beam-steerable antenna that is both compact and cost-effective, a design incorporating three of differential phase shifter pairs in a two-stage feeding network has been proposed. This configuration has led to the development of a 1 × 4 beam-scanning DRA array. To improve polarization purity, a 3D-printed DRA with a T-shaped-strip-loaded probe feeding structure has been implemented. The optimal DRA demonstrates significant cross-polarization reduction, with a maximum measured reduction of 8.2 dB at 4.75 GHz, maintaining the cross-polarization level around -15 dB

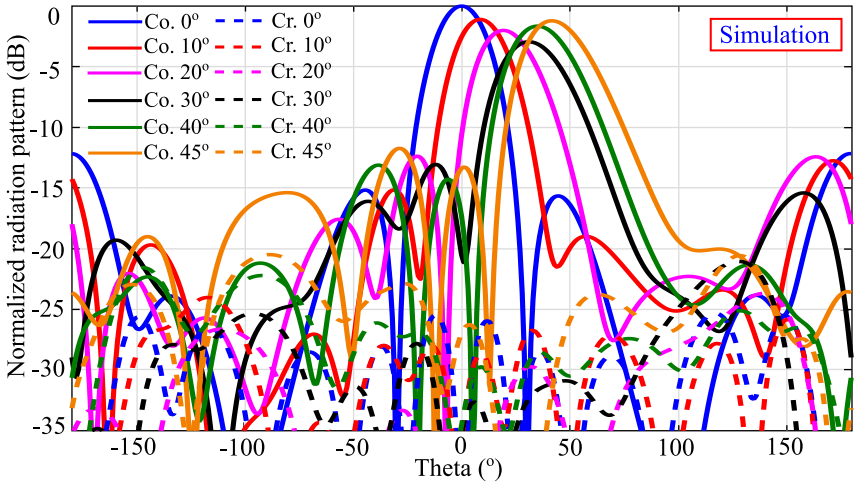

Figure 4.10. Simulated radiation patterns obtained when scanning from 0°, 10°, 20°, 30°, 40° to 45° in the H-plane at 4.75 GHz.

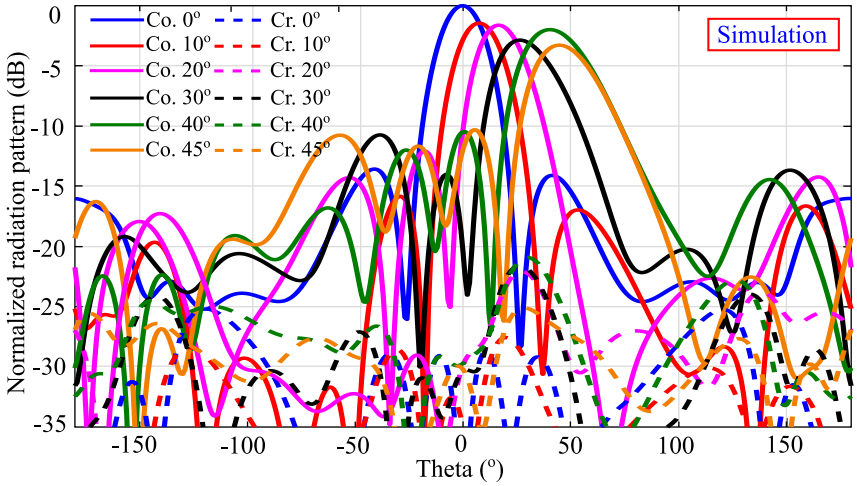

Figure 4.11. Simulated radiation patterns obtained when scanning from 0°, 10°, 20°, 30°, 40° to 45° in the H-plane at 5.25 GHz.

over entire operational bandwidth from 4.75 to 5.25 GHz. The optimized array has been estimated to successfully steer the main beam continuously from -45° to +45° across the frequency range of 4.75 to 5.25 GHz. This successful beam steering capability predicted for a linear array benefits from the efficiency of the reconfigurable feeding network, which will be validated experimentally in the next chapter.

Importantly, by seamlessly integrating the differential phase shifter pairs, the feeding network achieves a compact and low-cost design while ensuring that sufficient phase differences are provided to the antenna elements. This integration of phase shifter pairs offers a potential solution for applications with limited space and a need for cost-effectiveness.

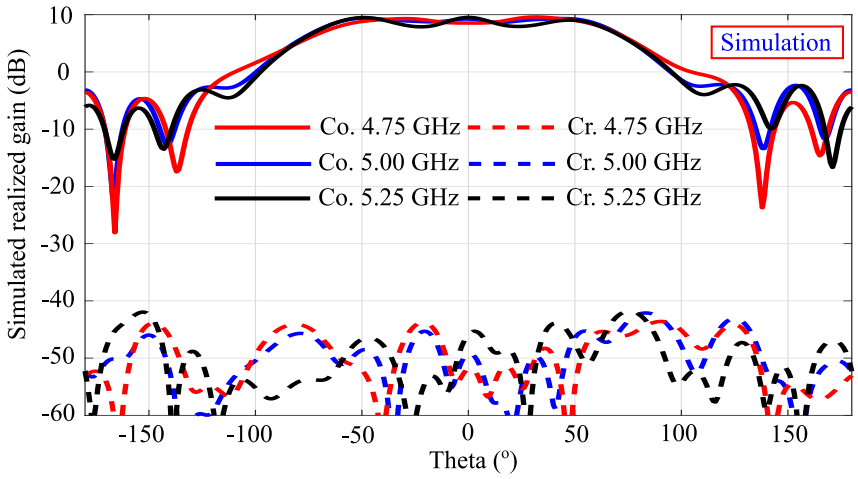

Figure 4.12. Simulated realized gain patterns in the E-plane when scanning at 0°

Chapter 5

Calibration Procedure and Measurements

AN accurate calibration procedure is proposed for the single-feed beam-steerable antenna proposed in the previous chapter. The beam steering is controlled by varactor-based phase shifters working in differential pairs. The calibration process consists of two steps, one for the feeding network and another for the remaining part of the array. Firstly, based on the performance curve of every phase shifter measured from dedicated sampling points on the circuit, a fast selection algorithm is employed to obtain the control voltages for all differential phase shifter pairs, according to the required phase differences. The final control voltages for a particular beam configuration are validated and fine-tuned on-board at the sampling points. Secondly, a pattern optimization approach is implemented to compensate the performance degradation due to the fabrication tolerances of the radiating elements, which cannot be considered in the first step. To verify the effectiveness of this procedure, the calibrated array is measured under various scenarios, including sum-pattern scanning from -45° to 45° and difference-pattern with null scanning from -30° to 30°.

Statement of Authorship

Title of Paper	Calibrated Design of Beam-Steerable Antennas Fed by Varactor-Based Phase Shifters
Publication Status	☑ Published ☐ Accepted for Publication ☐ Submitted for Publication ☐ Unpublished and Unsubmitted w ork w ritten in manuscript style
Publication Details	2023 17th European Conference on Antennas and Propagation (EuCAP), Florence, Italy, 2023, pp. 1-5, doi: 10.23919/EuCAP57121.2023.10133387.

Principal Author

Name of Principal Author (Candidate)	Yuan YUAN		
Contribution to the Paper	Under the supervision of C. Fumeaux and S. J. Chen, I performed the design, simulation, prototype development, measurements and wrote the manuscript for submission.		
Overall percentage (%)	60%		
Certification:	This paper reports on original research I conducted during the period of my Higher Degree by Research candidature and is not subject to any obligations or contractual agreements with a third party that would constrain its inclusion in this thesis. I am the primary author of this paper.		
Signature		Date	26/07/2023

Co-Author Contributions

By signing the Statement of Authorship, each author certifies that:

i. the candidate's stated contribution to the publication is accurate (as detailed above);

ii. permission is granted for the candidate in include the publication in the thesis; and

iii. the sum of all co-author contributions is equal to 100% less the candidate's stated contribution.

Name of Co-Author	Christophe Fumeaux		
Contribution to the Paper	I acted as supervisor for the candidate, aided in design, development, and measurements, revising the manuscript, and evaluating the final version of the manuscript. I give consent for Yuan YUAN to present this paper for examination towards the Doctorate of Philosophy.		
Signature		Date	27/07/2023

Name of Co-Author	Shengjian Jammy Chen		
Contribution to the Paper	I acted as supervisor for the candidate, aided in design, development, and measurements, revising the manuscript, and evaluating the final version of the manuscript. I give consent for Yuan YUAN to present this paper for examination towards the Doctorate of Philosophy.		
Signature		Date	29/07/2023

Please cut and paste additional co-author panels here as required.

Statement of Authorship

Title of Paper	Pattern Optimization of Beam-Reconfigurable Antenna Fed by Varactor-based Phase Shifters
Publication Status	☑ Published ☐ Accepted for Publication ☐ Submitted for Publication ☐ Unpublished and Unsubmitted w ork w ritten in manuscript style
Publication Details	2023 IEEE Radio and Antenna Days of the Indian Ocean (RADIO), Balaclava, Mauritius, 2023, pp. 1-2, doi: 10.1109/RADIO58424.2023.10146100.

Principal Author

Name of Principal Author (Candidate)	Yuan YUAN
Contribution to the Paper	Under the supervision of C. Fumeaux and S. J. Chen, I performed the design, simulation, prototype development, measurements and wrote the manuscript for submission.
Overall percentage (%)	60%
Certification:	This paper reports on original research I conducted during the period of my Higher Degree by Research candidature and is not subject to any obligations or contractual agreements with a third party that would constrain its inclusion in this thesis. I am the primary author of this paper.
Signature	Date 26/07/2023

Co-Author Contributions

By signing the Statement of Authorship, each author certifies that:

i. the candidate's stated contribution to the publication is accurate (as detailed above);

ii. permission is granted for the candidate in include the publication in the thesis; and

iii. the sum of all co-author contributions is equal to 100% less the candidate's stated contribution.

Name of Co-Author	Christophe Fumeaux
Contribution to the Paper	I acted as supervisor for the candidate, aided in design, development, and measurements, revising the manuscript, and evaluating the final version of the manuscript. I give consent for Yuan YUAN to present this paper for examination towards the Doctorate of Philosophy.
Signature	Date 27/07/2023

Name of Co-Author	Shengjian Jammy Chen
Contribution to the Paper	I acted as supervisor for the candidate, aided in design, development, and measurements, revising the manuscript, and evaluating the final version of the manuscript. I give consent for Yuan YUAN to present this paper for examination towards the Doctorate of Philosophy.
Signature	Date 20/07/2023

Please cut and paste additional co-author panels here as required.

5.1 Introduction

PATTERN-reconfigurable antennas are widely used in modern communications systems [2] to realize flexible beamforming, such as wide-angle scanning [150] or null scanning [151]. Especially, planar reconfigurable beam-steerable antennas based on active electronic components are being developed rapidly, because they possess advantages such as compact structure, low cost and low power consumption, as compared to traditional phased arrays [152] [153]. As for most beam-scanning arrays, multi-element pattern-reconfigurable antennas require a calibration procedure to accurately acquire the required amplitude and phase of the elements, with the aim of compensating distortions caused by factors such as manufacture tolerances, components variations and/or mutual coupling between elements [154] [155]. Such calibration procedure has already become a standard step before operation of phased arrays [156]. Generally, phased arrays adopt a closed-loop calibration which considers all components from input to radiant element as a whole unit, so as to obtain high degree of accuracy [157]. However, such a calibration process is generally complex and expensive. Therefore, a fast and accurate on-board calibration procedure is highly desirable for multi-element beam-steerable antennas based on low-cost varactor-based phase-shifters. This is critical since generally such arrays have less predictable behavior than classical phased arrays.

In this chapter, the calibration procedure for the beam-steering array proposed in Chapter 4 is demonstrated. The calibration process majorly involves two steps, one for the reconfigurable feeding network and the other for the remaining sections of the array. First of all, this single-feed array is controlled by six varactor-based phase shifters operating in differential pairs, which achieves a continuously tunable phase difference nearly covering 0° to 360°. As the specific operation principle relies on differential phases between two adjacent elements, non-unique combinations of relative phases are possible and the calibration is less predictable than in conventional phased arrays. To address this challenge, a fast and accurate calibration procedure and an optimization step are required.

To implement the first step of the calibration procedure, a small probing spot is added to the output of each phase shifter. At these sampling spots, the characteristic curves between control voltages and S_{21} parameters of each phase shifter are gathered. The control voltages required for all differential phase shifter pairs can be then compensated based on these curves using a fast selection algorithm based on multi-objective

optimization, with the aim of selecting the combination of differential phases with the lowest overall losses. Fine tuning and final validation of the required phase difference can be conveniently conducted at these probing spots. Up to this point, variations in components and fabrication tolerances of the reconfigurable feeding network have been taken into account and rectified.

The remaining parts of the array, e.g., the 3D-printed dielectric resonators, also may cause unexpected radiation pattern distortions such as imprecise beam direction, due to the variations and tolerances of these components. To correct these distortions, the second step, namely a pattern optimization procedure based on the calibration data of the feeding network, is followed. By selecting the appropriate control parameters (voltages applied on the varactors) on the phase shifter pairs, these variations can be compensated. To validate the proposed pattern optimization, two scenarios with precise beam direction control are demonstrated in this section. After pattern optimization, a beam direction exactly pointing to 30° from 39° at 4.75 GHz and from 36° at 5.25 GHz are achieved, which validate the proposed approach.

Following the proposed two-step calibration procedure, the presented measurement results will illustrate that the beam-steerable array successfully achieves precise sum-pattern scanning from -45° to 45° and null-scanning functionality from -30° to 30° in the H-plane. Experimental validation confirms that the introduced calibration procedure is accurate and easily implementable. In addition, by accurately controlling the differential phase shifter pairs within the feeding network, the beam-steerable dielectric resonator antenna (DRA) array offers unique functionalities, including frequency reconfigurability and beamforming flexibility to a certain extent.

The Chapter 5 is arranged as follows: Section 5.2 discusses the dedicated calibration procedure with its two steps. Section 5.3 showcases the measurement results of the beam-steerable array following the calibration process and the unique functionalities of the array.

5.2 Calibration Procedure

The 1 × 4 beam-steerable DRA array proposed in Chapter 4 has been fabricated and characterized experimentally to validate the design. The array prototype is illustrated in Fig. 5.1. The array configuration can be divided into two main groups: the first one consists of a reconfigurable feeding network located on the bottom of the substrate and

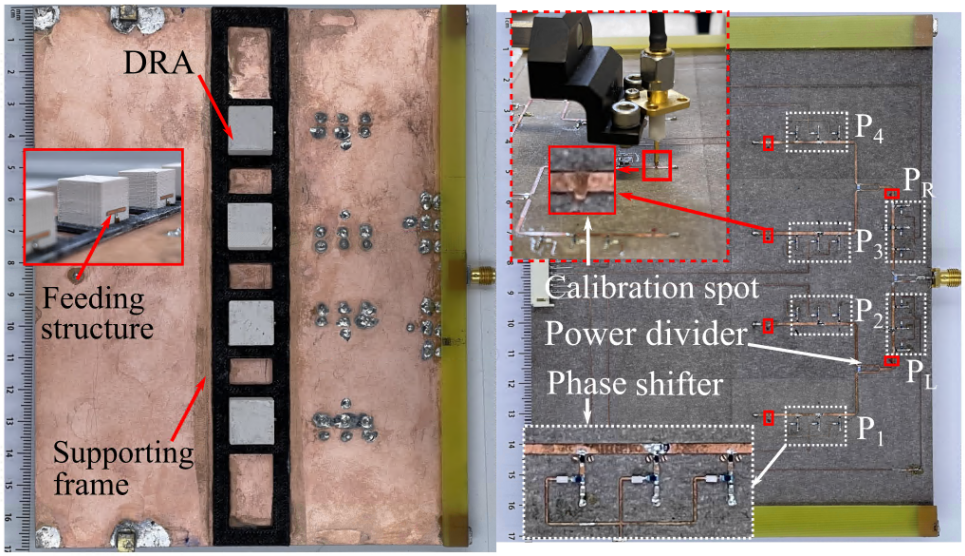

Figure 5.1. Photographs of the 1 × 4 linear DRA array, (a) front view, inset: T-shape-fed DRA elements, and (b) back view, inset: calibration probe collecting data from the calibration spots enlarged in a red dotted line, the sampling spots are in red solid lines, and the phase shifters are in white dotted lines labeled as P_L, P_R, P_1, P_2, P_3 and P_4.

the other part comprises four radiator antennas positioned on the top with a supporting frame. Considering the distinct structures within the two groups, the calibration procedure will be implemented in two steps. The first step involves calibrating the feeding network, while the second step focuses on compensating the distortions from the radiators.

5.2.1 Calibration for Feeding Network

For an array with equally excited elements, fast and accurate calibration and optimization are presented to compensate for component and fabrication tolerances of the feeding network, allowing to select the most efficient differential pair phase combinations. The calibration process contains three major steps, namely collection of phase-shifter calibration curves, fast selection algorithm implementation and on-board fine-tuning.

Step 1: Collecting the Phase-shifter Calibration Curves

As shown in the inset photo in Fig. 5.1(b), a probe is utilized to measure the complex S_{21} parameters on dedicated sampling spots whose physical distances to the corresponding phase shifters are precisely equal in every stage. Example of probed magnitudes and phases of S_{21} parameter curves are shown in Fig. 5.2(a) for the first-stage

pair P_L and P_R. Similar measured curves can be retrieved at other frequencies between 4.75 and 5.25 GHz. For the second-stage phase shifter pairs, the corresponding results shown in Fig. 5.2(b) display the measured curves of P_1 and P_2. For symmetrical elements, the curves of P_1 and P_4 are similar, and P_2 and P_3 are similar. These curves indicate that there exist small variations between the phase shifters' magnitude and phase characteristics, so calibration is required to achieve accurate beam control.

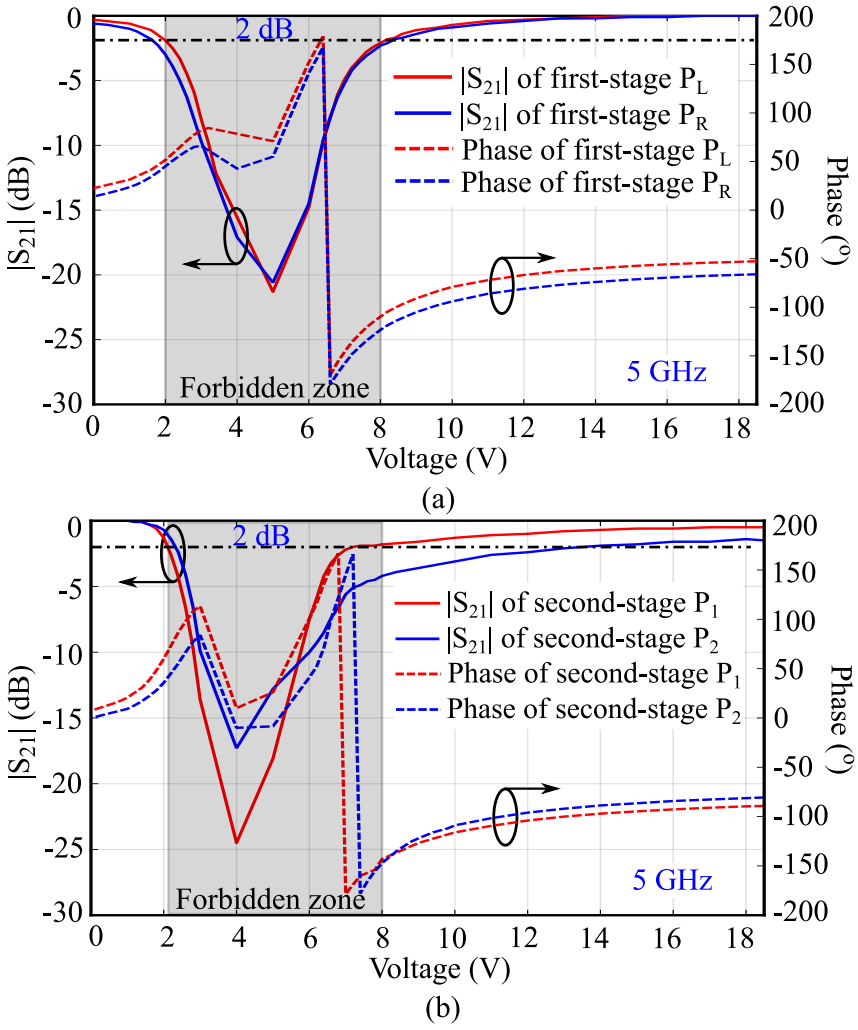

Figure 5.2. S_{21} parameters of (a) the first-stage pair P_L and P_R and (b) the second-stage pair P_1 and P_2 at 5 GHz. The forbidden zones with $|S_{21}| <$ -2 dB are shaded in gray.

Importantly, the calibration spots are defined right beside the host-lines with the aim to simplify finding their exact location and thus reduce measurement errors. It is worth to mention that the calibration is also possible without pre-marked sampling spots if

one can locate measurement points with equal distance to the relative phase shifters in each stage.

Step 2: Fast Selection Algorithm

Due to the differential working mode, there exist numerous possible phase choices at each output terminal to achieve the desired phase difference between two adjacent elements. For instance, a phase difference of 30° can be fulfilled when -106° and -146° are set as the two output phases, but the same phase difference can be achieved when -146° and -176° are chosen. Each phase combination will have a different insertion loss, since loss is mainly determined by the voltage-dependent loss in the varactors. This provides a freedom to select the best among various possible combinations for each required phase difference. A fast selection algorithm is adopted, which mainly includes two steps, namely an exhaustive calculation and a multi-objective optimization. An exhaustive list of all achievable phase differences is firstly calculated for each pair based on the measured curves. Secondly, for a desired phase difference, the best combination is determined using multi-objective optimization, i.e., considering simultaneously a phase tolerance of $\pm 5°$, the minimum achievable insertion loss level and a reflection coefficient $|S_{11}|$ of less than -10 dB.

For illustration, the algorithm will be applied here to generate radiation patterns with a null to be scanned to a given angle in the H-plane. Example of null-scanning states for given angles up to 30° are listed in Table 5.1, with $\Delta\phi_1$ denoting the phase difference for the first-stage phase shifter pair and $\Delta\phi_2$ corresponding to the phase difference for the two second-stage pairs. The algorithm is able to determine optimized control voltages from all the possible combinations using the multi-objective optimization. This algorithm is implemented using genetic algorithm (GA) in Matlab.

Step 3: On-board Fine-tuning

The final processing step is to validate the phase distribution of each feeding channel on the array. To this end, the feeding amplitude and phase are probed at the four sampling spots. Due to the imperfect isolation of the divider, there is still mutual influence between the two-stage phase shifter pairs. Hence, fine-tuning is necessary for the final sets of control voltages, especially if accurate beamforming (e.g., null-steering) is required.

Table 5.1. Fine-tuned control voltages of phase shifters

$\phi(^\circ)$	$\Delta\phi_1$*	$\Delta\phi_2$△	P_L	P_R	P_1	P_2	P_3	P_4
5.00 GHz								
0	180.0	0.0	2.1	8.3	0.0	1.1	0.8	0.0
-10	117.4	-31.6	0.0	8.7	6.8	9.9	7.6	10.4
-20	56.8	-61.6	18.2	7.8	6.8	18.5	7.2	18.3
-30	0.0	-90.0	18.4	12.4	10.7	0.0	12.2	0.0
4.75 GHz								
0	180.0	0.0	0.7	6.6	0.0	0.8	0.4	0.0
-10	117.4	-31.6	0.0	12.1	7.1	18.5	7.5	9.8
-20	56.8	-61.6	18.5	7.6	0.0	1.6	0.0	1.2
-30	0.0	-90.0	15.0	18.5	6.0	18.5	6.0	13.7
5.25 GHz								
0	180.0	0.0	9.3	2.3	0.0	0.0	0.0	0.0
-10	117.4	-31.6	0.0	11.7	9.4	18.5	10.3	18.5
-20	56.8	-61.6	3.0	0.0	0.0	3.1	0.0	3.1
-30	0.0	-90.0	18.3	18.3	12.3	1.2	10.8	0.0

* $\Delta\phi_1$ is the required phase difference in the first-stage pair P_L and P_R .
△ $\Delta\phi_2$ is the required phase difference in the second-stage pairs P_1 and P_2, P_3 and P_4.

At this stage, considerations have been made for variations in components and fabrication tolerances of the reconfigurable feeding network, and appropriate corrective measures have been implemented.

For illustration, final control voltages for all null-scanning states are obtained as listed in Table 5.1. Coupling between the paths may slightly shift the forbidden zone, which explains why some of the phase shifters operate at voltages between 2 and 8 V. Excited by these bias voltage combinations, the detected phase values of four outputs are able to satisfy the desired relative phases accurately.

In accordance with the sum-pattern scanning capability of the beam-steerable array estimated in Chapter 4, i.e., scanning its beam from -45° to 45°, the optimization process focuses on achieving maximum gain or minimizing side-lobe levels. The optimized values for maximum gain and relatively low side-lobe levels at frequencies 4.75, 5.00, and 5.25 GHz are presented in Table 5.2.

Table 5.2. Scan control voltages of phase-tuning units

Angle (°)	Phase shifters (Voltage : V)						Frequency (GHz)
	P_L	P_R	P_1	P_2	P_3	P_4	
0	18.0	18.0	15.0	15.0	15.0	15.0	5.00 (Set-C)
	0.0	0.0	0.0	0.0	0.0	0.0	5.00 (Set-D)
	18.0	18.0	18.0	18.0	18.0	18.0	4.75
	18.0	18.0	18.0	15.5	18.0	18.0	5.25
10	15.9	8.4	18.0	8.2	9.9	8.1	5.00
	18.0	7.7	12.6	7.9	9.1	7.2	4.75 (Set-A)
	18.0	9.0	13.0	9.3	12.6	8.9	5.25 (Set-B)
20	0.0	10.4	18.0	7.9	15.0	7.6	5.00
	0.0	12.4	14.3	6.8	14.2	6.5	4.75
	0.0	9.4	2.3	0.0	2.7	0.0	5.25
30	8.2	0.0	0.0	18.0	0.0	18.0	5.00
	7.0	0.9	0.0	18.0	0.0	18.0	4.75
	8.3	0.0	0.0	18.0	0.0	11.6	5.25
40	11.1	0.5	0.8	18.0	0	9.5	5.00
	8.4	0.9	0.0	18.0	0.0	18.0	4.75
	10.9	0.0	1.4	11.0	0.0	10.2	5.25
45	11.3	0.0	1.2	18.0	0.0	8.8	5.00
	13.6	0.0	0.0	18.0	0.2	9.8	4.75
	18.0	0.0	0.7	9.7	0.6	10.2	5.25

5.2.2 Pattern Optimization

The magnitude and phase of each output terminal (P_1 - P_4) can be obtained at the calibration points with a test probe. With this data collection, the magnitude and phase distribution before each antenna element can be optimized correspondingly for the feeding network, which would be sufficient for ideal cases, where no other variations are introduced by other antenna components. However, these variations do exist in reality which could lead to non-negligible deterioration on the radiation patterns. Two typical scenarios of imperfect patterns are shown in Fig. 5.3(a) and (b), where unexpected 9° and 6° angular offset is observed at 4.75 and 5.25 GHz for targeted 30° beam direction configuration, respectively. These angular offsets are due to the fabrication tolerance in the feeding probe and the 3D-printed radiating dielectric resonator (DR)

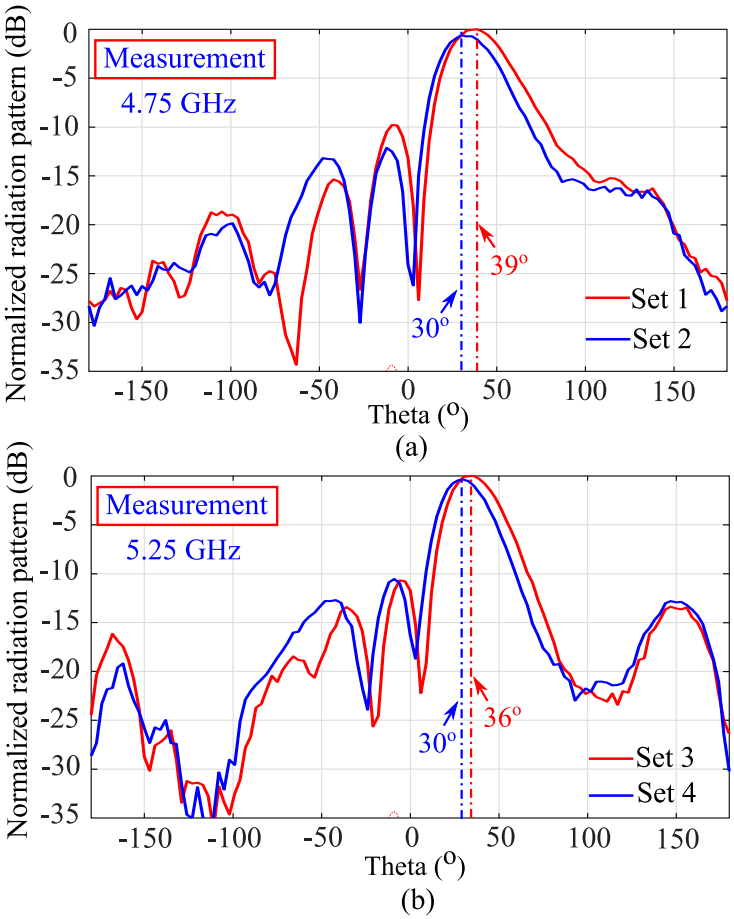

Figure 5.3. Measured normalized radiation patterns in the H-plane scanning to 30° at (a) 4.75 GHz and (b) 5.25 GHz.

elements, where an unpredicted phase shift is introduced. Therefore, a possible solution to this problem is to implement phase compensation directly based on array factor estimation.

For the first example case mentioned above, the measured normalized realized gain pattern targeting 30° main beam direction is shown in Fig. 5.3(a), using the calibration-based voltage control as given as Set-1 in Table 5.3. The beam direction is unexpectedly shifted to 39° which can be tuned back to 30° by reducing the phase difference between the two sub-group antenna elements, i.e., the group of two left-handside units and the group of two right-handside units. This method can be considered as an adjustment on the two-element array factor for the two sub-group elements, which is controlled by the first stage phase shifter pair. Based on this analysis, a phase difference offset of around -20° between the two sub-groups should provide a beam shift towards broadside, which can bring the main beam to 30°. With this -20° implemented between P_L and P_R as shown in Set-2 in Table 5.3, a new pattern measurement is then conducted to

Table 5.3. Control voltages of phase-tuning units when scanning to 30°

Angle	Phase shifters (Voltage : V)						Frequency
30°	P_L	P_R	P_1	P_2	P_3	P_4	(GHz)
Set-1	8.4	0.9	0.0	18.0	0.0	18.0	4.75
Set-2	7.0	0.9	0.0	18.0	0.0	18.0	
Set-3	8.8	0.0	0.0	18.0	0.7	12.1	5.25
Set-4	8.3	0.0	0.0	18.0	0.0	11.6	

check the optimization. The results are plotted in Fig. 5.3(a) in the blue curve, where the main beam accurately points towards 30°. This suggests that the optimization is successful.

The second scenario is shown in Fig. 5.3(b) when the targeted scanning angle is also 30° but at 5.25 GHz. A deviation of 6° in the main beam direction is observed when using the calibration-based voltage control (denoted as set-3 in Table 5.3). For this case, the effective phase difference at 5.25 GHz is calculated to be around 22° to compensate the pointing error in the first stage. However, in this scenario, reducing phase difference between the two sub-groups by around 22° in P_L and P_R would involve a large insertion loss due to the phase shifter characteristics. Instead, a combination of phase offset in the first and second stage of phase shifter pairs is utilized, i.e., a phase reduction of around 15° in P_L, and another increasing of around 10° in both P_3 and P_4. This leads to an overall phase compensation of around -22° in the first stage at 5.25 GHz. The measured gain pattern using this new voltage set (Set-4 in Table 5.3) is shown in Fig. 5.3(b), where the main beam direction is corrected to be exactly at 30°.

It can be seen the proposed pattern optimization method, as an essential addition to the first calibration step, is able to effectively correct unexpected pattern deterioration due to the effects from non-ideal antenna components, such as their feeding structure and the 3D-printed antenna elements.

At this stage, a comprehensive calibration procedure has been successfully carried out. The adjusted DC voltages for difference-pattern scanning and sum-pattern scanning are provided in Table 5.1 and Table 5.2, respectively. These modified voltages will be utilized in subsequent testing procedures.

5.3 Experimental Results

In this section, the calibration procedure for the varactor-controlled array is experimentally validated. Furthermore, the differential operation mode of the phase shifter pairs introduces additional flexibility to modify and optimize the array's pattern for maximum gain or reduced sidelobes. These modifications and optimizations will be demonstrated and explained in detail.

5.3.1 Reflection Coefficient

1) Sum-pattern scanning: Figure 5.4 illustrates the experimental results for the reflection coefficients at various sum-pattern scan states at 5.00 GHz. The simulated reflection coefficient at 0° is shown here for comparison, where a reasonable agreement is observed with measured data. The tested reflection coefficients are all below -10 dB at the operating frequencies, from 4.75 to 5.25 GHz, when scanning to 0°, 10°, 20°, 30°, 40° and 45°.

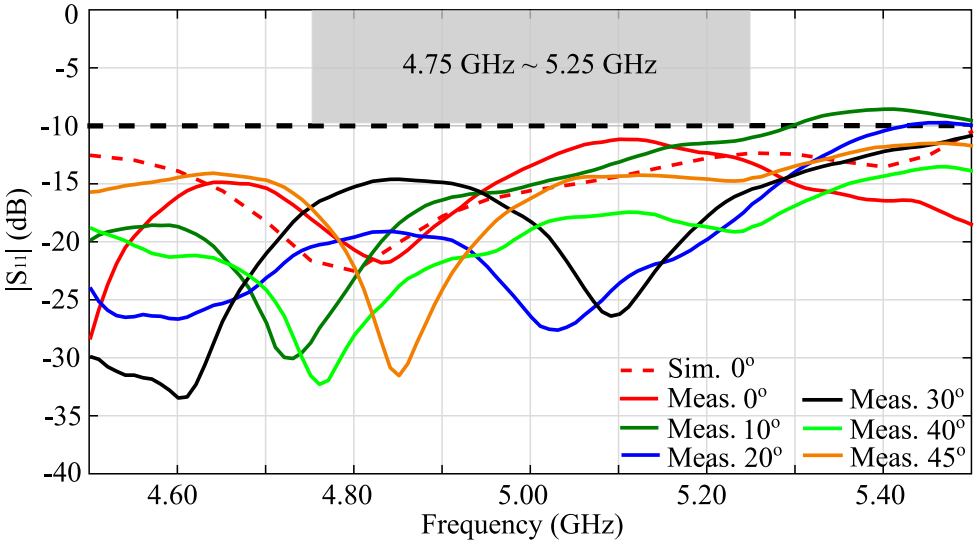

Figure 5.4. Simulated and measured results of reflection coefficient $|S_{11}|$ for various scan angles.

2) Difference-pattern scanning: The experimental results for the $|S_{11}|$ at difference-pattern scan states are illustrated in Fig. 5.5. The tested reflection coefficients at the single feed of the array are all below -10 dB at the intended operating frequencies when null-scanning to 0°, -10°, -20° and -30° at 5.00, 4.75 and 5.25 GHz. These results also illustrate the frequency-reconfigurable performance of the ar-

5.3.1 Reflection Coefficient

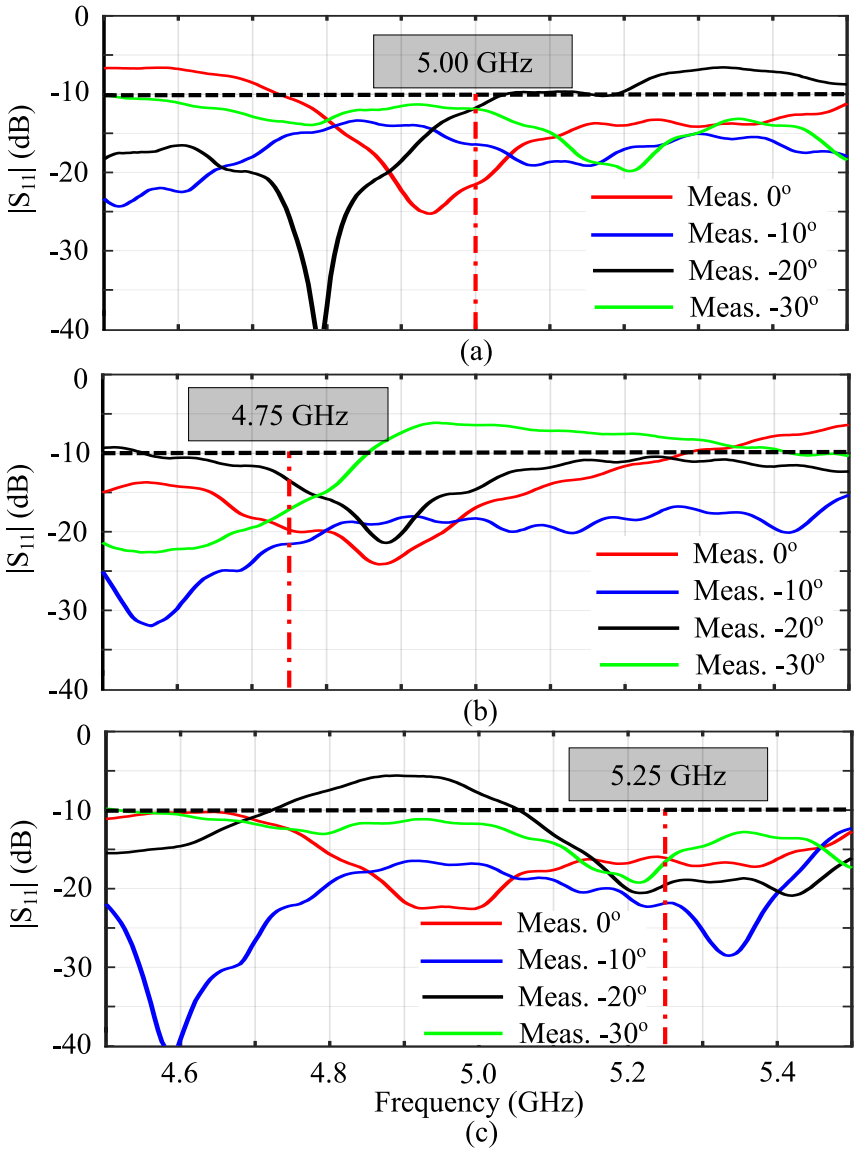

Figure 5.5. Measured reflection coefficients for various null-scan angles at (a) 5.00 GHz, (b) 4.75 GHz and (c) 5.25 GHz.

ray. From this point of view, it is significant to calibrate the control-voltage combinations at different frequencies for different scanning states accurately. The proposed calibration procedure allows to conveniently achieve optimal performance for all stages, despite the increased difficulty of predicting performance compared to a conventional phased array.

5.3.2 Beam Scanning Performance

1) Sum-pattern scanning: The radiation patterns have been measured in an anechoic chamber and the results are shown in Figs. 5.6, 5.7 and 5.8 at frequencies of 5.00, 4.75 and 5.25 GHz respectively. As observed in these plots, the array can scan its main beam from 0° to 45° continuously in the H-plane at 5.00 GHz with a maximum gain fluctuation of 2 dB. The array also realizes a reconfigurable pattern from 0° to 45° over the frequency range extending from 4.75 to 5.25 GHz, which is verified by the measurement results with gain fluctuations of 2.40 dB at 4.75 GHz and 2.53 dB at 5.25 GHz respectively.

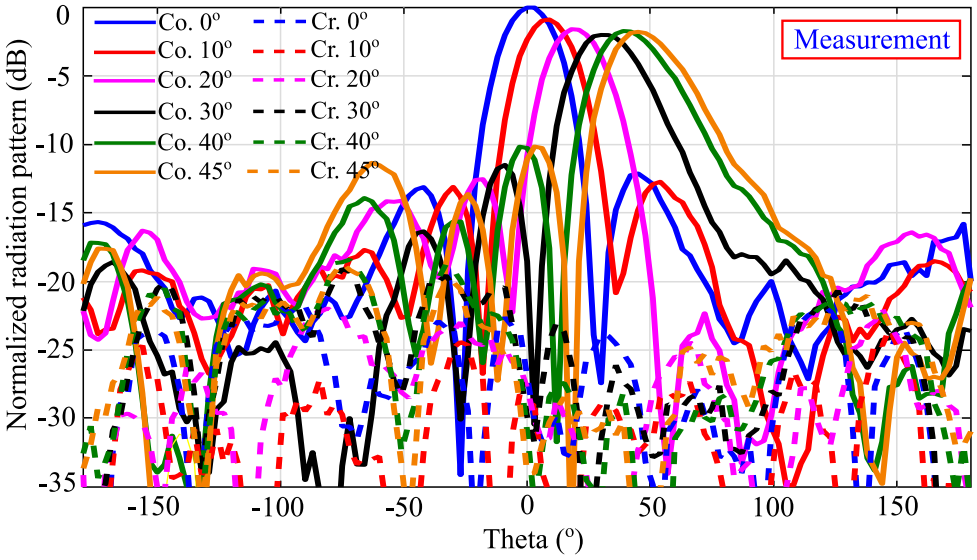

Figure 5.6. Measured radiation patterns obtained when scanning from 0°, 10°, 20°, 30°, 40° to 45° in the H-plane at 5.00 GHz.

In general, when an array scans to a large angle, an increased side-lobe level and beam broadening usually yield a noticeable drop in gain. However, a critical factor affecting the proposed array is the insertion loss caused by the varactor losses, which are dependent on the required phase values (as shown in Fig. 3.2(a)). Due to the complex relationship between phase shift and varactor state, the varactor losses are generally not monotonously increasing with the scan angle. As a consequence, the largest gain drop exists when the beam is steered towards 30°, which is mainly caused by the varactor insertion loss. According to the phase shifter pairs calibration data, the highest insertion loss are found when the phase difference are 180° (first stage) and 90° (second stage) which are the required phase differences to achieve the 30° scanning.

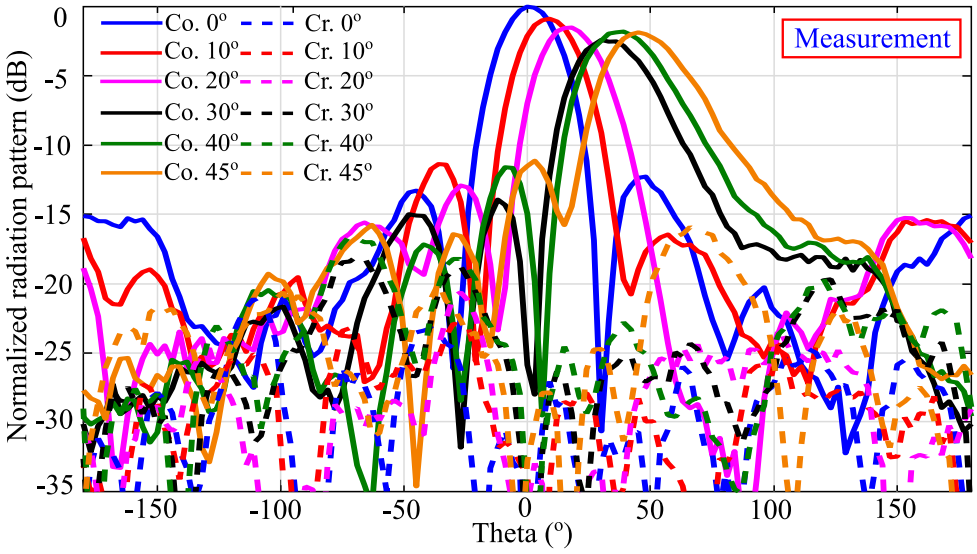

Figure 5.7. Measured radiation patterns obtained when scanning from 0°, 10°, 20°, 30°, 40° to 45° in the H-plane at 4.75 GHz.

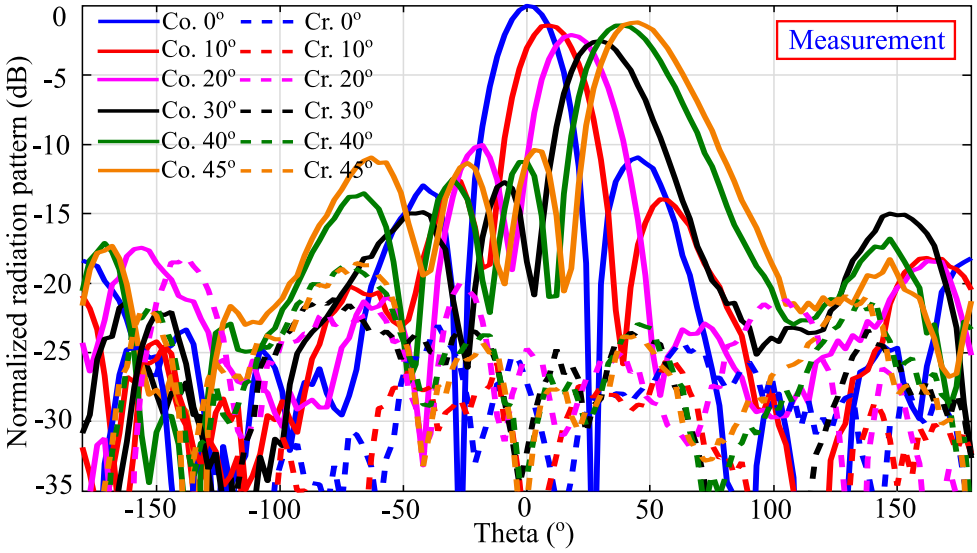

Figure 5.8. Measured radiation patterns obtained when scanning from 0°, 10°, 20°, 30°, 40° to 45° in the H-plane at 5.25 GHz.

The measured cross-polarization in the H-plane at 5.00 GHz as shown in Fig. 5.6 is below -18.4 dB when scanning from 0° to 45°. Similar cross-polarization levels can be observed in other measurements, with values less than -15.9 dB and -18.0 dB at 4.75 and 5.25 GHz correspondingly, as shown in Fig. 5.7 and Fig. 5.8.

2) Difference-pattern scanning: The standard scanning patterns and null-scanning radiation patterns have been measured and the results are shown in Figs. 5.9 - 5.11 at 5.00, 4.75 and 5.25 GHz, respectively.

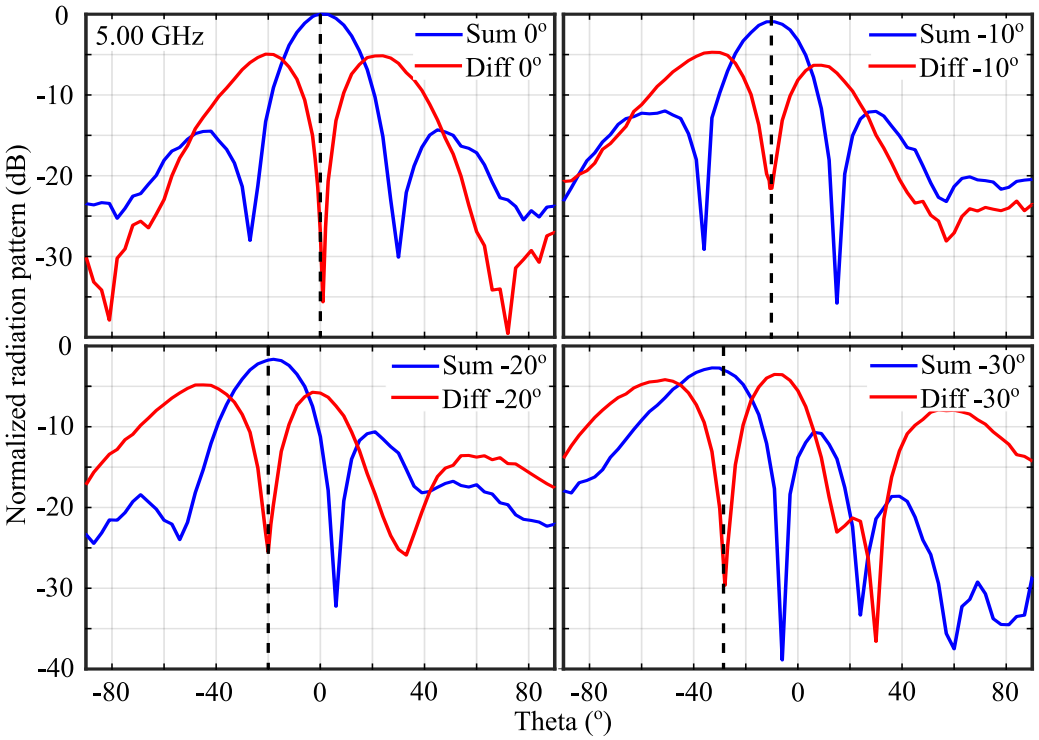

Figure 5.9. Measured scanning radiation patterns (sum) and null-scanning radiation patterns (difference) obtained when scanning at 0°, -10°, -20° and -30° in the H-plane at 5.00 GHz

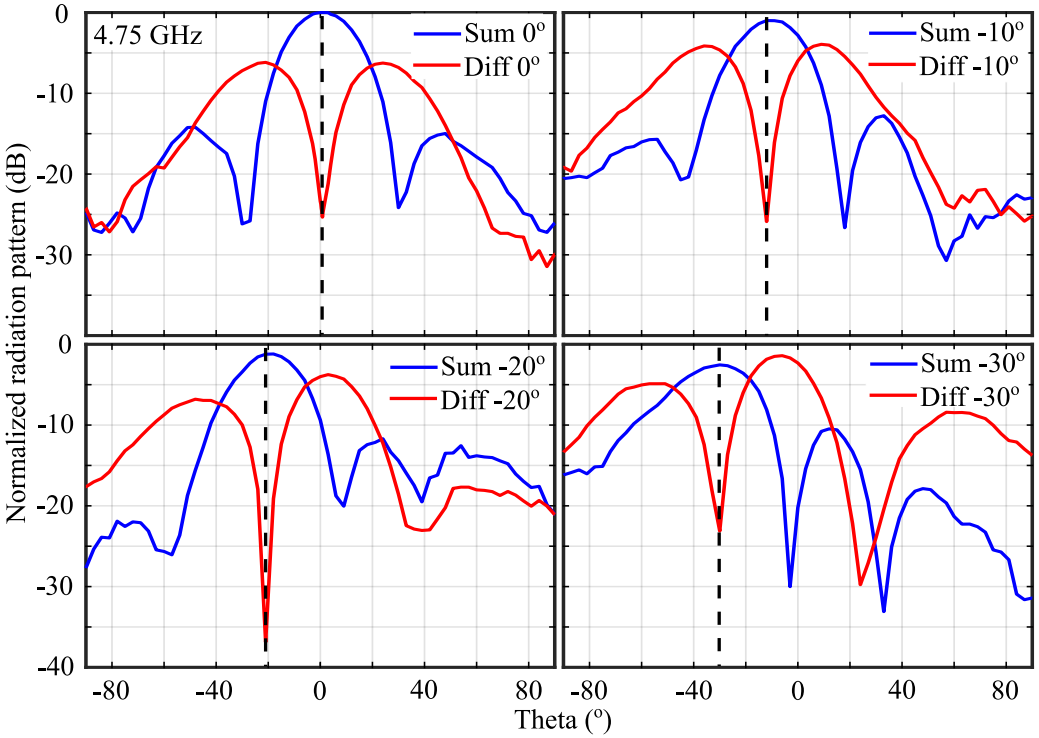

Figure 5.10. Measured scanning radiation patterns (sum) and null-scanning radiation patterns (difference) obtained when scanning at 0°, -10°, -20° and -30° in the H-plane at 4.75 GHz

5.3.2 Beam Scanning Performance

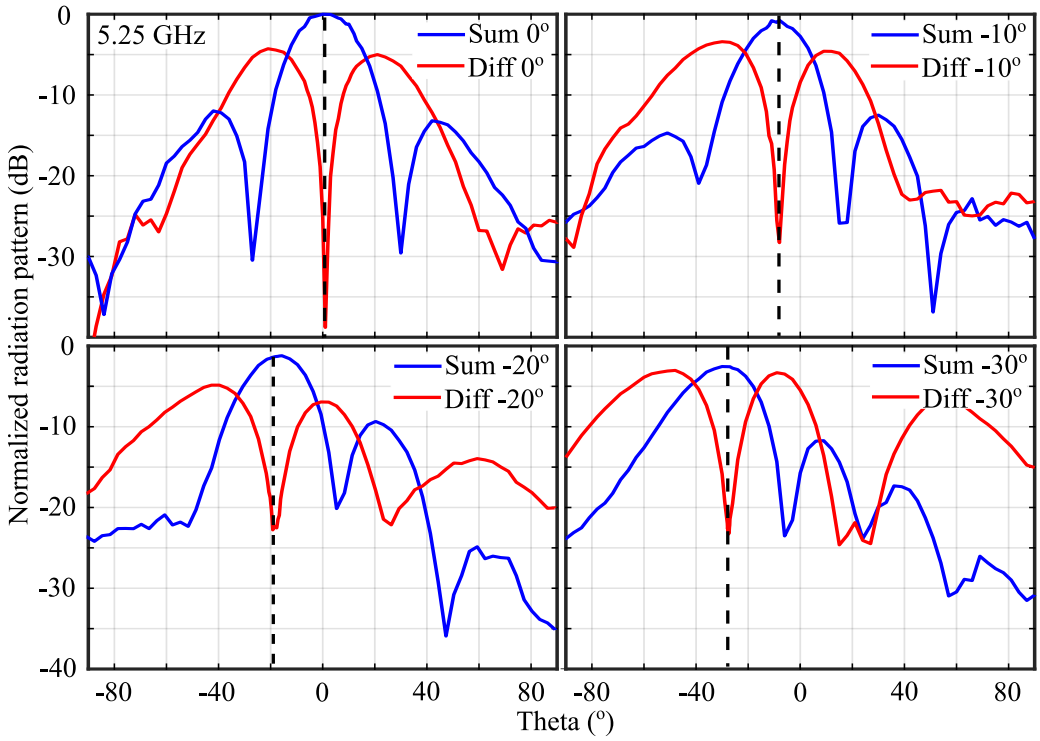

Figure 5.11. Measured scanning radiation patterns (sum) and null-scanning radiation patterns (difference) obtained when scanning at 0°, -10°, -20° and -30° in the H-plane at 5.25 GHz

As shown in Fig. 5.9, the null-depths are as low as -35.6 dB when scanning to 0° and less than -21.0 dB in the other null-scanning states at 5.00 GHz. The null-point position tolerances are less than 2.0°. Figure 5.10 illustrates the null-scanning patterns at 4.75 GHz with the null-depths lower than -24.6 dB and tolerances of the null-point smaller than 2.0°. Similar results are shown in Fig. 5.11 in which the null-depths are less than -22.8 dB and tolerances of the null-point are smaller than 2.5°. Theoretically, the nearly full 360° continuous phase tuning range offered by these three phase shifter pairs can steer the beam to any angle, provided the radiating element pattern is not considered. As shown in these figures, the array realizes the null-scanning of the beam from -30° to 0° continuously in the H-plane with deep null-depths and accurate null angle.

The determining factors for ideal pattern characteristics are mainly dependent on precise excitation phases which are obtained by the accurate calibration procedure.

5.3.3 Gain and Efficiency

As shown in Fig. 4.12, the simulated maximum realized gains in the E-plane at 4.75, 5.00 and 5.25 GHz are 9.59, 9.39 and 9.52 dBi respectively when the antenna scans towards broadside, whereas the corresponding measured values are 9.59, 9.19, and 9.25 dBi, as indicated in Fig. 5.12. Figure 5.13 summarizes the measured gain and total efficiency as a function of frequency for the case when the array radiates towards broadside from 4.75 to 5.25 GHz. The simulated total efficiencies for these cases are 88.3%, 83.9% and 75.9% respectively, while the estimated results (based on gain comparison) are 88.3%, 80.2% and 71.3% as shown in Fig. 5.13. The discrepancies are because of the imperfect fabrication and measurement.

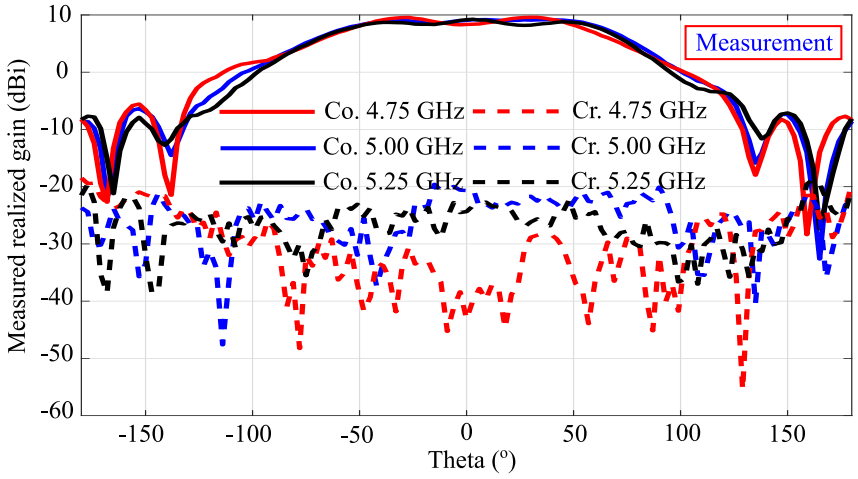

Figure 5.12. Measured realized gain patterns in the E-plane when scanning at 0°

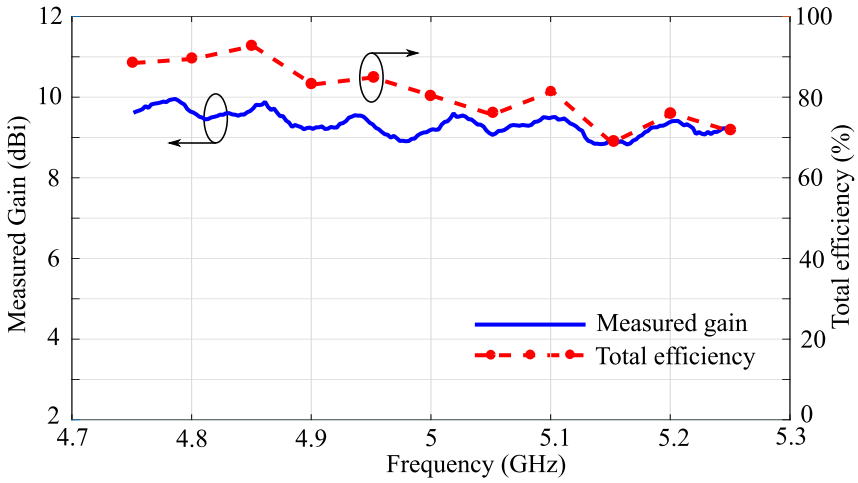

Figure 5.13. Measured maximum realized gain and total efficiency from 4.75 to 5.25 GHz when scanning at 0°.

5.3.4 Frequency-Reconfigurability

As mentioned before, the array also exhibits frequency-reconfigurability within the frequency range 4.75 to 5.25 GHz. This can be understood in the sense that voltages supplied to the six phase-tuning units can be optimized for each state at different frequencies. To illustrate the frequency-reconfigurability, two different voltages sets at different frequencies are chosen which are labeled in Table 5.2 as Set-A and Set-B. Figure 5.14(a) shows the patterns at 4.75 and 5.25 GHz when scanning to 10° with the varactor voltages of Set-A. Not only the reflection coefficient is -7.5 dB for 5.25 GHz under Set-A, but also the pattern is degraded at 5.25 GHz. This can however be improved significantly by optimizing the bias voltages specifically for operation at 5.25 GHz as illustrated with the results obtained using the varactor parameters of Set-B (red dotted line in Fig. 5.14(a)). Meanwhile, the reflection coefficient under Set-B is matched for 5.25 GHz as shown in Fig. 5.14(b). Therefore, separate sets are listed in Table 5.2 for different states of different frequencies hinting at the need of frequency-reconfigurability.

5.3.5 Beam Optimization and Correction

As mentioned, the magnitude of each element can in principle be adjusted during the calibration process due to the differential work mode of the phase-tuning unit pairs. In other words, a targeted phase difference could be realized by different sets of voltage pairs. This means that it is possible to select the best suitable amplitude sets to optimize or correct patterns by controlling the insertion loss of the phase-tuning unit. For instance, this can be exploited to optimize patterns for a symmetrical side-lobe level to a certain extent. Figure 5.15 illustrates a beam correction example with two radiation patterns when the array is excited in-phase with Set-D and an optimized Set-C, as listed in Table 5.2. Despite the beams in Set-C and Set-D both scanning to correctly 0°, it can be observed that the pattern with Set-D possesses a larger gain loss mainly caused by the larger insertion loss of varactors under 0 V bias and an asymmetric side-lobe level produced by the unavoidable phase imbalances arising from material and fabrication tolerances. By contrast, the pattern obtained with Set-C has less insertion loss caused by varactors and this sub-class combination could compensate the phase imbalance to some extent so that a symmetrical side-lobe distribution can be obtained, together with a 0.9 dB higher gain.

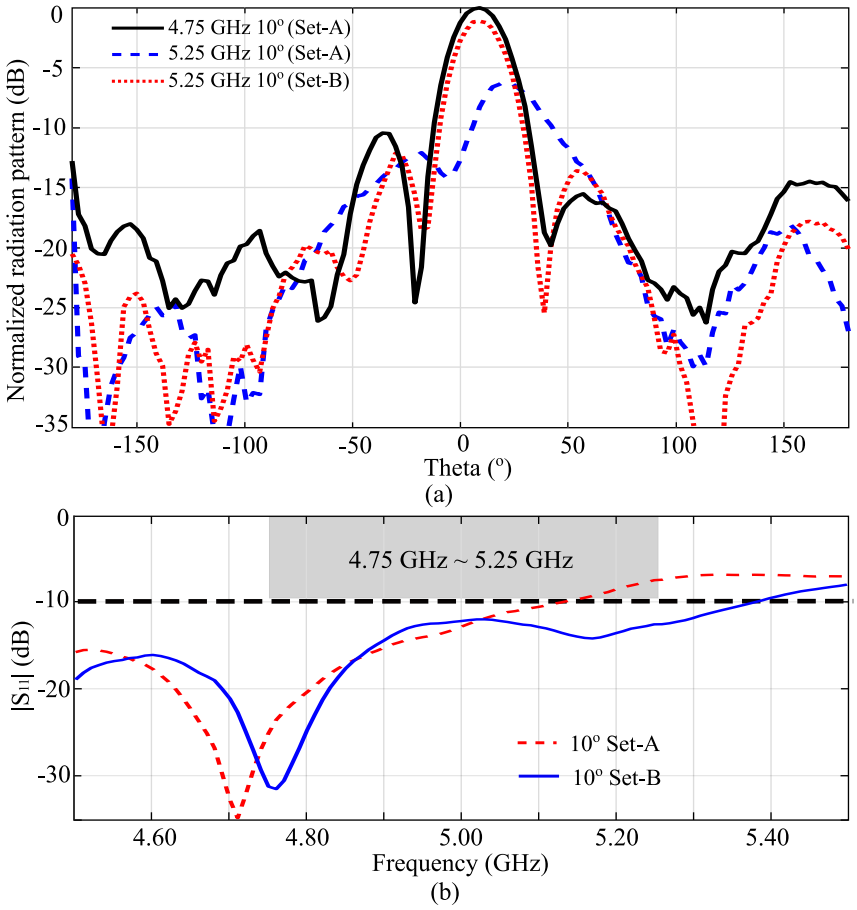

Figure 5.14. An example for frequency reconfigurability: (a) Patterns when scanning at 10° with different phase-tuning units sets, and (b) test results of reflection coefficient $|S_{11}|$ with Set-A and Set-B.

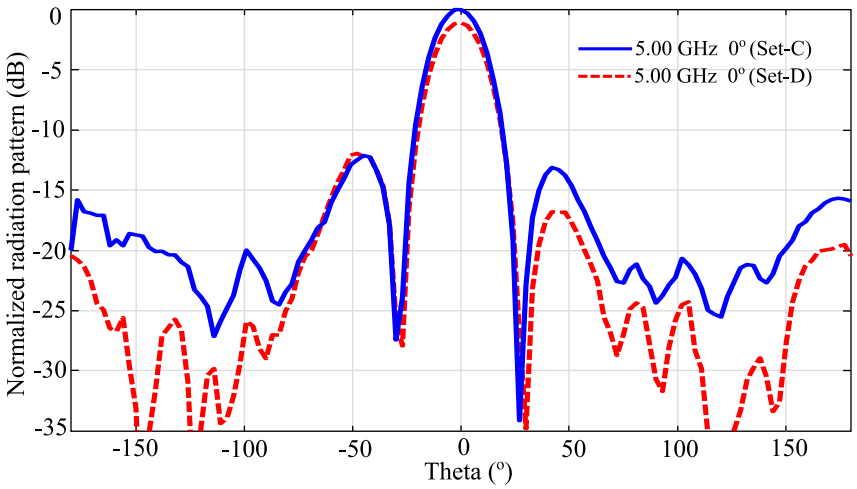

Figure 5.15. An example for beam-optimization-and-correction: scanning at 0° at 5.00 GHz.

5.4 Conclusion

An accurate calibration procedure has been proposed for beam-scanning antennas with a single feed, where the elements are controlled by varactor-based phase shifters. This procedure takes into account all the components of the array, including the reconfigurable feeding network and the radiator elements.

The first step of the processing considers the unconventional differential-phase control of the array and tolerances due to imperfect manufacture and components. The performance curves of the amplitude and the phase of each phase shifter are experimentally sampled firstly as the important foundation for the calibration process. Secondly, a fast selection algorithm is employed to determine the best control voltage combinations for these phase shifter pairs for any requested phase distribution. A fine-tuning step leads to the final control voltages for all scanning states in every channel based on on-board tested phase distributions.

The second part of the calibration is so-called a pattern optimization approach, which is utilized to compensate the performance degradation due to the fabrication tolerances of the radiating elements. These tolerances cannot be considered in the calibration of the feeding network. Firstly, the phase errors due to fabrication tolerance can be identified through comparing the ideal and measured radiation patterns. Second, the corresponding phase compensations obtained based on the feeding network calibration and array factor analysis are implemented to optimize the distorted pattern. Two examples with slightly off main beam direction when scanning to 30° at 4.75 and 5.25 GHz are featured to illustrate this optimization approach. Successful pattern correction for these two showcases illustrates that the proposed optimization is a critical method for beam-steerable array fed by varactor-based phase shifters to achieve accurate pattern manipulation for advanced applications.

To verify the effectiveness of this procedure, a sum-pattern scanning and a null-scanning of the array have been demonstrated. By comparing the sum-pattern scanning simulation results from Chapter 4 with the actual measurement data, a satisfactory level of agreement is observed. This agreement not only has demonstrated the effectiveness of the calibration procedure but also validated the beam-steering capabilities of the DRA array. As second demonstration, null-scanning from -30° to 30° has been obtained with the highest null-depth of -21.0 dB and null-position tolerance of less than 2.5° from 4.75 to 5.25 GHz. These precise null positions and appreciable null-depths have demonstrated that the dedicated calibration procedure enables accurate control

and reliable beam-steering capabilities for pattern-reconfigurable DRA arrays which are fed by varactor-based phase shifters.

It is worth emphasizing the unique functionalities of the beam-steerable DRA array: The controlling of differential phase shifter pairs in the array provides additional advantages, such as the frequency reconfigurability and the flexibility in modifying the magnitude to optimize the shape of the radiation patterns to a certain extent. The utilization of the differential mode enhances the array's anti-interference ability and beamforming flexibility, which make the array competitive for compact and cost-effective beam-steering applications.

Chapter 6

Transmission-Type Varactor-Based Tunable Attenuator

TUNABLE attenuators are important components in various fields, including radar systems, satellite communications and wireless networks. They provide a means to control the amplitude or power level of signals in a system. Specifically, transmission-type attenuators, which allow waves to pass through a transmission line while reducing signal amplitude, are associated with certain limitations. These limitations include a restricted range of attenuation, elevated return loss, and high insertion loss (the minimal achievable attenuation level).

To address these challenges, a transmission-type attenuator with varactor-based tunable attenuation is presented. The design consists in a series of shunt shorted-end stubs loaded with a resistor, a capacitor, and a varactor, which are located on one side of a 50 Ω host microstrip line. This configuration exhibits no interruption on the transmission line and thus allows a compact and low-loss structure amenable to circuit integration. This chapter demonstrates that a 3-stub attenuator is capable of providing tunable attenuation ranging from 1.0 to 13.5 dB while maintaining a reflection coefficient below -11.4 dB. Furthermore, it will be shown that by cascading the tunable stubs in larger numbers, a corresponding expanded attenuation range can be achieved.

6.1 Introduction

MICROWAVE devices such as phase-shifters [142] [48], couplers [158] [159], and/or attenuators with adjustable electromagnetic properties are essential components for advanced wireless systems. Especially, attenuators are needed for power control in many different applications, such as beam forming in communications systems [160] [161] or gain control in receivers [77] [162]. While the literature mainly considers fixed attenuators [81] [163], there have been great efforts invested in the development of reconfigurable attenuators offering dynamically variable attenuation levels [164] [165]. Of particular interest, attenuators implemented in planar technology are highly desirable as they allow integration with planar radio frequency (RF) systems.

Generally, planar attenuators can be classified in two categories based on their circuit structures:

i) Reflection-type attenuators: They achieve the attenuation by controlling reflection of the RF signal and thus they employ a dedicated structure to absorb the reflected RF signal. They are usually realized on multi-port devices such as 3-dB hybrid couplers [166] [167] [168] [78], rat-race devices [35] and combined-dividers [37] [169].

ii) Transmission-type attenuators: They allow RF signal transmission through the attenuator without significant reflection, however with a well-controlled signal absorbing mechanism which achieves the expected attenuation level. Therefore, compared to reflection-type attenuators, transmission-type attenuators generally offer a more compact structure and easier circuit integration.

There exists a limited number of transmission-type attenuators reported in the literature and the majority is operating at a fixed attenuation level [170] [163]. However, a few selected publications have contributed to the development of reconfigurable attenuators, i.e., devices offering dynamically variable attenuation [160] [161]. Some of the proposed implementations utilized novel materials such as graphene, with the aim of exploiting its tunable resistance under voltage control. In the transmission-mode approaches [171] [172] [173], nearly all implementations contained a gap in a host transmission line, which was then bridged by graphene layers. In [171], broadband characteristics were obtained covering a frequency range from 1 to 20 GHz with an

attenuation reaching up to 5.5 dB. Tunable attenuation ranges from 3 to 16 dB and 8 to 18 dB were reported in [172] and [173], respectively, indicating a relatively high minimum attenuation level, i.e., a high insertion loss. Several researchers also used graphene sandwich structures (GSS) or nanoplates loaded on various RF host transmission lines, such as microstrip lines [174] [175], substrate-integrated-waveguides (SIW) [176] and coplanar waveguides (CW) [177], to form broadband adjustable attenuators with around 12 dB tunable attenuation ranges and a 2 to 3 dB minimum attenuation level. In [178], two short-ended-pads were utilized on both sides of a microstrip line with gaps filled with graphene. Based on this structure, an evolution with series attenuators was designed with different numbers of graphene pair pads [179]. Large attenuation levels and broadband operation were demonstrated, however with a high reflection coefficient. In addition, all control voltages for these devices were supplied by external bias-tee blocks. A filtering attenuator based on graphene was reported in [180] which had a modest tunable attenuation from 1.7 - 8.4 dB with reflection coefficient less than -10 dB from 1.62 to 1.75 GHz. Overall, these aforementioned attenuators were based on non-standard fabrication techniques and materials, and thus might not be practically ready for mass production.

Besides graphene-based composites, transmission type attenuators have been commonly realized using electronic components such as RF micro-electromechanical systems (MEMS), PIN diodes and field-effect transistors (FETs). In [181], a low-cost planar RF MEMS-based attenuator operating from 21.5 to 26.5 GHz was introduced with a large attenuation tuning range of 16 dB and minimum attenuation of 1.2 dB. However, the phase shift caused by this attenuator reached up to 120°, which may be excessive for some applications. In contrast, a phase invariant attenuator was proposed in [182] with a phase decoupling circuit controlled by PIN diodes. The device had an attenuation range from 0.5 to 15.0 dB with a phase shift of 0.3 deg/dB and 3 GHz bandwidth, however, the reflection coefficient was not lower than -6.7 dB. All these examples from the literature demonstrate that it is challenging to design a transmission-type tunable attenuator with merits such as a large attenuation range, a small minimum attenuation level, a minimal phase shift, and importantly a low return loss, while being structurally simple, compact and embedded with its DC-control circuit (e.g., without the need of a bias-tee).

In this chapter, a compact planar transmission-type attenuator is proposed, which contains a straight-through 50 Ω host microstrip line and several varactor-loaded shorted

stubs implemented on one side of the line. An accurate equivalent-circuit model of the attenuator is developed first, allowing for a fast design and optimization process with a genetic algorithm (GA). To verify the method, a series of attenuators with selected numbers of stubs have been developed aiming at large attenuation ranges and minimum initial insertion loss. Full-wave simulations of the optimized attenuators illustrate that a continuous attenuation up to more than 10 dB can be achieved with a 3-stub attenuator, and up to more than 30 dB with a 9-stub attenuator at 5 GHz. Two 3-stub attenuators and a 9-stub attenuator have been fabricated and tested, with measured results confirming the expected performance level predicted in simulations. The test results demonstrate that the reflection coefficients remain below -11.0 dB from 4.75 to 5.25 GHz, with insertion losses of less than 1.0 dB for the 3-stub attenuators and smaller than 2.1 dB for the 9-stub version, while achieving tunable attenuation up to 13.5 dB when using 3 different stubs, and 32.7 dB for the 9-stub version. Particular emphasis is also placed on minimizing the phase variations between different attenuation levels. All the presented results verify the circuit model effectiveness and the promising performance of the proposed attenuator concept.

The following sections are arranged as follows: Section 6.2 introduces the attenuator working principle. Section 6.3 outlines the equivalent circuit model and optimization. Section 6.4 describes a series of selected attenuators designed based on GA optimizations of the circuit model, and verified with full-wave simulations. Section 6.5 then demonstrates three example prototypes and their experimental validations, followed by the conclusion.

6.2 Principle of Operation

The varactor-based transmission-type attenuator is composed of a 50 Ω microstrip host line and at least two end-shorted stubs loaded with lumped components. More specifically, each stub contains a varactor, a capacitor and a resistor along the stub length with an RF-shorting via at its end. To illustrate the general working principle, an attenuator with two stubs is shown as an example in Fig. 6.1(a). The input power P_{in} is attenuated to P_{out} after successive interactions with the two tuning stubs. In more details, part of the input signal is going through the host microstrip line while another part interacts with the first tuning stub. On this stub, a proportion of the power is accepted and then absorbed, while the rest is reflected. Similarly, the transmitted signal interacts with the second tuning stub, with part of the power moving forward on the host

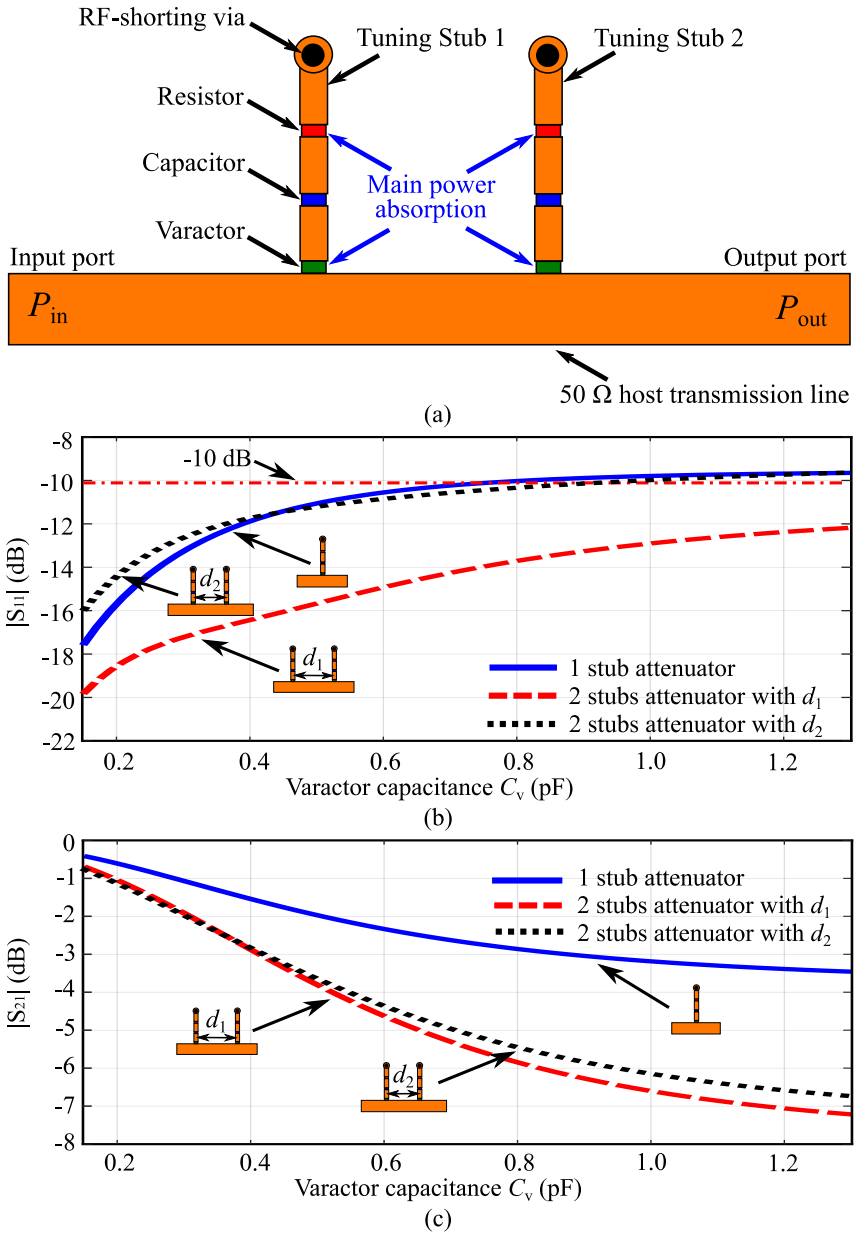

Figure 6.1. (a) The configuration of the proposed varactor-based attenuator with two stubs, (b) reflection coefficients and (c) transmission coefficients for typical attenuators with 1 stub and 2 stubs (with distance $d_1 = 7$ mm and $d_2 = 5$ mm), respectively.

line while the rest is either accepted and absorbed by the loaded stub, or is reflected. The proportion of the power accepted by the stubs can be tuned by controlling the varactor capacitances with the applied bias voltage. When the capacitance is increasing, the power accepted by the stubs increases correspondingly, because the associated RF currents become larger as the impedance of the varactor is lowered. The RF power is then dissipated predominantly in the resistor but also in the varactor series resistance, as indicated in Fig. 6.1(a).

Critically, the overall reflection of the device is the superposition of multiple reflections from the stubs, which can be controlled by manipulating the stubs' design such as their geometry, component-loading configuration, and distance to the next stub(s). For a given stub design, an optimal distance between the two stubs will yield cancellation of the returns from the two stubs, which in turn leads to a low reflection coefficient at the input port. To illustrate the effect, the reflection coefficients of a 1-stub attenuator and two 2-stub attenuators with distance d_1 = 7 mm and d_2 = 5 mm are compared in Fig. 6.1(b), where a much smaller reflection is produced from a 2-stub attenuator with an appropriate spacing d_1, although the attenuation levels for the two 2-stub devices are similar. This is the reason why at least two stubs with proper geometry are required for satisfactory impedance matching of the device.

Another characteristic of the proposed working principle is that, increasing the number of tuning stubs allows to obtain a larger attenuation through additional dissipation in the resistors. As shown in Fig. 6.1(c), the maximum attenuation for a single stub is slightly larger than 3 dB. Adding more stubs allows to increase the attenuation by a similar level of 3 dB. This topology of the attenuator is a very practical solution to resolve the aforementioned trade-offs of transmission-type attenuators, namely simultaneously achieving a large attenuation range as well as a low return loss.

It is also worth mentioning that the capacitor (see Fig. 6.1(a)) located between the varactor and resistor is utilized to adjust the operating band of the tuning stub, for a given commercially available varactor type. In the implementation presented in this section, the attenuator is designed for a center frequency of 5 GHz, with an operation bandwidth of 10%. Additionally, a phase shift is introduced due to the structure of the attenuator, which should be minimized for most applications. Therefore, minimization of the phase shift will also be considered in the later optimization process.

6.3 Attenuator Equivalent Circuit Model and Optimization

According to the topology of the attenuator, a generic circuit model of an attenuator with n tuning stubs is built as shown in Fig. 6.2. As depicted in Fig. 6.1, the attenuator is based on a 50 Ω host microstrip line which consists of $n + 1$ short sections separated by the n inserted varactor-based stubs. For a two-port network of cascaded structures, the [ABCD] matrix (denoted with bold **A** in this thesis) provides a convenient way

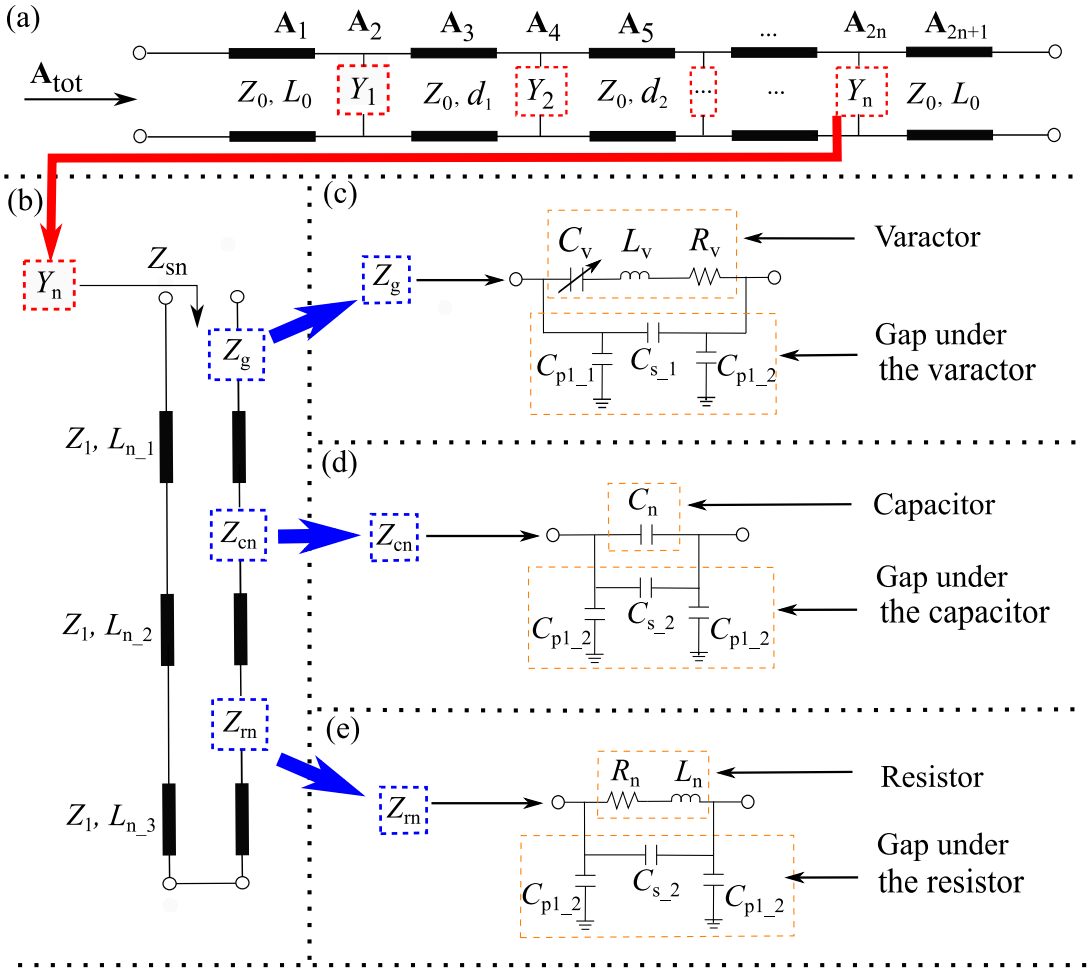

Figure 6.2. Equivalent circuit model: (a) A generic attenuator with n stubs, (b) the n-th tuning stub, (c) the varactor and its connection to the n-th stub, (d) the n-th capacitor and its connection to the n-th stub, and (e) the n-th resistor and its connection to the n-th stub.

of calculating the characteristics of the overall circuit by simple matrix multiplication, hence it is adopted here for the circuit model analysis.

As shown in Fig. 6.2(a), the attenuator can be considered as $n+1$ cascaded segments of microstrip transmission lines ($\mathbf{A}_1$, $\mathbf{A}_3$, $\mathbf{A}_5$...$\mathbf{A}_{2n+1}$) and n admittance branches ($\mathbf{A}_2$, $\mathbf{A}_4$, $\mathbf{A}_6$...$\mathbf{A}_{2n}$) in-between them. The matrix $\mathbf{A}_{tot}$ of the equivalent circuit model is obtained by multiplying $\mathbf{A}_1$ to $\mathbf{A}_{2n+1}$ in order as

$$\mathbf{A}_{tot} = \prod_{i=1}^{2n+1} \mathbf{A}_i = \mathbf{A}_1 \cdot \mathbf{A}_2 \cdot \mathbf{A}_3 \cdot \mathbf{A}_4 \cdot \mathbf{A}_5 \cdot \ldots \cdot \mathbf{A}_{2n} \cdot \mathbf{A}_{2n+1} \,. \tag{6.1}$$

The matrices $\mathbf{A}_1$, $\mathbf{A}_3$, $\mathbf{A}_5$, ..., $\mathbf{A}_{2n+1}$ represent each section of the host transmission lines with an impedance Z_0 of 50 Ω. The variable L_0 stands for the length of input and output parts of the microstrip line, and d_1, d_2, ..., d_{n-1} are physical distances between

adjacent admittance branches, e.g., d_1 is the distance between Y_1 and Y_2 and d_{n-1} is the distance between Y_{n-1} and Y_n. The matrices $\mathbf{A}_1$, $\mathbf{A}_3$, ..., $\mathbf{A}_{2n+1}$ are expressed as

$$\mathbf{A}_1 = \mathbf{A}_{2n+1} = \begin{bmatrix} \cos(\beta L_0) & j\sin(\beta L_0)\, Z_0 \\ j\sin(\beta L_0)/Z_0 & \cos(\beta L_0) \end{bmatrix} \tag{6.2}$$

$$\mathbf{A}_3 = \begin{bmatrix} \cos(\beta d_1) & j\sin(\beta d_1)\, Z_0 \\ j\sin(\beta d_1)/Z_0 & \cos(\beta d_1) \end{bmatrix} \tag{6.3}$$

...

$$\mathbf{A}_{2n-1} = \begin{bmatrix} \cos(\beta d_{n-1}) & j\sin(\beta d_{n-1})\, Z_0 \\ j\sin(\beta d_{n-1})/Z_0 & \cos(\beta d_{n-1}) \end{bmatrix} \tag{6.4}$$

where $\beta = 2\pi/\lambda_g$ and λ_g is the guided wavelength.

As shown in Fig. 6.2(b), the admittance Y_n is composed of six parts including three stub segments with impedance Z_1 and physical lengths L_{n_1}, L_{n_2} and L_{n_3}, respectively, inserted between a varactor denoted as Z_g, a capacitor Z_{cn}, a resistor Z_{rn}, and a via providing a shorted termination. The corresponding matrix of the admittance branch Y_n can be expressed as $\mathbf{A}_{stub\_n}$ obtained by multiplying 6 matrices, i.e.,

$$\begin{aligned} \mathbf{A}_{stub\_n} = & \begin{bmatrix} 1 & Z_g \\ 0 & 1 \end{bmatrix} \begin{bmatrix} \cos(\beta L_{n\_1}) & j\sin(\beta L_{n\_1})\, Z_1 \\ j\sin(\beta L_{n\_1})/Z_1 & \cos(\beta L_{n\_1}) \end{bmatrix} \\ & \begin{bmatrix} 1 & Z_{cn} \\ 0 & 1 \end{bmatrix} \begin{bmatrix} \cos(\beta L_{n\_2}) & j\sin(\beta L_{n\_2})\, Z_1 \\ j\sin(\beta L_{n\_2})/Z_1 & \cos(\beta L_{n\_2}) \end{bmatrix} \\ & \begin{bmatrix} 1 & Z_{rn} \\ 0 & 1 \end{bmatrix} \begin{bmatrix} \cos(\beta L_{n\_3}) & j\sin(\beta L_{n\_3})\, Z_1 \\ j\sin(\beta L_{n\_3})/Z_1 & \cos(\beta L_{n\_3}) \end{bmatrix}. \end{aligned} \tag{6.5}$$

The specific equivalent circuit model of the varactor is shown in Fig. 6.2(c), which is comprised of a series RLC circuit representing the varactor in isolation, two shunt capacitors C_{p1_1} and C_{p1_2} approximating the parasitic capacitances between the stub edges and ground, and a capacitor C_{s_1} in series standing for the capacitance between the two edges of the gap in the stub. As a result, the impedance Z_g of the varactor on stub-n can be expressed as (6.6) - (6.8) in Table 6.1, where $\omega = 2\pi f$ and f is the operating frequency. In (6.8), C_v, L_v, R_v represent the series RLC circuit components of the varactor in isolation. The variable C_v is the tunable capacitance, L_v is the parasitic inductance and R_v stands for the parasitic resistance.

The impedances for the capacitor and resistor can be found similarly. The equivalent circuit model of the capacitor is shown in Fig. 6.2(d), which consists of a capacitor

Table 6.1. Expressions of the components in the equivalent circuit model.

Model	Expression in equivalent circuit model	Label
Varactor	$Z_g = Z_{C_{p1\_1}} // Z_m // Z_{C_{p1\_2}}$	(6.6)
	$Z_{C_{p1\_1}} = -j\omega C_{p1\_1}$ $Z_{C_{p1\_2}} = -j\omega C_{p1\_2}$	(6.7)
	$Z_m = -j\omega C_{s\_1} + (1/(R_v + j\omega L_v - j\omega C_v))$	(6.8)
Capacitor	$Z_{cn} = Z_{C_{p1\_2}} // Z_{mc} // Z_{C_{p1\_2}}$	(6.9)
	$Z_{mc} = -j\omega C_{s\_2} + -j\omega C_n$	(6.10)
Resistor	$Z_{rn} = Z_{C_{p1\_2}} // Z_{mr} // Z_{C_{p1\_2}}$	(6.11)
	$Z_{mr} = -j\omega C_{s\_2} + (1/(R_n + j\omega L_r))$	(6.12)

C_n, two shunt capacitors C_{p1_2} approximating the parasitic capacitances between the same-width stub edges and ground, and a capacitor C_{s_2} in series standing for the capacitance between the two edges of the gap in the stub. These parts can be expressed as (6.9) - (6.10) in Table 6.1. Figure. 6.2(e) shows the equivalent circuit model of the resistor, which is comprised of a resistor R_n in series with an empirical parasite inductor L_n, two shunt capacitors C_{p1_2} and a capacitor C_{s_2} in series. These parts can be expressed as (6.11) and (6.12) in Table 6.1.

The values of C_{s_1}, C_{s_2}, C_{p1_1} and C_{p1_2} are calculated according to [183]. Finally, $\mathbf{A}_{2n}$ can be written as

$$\mathbf{A}_{2n} = \begin{bmatrix} 1 & 0 \\ 1/Z_{sn} & 1 \end{bmatrix} \ (n = 1, 2, 3, ...) \ , \tag{6.13}$$

where Z_{sn} is the input impedance when looking into each stub branch from the main 50 Ω microstrip line, which is expressed as:

$$Z_{sn} = \frac{\mathbf{A}_{stub\_n}(1,1)Z_l + \mathbf{A}_{stub\_n}(1,2)}{\mathbf{A}_{stub\_n}(2,1)Z_l + \mathbf{A}_{stub\_n}(2,2)} \ (n = 1, 2, 3, ...) \tag{6.14}$$

and Z_l is the load impedance which is zero here for the short end of the stub. The $\mathbf{A}_{tot}$ for the overall circuit is then obtained using (6.1), and the overall **S**-matrix can be computed from $\mathbf{A}_{tot}$ as discussed in [112].

With a given type of varactor, the attenuator with n stubs has $6n$ key variables which significantly control the reflection coefficient, attenuation range and phase shift, i.e., the stub characteristic impedance Z_1 (which is identical for all stubs), the lengths of each separate sections of the n-th stub L_{n_1}, L_{n_2} and L_{n_3}, the capacitor C_n and the resistor R_n (L_n represents the parasitic inductance of the resistor which is a fixed value

once the R_n is selected). In addition, the distances between the stubs from d_1 to d_{n-1} can be used to tune the reflection coefficient. The GA is utilized as a generic design tool here to determine optimal set of parameters since it is known to be very efficient for multi-objective optimization. An efficient GA optimization is enabled by the fast computations based on the equivalent circuit model and aims at maximizing the attenuation range while maintaining low return loss and an acceptably small phase shift. The objective function for the GA considers then the attenuation range, phase shift and reflection coefficient simultaneously and it is based on the following 3 steps:

Step 1: Define the multi-objective merit function, which targets minimum phase difference for an attenuation range larger than a threshold value (expressed in dB) and reflection coefficient smaller than -10 dB over the tuning span of the varactor capacitance.

Step 2: Generate chromosomes which contain the $6n$ key parameters mentioned before. For each generated combination, calculate the attenuator performance based on the merit function, apply mating, mutation and selection rules of the GA.

Step 3: Repeat Step 2 until convergence to a near-optimal combination of these $6n$ parameters is reached using the GA algorithm.

6.4 Selected Attenuator Designs

As found from optimization with the circuit model, increasing the number of varactor-based stubs allows to achieve a larger attenuation range, with each stub contributing approximately 3 dB to the overall attenuation. To illustrate and verify the optimization method and as an example of general application, a 10 dB value of maximal attenuation is selected in the first two examples, which include a configuration with 3 same stubs, and another one with 3 different stubs for additional degrees of freedom. The subsequent examples will demonstrate designs with 6 and 9 stubs for aiming at higher levels of attenuation.

6.4.1 3-Same-Stub Attenuator

Due to the large number of parameters in the circuit model shown in Fig. 6.2, we firstly study the case with the simplest structure, where the varactor-loaded short-ended stubs have all the same dimensions and distances between them. For a 3-stub design, this means that $n = 3$ is used in the GA optimization, however with a number of parameters reduced from 18 to only 7 since all stubs share the same dimensions.

In order to identify the optimization ranges of the most sensitive parameters and illustrate their effects, the influence of these parameters is simulated and analyzed individually. The parametric studies, including stub width W_2, the stub distance d, the capacitor value C and the resistor value R, are illustrated in Fig. 6.3 - Fig. 6.6. As depicted in Fig. 6.3, a wider stub width W_2 produces a smaller attenuation range however with a smaller phase difference, and its effect on the reflection level can be ignored. Importantly, an optimal W_2 range in between 0.4 and 0.8 mm can be identified, which can be set as the optimization range in the GA.

Moving to the next parameter, as shown in Fig. 6.4, a distance d of 3 mm yields the highest reflection level and attenuation range, but the flattest phase shifting curve. As d becomes larger, the reflection coefficient becomes smaller, with a slight effect on the attenuation level and phase shift. Therefore a small optimization range of distance from 5 to 10 mm can be set in the GA.

For the capacitor C, the S parameters for different C are compared in Fig. 6.5, illustrating that this parameter has a strong impact on the change rate and the range of the attenuation. For instance, when C = 0.4 pF is used, the attenuation level changes rapidly from 1.5 to 10 dB with the varactor capacitance varies from 0.15 to 0.60 pF. This configuration leads to a design with a large and fast-responding attenuation, only based on a small variation of varactor capacitance. As a result, this C value can be utilized to adjust the operating band of the attenuator. On that basis, C can be selected in a range from 0.2 to 0.4 pF, since the attenuation becomes far less than 10 dB for smaller values, while the phase difference increases for larger values of C.

Finally, according to the results in Fig. 6.6, the resistor on the stub has a significant effect on the attenuation level and phase shift. Despite that the attenuation can reach up to 15 dB when the R is 25 Ω, the phase shift becomes larger than 40°. Whereas, when R = 45 Ω is selected, the attenuation range is around 7.5 dB, which is marginal. Thus, an optimal value can be selected between 25 and 45 Ω. On the basis of these parameters

studies, a reasonable range for each of these parameters can be determined for further optimization by the GA. The optimal results are expected to provide a compromise between a large attenuation level, a low reflection coefficient and a small phase shift simultaneously.

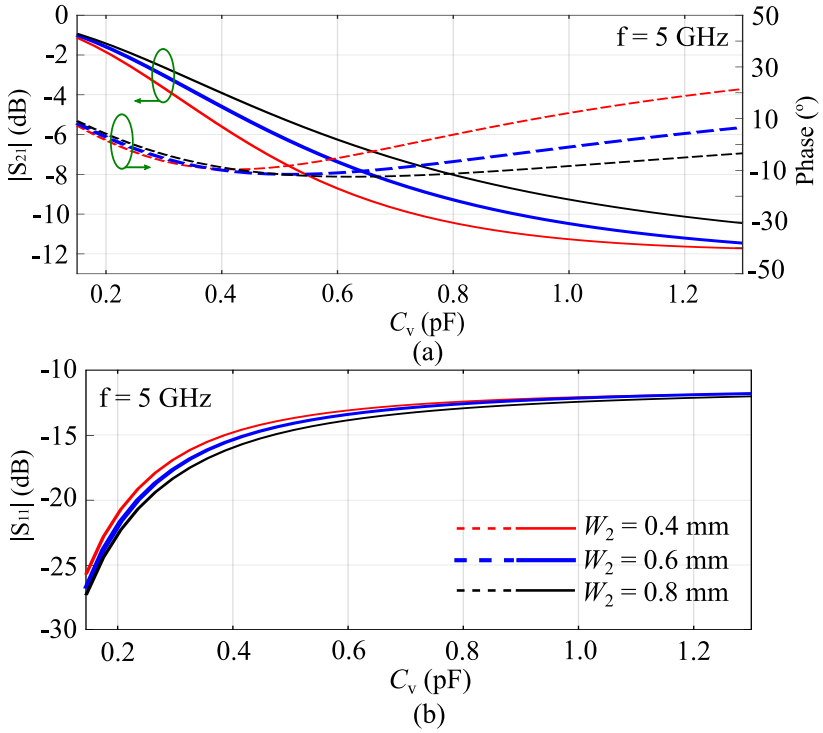

Figure 6.3. Parametric study of the stub width W_2: a) Magnitude and phase of S_{21} and b) reflection coefficient.

The geometry of the 3-same-stub attenuator is illustrated in Fig. 6.7 with variable parameters W_2, C, R, d, L_1, L_2 and L_3. As for the connection length L_1, L_2 and L_3, they are selected in available ranges to interact with other parameters to obtain the best trade-off in phase difference and attenuation level, while satisfying the smallest space for components loading. It is worth to mention that the reflection coefficients for all the parametric studies are typically less than -10 dB, which also verify the operation principle where a low reflection can be achieved, when reflections from two or more stubs can be design to cancel each other by adjustment of the inter-stub distances.

The device is designed on a 0.76 mm thick Rogers Diclad 880 with relative permittivity of 2.2 and loss tangent of 0.0009 at 5.0 GHz. The varactor adopted in this design is of type MA46H120, which has a tunable capacitance range between 0.15 to 1.30 pF controlled by a single bias voltage over the range 18 to 0 V. It has a parasitic inductance of 0.05 nH and a resistance of 2 Ω [109] [184]. As shown in Fig. 6.7, all the stubs

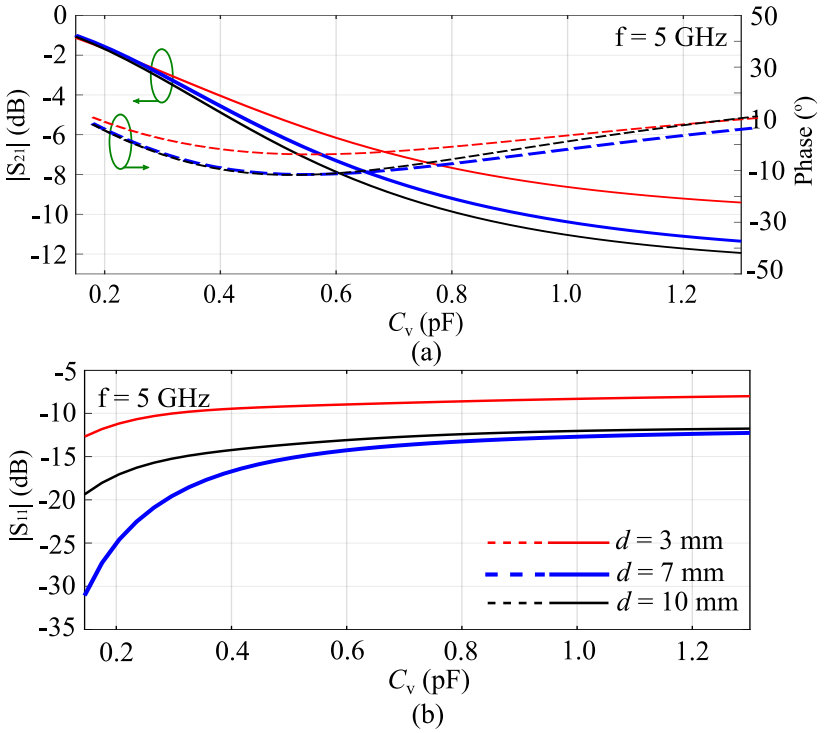

Figure 6.4. Parametric study of the distance d: a) Magnitude and phase of S_{21} and b) reflection coefficient.

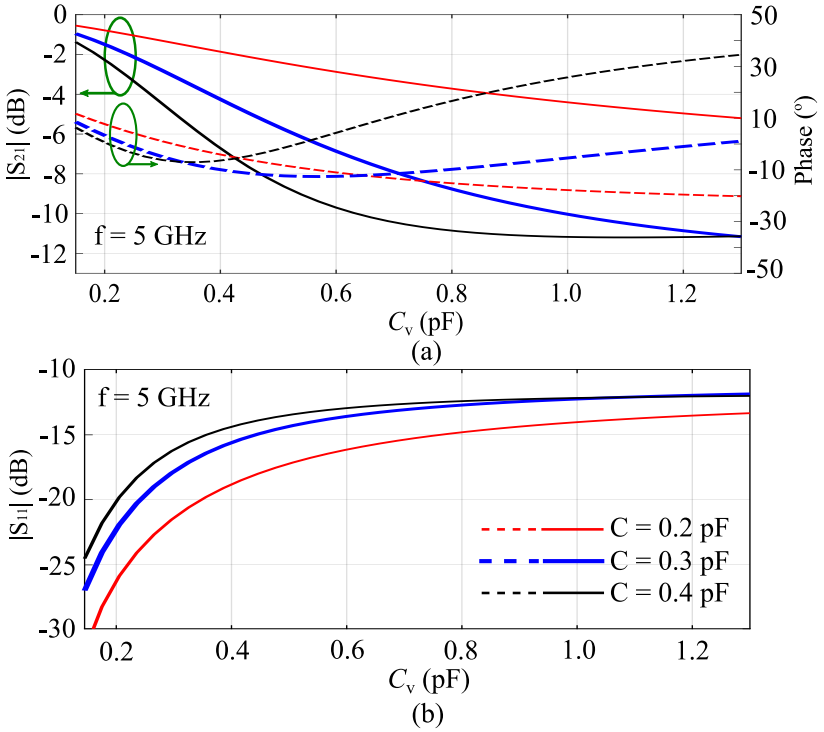

Figure 6.5. Parametric study of the capacitor C: a) Magnitude and phase of S_{21} and b) reflection coefficient.

6.4.1 3-Same-Stub Attenuator

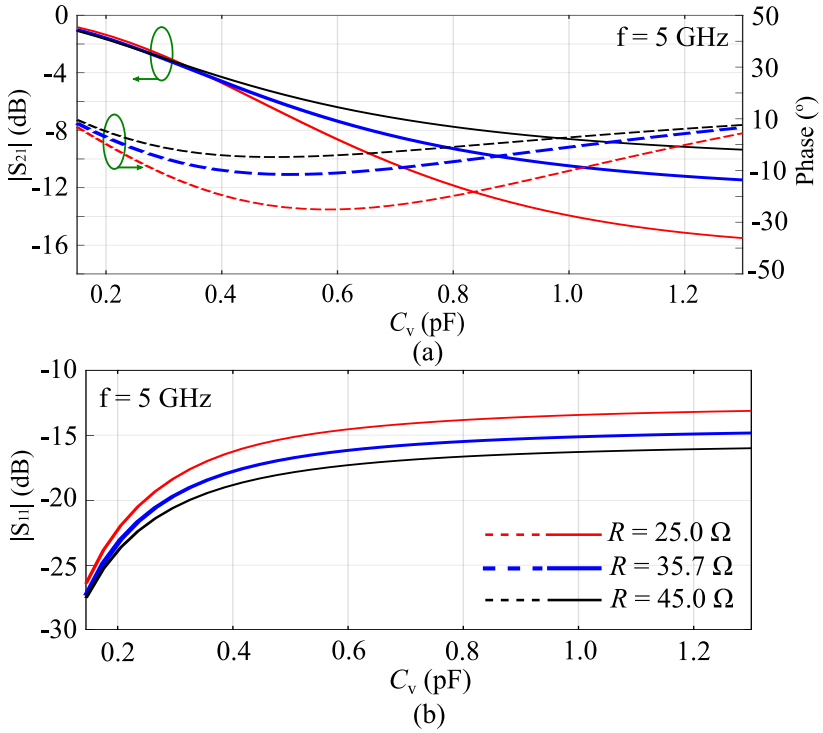

Figure 6.6. Parametric study of the resistor R: a) Magnitude and phase of S_{21} and b) reflection coefficient.

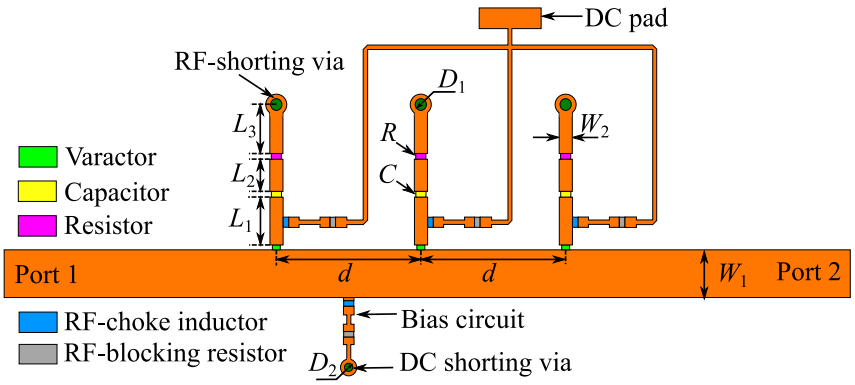

Figure 6.7. Geometry of the proposed attenuator with 3 same varactor-loaded shorted stubs. The optimized parameters are: $W_1 = 2.32$ mm, $W_2 = 0.60$ mm, $L_1 = 2.20$ mm, $L_2 = 1.40$ mm, $L_3 = 2.20$ mm, $C = 0.30$ pF, $R = 35.70\ \Omega$, $d = 7.00$ mm, $D_1 = 0.60$ mm, and $D_2 = 0.40$ mm.

loaded with varactors are added onto a 50 Ω host microstrip line with a width W_1 = 2.32 mm. The bias network contains an RF-choke inductor of 15 nH in series with an RF-blocking resistor of 1000 Ω. The bias lines connected to the DC voltage are chosen to be 0.2 mm wide to increase their inductance and minimize radiation. The varactors, host microstrip line and the bias circuit parameters will remain the same in the other designs.

The GA is run multiple independent times, to obtain optimized results which achieve an attenuation range of at least 10 dB while satisfying the condition of a reflection coefficient below -10 dB over the capacitor tuning span of the varactor, and keeping a relatively low phase difference. The optimized parameters are listed in the center column in Table 6.2.

Table 6.2. Parameters of equivalent circuit method and full-wave method for the final designs.

Name	Equivalent circuit variables	Full-wave variables
W_2	0.60 mm	0.60 mm
L_1	2.58 mm	2.20 mm
L_2	1.40 mm	1.40 mm
L_3	2.77 mm	2.20 mm
C	0.30 pF	0.30 pF
R	35.70 Ω	35.70 Ω
d	7.00 mm	7.00 mm

On the basis of the optimized circuit model findings, full-wave simulations are performed with Ansys HFSS 2021 to validate and refine the design. The final parameters are listed in the right column in Table 6.2. The effective length of the L_1 in the circuit model is 0.38 mm longer than the full-wave results, which is due to the effect of the varactor. The equivalent length of the $L_3(circuit)$ in the circuit model is determined by the physical length L_3 of the strip, but also combines the dependence on the shorting via radius D_1, stub width W_2 and substrate thickness t as set-up in the full-wave model. It is empirically found that the equivalent $L_3(circuit)$ can be expressed as

$$L_3(circuit) = L_3 + t - \Delta L, \tag{6.15}$$

where ΔL = 0.19 mm is an empirically found length compensating the additional inductance formed by the shorting via and irregular stub width around the via.

In terms of the device performance, reflection coefficients no higher than -12 dB are obtained from the equivalent circuit model and full-wave simulation, as shown in Fig. 6.8. The simulated and calculated transmission coefficients with magnitude and phase of the attenuator at 4.75, 5.00 and 5.25 GHz are in good agreement as shown in Fig. 6.9. This verifies the correspondence between the equivalent circuit analysis and the full-wave simulations, which suggests that the circuit model is sufficiently accurate for engineering design purpose. Furthermore, a continuously tunable attenuation from

1.0 to 11.5 dB is predicted at 5.00 GHz with a maximum phase shift of 19.8° as shown in Fig. 6.9(a). The results of Figs. 6.9(b) and (c) show attenuation ranges of 0.8 - 10.0 dB at 4.75 GHz and 1.4 - 11.5 dB at 5.25 GHz with phase shifts below 25.1° and 33.3° respectively.

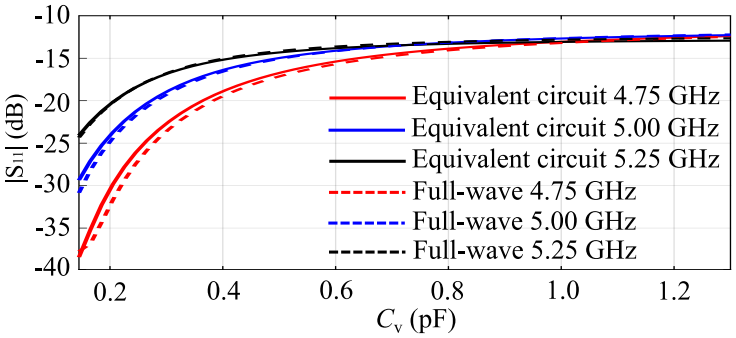

Figure 6.8. Reflection coefficients of the final optimized design of 3-same-stub attenuator obtained from the equivalent circuit model and full-wave simulation at 4.75, 5.00 and 5.25 GHz.

6.4.2 3-Different-Stub Attenuator

To increase the number of degrees of freedom, we optimize the full-variable 3-stub (or $n = 3$) attenuator model based on the equivalent circuit method. The optimization procedure is similar as shown in the previous case, with the number of variables increased to 18 to fully describe the 3 different stubs.

The geometry of the attenuator with 3 different stubs is illustrated in Fig. 6.10 with the 18 optimized variable parameters listed in the caption. The optimized resistors for the 3 stubs are kept the same at 25 Ω, and the distances between the stubs are selected to be identical as before due to their similar impact on reflection.

The reflection coefficients of the attenuator in the whole frequency band from 4.75 to 5.25 GHz is less than -10.3 dB as shown in Fig. 6.11. The simulated and calculated transmission coefficients of the attenuator are also in good agreement as shown in Fig. 6.12. The attenuator realizes 1.0 - 12.6 dB continuously tunable attenuation at 5.0 GHz with a phase shift of less than 15.2° as shown in Fig. 6.12(a). The corresponding tunable attenuation ranges from 0.8 to 10.5 dB at 4.75 GHz and from 1.6 to 13.1 dB at 5.25 GHz, as displayed in Fig. 6.12(b) and (c), with phase shifts below 20° and 35°, respectively.

So far, the two attenuators, i.e., 3-same-stub attenuator and 3-different-stub attenuator, satisfy the optimization aims and validate the design method. The optimized performances of the two devices are summarized for direct comparison in Table 6.3. It is

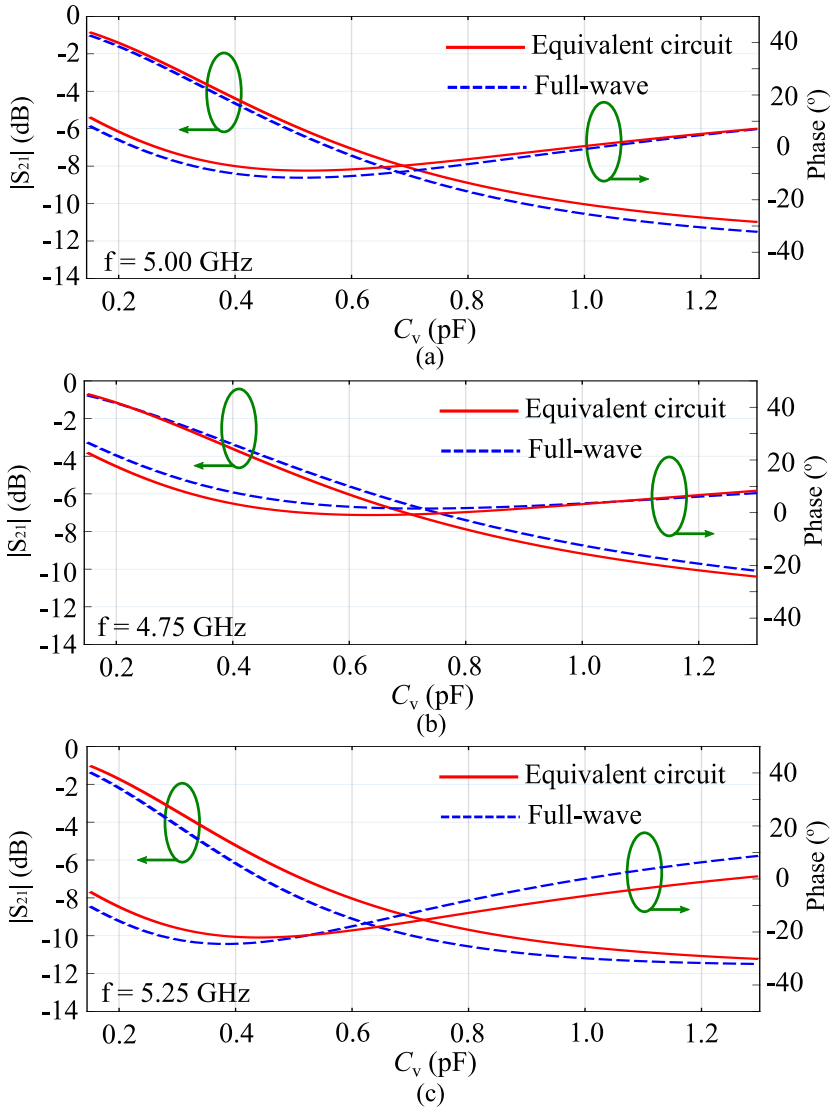

Figure 6.9. S_{21} magnitude and phase values of the final optimized design of 3-same-stub attenuator obtained from the equivalent circuit model and full-wave simulation at (a) 5.00 GHz, (b) 4.75 GHz and (c) 5.25 GHz.

observed that the 3-different-stub attenuator exhibits a larger attenuation range than the 3-same-stub one and maintains a small phase shift at 5 GHz, while the 3-same-stub attenuator has better matching performance and simpler structure.

6.4.3 Extended Designs for Higher Attenuation Levels

The previous paragraph has demonstrated that attenuators with 3 stubs are able to yield 10 dB tunable attenuation. As mentioned, the achievable attenuation range is dependent on the number of stubs. From straightforward extrapolation, it is expected

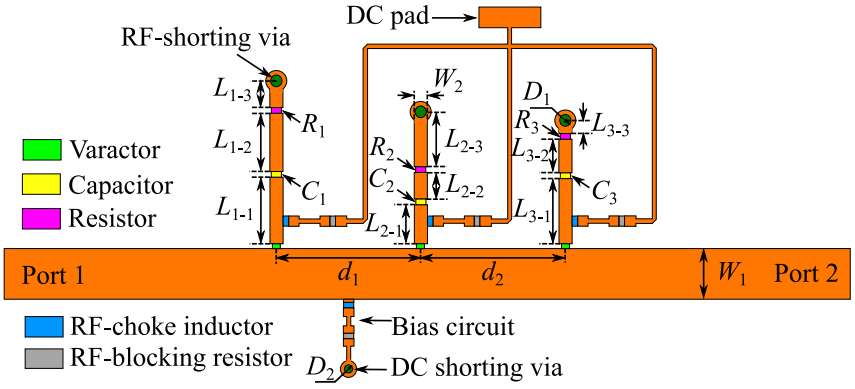

Figure 6.10. Geometry of the proposed attenuator with 3 different shorted varactor-loaded stubs. The optimized parameters are: $W_1 = 2.32$ mm, $W_2 = 0.60$ mm, $L_{1-1} = 3.22$ mm, $L_{1-2} = 2.78$ mm, $L_{1-3} = 1.29$ mm, $C_1 = 0.20$ pF, $R_1 = 25.00\ \Omega$, $L_{2-1} = 1.89$ mm, $L_{2-2} = 1.26$ mm, $L_{2-3} = 2.65$ mm, $C_2 = 0.60$ pF, $R_2 = 25.00\ \Omega$, $L_{3-1} = 3.15$ mm, $L_{3-2} = 1.60$ mm, $L_{3-3} = 0.63$ mm, $C_3 = 0.30$ pF, $R_3 = 25.00\ \Omega$, $d_1 = 7.00$ mm, $d_2 = 7.00$ mm, $D_1 = 0.60$ mm, and $D_2 = 0.40$ mm.

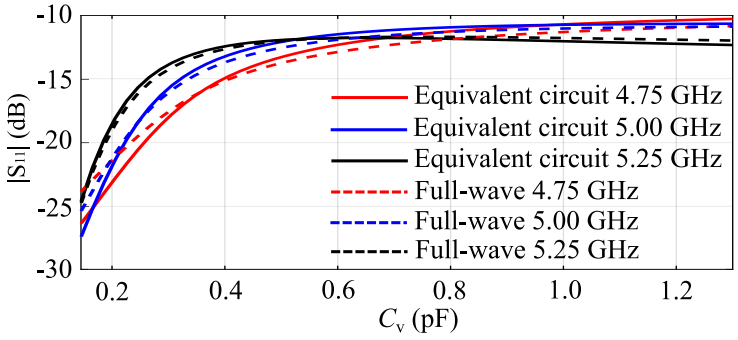

Figure 6.11. Reflection coefficients of the final optimized design of 3-different-stub attenuator obtained from the equivalent circuit model and full-wave simulation at 4.75, 5.00 and 5.25 GHz.

that $3n$ stubs could reach $10n$ dB attenuation. To investigate the practicality of these considerations, 6-stub and 9-stub attenuators with 20 dB and 30 dB attenuation, respectively, are discussed in this section. The design can be extended from the 3-same-stub attenuator by adding further stubs with the same parameters. The geometries of the 6-stub and 9-stub attenuators are shown in Fig. 6.13, and all the stubs are controlled by a single bias voltage over the range 18 to 0 V.

The 6-stub and 9-stub attenuators have been simulated using the full-wave method, and the simulation results are shown and compared in Fig. 6.14 and Fig. 6.15 with those of the 3-stub attenuator. The performance characteristics of the 6-stub and 9-stub attenuators are listed in Table 6.4. As expected, the devices achieve an attenuation of 21.3 dB with 6 stubs, and 31.5 dB with 9 stubs at 5.0 GHz, with reflection coefficients below -10 dB as shown in Fig. 6.14. This confirms that every set of 3 stubs adds nearly

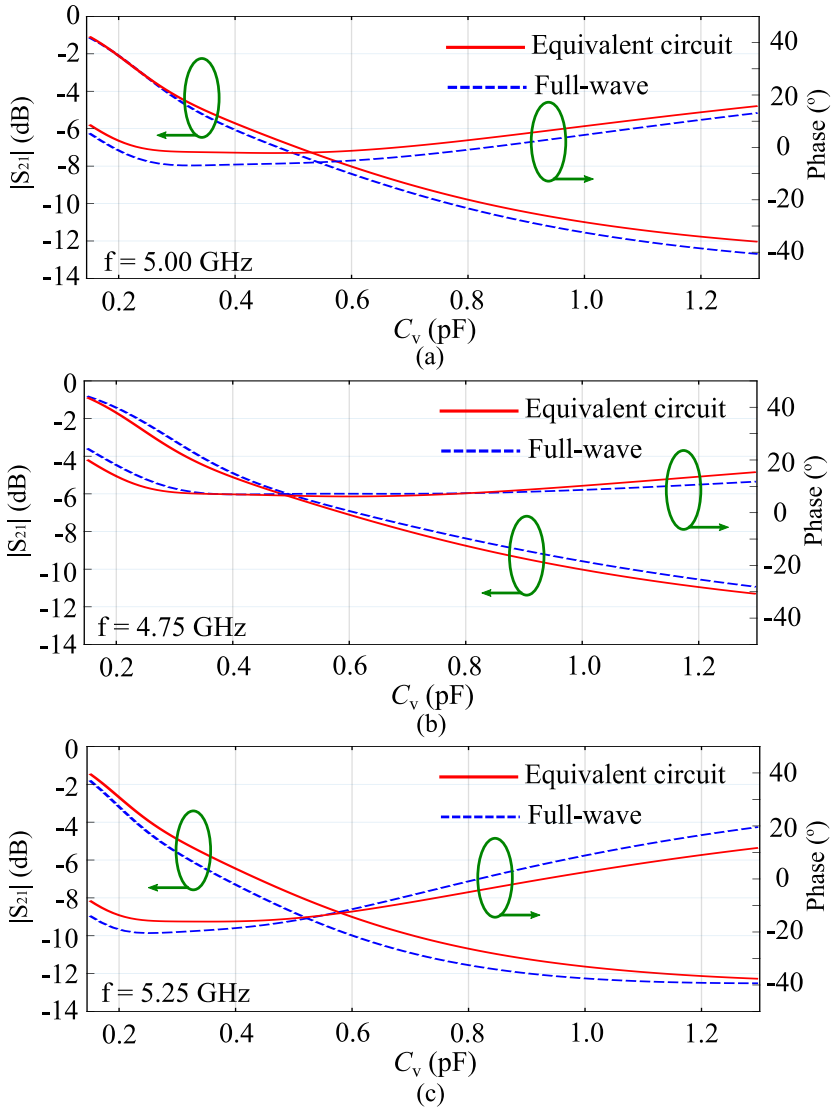

Figure 6.12. S_{21} magnitude and phase values of the final optimized design of 3-different-stub attenuator obtained from the equivalent circuit model and full-wave simulation at (a) 5.00 GHz, (b) 4.75 GHz and (c) 5.25 GHz.

10 dB attenuation and 20° in phase shift. Therefore, the attenuator topology proposed in this thesis addresses the typical issue of limited attenuation and large reflection coefficient of the transmission-type attenuators.

6.5 Experimental Verification

To verify the proposed optimization and design method, three attenuator prototypes with 3-same-stub, 3-different-stub and 9-same-stub have been fabricated and measured, as shown in Fig. 6.16. A 50 Ω reference microstrip transmission line is printed

Table 6.3. Performance of the two optimized attenuators with 3 same stubs (Model1) and 3 different stubs (Model2).

Freq.	Type	Min. IL	Max. IL	$\Delta\phi$	Max. $\lvert S_{11}\rvert$
5.00 GHz	Model1	1.0 dB	11.5 dB	19.8°	-12.2 dB
	Model2	1.0 dB	12.6 dB	15.2°	-10.3 dB
4.75 GHz	Model1	0.8 dB	10.1 dB	25.1°	-12.5 dB
	Model2	0.8 dB	10.5 dB	20.0°	-10.3 dB
5.25 GHz	Model1	1.4 dB	11.5 dB	33.3°	-12.7 dB
	Model2	1.6 dB	13.1 dB	35.0°	-10.9 dB

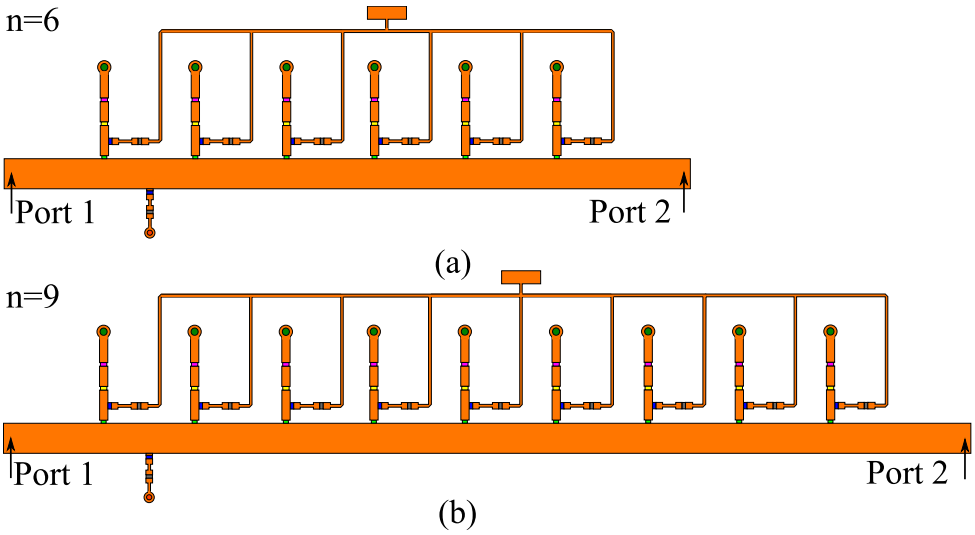

Figure 6.13. Geometries of the proposed attenuators with identical shorted varactor-loaded stubs: (a) 6-stub and (b) 9-stub.

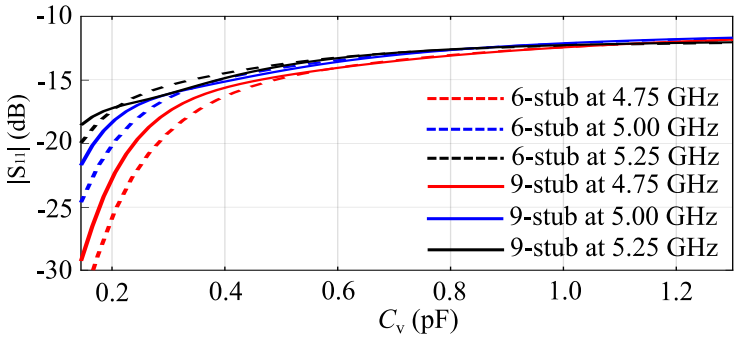

Figure 6.14. Reflection coefficients of the final optimized design of two attenuators with 6-stub and 9-stub respectively, obtained from full-wave simulation at 4.75, 5.00 and 5.25 GHz.

next to each attenuator which is used for calibration of the insertion loss purely due to the host line.

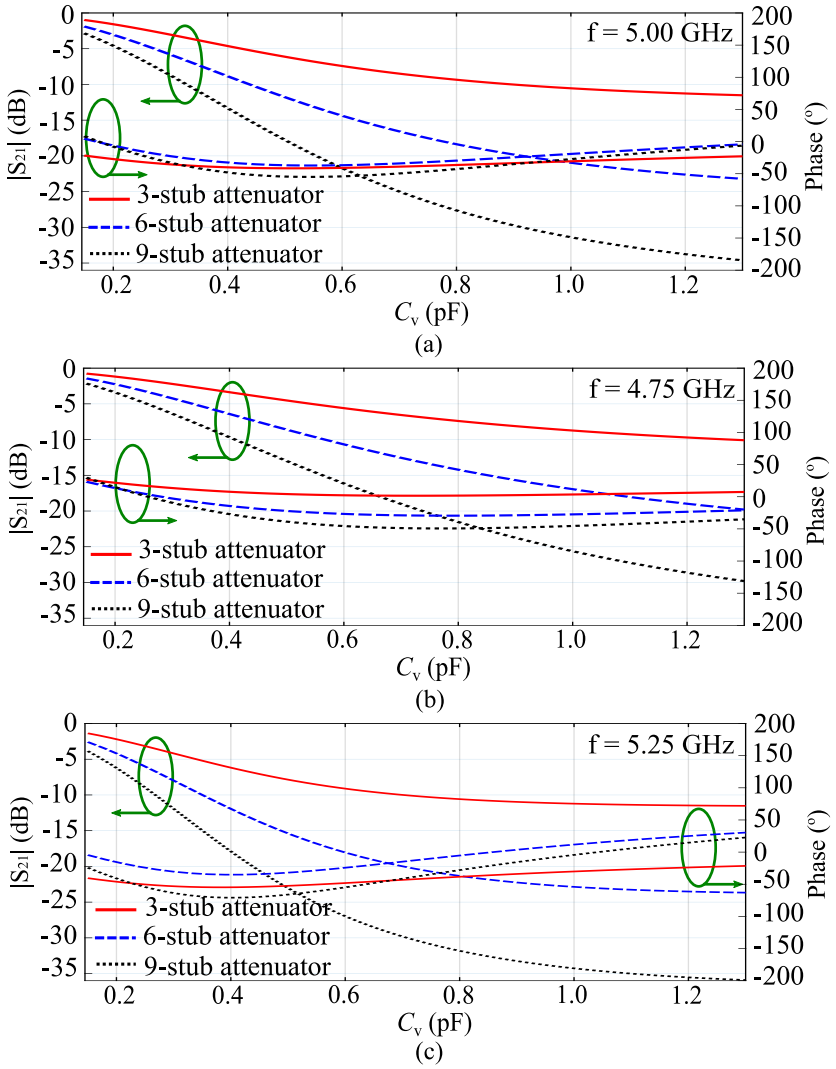

Figure 6.15. S_{21} magnitude and phase values of the final optimized design of three attenuators with 3-stub, 6-stub and 9-stub respectively, obtained from full-wave simulation at (a) 5.00 GHz, (b) 4.75 GHz and (c) 5.25 GHz.

Table 6.4. Characteristics of the 6-stub and 9-stub attenuators.

Freq.	Type	Min. IL	Max. IL	$\Delta\phi$	Max. $\lvert S_{11}\rvert$
5.00 GHz	6 stubs	1.9 dB	23.2 dB	41.7°	-11.7 dB
	9 stubs	2.8 dB	34.3 dB	63.2°	-11.7 dB
4.75 GHz	6 stubs	1.4 dB	19.8 dB	52.5°	-11.9 dB
	9 stubs	2.1 dB	29.4 dB	79.6°	-11.8 dB
5.25 GHz	6 stubs	2.6 dB	23.7 dB	21.1°	-12.1 dB
	9 stubs	3.8 dB	35.7 dB	92.0°	-12.1 dB

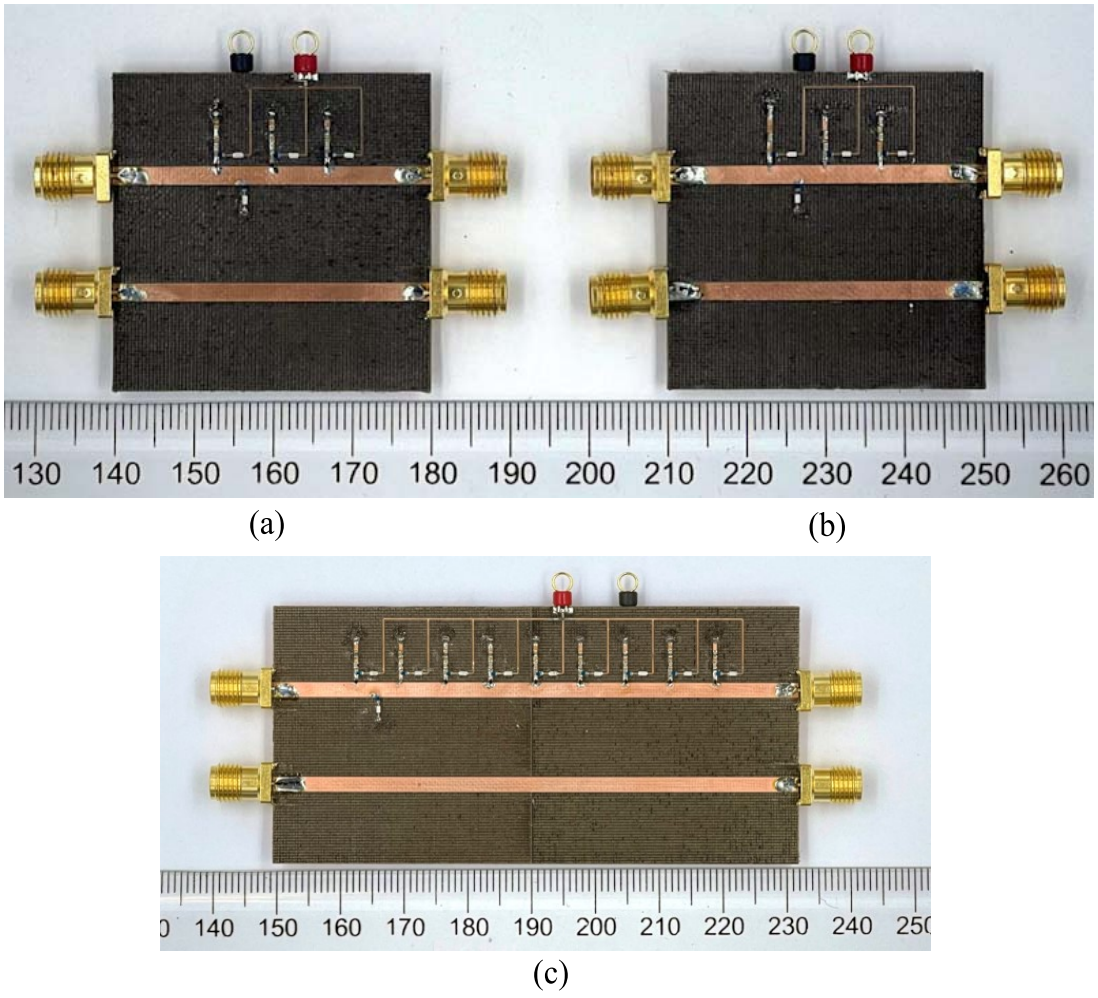

Figure 6.16. Prototypes of three attenuators: (a) 3-same-stub attenuator, (b) 3-different-stub attenuator and (c) 9-stub attenuator. The red test pins are for DC bias circuit connections, and the black ones are for the DC ground connections. A through 50 Ω transmission line is added on each board as reference.

6.5.1 Reflection Coefficient

The measured reflection coefficients of the prototypes are shown in Fig. 6.17. The simulated and measured reflection coefficients of the three attenuators at 5 GHz are listed in the last column in Table 6.5 for direct comparison, where a reasonable agreement is observed with measured data. The measured reflection coefficients of the three attenuators are all below -11.0 dB at the operating frequencies from 4.75 to 5.25 GHz.

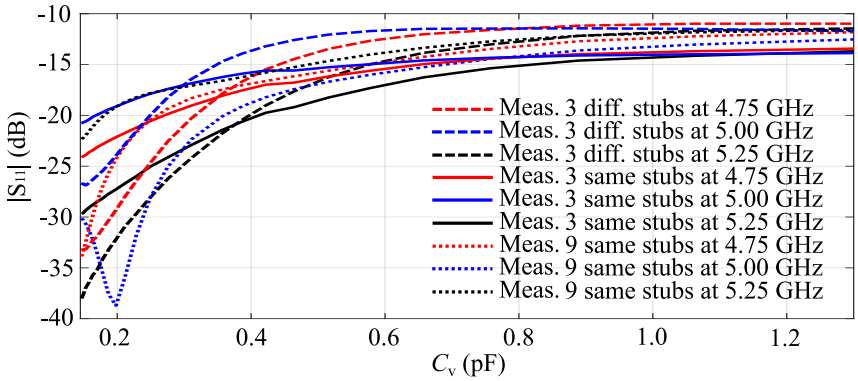

Figure 6.17. Measured reflection coefficients for the three attenuator prototypes, i.e., 3-same-stub attenuator, 3-different-stub attenuator and 9-stub attenuator, at 4.75, 5.00 and 5.25 GHz.

Table 6.5. Simulated and measured characteristics of the three prototypes at 5.0 GHz.

Attenuator	Method	Min. IL	Max. IL	$\Delta\phi$	Max. $\lvert S_{11}\rvert$
3-same -stub	Sim.	1.0 dB	11.5 dB	19.8°	-12.2 dB
	Meas.	1.0 dB	11.2 dB	24.6°	-13.4 dB
3-different -stub	Sim.	1.0 dB	12.6 dB	15.2°	-10.3 dB
	Meas.	1.0 dB	13.5 dB	23.4°	-11.4 dB
9-stub	Sim.	2.8 dB	34.3 dB	63.2°	-11.7 dB
	Meas.	2.1 dB	32.7 dB	82.3°	-11.8 dB

6.5.2 Transmission Characteristics

The measured transmission coefficient magnitudes and phases of the three attenuators are shown in Fig. 6.18. The simulated and measured attenuation levels and phase shifts at 5.0 GHz are compared in Table 6.5. It can be observed that the optimized 3-stub attenuators are able to reach more than 10 dB attenuation, with continuous tunability. The 3-same-stub attenuator has an attenuation range from 1.0 to 11.2 dB with 24.6° phase shift, which is shown in Fig. 6.18(a). Notably, the 3-different-stub attenuator can reach attenuation up to 13.5 dB from 1.0 dB with a phase shift of less than 23.4°. Considering that every set of three stubs produces around 10 dB attenuation, the 9-stub attenuator prototype reaches a performance consistent with the simulated results, i.e., a 30.6 dB attenuation span is realized with a small initial attenuation of less than 2.1 dB and 82.3° phase shift. The tested phase shifts are all slightly larger than the simulated ones, which can be due to the fabrication and material tolerance.

Sub-figures 6.18(b) and (c) show the measured attenuation characteristics of the three attenuator prototypes at 4.75 GHz and 5.25 GHz. The tuning attenuation span are

8.9 dB, 10.8 dB and 24.9 dB for 3-same-stub attenuator, 3-different-stub attenuator and 9-stub attenuator in order at 4.75 GHz, while they reach 10.9 dB, 12.6 dB and 33.8 dB correspondingly at 5.25 GHz.

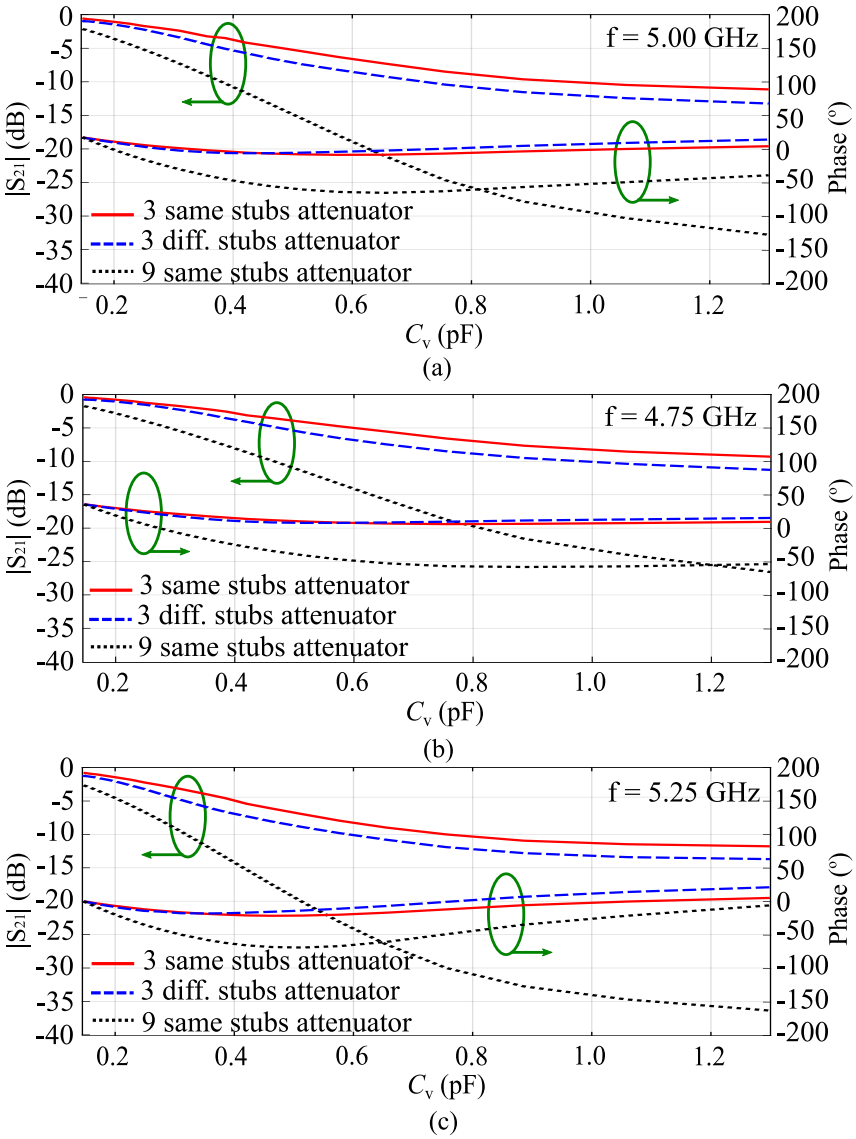

Figure 6.18. Measured S_{21} magnitude and phase values of the three attenuator prototypes, i.e., 3-same-stub attenuator, 3-different-stub attenuator and 9-stub attenuator, at (a) 5.00 GHz, (b) 4.75 GHz and (c) 5.25 GHz.

All these results verify the effectiveness of the optimized attenuators, which can supply a large continuously tunable attenuation range with a small initial insertion loss value, small phase shift and good matching performance.

6.6 Conclusion

An attenuator topology based on a 50 Ω host microstrip line equipped with several side-loaded shorted-end varactor-based stubs has been proposed. The shorted-end stubs includes lumped components including varactors, capacitors, and resistors. All these stubs stand on the same side of the host line resulting in a compact and low-loss structure. An accurate equivalent circuit for general attenuator modelling has been proposed allowing fast optimization of the structure with a GA, and leading to an efficient design method. To verify the concept, 3-stub attenuators have been optimized for a typical attenuation of 10 dB. The successful validation of the equivalent circuit model with full-wave simulations suggests that the circuit approach is efficient and accurate. A set of attenuators with large attenuation levels has been also developed with different stubs numbers, namely a 6-stub and a 9-stub attenuator with 20 dB and 30 dB attenuation at 5 GHz. Three prototypes have been fabricated and tested, i.e., the configurations with 3 identical stubs, 3 different stubs and 9 identical subs. The tested results show that the optimized 3-stub attenuator is able to supply an attenuation up to 13.5 dB from 1.0 dB with a phase shift of less than 23.4°, while the 9-stub version can produce up to 32.7 dB attenuation, however with a relatively larger phase shift up to 82.3°. The proposed attenuator concept has been demonstrated to offer a continuous large attenuation tuning range with a small initial value of insertion loss, combined with relevant merits including small phase shift and good matching performance. Importantly, this compact and flexible topology enables seamless integration into microwave systems with simple control circuit.

Chapter 7

Varactor-Based Frequency-Switchable Diplexer

DIPLEXERS enable microwave systems to transmit and receive signals at different frequencies simultaneously by separating them into different physical output ports. Adding reconfigurability to a diplexer allows to adapt the operation of the different channels. Generally, the major challenge for a reconfigurable diplexer is to find an effective method to make the common input port simultaneously matched at both frequency channels, while having a high isolation between the different channels, and retaining a compact size and low insertion loss level.

To address these challenges, a varactor-based frequency-switchable diplexer is proposed in this chapter. The design is an expanded application of the varactor-based phase shifter tuning unit presented in Chapter 3. The diplexer offers the capability to simultaneously support two different operation bands, similarly to conventional diplexers. Importantly, it also allows to swap the two operation bands across the two output ports. Meanwhile, this planar diplexer maintains a simple and seamless integration topology, resulting in a compact size, a low insertion loss, and an excellent port matching. These merits make it highly suitable for low-cost planar microwave applications.

7.1 Introduction

DIPLEXERS play crucial roles in various communications systems, including wireless networks [185], satellite systems [186], and radar systems [187], since they allow simultaneous transmission and reception in different frequency bands using a single antenna, which can reduce the system size and complexity [188]. Generally, to enhance the versatility of transceiver systems in multi-band applications, reconfigurable diplexers are highly desired. A traditional solution to realize reconfigurable diplexers is to properly align two or more reconfigurable filter structure response to different frequencies [189] [190] [191]. According to the type of frequency tunability, reconfigurable diplexers can be classified in two categories, namely continuously tunable diplexers [192] [193] [194] and switchable diplexers. A tunable microstrip diplexer was presented based on two dual-mode square loop resonators with reconfigurable filtering characteristics in [192], which created two tunable channels: The first channel had a tunable band between 1.23 - 1.43 GHz and 1.35 - 1.64 GHz, while the second was between 2.07 – 2.31 GHz and 2.14 – 2.51 GHz, with an insertion loss between 2.2 and 7.8 dB. In [193], a two channel tunable diplexer allowed frequency tuning in a lower channel from 0.498 - 0.995 GHz and in a high channel from 0.974 - 1.657 GHz, with an insertion loss from 1.0 to 4.6 dB and an isolation larger than 16.4 dB. Another tunable diplexer proposed in [194] was formed directly from two independently designed dual-mode band-pass filters without any additional matching network at the common port, thus achieving a design flexibility and a compact size. It produced two tunable frequency bands, i.e., 1.2 to 1.8 GHz and 2.0 to 2.6 GHz, with an insertion loss between 3.5 to 6.3 dB. Generally, tunable diplexers offer a large dynamic frequency tuning range but suffer a relative high insertion loss level and require complex structures. Oppositely, switchable diplexers typically achieve a much lower insertion loss, which is generally desired in practical applications.

Focusing on switchable diplexers, it is apparent that many attempts have been made to achieve multi-operation modes, low insertion loss levels and compact structures [95, 96, 195–200].

i) Multi-mode switchable diplexers based on PIN diodes typically enable to switch both bands on or off independently. For example, two diplexers were demonstrated for four operation modes, namely both channels on, low-on high-off, low-off high-on, and both off, with an insertion loss between 1.82 to 2.08 dB in [95] and 2.10 to 2.21 dB in [96]. Generally speaking, the complexity of the structures will

increase the insertion loss of the diplexer and its fabrication cost. Importantly, the operation band is typically fixed in one dedicated channel with a switch only controlling its on or off state.

ii) Some efforts have been employed to decrease the insertion loss level by reducing the number of components, such as PIN diodes and varactors. For example, in [198], the authors realized a diplexer by using two balanced open-circuited stubs to produce dual bands with two dual-frequency in each, i.e., 10 and 19 GHz, and 12 and 21 GHz, with an insertion loss of 0.4 to 3.4 dB. As reported in [197], based on a coupled-multi-line filtering sections, a diplexer was produced to operate in two channels with center frequencies of 1.60 and 1.78 GHz and an insertion loss of 1.3 and 1.5 dB respectively. A diplexer operating at 1.0 and 1.2 GHz with corresponding insertion loss of 0.3 and 0.4 dB was presented in [201], by combining a J-inverters impedance conversion and quarter-wavelength open stubs. Another simple diplexer proposed in [196], was created by two square cavities with different triangular slots loaded to supply two operation bands with center frequencies of 6.16 and 7.72 GHz and an insertion loss of 0.83 and 0.77 dB, respectively. It can be seen that although it does not contain any electronic lumped components and thus achieves low insertion loss levels, the frequency-selective structure is complex, and the flexibility of frequency shift is sacrificed in the sense that the device can only work in two fixed frequency bands through specific channels at a time.

iii) Research efforts have also been invested to obtain reconfigurable diplexers with a compact size and low insertion loss. A switchable filtering diplexer containing two multi-coupled resonator filters sharing a switchable L-shaped resonator was proposed in [200], with a co-design method applied to reduce the size and insertion loss. This diplexer could switch its working frequency between 2.35 and 3.50 GHz using 5 PIN diodes as the control, achieving an insertion loss of 1.30 and 1.34 dB. However, although the diplexer maintained compact size and low insertion loss, the filter response structure and the control method complex, so likely leading to a relative high cost. In addition, the operation frequency was also fixed in a dedicated channel, which could only be controlled to yield on or off state.

One can observe that the challenge in switchable diplexer design is to obtain multiple operation modes, a simple and compact structure, and a low insertion loss level, while

maintaining good match and a high isolation level between the different frequency channels.

To address this challenge in switchable diplexer design, a compact varactor-based frequency-switchable diplexer is proposed in this chapter. The switchable diplexer consists of two identical frequency-selective units located symmetrically on a T-junction with equal power division. This unit is designed on a 50 Ω transmission line with two varactor-loaded short-ended stubs standing on one side of the line. The topology of the unit enables seamless integration to planar microwave systems with low insertion loss and compact size. By changing the bias voltage to the two varactors, specific frequencies are enabled or disabled to pass through the transmission line, thus realizing the frequency selectivity. The unit is optimized aiming to cover two operation bands, i.e., low band from 2.4 to 2.5 GHz and high band from 5.725 to 5.825 GHz. Correspondingly, the diplexer is able to generate five operation modes, i.e., both channels allowing both the low and high bands (high + low, high + low), allowing only the low band (low, low), allowing only the high band (high, high), and allowing one branch on the low band and the other branch on the high band (low, high) or vice versa (high, low). Importantly, the unique characteristic of the proposed device is that it cannot only realize the diplexing function for two specific frequencies working in different channels at a time, but it can also swap the working frequency on its two channels. This frequency swapping between two different channels reduces the design complexity for different frequencies and increases the link adaptability. It is noted that the same operation frequency states, i.e., (high + low, high + low), (low, low) and (high, high), can also operate as frequency-reconfigurable power dividers.

To verify the concept, a frequency-selective unit and a frequency-switchable diplexer have been fabricated and experimentally characterized. The fabricated prototype diplexer operates at five states with different frequency combinations between two operating bands. All the findings verify the effectiveness and the performance of the proposed frequency-switchable diplexer. The following sections are arranged as follows: Section 7.2 introduces the frequency-selective unit concept and its design, and experimental verification. The concept of the diplexer is proposed in Section 7.3, with its design and experimentally validation, followed by concluding remarks.

7.2 Frequency-Selective Unit

7.2.1 Working Principle and Design

Generally, a diplexer is formed by combining two frequency filtering structures which critically determine the operation bands, insertion loss, reflection coefficients, and suppression of the unwanted frequencies. A varactor-based frequency-selective unit is implemented in this section, with its topology shown in Fig. 7.1.

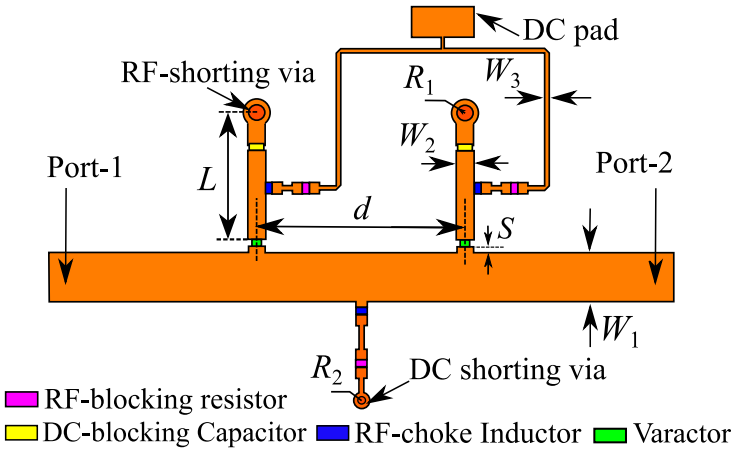

Figure 7.1. Geometry of the proposed frequency-selective unit with two varactor-loaded stubs. The dimensions are: $W_1 = 2.32$ mm, $W_2 = 0.80$ mm, $W_3 = 0.20$ mm, $L = 6.00$ mm, $R_1 = 0.40$ mm, $R_2 = 0.20$ mm, $S = 0.30$ mm and $d = 10.00$ mm.

As depicted in Fig. 7.1, the frequency-selective unit contains a 50 Ω microstrip transmission line loaded with two shunt varactors which are terminated with short-ended stubs. The unit is designed on a 0.76 mm thick Rogers Diclad 880 with relative permittivity of 2.2 and loss tangent of 0.0009. The varactor adopted in this design is MA46H120 which has a parasitic inductance of 0.05 nH and a resistance of 2 Ω [109] [184]. As shown in Fig. 7.1, the bias network consists of an RF-choke inductor of 15 nH in series with an RF-blocking resistor of 1000 Ω. A 220 pF DC-blocking capacitor is inserted into the top section of the stub close to the RF-shorting via. The microstrip bias lines connected to the DC voltage are chosen to be 0.2 mm wide to increase their inductance and minimize radiation. The unit is tuned by a DC bias voltage applied to the two varactors simultaneously from the DC pad. By changing the bias voltage, it becomes possible to enable or disable specific frequencies passing through the microstrip transmission line, thereby providing a frequency-selective functionality.

7.2.1 Working Principle and Design

Full-wave simulations with Ansys HFSS 2021 are deployed to illustrate the frequency-selective functionality of the unit model. The characteristics of the S-parameters are shown in Fig. 7.2. As shown by the inset in Fig. 7.2(a), the varactor provides a capac-

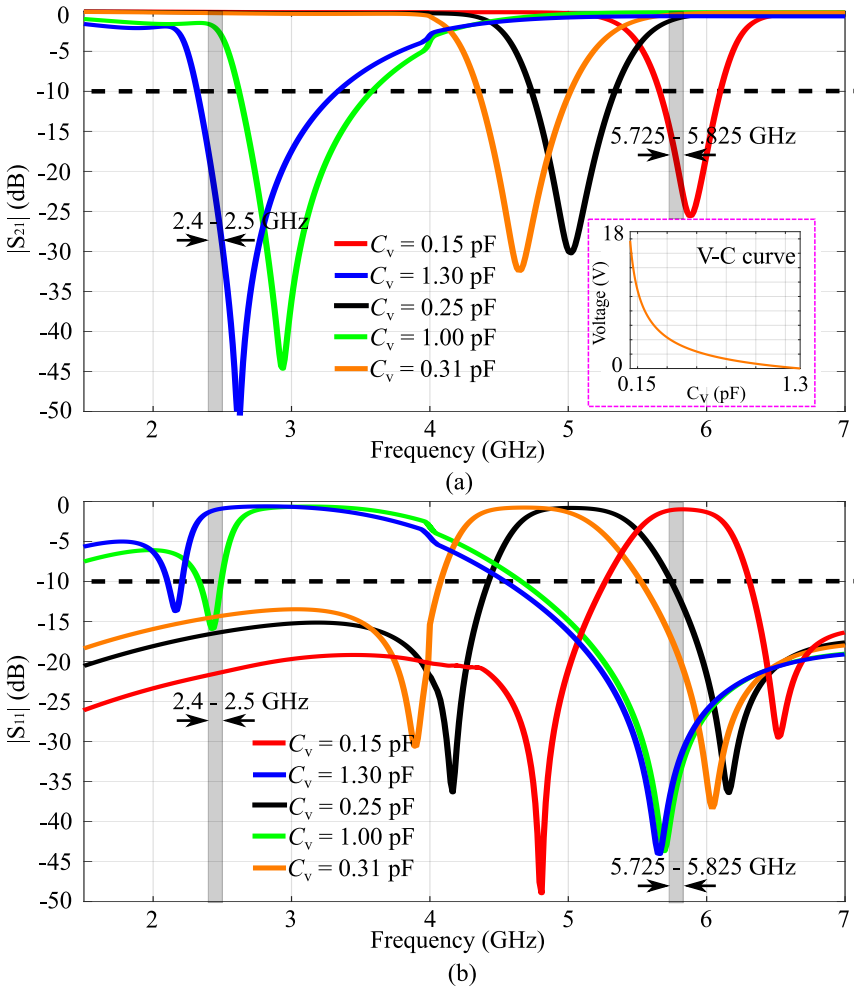

Figure 7.2. (a) S_{21} magnitude curves of a frequency-selective unit under five typical bias voltages, i.e., 0.15 pF (red line), 1.30 pF (blue line), 0.25 pF (black line), 1.00 pF (green line) and 0.31 pF (orange line), inset: Reverse voltage-capacitance control curve of the varactor, and (b) corresponding reflection coefficients curves.

itance value from 0.15 to 1.30 pF for a bias voltage from 18 to 0 V. It can be seen that proper bias voltage allows the stop-band to move within a certain frequency range, thus achieving two available bands on outside of the stop-band. For example, when the tunable capacitance of the varactors is set as 0.15 pF, the frequency at 5.80 GHz is blocked in the stop-band while the low frequency at 2.45 GHz can pass through the structure. In contrast, if the capacitance is tuned to 1.30 pF, the high frequency of 5.80 GHz becomes enabled but the 2.45 GHz band is disabled on the transmission line. Furthermore, there exists a proper capacitance value allowing both frequencies, i.e.,

2.45 and 5.80 GHz, to be enabled simultaneously, which happens at a value of 0.31 pF as shown in Fig. 7.2. Typical simulation results are listed in Table 7.1, illustrating that reflection coefficients are below -13.6 dB in all three states. The magnitudes of S_{21} are

Table 7.1. Typical simulated S-parameters of the frequency-selective unit

C_v	S_{11}		S_{21}	
	2.45 GHz	5.80 GHz	2.45 GHz	5.80 GHz
0.15 pF	-21.53 dB	-1.00 dB	-0.07 dB	-20.35 dB
1.30 pF	-1.08 dB	-34.83 dB	-23.5 dB	-0.12 dB
0.95 pF	-13.60 dB	-32.63 dB	-1.43 dB	-0.13 dB

-0.07 and -0.12 dB for the states where a single frequency is allowed to pass through, at 2.45 and 5.80 GHz respectively, with an isolation of the corresponding stop frequencies reaching 20.35 at 5.80 GHz and 23.50 dB at 2.45 GHz. For the dual-band mode under the bias voltage of 0.31 pF, the insertion losses are 0.23 dB at 2.45 GHz and 0.35 dB at 5.80 GHz. It can be seen from Fig. 7.2 that the voltage sets are not unique for dual-band operation: They could be adjusted in a large range with a stop-band in between the two available bands, i.e., from 0.25 to 1.00 pF in the proposed unit. This feature provides a flexibility to select the optimal voltages according to the required related characteristics, including the reflection coefficients and insertion loss levels.

7.2.2 Fabrication and Measurement

To verify the proposed design concept, a prototype of a stand-alone frequency-selective unit prototype is fabricated as displayed in Fig. 7.3.

A reference 50 Ω microstrip transmission line is printed on the same substrate, and is used to calibrate the insertion loss purely due to the line and connectors. Two test pins soldered on the unit are used for the DC bias and ground connections, respectively. The measured performance of the prototype is compared with the results obtained from full-wave simulation in Fig. 7.2, where a reasonable agreement is observed.

When the C_v is set as 0.15 pF, the unit in simulation operates in low band from 1.50 to 5.26 GHz with maximum insertion loss of 0.89 dB. When the C_v is set as 1.3 pF, the unit works in the high band from 4.56 to 7.00 GHz with an insertion loss smaller than 0.72 dB. If the C_v is set at 0.31 pF, the unit operates in the dual band state from 1.50 to 4.03 GHz and from 5.53 to 7.00 GHz with an insertion loss less than 1 dB.

7.2.2 Fabrication and Measurement

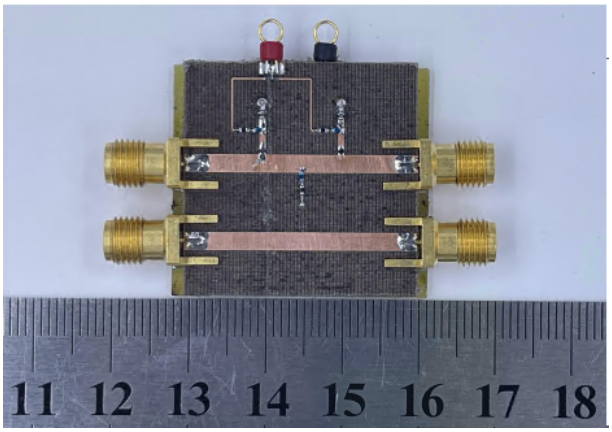

Figure 7.3. Prototype of the frequency-selective unit. The dark red test pin is for DC bias circuit connection, and the black one is for the DC ground connection. A through 50 Ω transmission line is added on the same board as reference.

For the measured results as shown in Fig. 7.3, when the voltage is set as 18 V, the unit works in low band from 1.50 to 3.04 GHz with an insertion loss less than 0.77 dB. If the voltage is tuned to 0 V, the unit operates in the high band from 4.47 to 7.00 GHz with maximum insertion loss of 0.87 dB. When a bias voltage of 6 V is applied on the unit, it operates in the dual-band state from 1.50 to 2.82 GHz and from 5.46 to 7.00 GHz with an insertion loss smaller than 0.59 and 1.16 dB respectively.

In addition, the reflection coefficients are all less than -10 dB in the aforementioned operation bands. As for the stop-band suppression, when the voltage is set to 18 V, the amplitude of S_{21} is -28.2 dB at 5.80 GHz, while the corresponding value is -32.7 dB at 2.45 GHz under the voltage set as 0 V. It can be seen that there are small missmatched ranges from 3.04 to 3.37 GHz, when the unit works under the bias voltages of 18 V and 6 V. These missmatched bands reduce the bandwidths of the low band part due to the fabrication and measurement tolerances. Another offset between the simulated and measured results caused by these tolerances is observed for the $|S_{21}|$ curves when the voltage is set as 0 V, with the stop band at lower frequency shifting slightly to the left, but still well covering the low band centered at 2.45 GHz. All the findings demonstrate that the unit provides frequency selectivity and a competitive solution to be exploited for further diplexer design, as shown in the next section.

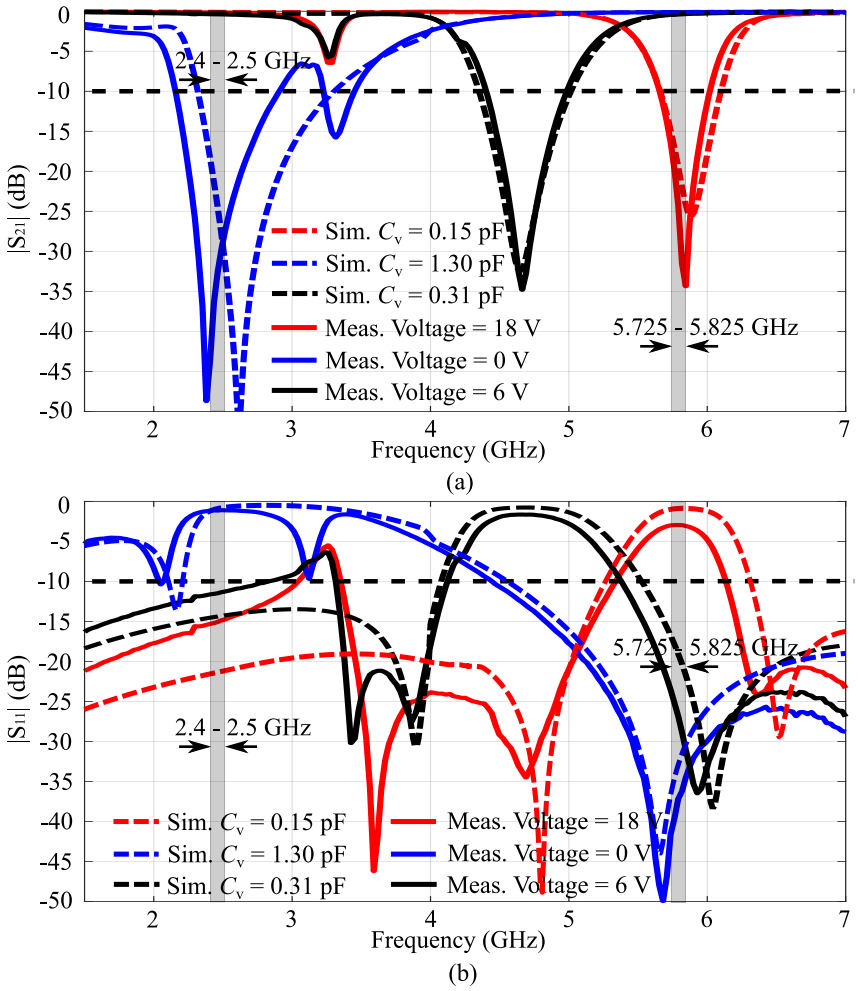

Figure 7.4. Frequency-selective unit prototype performance, showing the simulated and measured (a) S_{21} magnitude and (b) S_{11} magnitude.

7.3 Frequency-Switchable Diplexer

7.3.1 Operation Principle and Design

Based on the proposed design of the previous section, the frequency response of the basic frequency-selective unit is only controlled by a single bias voltage, which reduces the design complexity when combining multiple units for two or more specific operation channels. On that basis, a frequency-switchable diplexer is presented, which contains a T-junction with equal power division and two identical frequency-selective units. The geometry of the proposed diplexer is illustrated in Fig. 7.5. In general, a T-junction divider is a good solution for a switchable diplexer to obtain a low reflection level at the common port [202] [203]. Therefore, a simple T-junction equal-power divider with input impedance of 50 Ω to Port-1 is utilized here, followed by

7.3.1 Operation Principle and Design

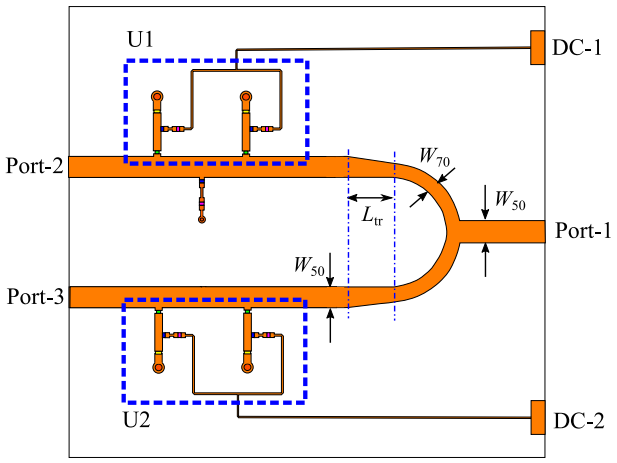

Figure 7.5. Geometry of the proposed frequency-switchable diplexer with two frequency-selective units. The dimensions are: W_{50} = 2.32 mm, W_{70} = 1.55 mm, L_{70} = 10.80 mm and L_{tr} = 5.90 mm.

tapered transmission line sections with length of L_{tr} to the 50 Ω output branches. Two frequency-selective units, labeled as U1 and U2, are located symmetrically on the two output lines to the Port-2 and Port-3 respectively. Two separate DC voltages from a power supply are used to manually control varactor capacitances C_{v1} and C_{v2}, and thus specific frequencies can selectively pass through the two units U1 and U2. The frequency-switchable diplexer supplies five operation modes which are listed in Table 7.2, namely State-1 (Port-2: low band, Port-3: high band), State-2 (Port-2: high band, Port-3: low band), State-3 (both ports: low and high bands), State-4 (both ports: low band), and State-5 (both ports: high band). As shown in Fig. 7.6(a), when the

Table 7.2. Operation states of the frequency-switchable diplexer

States label	C_{v1} (U1)	C_{v2} (U2)	Port-2	Port-3
1	0.15 pF	1.30 pF	F_1*	F_2◇
2	1.30 pF	0.15 pF	F_2	F_1
3	0.85 pF	0.85 pF	F_1 + F_2	F_1 + F_2
4	0.15 pF	0.15 pF	F_1	F_1
5	1.30 pF	1.30 pF	F_2	F_2

* F_1 stands for the low band centered at 2.45 GHz.

◇ F_2 stands for the high band centered at 5.80 GHz.

C_{v1} and C_{v2} are set to 0.15 pF and 1.3 pF, two frequency bands are created with each transmitted through a dedicated port, i.e., the low band (2.25 to 2.84 GHz) centered at 2.45 GHz to Port-2 and the high band (5.58 to 5.87 GHz) centered at 5.80 GHz to Port-3, with the $|S_{11}|$ less than -10 dB and $|S_{23}|$ less than -20 dB simultaneously. The

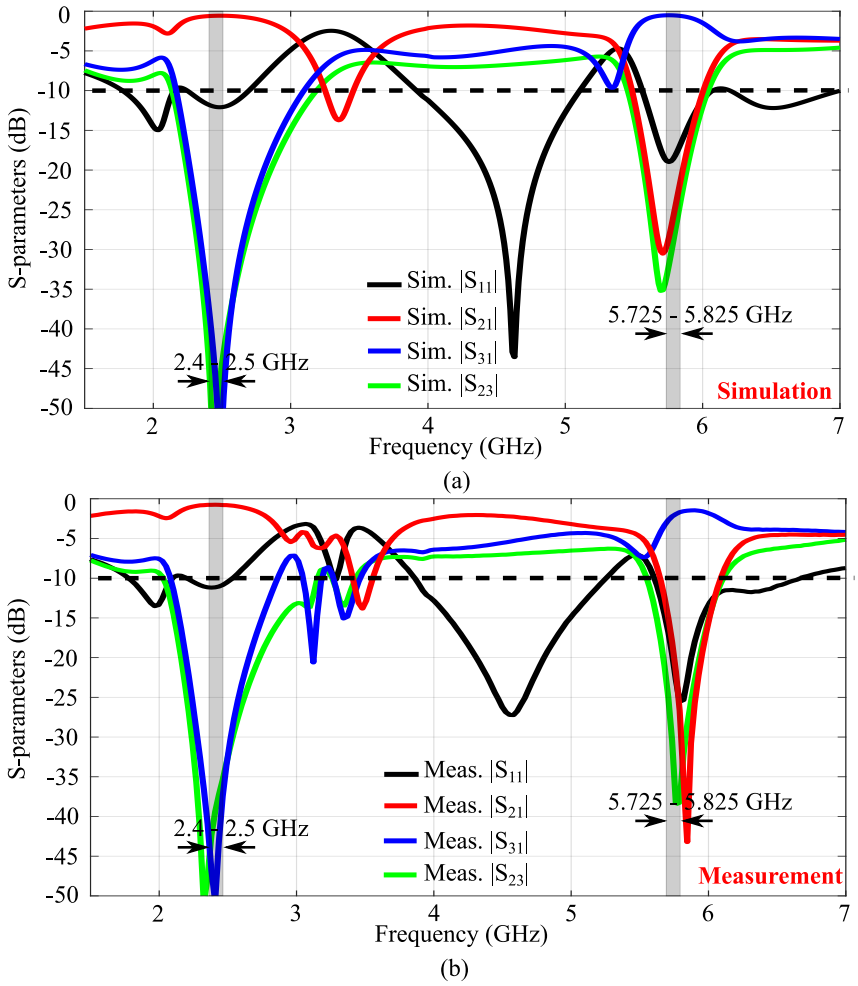

Figure 7.6. *S*-parameter characteristics of the frequency-switchable diplexer in State-1: (a) Simulated results with C_{v1} as 0.15 pF and C_{v2} as 1.30 pF, and (b) measured results with DC-1 as 18 V and DC-2 as 0 V.

simulated insertion loss levels of the two available pass bands are less than 1.38 dB and 1.15 dB respectively. The isolation characteristics in State-1 shown in Fig. 7.6(a) are -56.28 dB at 2.45 GHz and -27.69 dB at 5.80 GHz. When the bias voltages applied on the two branches are exchanged, i.e., C_{v1} and C_{v2} are set to 1.30 pF and 0.15 pF, the low band is swapped to Port-3 while the high band is passing through to Port-2, as displayed in the simulated results of Fig. 7.7(a). Since the two different frequencies can be switched between the two channels, this diplexer is said to be working in a frequency switchable mode. As a result, the performance of State-2 is ideally symmetrical and identical to State-1 with the same transmission and reflection characteristics, but the working band is swapped. In this operation modality, the frequency selectivity is only

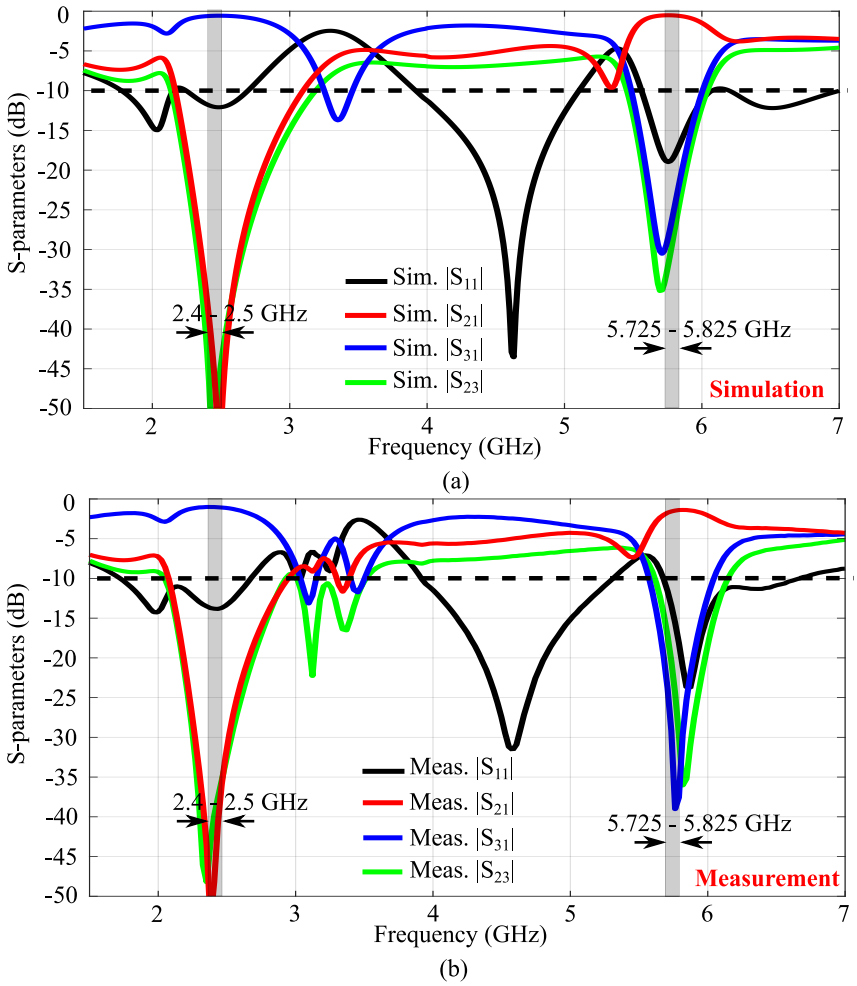

Figure 7.7. *S*-parameter characteristics of the frequency-switchable diplexer in State-2: (a) Simulated results with C_{v1} as 1.30 pF and C_{v2} as 0.15 pF, and (b) measured results with DC-1 as 0 V and DC-2 as 18 V.

controlled by the bias voltages, greatly reducing the design complexity. It is also emphasized that the diplexer is simply realized with two identical units integrated onto the divider.

The next operation mode is State-3, where the capacitance values are identical in both units and set as 0.85 pF to offer a dual-band mode, which enables simultaneous operation for both channels in the low band from 2.18 to 2.85 GHz and high band from 4.65 to 7.00 GHz, as shown in Fig. 7.8(a). In this state, a capacitance changing from 0.25 pF to 1.00 pF is acceptable to realize dual-band mode in each single unit. Following from the State-3, the C_{v1} and C_{v2} are then both tuned to 0.15 pF, which allows a single low-frequency band to pass through the divider. At the other end of the capacitance range, the high frequency bands can be selected for both channels when C_{v1} and C_{v2} are tuned to 1.30 pF simultaneously. Good match at Port-1 can be obtained, as

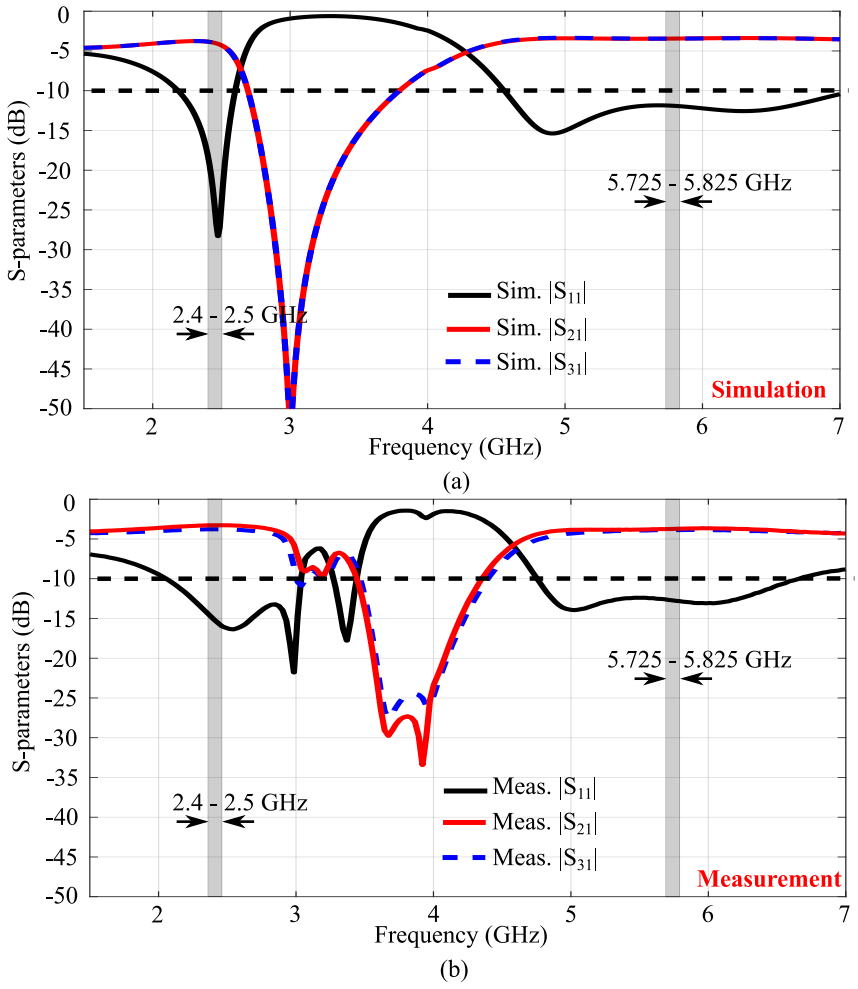

Figure 7.8. *S*-parameter characteristics of the frequency-switchable diplexer in State-3: (a) Simulated results with C_{v1} as 0.85 pF and C_{v2} as 0.85 pF, and (b) measured results with DC-1 as 3 V and DC-2 as 3 V.

shown in Fig. 7.9(a) and Fig. 7.10(a), with the transmission characteristics of $|S_{21}|$ and $|S_{31}|$ exhibiting single-frequency operation states.

7.3.2 Fabrication and Measurement

A prototype of the proposed frequency-switchable diplexer has been fabricated and measured for experimental validation, as displayed in Fig. 7.11. Three test pins soldered on the diplexer are used for the DC bias (two dark red pins) and ground (black pin) connections, respectively. The measured performance of the prototype is shown in Fig. 7.6(b) - Fig. 7.10(b). Considering a specification for the reflection coefficients to be less than -10 dB and the channel isolation to be larger than 20 dB, as depicted in Fig. 7.6(b), Port-2 enables a low band from 2.16 to 2.65 GHz under a bias voltage

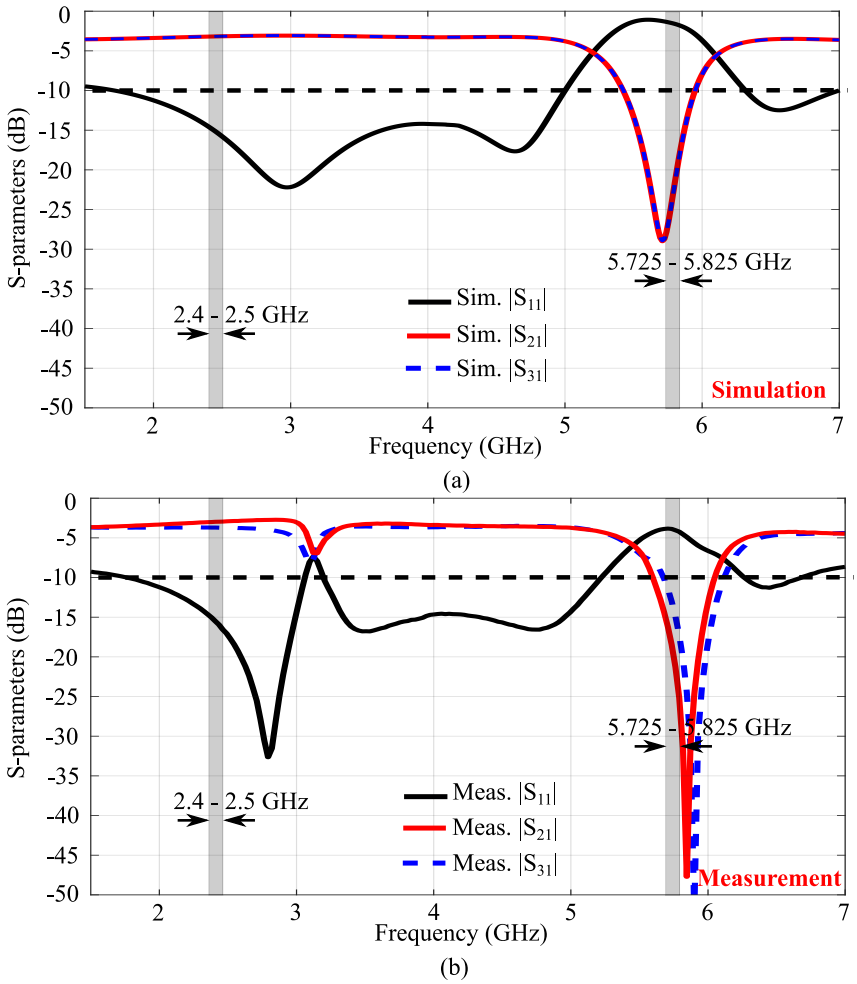

Figure 7.9. *S*-parameter characteristics of the frequency-switchable diplexer in State-4: (a) Simulated results with C_{v1} as 0.15 pF and C_{v2} as 0.15 pF, and (b) measured results with DC-1 as 18 V and DC-2 as 18 V.

U1 = 18 V, while Port-3 allows the high band from 5.70 to 5.93 GHz with a bias voltage U2 = 0 V. This corresponds to State-1, which achieves an insertion loss less than 1.36 dB and 2.34 dB respectively. When U1 is set to 0 V and U2 is set to 18 V, the operation state is State-2, where a high band from 5.65 to 5.9 GHz is allowed to Port-2, and the low band from 2.2 to 2.52 GHz goes to Port-3 with corresponding insertion losses of less than 2.0 dB and 1.2 dB, as depicted from Fig. 7.7(b). High isolations are obtained at 2.45 GHz and 5.80 GHz at levels of -37.5 dB and -35.2 dB in State-1, and -37.2 dB and -28.5 dB in State-2, respectively. Finally, when the voltages are set the same to 18, 0 and 3 V, the diplexer becomes a frequency-reconfigurable divider with the two channels operating at the same frequency. Comparing the results from full-wave simulations and these experimental results, in Fig. 7.6 - Fig. 7.10, a reasonable agreement is observed, thus validating the frequency-switchable diplexer concept. The discrepancies between

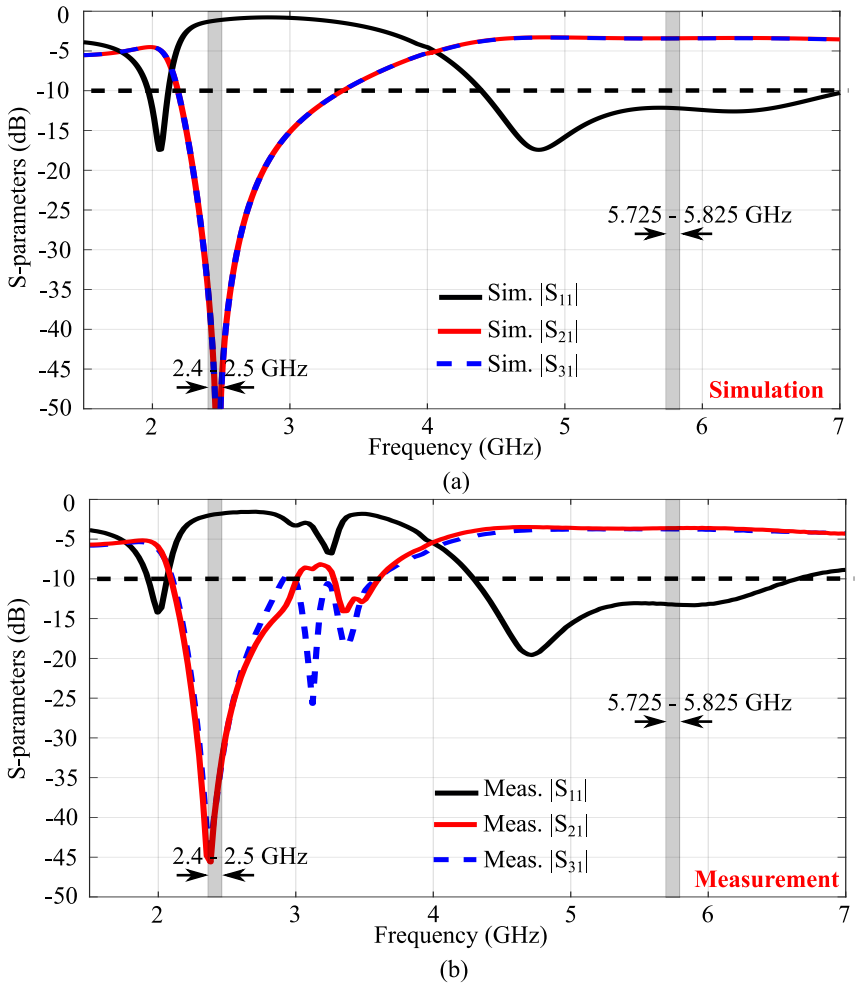

Figure 7.10. *S*-parameter characteristics of the frequency-switchable diplexer in State-5: (a) Simulated results with C_{v1} as 1.3 pF and C_{v2} as 1.3 pF, and (b) measured results with DC-1 as 0 V and DC-2 as 0 V.

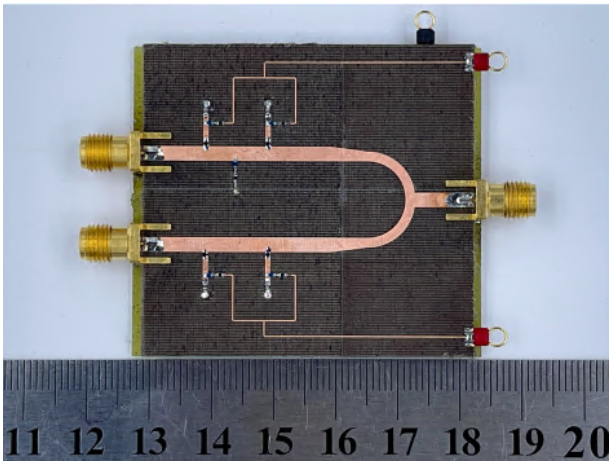

Figure 7.11. Prototype of the frequency-switchable diplexer. Two dark red test pins are for DC bias circuit connections, and the black one is for the ground connection.

simulation and measurement are due to fabrication and measurement tolerances. For example, in Fig. 7.8, a discrepancy between the simulated and measured results in the lower band can be identified as a shift of the curve to higher frequencies, which does not affect the operation and performance of the diplexer significantly.

7.4 Conclusion

A compact varactor-based frequency-switchable diplexer has been presented in this chapter. The proposed diplexer consists of two identical frequency-selective units which are standing symmetrically on the two output branches of a T-junction equal-power divider. The frequency-selective unit exhibits the advantages of low insertion loss, low reflection coefficients, compact size, high suppression for the undesired band, and its frequency response is only controlled by a single bias voltage. Based on this design, a frequency-switchable diplexer consisting of two identical units has been proposed, which has a compact size and achieves low insertion loss level and a high isolation when the output branches operate at different frequency bands. It is worth to mention that the frequency-switchable diplexer not only can realize two specific frequencies working in different channels at a time, but it also can swap the working frequencies on its two channels. This frequency swapping enables the diplexer to hold a symmetrical construction which reduces the design complexity for different frequencies and increases the link adaptability. In addition, when the bias voltages applied on the units are the same, the diplexer can turn into a frequency-reconfigurable equal-power divider, allowing a multi-functional application as well. All these results imply that the proposed frequency switchable diplexer is a promising solution to supply various frequency reconfigurable functions. On the basis of this performance, it can be utilized in an antenna system to produce frequency reconfigurability, which will be discussed in detail in Chapter 8.

Chapter 8

Pattern- and Frequency-Reconfigurable Antenna Array

PATTERN- and frequency-reconfigurable antennas offer a great flexibility and adaptability in wireless communications systems and have gained wide attention in the recent literature. This chapter presents a reconfigurable two-element antenna array, where the frequency reconfigurability is achieved through the feeding network which is a frequency-switchable diplexer. Combining this reconfigurable feeding network with a reflector plate between the elements of the array, two directional radiation patterns in opposite direction, or a bidirectional pattern with two switchable frequency bands can be obtained in different operating states. This pattern- and frequency-reconfigurable antenna array maintains a simple structure, small insertion loss, and low reflection coefficient using a single port for all three operation modes, making it a highly promising design for low-cost and compact communications applications.

8.1 Introduction

PATTERN- and frequency-reconfigurable antennas have been developed widely in the recent years. Large efforts have been invested to create various reconfiguration modalities. In general, by controlling tunable electronic components loaded on the structure, the effective electrical length of the radiators can be modified which can yield pattern and/or frequency reconfigurations [204, 205]. In [204], the authors utilized a reconfigurable parasitic stripline near the radiating dipole, which was controlled by PIN diodes to create an equivalent metal sheet below the dipole. This enabled the antenna main beam to be switched to five directions at a single frequency. In [205], a frequency-reconfigurable antenna with omnidirectional patterns was proposed with the ability to shift five operation subbands in an ultra-wideband (UWB) range of 6.0 to 10.6 GHz by the control of five PIN diodes. These reconfigurable antennas employed the control structures, electronic components and bias circuits around the radiators, which may lead to a complex topology.

In addition to changing the effective geometrical structure of the radiators, altering the feeding structure to achieve reconfigurability is also a common alternative method, which simplifies the design of radiators and may reduce the impact of the tuning components on the radiation performance [206] [207] [208]. In [206], two operation modes were generated on a wideband Vivaldi antenna structure by switching between two feeding paths. The switching of PIN diodes allowed to create a monopole mode with a bidirectional pattern and a Vivaldi mode with a directional pattern operating from 2.7 to 12.0 GHz. Switchable broadside and conical beams were obtained similarly in [207], which was achieved by switching PIN diodes on the feeding structure to create a wideband monopole patch or a wideband L-probe fed patch. In [208], three switchable endfire patterns, including a left directional pattern, a right directional pattern and a bidirectional pattern, were achieved by switching PIN diodes on a feeding balun to excite the left, right or both radiators in a single operation band extending from 1.98 to 2.06 GHz. Generally, the principle of utilizing switchable feeding paths aims at enabling the operation of different radiator parts that realize a corresponding specific pattern at a time.

To make the antenna multi-functional, a pattern and frequency reconfigurable antenna was presented in [97]. Utilizing a varator-tuned T-junction, the patch coupling between a two-element array was modified to create a frequency-tunable range from 2.15 to 2.38 GHz with a beam that could be continuously scanned from -23° to 23°. However,

the frequency tunability remained limited in a relatively small range. In [209], a dual-band pattern reconfigurable antenna was proposed combining a wideband Wilkinson divider and two single-port-single-through switches, which produced two individually controlled signal paths to two symmetrical dual-band radiation slots. The antenna was able to operate in three states, including [left on / right off], [left off / right on] and [left on / right on] with dual-band operation at 2.4 and 5.2 GHz simultaneously. However, the two operation frequencies were not separately controllable, which is a desired performance for some practical applications.

In order to extend functionality to further application requirements, a simple pattern- and frequency-reconfigurable two-element antenna array is proposed in this chapter, fed by the frequency-switchable diplexer presented in Chapter 7. This feeding network supplies two individually tunable signal paths to enable low-band and high-band operation on each path separately. In combination with a simple isolation metal screen located between two wideband monopole elements, three types of endfire patterns are created in a unique set of three different modes of operation, including [left directional pattern in low band / right directional pattern in high band], [left directional pattern in high band / right directional pattern in low band], and [bidirectional patterns in dual-band]. The following sections are arranged as follows: Section 8.2 introduces the array design, which combines two wideband monopole elements and a frequency-switchable diplexer feeding network. This section also contains the performance predictions from simulations. The pattern and frequency reconfigurable antenna array is fabricated and experimentally validated in Section 8.3, followed by concluding remarks.

8.2 Pattern- and Frequency-Reconfigurable Antenna Array Design

8.2.1 Array Design

A two-element pattern- and frequency-reconfigurable antenna array is proposed in this section which is shown in Fig. 8.1. The general configuration of the array shown in Fig. 8.1(a), consists of three major groups from bottom to top: a frequency-switchable diplexer positioned on the bottom horizontal substrate, a vertically oriented radiation board with two probe-fed wideband circular monopole elements standing on the top

8.2.1 Array Design

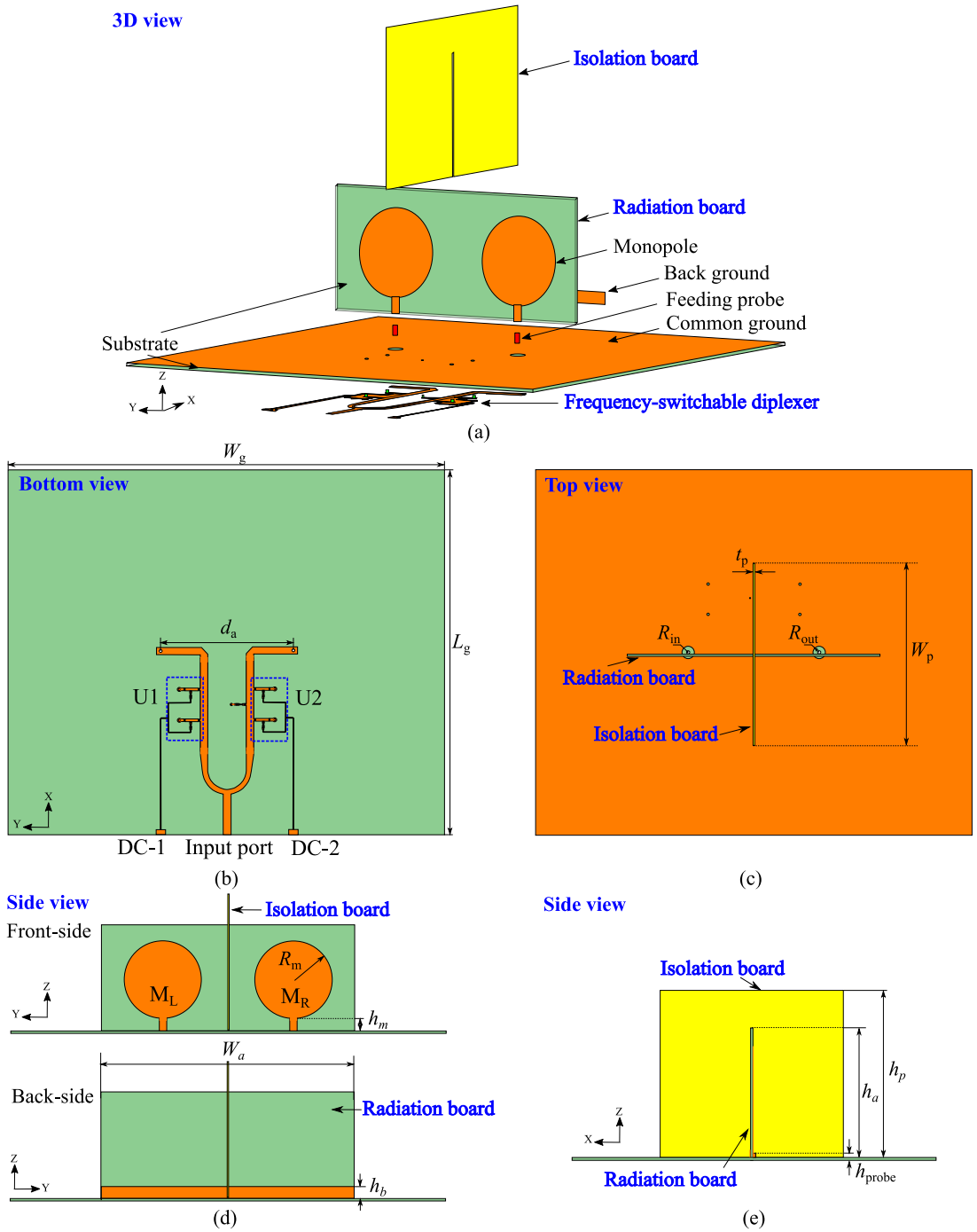

Figure 8.1. The configuration of the pattern- and frequency-reconfigurable array: (a) Exploded 3D perspective view of the whole array, (b) feeding network layout (bottom-view of the array), (c) top-view of the array, (d) side-view of the array with front and back structures of the monopole elements (YoZ plane), and (e) side-view of the array (XoZ plane). Critical dimensions are W_g = 143.0 mm, L_g = 120.0 mm, d_a = 43.0 mm, W_p = 60.0 mm, h_p = 45.0 mm, t_p = 1.0 mm, W_a = 83.0 mm, h_a = 35.0 mm, h_b = 4.0 mm,h_m = 4.1 mm, h_{probe} = 2.5 mm, R_m = 12.8 mm, R_{in} = 0.5 mm, and R_{out} = 2.0 mm.

of the substrate, and an isolation board cross-located in the middle of the two elements. The diplexer and radiation board are realized on two 0.76 mm thick substrates of Rogers Diclad 880 with relative permittivity of 2.2 and loss tangent of 0.0009, and they share a common ground. Each circular monopole element with a 50 Ω feeding microstrip line is excited by a copper probe which is connected to the diplexer on the other side of the substrate.

As shown in Fig. 8.1(b), the frequency-switchable diplexer is similar to the device presented in Chapter 7 with two 50 Ω extension microstrip lines to feed the monopole elements. The ground plane of the diplexer, denoted as common ground in Fig. 8.1(a), serves as the array ground as well. The frequency selective units, which are denoted as U1 and U2, have been validated in Chapter 7 with their frequency responses only depending on two separate DC voltages from a power supply. They are utilized in the frequency-switchable diplexer to electrically control two industrial, scientific, and medical (ISM) bands through the two signal paths individually, i.e., a low band from 2.4 to 2.5 GHz and a high band from 5.725 to 5.825 GHz. Two wideband monopoles, labelled as M_L and M_R, with a partial back ground on the other side of the radiation board as shown in Fig. 8.1(d), are chosen as the radiating elements, since they have bidirectional patterns when they operates together. The feeding of the monopoles M_L and M_R are separately controlled by U1 and U2 correspondingly. The distance between the two monopole elements is 43 mm corresponding to 0.83 wavelength in free space at 5.80 GHz and 0.35 wavelength in free space at 2.45 GHz. The two monopoles are separated by a vertical transverse isolation metallic plate, with the geometry shown in Figs. 8.1(c) and (e). The distance between the monopoles and the isolation plane are optimized to effectively realize the main beams pointing to the left or the right in endfire direction in the YoZ plane when the monopole elements are operating at different frequencies, with an unbalance larger than 10 dB between the maximum levels of their left and right radiation maxima for each directional pattern. Meanwhile, the optimized array is also able to operate with bidirectional patterns when the two elements are working at the same frequency.

8.2.2 Array Performance

As depicted in Fig. 8.2, the designed array aims to realize three operation modes, including Mode-1 with the left monopole (M_L) low-band and the right monopole (M_R)

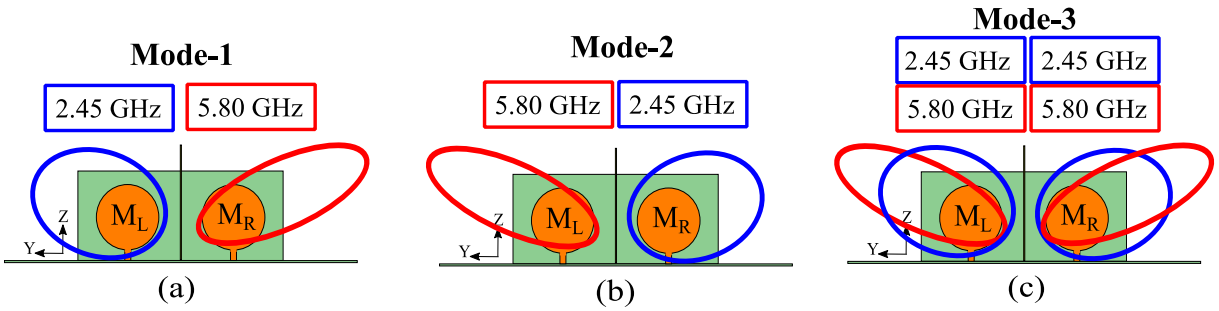

Figure 8.2. Three operation modes of the pattern- and frequency-reconfigurable antenna array, including (a) Mode-1, (b) Mode-2, and (c) Mode-3.

high-band patterns as shown in Fig. 8.2(a), Mode-2 with M_L high-band and M_R low-band patterns as shown in Fig. 8.2(b), and Mode-3 with dual-band operation in bidirectional patterns as shown in Fig. 8.2(c). To illustrate the general performance of the array, two typical frequencies in two bands, i.e., 2.45 GHz and 5.80 GHz, are utilized to describe the patterns states in three operation modes. It is worth to mention that the frequency-switchable diplexer can theoretically supply five operation modes to the array elements, which has been verified in Chapter 7. However, among the five operation modes, single low band, single high band and dual-band modes produce the same radiation patterns as Mode-3 at a fixed frequency. Therefore, without loss of generality, only the operation modes operating at dual frequencies are discussed in this array. The proposed pattern- and frequency-reconfigurable antenna array is simulated using Ansys HFSS 2021.

1) Reflection coefficient:

   The frequency selectivity of the frequency-switchable diplexer, has been verified in Chapter 7. Its S-parameter characteristics in the three modes are shown in Fig. 8.3. It can be seen that the operation bands in Mode-1 and Mode-2 are comprehensively determined by the reflection coefficients $|S_{11}|$, the insertion loss to each port $|S_{21}|$ or $|S_{31}|$, and the isolation levels $|S_{32}|$ at the unwanted frequencies. In addition, the bandwidth defined in Mode-3 is limited by the reflection coefficients $|S_{11}|$ and the insertion loss to each port $|S_{21}|$ and $|S_{31}|$. The specification of the isolation level at 2.45 GHz and 5.80 GHz is set as larger than 20 dB, while the loss added by the frequency selective unit is set as less than 1 dB, since it is empirically found that the determined bands are enough for completely covering the two ISM bands.

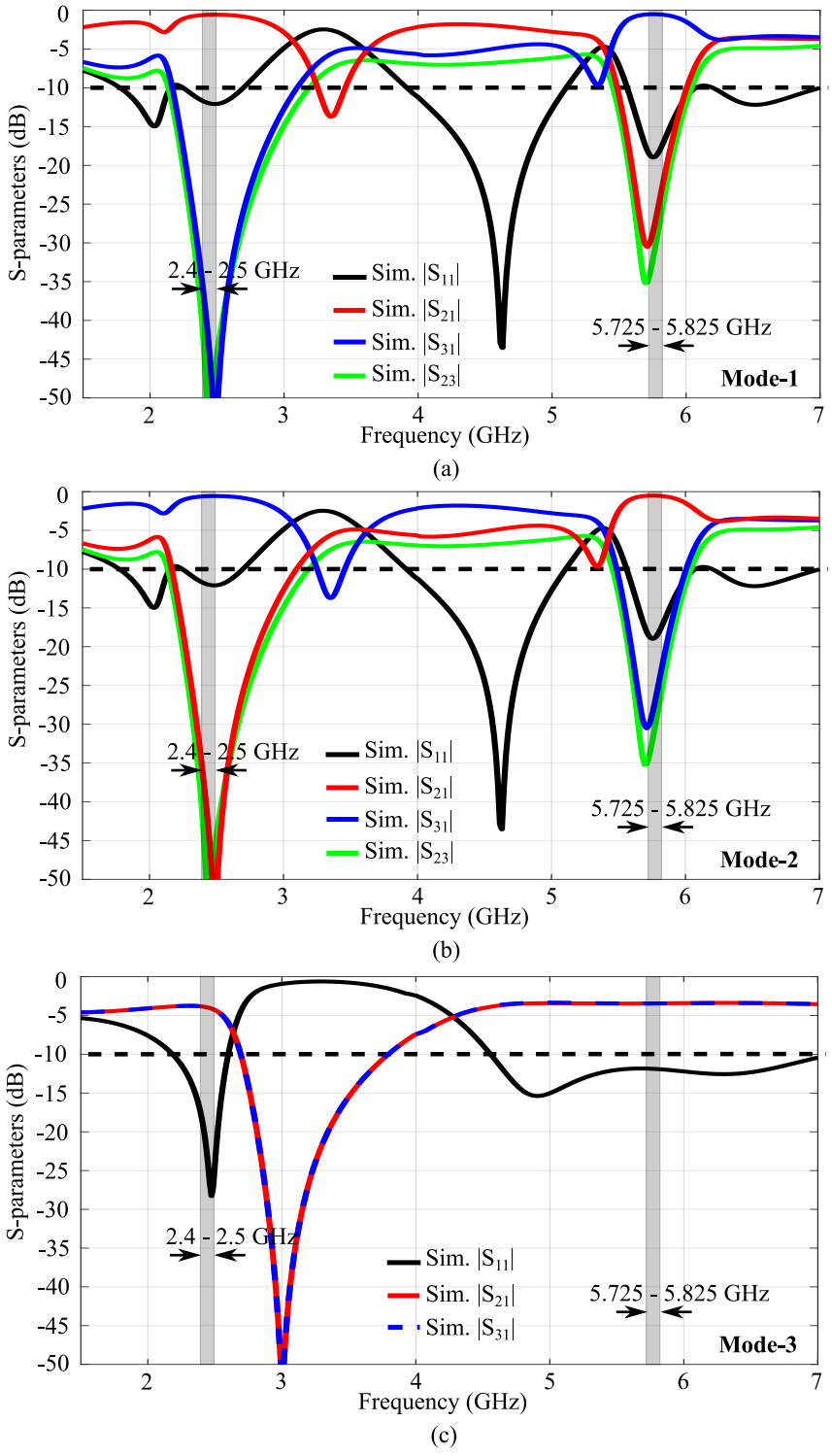

Figure 8.3. Simulated *S*-parameter characteristics of the frequency-switchable diplexer proposed in Chapter 7 for the three operation modes with two highlighted grey regions indicating the two ISM bands, i.e., the low band from 2.4 to 2.5 GHz and the high band from 5.725 to 5.825 GHz, (a) Mode-1, (b) Mode-2, and (c) Mode-3.

The simulated reflection coefficients of the single port antenna at the three mentioned modes are displayed in Fig. 8.4, and the operation bands in each working mode are listed in Table 8.1, as specified for a reflection coefficient lower than -10 dB, an insertion loss due to the frequency-selective unit of less than 1 dB and an isolation at 2.45 GHz and 5.80 GHz larger than 20 dB. It can be seen that the two desired ISM bands are completely covered at the three operation modes.

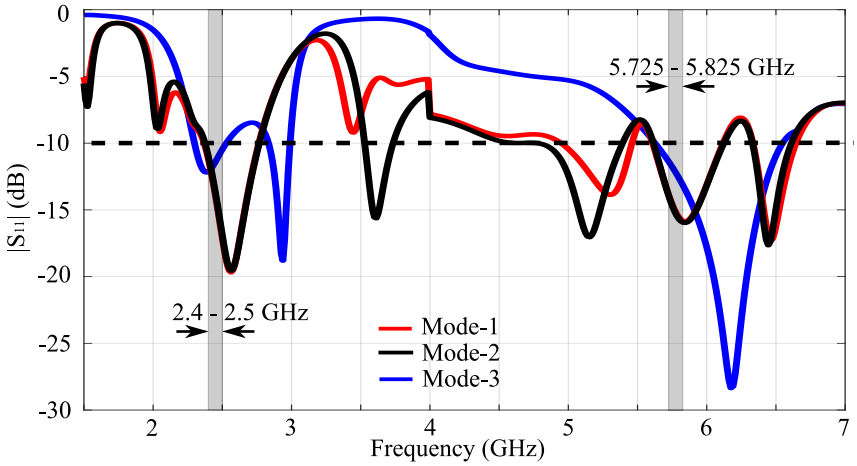

Figure 8.4. Simulated reflection coefficients for the three operation modes with two highlighted grey regions indicating the two ISM bands, i.e., the low band from 2.4 to 2.5 GHz and the high band from 5.725 to 5.825 GHz.

Table 8.1. Simulated operation bands of the pattern- and frequency-reconfigurable antenna array

Mode	C_{v1} (U1) (pF)	C_{v2} (U2) (pF)	M_L (GHz)	M_R (GHz)
1	0.15	1.30	2.38 - 2.76	5.62 - 6.11
2	1.30	0.15	5.62 - 6.11	2.38 - 2.76
3	0.70	0.70	2.30 -2.53, 5.63 - 6.53	2.30 -2.53, 5.63 - 6.53

2) 3D Radiation patterns:

The simulated 3D radiation patterns of the three operation modes in the YoZ plane at 2.45 and 5.80 GHz are depicted in Figs. 8.5(a), (b) and (c), respectively. In Mode-1, the simulation predicts that the main beam of the left monopole M_L working at the low band will point to the left while the pattern of the right monopole M_R working in the high band will point its main beam to the right

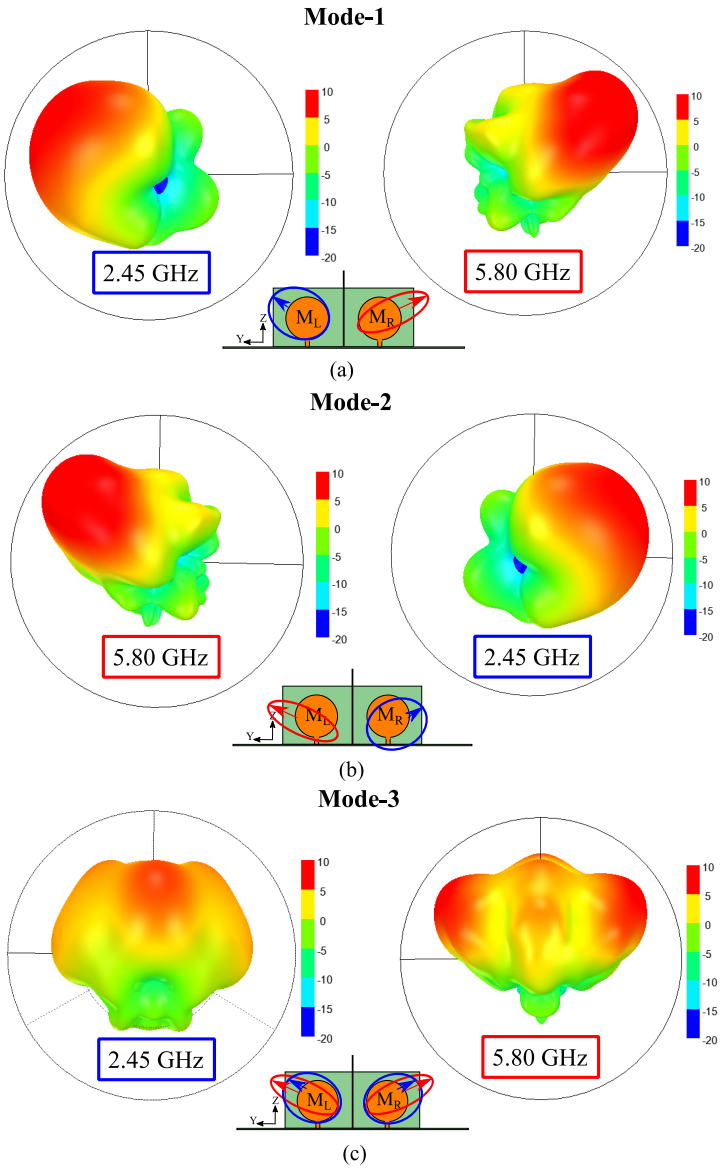

Figure 8.5. Simulated 3D radiation patterns of the array in YoZ plane for the three operation modes, including (a) Mode-1, (b) Mode-2, and (c) Mode-3.

direction, as illustrated in Fig. 8.5(a). Correspondingly, in Mode-2, the left directional pattern of M_L operates at high band and the right directional pattern of M_R is switched to low band as shown in Fig. 8.5(b). In dual-band Mode-3, two bidirectional patterns shown in Fig. 8.5(c) are obtained at both 2.45 and 5.80 GHz with two balanced left and right beams. Due to the monopoles M_L and M_R being able to swap their operation frequencies, as well as creating directional patterns or bidirectional patterns, this array is said to exhibit both pattern- and frequency-reconfigurabilities.

The simulated performance will be discussed in detail together with the measured results in Section 8.3.

8.3 Fabrication and Measurement

8.3.1 Array Prototype

The two-element pattern- and frequency-reconfigurable antenna array has been fabricated and experimentally characterized to validate the design. The array prototype is illustrated in Fig. 8.6. As shown in Fig. 8.6(a), the radiation board is fixed on the top of

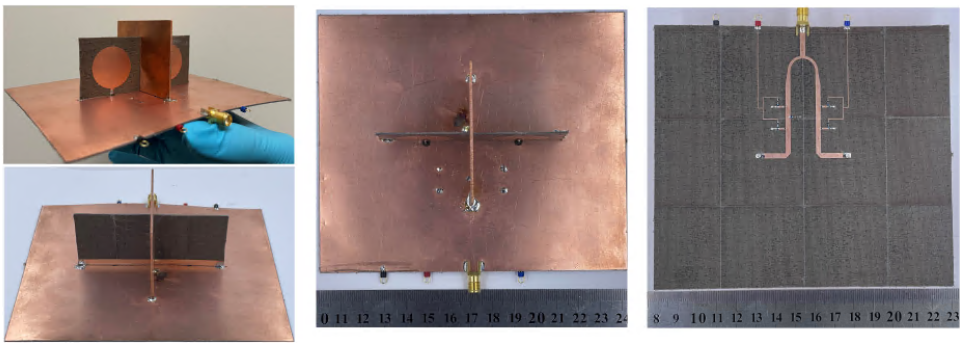

(a) (b) (c)

Figure 8.6. Photographs of the two-element pattern- and frequency-reconfigurable antenna array. (a) Front and back views of the radiation board, (b) top view and (c) bottom view of the array. The blue and dark red test pins are for DC bias circuit connections, and the black one is for the DC ground connection.

the diplexer board by connecting the two feeding probes onto the circular monopoles and soldering the back ground onto the common ground. The isolation board is standing in the middle and affixed with several soldering points on the common ground as depicted in Fig. 8.6(b). Three colored test pins are utilized to apply the bias voltages through thin DC lines.

8.3.2 Experimental Results

1) Reflection coefficient:

It is worth to mention that a similar on-board collection method, as proposed in Chapter 5, is required here to sample the magnitudes of the $|S_{21}|$ and $|S_{31}|$ parameters at the end of two signal branches. This data is collected and analyzed to

examine the insertion loss and check that the drop associated with the frequency-selective unit remains below 1 dB, together with an isolation level larger than 20 dB at 2.45 GHz and 5.80 GHz, which are important specifications to determine the corresponding working bands in the three operation modes.

The measured reflection coefficients are compared with the results obtained from the simulations in Fig. 8.4 at the three operation modes, which are illustrated in Fig. 8.7. Correspondingly, the simulation working bands in each mode are highlighted in red regions, and the measured operation bands are illustrated as blue regions, as also listed in Table 8.2.

Table 8.2. Measured operation bands of the pattern- and frequency-reconfigurable antenna array

Mode	$DC1$ (U1) (V)	$DC2$ (U2) (V)	M_L (GHz)	M_R (GHz)
1	16.0	0.9	2.39 - 2.57	5.70 - 6.12
2	0.9	14.2	5.71 - 6.12	2.39 - 2.57
3	1.8	1.5	2.38 -2.57, 5.00 - 6.14	2.30 -2.57, 5.57 - 6.12

It can be seen from Figs. 8.7(a), (b) and (c) that the proposed array can cover the required two ISM bands, i.e., the low band from 2.4 to 2.5 GHz and the high band from 5.725 to 5.825 GHz. The experimental data exhibits a reasonable qualitative agreement with the simulated results.

2) Radiation patterns:

The simulated and measured radiation patterns of the proposed array at 2.45 and 5.80 GHz in the three operation modes are displayed in Fig. 8.8.

Mode-1

When the array operates in Mode-1, the monopole M_L is excited at 2.45 GHz with a left pointing directional pattern, while the monopole M_R is working at 5.80 GHz with a right directional pattern, as illustrated in Fig. 8.8(a). The simulated difference between the left main beam and the right beam gain is 10.0 dB at 2.45 GHz, and the corresponding value is 12.1 dB at 5.80 GHz for the swapped patterns, i.e., between left beam gain and right main beam. The measured left-to-right ratios are 8.7 dB at 2.45 GHz and 12.7 dB at 5.80 GHz. The smaller left-to-right ratio at 2.45 GHz is due to the fabrication and measurement tolerance.

8.3.2 Experimental Results

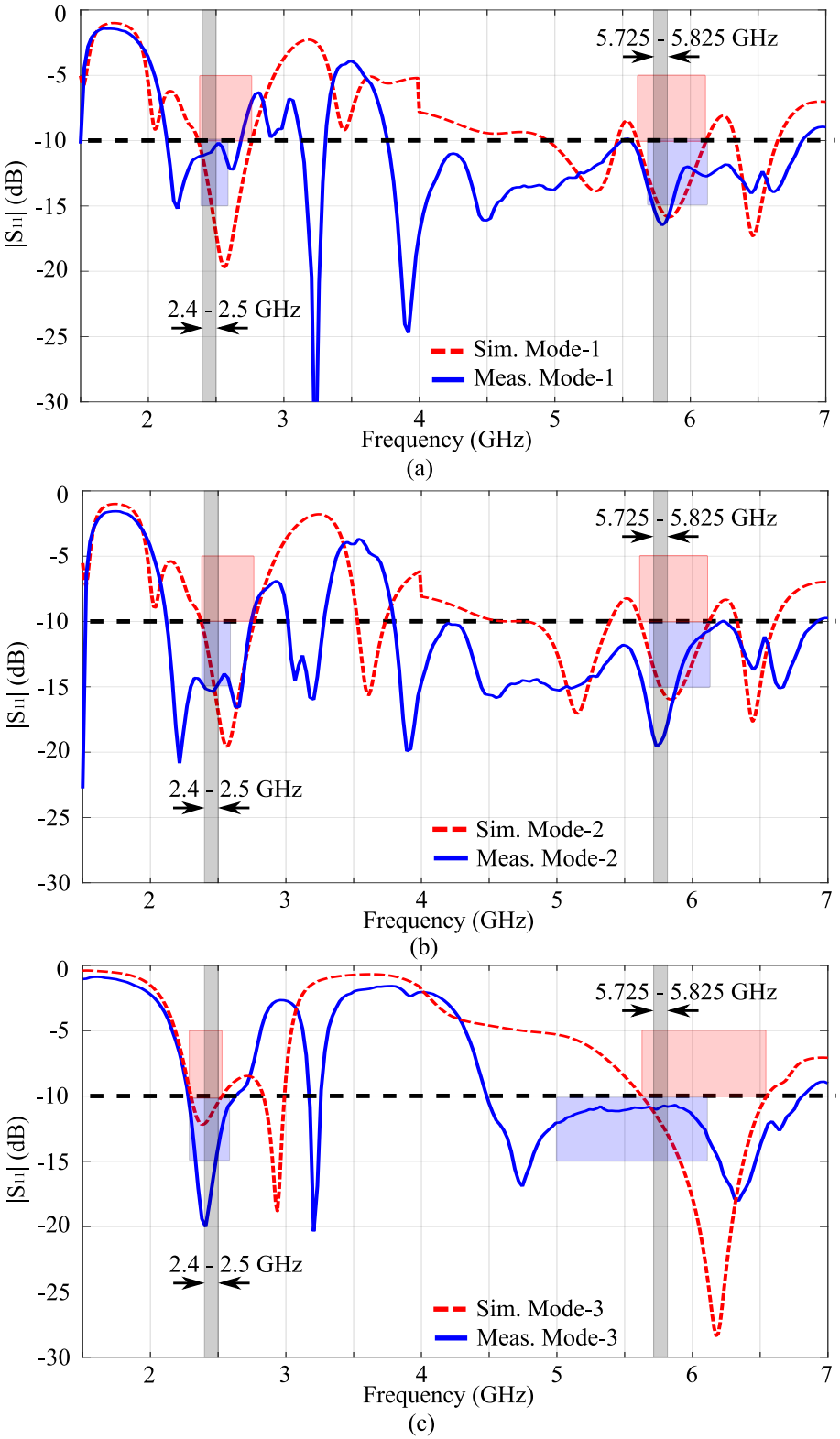

Figure 8.7. Measured and simulated reflection coefficients for three operation modes, i.e., (a) Mode-1, (b) Mode-2, and (c) Mode-3, with two highlighted grey regions indicating the two ISM bands, i.e., the low band from 2.4 to 2.5 GHz and the high band from 5.725 to 5.825 GHz.

Mode-2

Correspondingly, in Mode-2, the operation between the two monopoles is swapped, with monopole M_L operating at 5.80 GHz with a left directional pattern and monopole M_R being switched to 2.45 GHz with a right directional pattern, as shown in Fig. 8.8(b). In this scenario, the same simulated left-to-right ratios are observed as in Mode-1 due to symmetry, since the two modes has swapped the excitation between the two antennas. Measured left-to-right ratios are 12.1 dB at 5.80 GHz and 8.8 dB at 2.45 GHz. It is observed as expected that the patterns in Mode-1 and Mode-2 are mirror-symmetric.

Mode-3

As for dual-band Mode-3, two bidirectional patterns are produced at both 2.45 and 5.80 GHz with two beams pointing to endfire directions as shown in Fig. 8.8(c). The measured unbalance between the left and right beams are 1.26 dB and 0.33 dB at 2.45 and 5.80 GHz, respectively, which is attributed to the fabrication and measurement tolerance.

Cross-polarization

Simulated and measured normalized radiation patterns of the array in YoZ plane for three operation modes at 2.45 and 5.80 GHz are shown in Fig. 8.8. When the co-polarization pattern works in three modes expressing the pattern-reconfigurations, the simulated cross polarization levels in the three operation modes are less than -20 dB at 2.45 and 5.80 GHz. The measured cross polarization levels in the three operation modes are less than -17.8 dB at 2.45 GHz and -16.7 dB at 5.80 GHz.

3) Gain and efficiency:

The simulated realized gains are 5.93 dBi and 8.27 dBi at 2.45 and 5.80 GHz respectively in Mode-1, with corresponding total efficiencies of 92% and 93.5%. The same results are obtained when swapping the operation of the monopoles in Mode-2 as confirmed in simulation. In addition, the realized gains become 2.14 dBi and 5.80 dBi at 2.45 and 5.80 GHz respectively in Mode-3, with corresponding total efficiencies of 88% and 95.9%.

The measured realized gains are 5.90 dBi and 7.67 dBi at 2.45 and 5.80 GHz respectively in Mode-1, with corresponding total efficiencies of 91.4% and 81.5%.

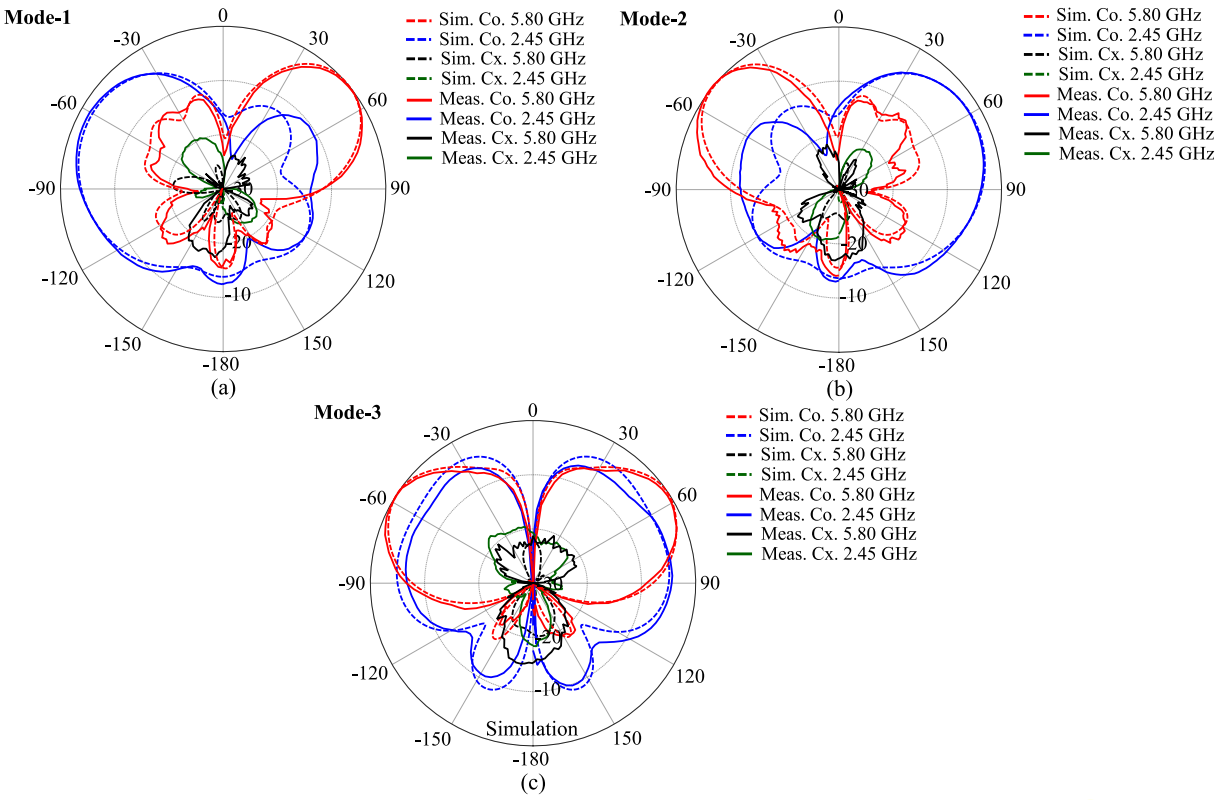

Figure 8.8. Simulated and measured normalized radiation patterns of the array in YoZ plane for three operation modes at 2.45 and 5.80 GHz. (a) Mode-1, (b) Mode-2, and (c) Mode-3.

Similarly, the measured realized gains in Mode-2 are 5.65 dBi and 7.82 dBi at 2.45 and 5.80 GHz respectively, with total efficiencies of 86.3% and 84.1%. Finally, the measured results yield realized gains of 1.76 dBi and 5.95 dBi at 2.45 and 5.80 GHz respectively in Mode-3, with corresponding total efficiencies of 81.0% and 99.1%.

A reasonable agreement is observed between the measured and simulated results, which successfully validate the array functionality as designed, with pattern and frequency reconfigurabilities achieved simultaneously.

8.4 Conclusion

A two-element pattern- and frequency-reconfigurable antenna array with unique functionality has been proposed in this chapter. The two elements are fed by a frequency-switchable diplexer that enables the array to adjust its working frequency on each monopole individually, which realizes the frequency reconfigurability of the array. Combining the effect of an isolation metallic board cross-located in-between the two

elements, two swappable directional patterns in opposite directions for the low- and high-band of operation can be produced, or alternatively bidirectional patterns at either band, illustrating the pattern reconfigurability of the array. A prototype of the array has been fabricated and measured to validate the concept. All measured results are in a reasonable agreement with simulated results, which have validated the pattern- and frequency-reconfigurable characteristics of the array.

By utilizing a frequency-switchable diplexer and an isolation board, the array achieves pattern- and frequency-reconfigurable performance simultaneously, without any other control circuits and electronic components on the antenna radiator structure. Such simple combination makes the array competitive as a compact and versatile reconfigurable antenna for low-cost communications applications.

Chapter 9

Thesis Summary and Conclusion

THE research on varactor-based reconfigurable microwave components presented in this thesis has been classified into three major parts, respectively dedicated to phase shifters, attenuators and diplexers. The first part has focused on a novel concept of varactor-based differential phase shifter pair and its application in a beam-steerable reconfigurable antenna array, with corresponding dedicated calibration procedure. In the second part, a series of tunable varactor-based transmission-type attenuators have been developed. Finally, the third part has presented a varactor-based frequency-switchable diplexer and its application in a two-element pattern- and frequency-reconfigurable antenna array. As the last chapter of this thesis, this chapter summarizes all these three self-contained parts and discusses possible related future works.

9.1 Summary Preamble

THE research presented in this dissertation has been mostly dedicated to varactor-based microwave devices, namely, differential phase shifter pairs, tunable transmission attenuators and frequency-switchable diplexers, and their related applications in reconfigurable antenna arrays. The self-contained contributions are correspondingly summarized in this chapter as three major topical parts. In addition, the potential possible further works in these three directions are suggested as well.

9.2 Varactor-Based Differential Phase Shifter Pair and Its Application

This major part of the thesis includes Chapters 3 to 5 which have focused on a novel varactor-based differential phase shifter pair, and its application as a feeding network in a beam-steerable reconfigurable antenna array. These three chapters have placed the emphasis on exploring appropriate approaches to achieve the maximum phase shift at the lowest complexity level. The proposed differential phase shifter pair was shown to produce a full 360° phase difference span. A pattern reconfigurable antenna array was designed with three such phase shifter pairs integrated in its feed, which enable its main beam to be steered from -45° to 45° continuously. This section summarizes the original contributions and considers promising future works.

9.2.1 Summary of Original Contributions

• Based on a novel concept of operation in differential mode, a varactor-based differential phase shifter pair has been proposed first, which consists of two identical phase-tuning units. The phase-tuning unit is realized on a 50 Ω microstrip transmission line with several varactor-loaded short-ended stubs standing on its edge. A full 360° phase shift range can be created by a pair of these phase-tuning units working in differential mode, which offers a low-loss and seamless integrable planar structure. Based on an accurate equivalent circuit model developed for this phase shifter unit, fast calculations are possible, thus allowing design and optimization of the structure with a genetic algorithm (GA). A pair of phase-tuning units equipped each with three varactor-loaded stubs has been identified

as a practical solution to supply a continuously tunable phase difference nearly covering 0° to 360°. To validate the design, a 3-stub phase-tuning unit prototype has been experimentally characterized. The measured results have shown the expected phase tuning range covering nearly 0° to 360° when the units are operated in pair, with two symmetrical 11°-wide blind zones, and a maximum insertion loss of 1.74 dB at 5.00 GHz and 2.04 dB from 4.75 to 5.25 GHz [48].

• To enhance the phase-tuning ability to a full 360° without any phase gaps, as well as to reduce the cost of the unit, an optimized phase-tuning unit has been further developed based on a similar topology. Compared to the original design, the optimized phase-tuning unit is realized on a substrate with lower permittivity and consists of two extra open-ended stubs located in between the three short-ended stubs. Therefore, the new device no longer requires isolation vias and it achieves a full 360° phase difference range with an insertion loss of less than 2.3 dB at 5 GHz. Experimental results have verified the successful operation of the enhanced phase shifter pair, demonstrating it as a promising phase shifter solution for compact and low-cost devices in microwave and antenna engineering [49].

• Based on 3D printing technology, a dielectric resonator antenna (DRA) with high polarization purity has been proposed. To reduce the cross-polarization level, an optimized T-shaped feeding structure instead of the conventional probe excitation has been employed. The T-shaped feeding structure was shown to effectively reduce the cross-polarization level to around -15 dB over the entire operational bandwidth from 4.75 to 5.25 GHz. The design outcomes built a crucial foundation for an antenna array exhibiting low cross-polarization level when utilizing the DRAs as elements [50].

• As a conceptual proof for the differential phase shifter pair technique, a 1 × 4 beam-steerable DRA array fed by a feeding network comprising three phase shifter pairs, has been then designed and fabricated to validate the practicality of the proposed differential phase shifter pairs. This phase shifter pair can be directly integrated with 50 Ω transmission lines of the feeding network, simplifying the beam control network structure significantly. The array operation was successfully demonstrated through sum-pattern scanning from -45° to 45° [48] and difference-pattern operation with null scanning from -30° to 30° [51]

• Before the experimental validation of the radiation patterns, a dedicated calibration procedure is required for the beam-steerable antenna controlled by varactor-based phase shifters operating in differential pairs. This accurate calibration procedure majorly involves two steps, one for the feeding network containing the differential phase shifter pairs, and the other for the remaining sections of the array including the radiating elements. The first step of the procedure considers the unconventional differential-phase control of the array and tolerances due to imperfect manufacture and components. Based on the performance curve of each phase-tuning unit, a fast selection algorithm has been used to set the control voltages for all differential phase shifter pairs according to the required phase differences. The final control voltages for a specific beam state have been validated and fine-tuned on-board at dedicated sampling points [51]. The second step of the calibration is so-called a pattern optimization approach, which is employed to correct degradation due to the fabrication tolerances of the radiating elements, which have not been considered in the first step. Such phase errors due to fabrication tolerance can be identified through analysing the ideal and measured radiation patterns. Then corresponding phase compensations are implemented to optimize the distorted pattern, based on the feeding network calibration and array factor analysis [52]. The beam-steerable antenna array has been measured under various scenarios following this calibration procedure, to verify its effectiveness in improving beam steering accuracy.

9.2.2 Future Work

Further simplification of the phase tuning unit

The optimized phase tuning unit has been implemented to produce a full 360° phase shift range in a differential pair. The evolved design was implemented on a low-cost substrate board, and removed the need of isolation vias used in original unit. This evolution reduces the difficulty of the fabrication to a certain extent. In order to further reduce the cost of design, based on the principle of 1/4 impedance transformation, the shorting vias at the end of the stubs can be replaced by extended microstrip lines, allowing to eliminate both the vias and the DC blocking capacitors, thus further simplifying the construction of the unit.

Automated design of the calibration procedure

An accurate two-step calibration procedure has been presented in this thesis. All the control voltages groups for various scenarios have been manipulated by hand from three stand-alone power supplies. The bias control could be automated with all combinations pre-measured and stored in a data processing component, e.g., a digital signal processing (DSP) chip or a field programmable gate arrays (FPGA) module. In this way, the rapid scanning of the antenna beam could be realized, laying a solid foundation for integration with complete microwave systems.

9.3 Varactor-Based Tunable Transmission-Type Attenuators

This part of the thesis consists of Chapter 6 which has described a series of tunable varactor-based transmission-type attenuators. This chapter has introduced approaches to push further the limitations in traditional transmission-type attenuator designs, including a restricted range of attenuation, elevated return loss, and high insertion loss (the minimal achievable attenuation level). This section summarizes the original contributions and considers related future works.

9.3.1 Summary of Original Contributions

- A varactor-based tunable transmission-type attenuator has been developed. It consists of a 50 Ω host microstrip line loaded with several edge-mounted shorted-end varactor-based stubs. The stubs are equipped with lumped components, including varactors, capacitors and resistors in order. The simple topology makes the attenuator a compact and low-loss structure, and allows seamless integration with 50 Ω microwave systems. A fast optimization of the structure with a GA has been proposed based on an accurate equivalent circuit for general attenuator modelling, which leads to an efficient design method. Comparing circuit-based results with full-wave simulations, a reasonable agreement has verified the accuracy of the equivalent circuit model.

- To validate the design, a series of attenuators with three to nine stubs have been developed following the proposed method. The design of multiple devices

allowed to investigate the achievable performance for different stub numbers. The proposed attenuators can produce continuously tunable attenuation levels of around 1 - 10 dB with 3 stubs, 2 - 20 dB with 6 stubs and 3 - 30 dB with 9 stubs at 5 GHz. Three prototypes have been fabricated and tested, namely devices with 3 identical stubs, 3 different stubs and 9 identical subs. The tested results show that the optimized 3-stub attenuators are able to supply attenuation up to 13.5 dB from 1.0 dB with a phase shift of less than 23.4°, while the 9-stub version can produce up to 32.7 dB attenuation with a relatively larger phase range up to 82.3°.

9.3.2 Future Work

Wide-band attenuator design strategy

The proposed attenuator concept has been demonstrated to allow a compact and flexible topology, which enables seamless integration into microwave circuitry with simple control circuit. It offers a continuous large attenuation tuning range with a small initial value of insertion loss, combined with relevant merits including small phase shift and good matching performance. However, the demonstrated operation band remained limited to a range extending from 4.75 to 5.25 GHz (10% bandwidth centered at 5.00 GHz). The lumped capacitors equipped on the short-ended stub between varactors and resistors, have been identified as a cause of the operation band limitation to some extent. By replacing these fixed capacitors by tunable ones, a frequency reconfigurable characteristics can be obtained. Therefore, a promising research subject can be employed to increase the operation band of the attenuator with frequency reconfigurability, while still maintaining the other performances nearly the same.

Combination of the attenuators with the differential phase shifters

As mentioned in Section 9.2, a differential phase shifter pair has been validated in a 1×4 beam-steerable antenna array, with sufficient phase difference for each beam scan scenario. To make the pattern reconfigurable antenna array more competitive, the phase and magnitude of the elements would need to be manipulated simultaneously, which can produce not only the capabilities of the beam scanning, but also the controls of the beamwidth and sidelode levels. Importantly, the proposed phase shifter pairs

and attenuators both could be seamlessly integrated together with 50 Ω microstrip lines, which would allow a relative compact structure of the feeding network with a slightly longer feeding lines.

9.4 Varactor-Based Frequency-Switchable Diplexer

This last part of the thesis includes Chapters 7 and 8 which have focused on a varactor-based frequency-switchable diplexer design. These chapters have developed approaches to match the input port in all operation modes, while maintaining a low coupling coefficient between the different channels, and exhibiting a simple and compact structure with low insertion loss. This section summarizes the original contributions and considers possible future works.

9.4.1 Summary of Original Contributions

• As an extension of the structural performance of the phase shifter unit, a varactor-based frequency-selective unit has been developed. The unit contains a 50 Ω host microstrip line loaded with two shunt varactor-loaded shorted-end varactor-based stubs. By varying the bias voltage, the frequency-selective unit can enable or disable specific frequencies passing through the microstrip transmission line, thus providing a frequency-selective functionality. To verify the concept, a prototype of the unit has been experimentally characterized. When voltages are set as 18 V and 0 V, the unit operates in low band from 1.50 to 3.04 GHz with maximum insertion loss of 0.77 dB, and high band from 4.47 to 7.00 GHz with insertion loss smaller than 0.87 dB, respectively. If the voltage is tuned to 6 V, it will work in dual band from 1.50 to 2.82 GHz and from 5.46 to 7.00 GHz with an insertion loss smaller than 1.16 dB. The reflection coefficients are all less than -10 dB. In addition, the stop-band suppression is appreciable when working at a single frequency: The amplitude of S_{21} is -28.2 dB at 5.8 GHz (DC = 18 V), while the value is -32.7 dB at 2.45 GHz (DC = 0 V).

• Based on the frequency-selective unit concept, a frequency-switchable diplexer has been proposed with unique functionality. The proposed diplexer is formed by two identical frequency-selective units which are integrated symmetrically on the two output branches of a T-junction equal-power divider. This arrangement

creates a frequency-switchable diplexer, which supplies five operation modes, aiming to cover two operation bands, i.e., a low band extending from 2.4 to 2.5 GHz and a high band covering 5.725 to 5.825 GHz. Correspondingly, the five operation modes can be described as: both channels on the low and high bands (high + low, high + low), both on the low band (low, low), both on the high band (high, high), one on the low and the other on the high band (low, high), and inversely, one on the high and the other on the low band (high, low). The prototype has been measured to validate the design. It is worth to emphasize that this frequency-switchable diplexer cannot only realize two specific frequencies working in different channels at a time, but it can also swap the working frequency on its two channels. This unique capability allows a symmetrical construction, which can reduce the design complexity for different frequencies. The diplexer can turn into a frequency reconfigurable equal-power divider, when applying the same voltages on the two units, allowing a multi-functional application as well [210].

• Utilizing the frequency reconfigurability of the diplexer, a two-element antenna array has been implemented which is fed by the frequency-switchable diplexer. The array has not only realized frequency reconfiguration enabled by the diplexer feeding network, but also achieved pattern reconfiguration enabled by a transverse metallic screen in the middle of the array. In this configuration, the antenna array has been verified to operate in three modes, i.e., a left directional pattern at 2.45 GHz + a right directional pattern at 5.80 GHz, a left directional pattern at 5.80 GHz + a right directional pattern at 2.45 GHz, and bidirectional patterns with dual-band performance. Utilizing the frequency-switchable diplexer feeding network and the isolation screen, the array achieves pattern- and frequency-reconfigurable performance simultaneously, which provides unique dual-band functionalities for compact and low-cost communications applications [210].

9.4.2 Future Work

Multi-port diplexer

The frequency selectivity is controlled by two bias voltages, which allows identical construction on each output branch. It is likely possible to combine three or more

equal-power dividers in series to create more output paths and realize multi-port frequency controls by integrating identical frequency-selective units on the branches. In such a design, it is anticipated that the last stage of equal-power dividers, where the frequency-selective units would be located, could be still T-junction dividers to achieve a good match at the common port. However, the first-stage divider which is used to connect the sub-diplexers, could be a Wilkinson equal-power divider to reach higher isolation between its output paths. This application will create additional operation modes to meet the requirements of multi-band scenarios in communications applications.

Multi-band frequency-switchable diplexer

Since the frequency-selective unit maintains the same topology as the phase-tuning unit, it is possible to expand the function of a frequency-selective unit by increasing the number of stubs. When the unit is loaded with three varactor-loaded short-ended stubs, additional operation bands could be excited, which could be controlled to some extent. Solving this challenging problem would open a possibility to obtain a multi-band frequency-switchable diplexer. In this case, a differential phase shifter pair would become a frequency-switchable diplexer, which will greatly enhance the functionality of this design concept for current multi-band and multi-functional communications applications.

9.5 Concluding Statement

For reconfigurable antenna arrays, individually controlling the amplitude and phase of each element is highly desirable to achieve various states of pattern reconfiguration, such as beam scanning or null steering. In addition, the ability of adjusting the operating frequency of the unit can further enhance the functionality of reconfigurable antenna arrays. Based on such application requirements, the research presented in this thesis has focused on three typical varactor-based reconfigurable microwave components, including phase shifters, attenuators and diplexers, as building blocks for reconfigurable feeding networks. Low-cost and compact reconfigurable antenna arrays can be realized using such feeding networks.

The reconfigurable microwave devices presented in this thesis, i.e., phase shifters, attenuators and diplexers, exhibit a range of advantages, including compact size, low-cost and low power consumption. Based on these devices, reconfigurable feeding networks can be created with multiple functionalities, including phase control, magnitude manipulation, and frequency selectivity. It is worth to emphasize that the three proposed reconfigurable microwave devices all employ a similar topology based on varactor-based stubs on a 50 Ω microstrip transmission line. This guarantees their compact and seamless integration with microstrip lines in a microwave feeding network. Therefore, reconfigurable antenna arrays excited by such feeding networks have the potential to achieve agility in muti-functional applications with low-cost planar microwave systems.

To conclude, it is envisioned that, the presented concept of utilizing tunable varactor-based microwave components to realize reconfigurable feeding networks for low-cost antenna arrays, and its evolutions can provide low-cost and versatile antenna solutions for advanced applications, including the internet-of-things (IoT) systems, wireless communications, remote sensing, radar systems, beamforming and multiple-input multiple-output (MIMO) systems.

Bibliography

[1] J. T. Bernhard, "Reconfigurable antennas," *Synthesis lectures on antennas*, vol. 2, no. 1, pp. 1–66, 2007.

[2] C. G. Christodoulou, Y. Tawk, S. A. Lane, and S. R. Erwin, "Reconfigurable antennas for wireless and space applications," *Proceedings of the IEEE*, vol. 100, no. 7, pp. 2250–2261, 2012.

[3] N. Hussain, A. Ghaffar, S. I. Naqvi, A. Iftikhar, D. E. Anagnostou, and H. H. Tran, "A conformal frequency reconfigurable antenna with multiband and wideband characteristics," *Sensors*, vol. 22, no. 7, p. 2601, 2022.

[4] T. Prakash, R. K. Chaudhary, and R. K. Gangwar, "Pattern-reconfigurable antenna in azimuth plane using sp3t reconfigurable switching network," *IET Microwaves, Antennas & Propagation*, vol. 15, no. 1, pp. 62–68, 2021.

[5] L. Ran, D.-P. Yang, and S.-Y. Wang, "A mode-combination-based polarization-reconfigurable antenna," *International Journal of RF and Microwave Computer-Aided Engineering*, vol. 32, no. 4, p. e23066, 2022.

[6] N. Nguyen-Trong, L. Hall, and C. Fumeaux, "A frequency-and polarization-reconfigurable stub-loaded microstrip patch antenna," *IEEE Transactions on Antennas and Propagation*, vol. 63, no. 11, pp. 5235–5240, 2015.

[7] S. N. M. Zainarry, N. Nguyen-Trong, and C. Fumeaux, "A frequency-and pattern-reconfigurable two-element array antenna," *IEEE Antennas and Wireless Propagation Letters*, vol. 17, no. 4, pp. 617–620, 2018.

[8] P. Thanki and F. Raval, "Fork-shaped frequency and pattern reconfigurable antenna," *International journal of communication systems*, vol. 33, no. 17, p. e4613, 2020.

[9] N. Ojaroudi Parchin, H. Jahanbakhsh Basherlou, Y. I. Al-Yasir, A. M. Abdulkhaleq, and R. A. Abd-Alhameed, "Reconfigurable antennas: Switching techniques—a survey," *Electronics*, vol. 9, no. 2, p. 336, 2020.

[10] A. Ebrahimi, G. Beziuk, K. Ghorbani, and F. Martin, "Tunable phase shifters using composite inductive-capacitive loaded slow-wave transmission lines," *AEU-International Journal of Electronics and Communications*, vol. 148, p. 154155, 2022.

[11] A. Bhattacharjee and S. Dwari, "Design of an anisotropic reconfigurable reflective polarization converter for realizing circular polarization-reconfigurable antenna," *IEEE Antennas and Wireless Propagation Letters*, vol. 21, no. 12, pp. 2392–2396, 2022.

[12] A. Ali, K. Topalli, M. Ramzan, M. Alibakhshikenari, T. M. Khan, A. Altintas, and P. Colantonio, "Optically reconfigurable planar monopole antenna for cognitive radio application," *Microwave and Optical Technology Letters*, vol. 61, no. 4, pp. 1110–1115, 2019.

[13] P. Lin, Y. Wu, Z. Wu, R. Zhuo, and J. Huangfu, "Optically switched multiband antenna based on vivaldi structure," *Scientific Reports*, vol. 12, no. 1, p. 15654, 2022.

[14] Y. Cao, P. Feng, and S. Yan, "Design of a pattern reconfigurable antenna for wide-angle scanning phased array applications," *Microwave and Optical Technology Letters*, vol. 64, no. 5, pp. 953–961, 2022.

[15] S. Fofana, B. Fuchs, S. Avrillon, F. Colombel, L. Leze, and S. Palud, "Reconfigurable antenna array with reduced power consumption—synthesis methods and experimental validations in s-band," *IEEE Transactions on Antennas and Propagation*, vol. 69, no. 4, pp. 2023–2030, 2020.

[16] Z. Ren, S.-S. Qi, and W. Wu, "Broadband pattern-reconfigurable water loop antenna, pattern-reconfigurable water loop antenna," *IET Microwaves, Antennas & Propagation*, vol. 15, no. 12, pp. 1618–1624, 2021.

[17] W. Zhang, Y. Li, and Z. Zhang, "A reconfigurable reflectarray antenna with an 8 μm-thick layer of liquid crystal," *IEEE Transactions on Antennas and Propagation*, vol. 70, no. 4, pp. 2770–2778, 2021.

[18] Y. Zhang, S. Lin, Z. Yang, B. Li, J. Cui, and J. Jiao, "A pattern-and frequency-reconfigurable antenna using liquid metal," *Microwave and Optical Technology Letters*, vol. 63, no. 5, pp. 1499–1506, 2021.

[19] H.-F. Wu, Y.-H. Wei, T.-R. Chen, and J.-S. Row, "Quad-polarization reconfigurable antenna with wideband operation," *Microwave and Optical Technology Letters*, vol. 61, no. 9, pp. 2080–2087, 2019.

[20] G.-P. Jin, M.-L. Li, Y.-C. Xu, J. Yang, and S.-W. Liao, "Differentially fed six-beam switchable reconfigurable antenna," *IET Microwaves, Antennas & Propagation*, vol. 14, no. 7, pp. 573–577, 2020.

[21] J. Zhang, S. Yan, and G. A. Vandenbosch, "Metamaterial-inspired dual-band frequency-reconfigurable antenna with pattern diversity," *Electronics Letters*, vol. 55, no. 10, pp. 573–574, 2019.

[22] M. Al Ahmad, S. Kabeer, A. A. Sanad, and L. J. Olule, "Compact single-varactor diode frequency-reconfigurable microstrip patch antenna," *IET Microwaves, Antennas & Propagation*, vol. 15, no. 9, pp. 1100–1107, 2021.

[23] S. Goel and N. Gupta, "Design, optimization and analysis of reconfigurable antenna using rf mems switch," *Microsystem Technologies*, vol. 26, pp. 2829–2837, 2020.

[24] K. S. Rao, P. Naveena, and K. G. Sravani, "Materials impact on the performance analysis and optimization of rf mems switch for 5g reconfigurable antenna," *Transactions on Electrical and Electronic Materials*, vol. 20, pp. 315–327, 2019.

[25] F. Amin, Y. Liu, Y. Zhao, and S. Hu, "Compact and low-loss phase shifters and multibit phase shifters based on inverted-e topology," *IEEE Transactions on Microwave Theory and Techniques*, vol. 69, no. 4, pp. 2120–2129, 2021.

[26] X. Li, H. Fu, K. Ma, and J. Hu, "A 2.4–4-ghz wideband 7-bit phase shifter with low rms phase/amplitude error in 0.5-μm gaas technology," *IEEE Transactions on Microwave Theory and Techniques*, vol. 70, no. 2, pp. 1292–1301, 2021.

[27] M. Yasir and P. Savi, "Commercial graphene nanoplatelets-based tunable attenuator," *Electronics letters*, vol. 56, no. 4, pp. 184–187, 2020.

[28] H. Chen, Z. G. Liu, W. B. Lu, A. Q. Zhang, and H. Chen, "A broadband tunable coaxial attenuator based on graphene," *IEEE Access*, vol. 7, pp. 127 593–127 599, 2019.

[29] S. I. Yahya, A. Rezaei, and L. Nouri, "Design and performance of microstrip diplexers: A review," *ARO-The Scientific Journal of Koya University*, vol. 8, no. 1, pp. 38–49, 2020.

[30] Z. Wei, X. Chen, X. Zhu, P.-L. Chi, R. Xu, and T. Yang, "Novel passive vector-sum amplitude-variable phase shifter with integrated reconfigurable filtering function," *IEEE Transactions on Microwave Theory and Techniques*, vol. 70, no. 7, pp. 3511–3523, 2022.

[31] H. Ren, M. Zhou, Y. Gu, and B. Arigong, "A tunable transmission line with controllable phase shifting and characteristic impedance," *IEEE Transactions on Circuits and Systems II: Express Briefs*, vol. 67, no. 10, pp. 1720–1724, 2019.

[32] M. Nikfalazar, A. Mehmood, M. Sohrabi, M. Mikolajek, A. Wiens, H. Maune, C. Kohler, J. R. Binder, and R. Jakoby, "Steerable dielectric resonator phased-array antenna based on inkjet-printed tunable phase shifter with bst metal-insulator-metal varactors," *IEEE Antennas and Wireless Propagation Letters*, vol. 15, pp. 877–880, 2015.

[33] Y. Ji, L. Ge, J. Wang, Q. Chen, W. Wu, and Y. Li, "Reconfigurable phased-array antenna using continuously tunable substrate integrated waveguide phase shifter," *IEEE Transactions on Antennas and Propagation*, vol. 67, no. 11, pp. 6894–6908, 2019.

[34] K. Park, S. Lee, and S. Jeon, "A new compact cmos distributed digital attenuator," *IEEE Transactions on Microwave Theory and Techniques*, vol. 68, no. 11, pp. 4631–4640, 2020.

[35] C. E. Saavedra and Y. Zheng, "Ring-hybrid microwave voltage-variable attenuator using hfet transistors," *IEEE transactions on microwave theory and techniques*, vol. 53, no. 7, pp. 2430–2434, 2005.

[36] M.-C. J. Chik and K.-K. M. Cheng, "A novel, varactor-based microwave attenuator with wide tuning ratio and flat insertion loss response," in *2014 IEEE MTT-S International Microwave Symposium (IMS2014)*. IEEE, 2014, pp. 1–3.

[37] K.-K. M. Cheng and M.-C. J. Chik, "A varactor-based variable attenuator design with enhanced linearity performance," *IEEE Transactions on Microwave Theory and Techniques*, vol. 63, no. 10, pp. 3191–3198, 2015.

[38] S. Roshani, S. I. Yahya, Y. S. Mezaal, M. A. Chaudhary, A. A. Al-Hilali, A. Mojirleilani, and S. Roshani, "Design of a compact quad-channel microstrip diplexer for l and s band applications," *Micromachines*, vol. 14, no. 3, p. 553, 2023.

[39] M.-H. Weng, C.-Y. Hung, and Y.-K. Su, "A hairpin line diplexer for direct sequence ultra-wideband wireless communications," *IEEE Microwave and Wireless Components Letters*, vol. 17, no. 7, pp. 519–521, 2007.

[40] C.-F. Chen, T.-Y. Huang, C.-P. Chou, and R.-B. Wu, "Microstrip diplexers design with common resonator sections for compact size, but high isolation," *IEEE Transactions on Microwave Theory and Techniques*, vol. 54, no. 5, pp. 1945–1952, 2006.

[41] M. Makimoto and S. Yamashita, "Bandpass filters using parallel coupled stripline stepped impedance resonators," *IEEE Transactions on microwave theory and techniques*, vol. 28, no. 12, pp. 1413–1417, 1980.

[42] C.-S. Ye, Y.-K. Su, M.-H. Weng, and C.-Y. Hung, "A microstrip ring-like diplexer for bluetooth and uwb application," *Microwave and Optical Technology Letters*, vol. 51, no. 6, pp. 1518–1520, 2009.

[43] Y.-Y. Bai, S. Xiao, M.-C. Tang, Z.-F. Ding, and B.-Z. Wang, "Wide-angle scanning phased array with pattern reconfigurable elements," *IEEE Transactions on Antennas and Propagation*, vol. 59, no. 11, pp. 4071–4076, 2011.

[44] M. W. Young, S. Yong, and J. T. Bernhard, "A miniaturized frequency reconfigurable antenna with single bias, dual varactor tuning," *IEEE Transactions on Antennas and Propagation*, vol. 63, no. 3, pp. 946–951, 2015.

[45] H. N. Chu and T.-G. Ma, "Beamwidth switchable planar microstrip series-fed slot array using reconfigurable synthesized transmission lines," *IEEE Transactions on Antennas and Propagation*, vol. 65, no. 7, pp. 3766–3771, 2017.

[46] A. Zohur, H. Mopidevi, D. Rodrigo, M. Unlu, L. Jofre, and B. A. Cetiner, "Rf mems reconfigurable two-band antenna," *IEEE Antennas and Wireless Propagation Letters*, vol. 12, pp. 72–75, 2013.

[47] P.-L. Chi, S.-S. Wu, and Y.-D. Lin, "Integrated antennas and diplexers for dual-band wireless local area network (wlan) system," in *2005 Asia-Pacific Microwave Conference Proceedings*, vol. 4, 2005, pp. 4 pp.–.

[48] Y. Yuan, S. J. Chen, and C. Fumeaux, "Varactor-based phase shifters operating in differential pairs for beam-steerable antennas," *IEEE Transactions on Antennas and Propagation*, vol. 70, no. 9, pp. 7670–7682, 2022.

[49] ——, "Varactor-based 360° differential phase shifter pair," in *2023 5th Australian Microwave Symposium (AMS)*. IEEE, 2023, pp. 29–30.

[50] ——, "A 3d-printed hybrid dielectric resonator antenna with low cross-polarization," in *2022 International Symposium on Antennas and Propagation (ISAP)*. IEEE, 2022, pp. 79–80.

[51] ——, "Calibrated design of beam-steerable antennas fed by varactor-based phase shifters," in *the 17th European Conference on Antennas Propagation (EuCAP)*. IEEE, 2023, pp. 79–80.

[52] ——, "Pattern optimization of beam-reconfigurable antenna fed by varactor-based phase shifters," in *The 8th edition of the IEEE RADIO international conference (RADIO)*. IEEE, 2023, pp. 79–80.

[53] Y.-W. Lin, Y.-C. Chou, and C.-Y. Chang, "A balanced digital phase shifter by a novel switching-mode topology," *IEEE transactions on Microwave Theory and Techniques*, vol. 61, no. 6, pp. 2361–2370, 2013.

[54] A. Malczewski, S. Eshelman, B. Pillans, J. Ehmke, and C. Goldsmith, "X-band rf mems phase shifters for phased array applications," *IEEE Microwave and Guided Wave Letters*, vol. 9, no. 12, pp. 517–519, 1999.

[55] B. Lakshminarayanan and T. Weller, "Design and modeling of 4-bit slow-wave mems phase shifters," *IEEE Transactions on Microwave Theory and Techniques*, vol. 54, no. 1, pp. 120–127, 2006.

[56] K. Miyaguchi, M. Hieda, K. Nakahara, H. Kurusu, M. Nii, M. Kasahara, T. Takagi, and S. Urasaki, "An ultra-broad-band reflection-type phase-shifter mmic with series and parallel lc circuits," *IEEE Transactions on Microwave Theory and Techniques*, vol. 49, no. 12, pp. 2446–2452, 2001.

[57] D.-W. Kang and S. Hong, "A 4-bit cmos phase shifter using distributed active switches," *IEEE transactions on microwave theory and techniques*, vol. 55, no. 7, pp. 1476–1483, 2007.

[58] K. T. Trinh, J. Feng, S. H. Shehab, and N. C. Karmakar, "1.4 ghz low-cost pin diode phase shifter for *L* -band radiometer antenna," *IEEE Access*, vol. 7, pp. 95 274–95 284, 2019.

[59] S. Pan, X. Ye, Y. Zhang, and F. Zhang, "Microwave photonic array radars," *IEEE Journal of Microwaves*, vol. 1, no. 1, pp. 176–190, 2021.

[60] T. Li, E. H. W. Chan, X. Wang, X. Feng, and B. Guan, "All-optical photonic microwave phase shifter requiring only a single dc voltage control," *IEEE Photonics Journal*, vol. 8, no. 4, pp. 1–8, 2016.

[61] K. Ghorbani, A. Mitchell, R. Waterhouse, and M. Austin, "A novel wide-band tunable rf phase shifter using a variable optical directional coupler," *IEEE Transactions on Microwave Theory and Techniques*, vol. 47, no. 5, pp. 645–648, 1999.

[62] A. Ebrahimi, G. Beziuk, K. Ghorbani, and F. Martin, "Tunable phase shifters using composite inductive-capacitive loaded slow-wave transmission lines," *AEU-International Journal of Electronics and Communications*, vol. 148, p. 154155, 2022.

[63] C. Boyd, "Ferrite rotary-field phase shifters: a survey of current technology and applications," in *1993 SBMO Int'l Microwave Conference/Brazil Proceedings*, 1993, pp. 305–310.

[64] A. Nafe and A. Shamim, "An integrable siw phase shifter in a partially magnetized ferrite ltcc package," *IEEE Transactions on Microwave Theory and Techniques*, vol. 63, no. 7, pp. 2264–2274, 2015.

[65] C. Ding, Y. J. Guo, P.-Y. Qin, T. S. Bird, and Y. Yang, "A defected microstrip structure (dms)-based phase shifter and its application to beamforming antennas," *IEEE Transactions on Antennas and Propagation*, vol. 62, no. 2, pp. 641–651, 2014.

[66] J. Tang, S. Xu, F. Yang, and M. Li, "Design of a wideband reconfigurable transmitarrray element using a novel phase shifter with varactors and pin diodes," in *2019 International Symposium on Antennas and Propagation (ISAP)*, 2019, pp. 1–2.

[67] F. Ellinger, H. Jackel, and W. Bachtold, "Varactor-loaded transmission-line phase shifter at c-band using lumped elements," *IEEE Transactions on Microwave Theory and Techniques*, vol. 51, no. 4, pp. 1135–1140, 2003.

[68] J. Tang, S. Xu, F. Yang, and M. Li, "Design and measurement of a reconfigurable transmitarray antenna with compact varactor-based phase shifters," *IEEE Antennas and Wireless Propagation Letters*, vol. 20, no. 10, pp. 1998–2002, 2021.

[69] T. Wang, W. Jiang, R. Divan, D. Rosenmann, L. E. Ocola, Y. Peng, and G. Wang, "Novel electrically tunable microwave solenoid inductor and compact phase shifter utilizing permaloy and pzt thin films," *IEEE Transactions on Microwave Theory and Techniques*, vol. 65, no. 10, pp. 3569–3577, 2017.

[70] N. Barker and G. Rebeiz, "Optimization of distributed MEMS transmission-line phase shifters-u-band and w-band designs," *IEEE Transactions on Microwave Theory and Techniques*, vol. 48, no. 11, pp. 1957–1966, 2000.

[71] S. A. Ibrahim, Z. Wang, and R. Farrell, "An MEMS phase shifter with high power handling for electronic beam tilt in base station antennas," *IEEE Microwave and Wireless Components Letters*, vol. 27, no. 3, pp. 269–271, 2017.

[72] M. Yasir, S. Bistarelli, A. Cataldo, M. Bozzi, L. Perregrini, and S. Bellucci, "Tunable phase shifter based on few-layer graphene flakes," *IEEE Microwave and Wireless Components Letters*, vol. 29, no. 1, pp. 47–49, 2019.

[73] W. Hu, D. Zhang, M. J. Lancaster, T. W. Button, and B. Su, "Investigation of ferroelectric thick-film varactors for microwave phase shifters," *IEEE Transactions on Microwave Theory and Techniques*, vol. 55, no. 2, pp. 418–424, 2007.

[74] B. Aja, E. Artal, E. Villa, L. de la Fuente, and J. P. Pascual, "Microstrip broadband thin-film attenuators without via-hole-ground at millimeter wave frequencies," *AEU-International Journal of Electronics and Communications*, vol. 100, pp. 119–126, 2019.

[75] J. Li, W. He, K.-D. Xu, J. Chen, and X. Y. Zhang, "Compact tunable broadband filtering attenuator based on variable resistors," *IEEE Microwave and Wireless Technology Letters*, pp. 1–4, 2023.

[76] C. L. Lez, R. Allanic, D. L. Berre, C. Quendo, R. Sauvage, A. Leuliet, T. Merlet, D. S. De Vasconcellos, V. Grimal, D. Valente, and J. Billoué, "Fully integrated bandpass filter with high isolation attenuator function using semi-conductor distributed doped areas," in *2022 Asia-Pacific Microwave Conference (APMC)*, 2022, pp. 443–445.

[77] C. Trent and T. Weller, "S-band reflection type variable attenuator," *IEEE Microwave and Wireless Components Letters*, vol. 12, no. 7, pp. 243–245, 2002.

[78] S. Bulja and A. Grebennikov, "Variable reflection-type attenuators based on varactor diodes," *IEEE Transactions on Microwave Theory and Techniques*, vol. 60, no. 12, pp. 3719–3727, 2012.

[79] Z. Wei, S. Chen, X. Zhu, P.-L. Chi, R. Xu, and T. Yang, "Reconfigurable filtering attenuator with continuously tunable center frequency and amplitude," in *2022 IEEE/MTT-S International Microwave Symposium - IMS 2022*, 2022, pp. 187–190.

[80] J. Chen, X. Wang, Z.-C. Lin, L. Li, and C. Fan, "Filtering power divider with tunable attenuation based on graphene nanoplates," *IEEE Microwave and Wireless Components Letters*, vol. 32, no. 8, pp. 960–963, 2022.

[81] Z. Liu, L. Zhu, and G. Xiao, "A novel microwave attenuator on multilayered substrate integrated waveguide," *IEEE Transactions on Components, Packaging and Manufacturing Technology*, vol. 6, no. 7, pp. 1106–1112, 2016.

[82] H. Chen, W.-B. Lu, Z.-G. Liu, and A.-Q. Zhang, "A review of dynamically tunable attenuators based on graphene," in *2019 IEEE MTT-S International Wireless Symposium (IWS)*, 2019, pp. 1–3.

[83] Z. Wang, Y. Fang, Q. Zhang, Z. Zhu, Z. Xie, H. Wang, and Q. Zhang, "A voltage controlled attenuator based on multilayer graphene," *IEEE Microwave and Wireless Technology Letters*, pp. 1–4, 2023.

[84] L. Ju, Z.-G. Liu, B.-Y. Yu, H. Chen, Z.-D. Xiao, and W.-B. Lu, "Stretchable and dynamically tunable attenuator based on graphene," *IEEE Transactions on Microwave Theory and Techniques*, vol. 70, no. 6, pp. 2999–3008, 2022.

[85] Z.-C. Lin, Y. Liu, L. Li, J. Li, J. Chen, J. Xu, and K.-D. Xu, "Dual-band bandpass filter with independently tunable attenuation characteristics using graphene nanoplates," *IEEE Transactions on Plasma Science*, vol. 50, no. 12, pp. 5031–5037, 2022.

[86] B. Wu, Y. Zhang, H. Zu, C. Fan, and W. Lu, "Tunable grounded coplanar waveguide attenuator based on graphene nanoplates," *IEEE Microwave and Wireless Components Letters*, vol. 29, no. 5, pp. 330–332, 2019.

[87] B. Pal, M. K. Mandal, M. Kahar, and S. Dwari, "Filtering attenuator with electronically tunable attenuation," in *2021 IEEE MTT-S International Microwave and RF Conference (IMARC)*, 2021, pp. 1–4.

[88] S.-H. Kim, K.-H. Son, E.-K. Kim, Y. Kim, and Y.-C. Yoon, "Attenuator using lossy left-handed transmission line and its applications," in *2009 Asia Pacific Microwave Conference*, 2009, pp. 681–684.

[89] A. Raeesi, H. Al-Saedi, A. Palizban, A. Taeb, W. M. Abdel-Wahab, S. Gigoyan, and S. Safavi-Naeini, "Low-cost planar rf mems-based attenuator," in *2019 IEEE MTT-S International Microwave Symposium (IMS)*, 2019, pp. 869–872.

[90] J. Iannacci, C. Tschoban, J. Reyes, U. Maaß, M. Huhn, I. Ndip, and H. Pötter, "Rf-mems for 5g mobile communications: A basic attenuator module demonstrated up to 50 ghz," in *2016 IEEE SENSORS*, 2016, pp. 1–3.

[91] W. Gosling, "Voltage controlled attenuators using field effect transistors," *IEEE Transactions on Audio*, vol. AU-13, no. 5, pp. 112–120, 1965.

[92] L. Gao, T.-W. Lin, and G. M. Rebeiz, "Design of tunable multi-pole multi-zero bandpass filters and diplexer with high selectivity and isolation," *IEEE Transactions on Circuits and Systems I: Regular Papers*, vol. 66, no. 10, pp. 3831–3842, 2019.

[93] T. Yang and G. M. Rebeiz, "Three-pole 1.3–2.4-ghz diplexer and 1.1–2.45-ghz dual-band filter with common resonator topology and flexible tuning capabilities," *IEEE Transactions on Microwave Theory and Techniques*, vol. 61, no. 10, pp. 3613–3624, 2013.

[94] A. Kursad Gorur, E. Dogan, C. Karpuz, and A. Gorur, "Design of tunable microstrip diplexer with reconfigurable filtering characteristics based on dual-mode square loop resonators," *IET Microwaves, Antennas & Propagation*, vol. 14, no. 13, pp. 1587–1594, 2020.

[95] J. Xu, "Compact switchable bandpass filter and its application to switchable diplexer design," *IEEE Microwave and Wireless Components Letters*, vol. 26, no. 1, pp. 13–15, 2016.

[96] S.-C. Weng, K.-W. Hsu, and W.-H. Tu, "Switchable and high-isolation diplexer with wide stop-band," *IEEE microwave and wireless components letters*, vol. 24, no. 6, pp. 373–375, 2014.

[97] S. N. M. Zainarry, N. Nguyen-Trong, and C. Fumeaux, "A frequency- and pattern-reconfigurable two-element array antenna," *IEEE Antennas and Wireless Propagation Letters*, vol. 17, no. 4, pp. 617–620, 2018.

[98] Y. P. Selvam, M. Kanagasabai, M. G. N. Alsath, S. Velan, S. Kingsly, S. Subbaraj, Y. V. Ramana Rao, R. Srinivasan, A. K. Varadhan, and M. Karuppiah, "A low-profile frequency- and pattern-reconfigurable antenna," *IEEE Antennas and Wireless Propagation Letters*, vol. 16, pp. 3047–3050, 2017.

[99] H. A. Majid, M. K. A. Rahim, M. R. Hamid, and M. F. Ismail, "Frequency and pattern reconfigurable slot antenna," *IEEE Transactions on Antennas and Propagation*, vol. 62, no. 10, pp. 5339–5343, 2014.

[100] M. Nikfalazar, A. Mehmood, M. Sohrabi, M. Mikolajek, A. Wiens, H. Maune, C. Kohler, J. R. Binder, and R. Jakoby, "Steerable dielectric resonator phased-array antenna based on inkjet-printed tunable phase shifter with BST Metal-Insulator-Metal varactors," *IEEE Antennas and Wireless Propagation Letters*, vol. 15, pp. 877–880, 2016.

[101] Y. Ji, L. Ge, J. Wang, Q. Chen, W. Wu, and Y. Li, "Reconfigurable phased-array antenna using continuously tunable substrate integrated waveguide phase shifter," *IEEE Transactions on Antennas and Propagation*, vol. 67, no. 11, pp. 6894–6908, 2019.

[102] A. Ohadi and G. V. Eleftheriades, "A continuously tunable phase shifter using surface waves," *IEEE Journal of Microwaves*, vol. 1, no. 4, pp. 989–996, 2021.

[103] S. Sheng, H. Chen, J. Wen, and H. Liu, "Simulation and fabrication of broadband tunable phase shifter based on transmission line metamaterial," *Radioengineering*, vol. 28, no. 3, pp. 585–590, 2019.

[104] P. Li, J. Niu, J. Fu, W. Chen, B. Lv, Z. Wang, and A. Li, "A novel 360° continuously tunable phase shifter based on varactor-loaded CRLH transmission line at exact 2.4 GHz," *Proceedings of 2016 IEEE International Conference on Electronic Information and Communication Technology, ICEICT 2016*, no. Iceict, pp. 583–585, 2017.

[105] R. Bourtoutian and P. Ferrari, "Tapered distributed analogue tunable phase shifter with low insertion and return loss," *Electronics Letters*, vol. 41, no. 15, pp. 852–854, 2005.

[106] A. Singh and M. K. Mandal, "Electronically tunable reflection type phase shifters," *IEEE Transactions on Circuits and Systems II: Express Briefs*, vol. 67, no. 3, pp. 425–429, 2020.

[107] C. S. Lin, S. F. Chang, and W. C. Hsiao, "A full-360° reflection-type phase shifter with constant insertion loss," *IEEE Microwave and Wireless Components Letters*, vol. 18, no. 2, pp. 106–108, 2008.

[108] H. Ren, M. Zhou, Y. Gu, and B. Arigong, "A tunable transmission line with controllable phase shifting and characteristic impedance," *IEEE Transactions on Circuits and Systems II: Express Briefs*, vol. 67, no. 10, pp. 1720–1724, 2020.

[109] N. Nguyen-Trong, T. Kaufmann, L. Hall, and C. Fumeaux, "Analysis and design of a reconfigurable antenna based on half-mode substrate-integrated cavity," *IEEE Transactions on Antennas and Propagation*, vol. 63, no. 8, pp. 3345–3353, 2015.

[110] T. C. Edwards and M. B. Steer, *Transmission Line Theory*, 2016, pp. 76–88.

[111] K. Gupta, R. Garg, and I. Bahl, *Microstrip lines and slotlines (Dedham, MA: Artech House)*. Inc, 1979.

[112] D. Frickey, "Conversions between s, z, y, h, abcd, and t parameters which are valid for complex source and load impedances," *IEEE Transactions on Microwave Theory and Techniques*, vol. 42, no. 2, pp. 205–211, 1994.

[113] M. Abramson, "Genetic algorithm and direct search toolbox user's guide for use with matlab," *The MathWorks*, 2004.

[114] J. Costantine, Y. Tawk, S. E. Barbin, and C. G. Christodoulou, "Reconfigurable antennas: Design and applications," *Proceedings of the IEEE*, vol. 103, no. 3, pp. 424–437, 2015.

[115] K. Paramayudha, S. J. Chen, T. Kaufmann, W. Withayachumnankul, and C. Fumeaux, "Triple-band reconfigurable low-profile monopolar antenna with independent tunability," *IEEE Open Journal of Antennas and Propagation*, vol. 1, pp. 47–56, 2020.

[116] Q. H. Dang, S. J. Chen, D. C. Ranasinghe, and C. Fumeaux, "A frequency-reconfigurable wearable textile antenna with one octave tuning range," *IEEE Transactions on Antennas and Propagation*, 2021.

[117] M. W. Young, S. Yong, and J. T. Bernhard, "A miniaturized frequency reconfigurable antenna with single bias, dual varactor tuning," *IEEE Transactions on Antennas and Propagation*, vol. 63, no. 3, pp. 946–951, 2015.

[118] R. Li, H. Yang, B. Liu, Y. Qin, and Y. Cui, "Theory and realization of a pattern-reconfigurable antenna based on two dipoles," *IEEE Antennas and Wireless Propagation Letters*, vol. 17, no. 7, pp. 1291–1295, 2018.

[119] W. Zhang, Y. Li, Z. Zhang, and Z. Feng, "A pattern-reconfigurable aircraft antenna with low wind drag," *IEEE Transactions on Antennas and Propagation*, vol. 68, no. 6, pp. 4397–4405, 2020.

[120] H. Tian, L. Jiang, and T. Itoh, "A compact single-element pattern reconfigurable antenna with wide-angle scanning tuned by a single varactor," *Progress In Electromagnetics Research C*, vol. 92, no. April, pp. 137–150, 2019.

[121] L. Kang, H. Li, J. Zhou, S. Zheng, and S. Gao, "A mode-reconfigurable orbital angular momentum antenna with simplified feeding scheme," *IEEE Transactions on Antennas and Propagation*, vol. 67, no. 7, pp. 4866–4871, 2019.

[122] N. Zhu, X.-X. Yang, T. Lou, Q. Cao, and S. Gao, "Broadband polarization-reconfigurable slot antenna and array with compact feed network," *IEEE Antennas and Wireless Propagation Letters*, vol. 18, no. 6, pp. 1293–1297, 2019.

[123] L. Kang, H. Li, B. Tang, X. Wang, and J. Zhou, "Quad-polarization-reconfigurable antenna with a compact and switchable feed," *IEEE Antennas and Wireless Propagation Letters*, vol. 20, no. 4, pp. 548–552, 2021.

[124] L. Ge, Y. Li, J. Wang, and C. Y. D. Sim, "A low-profile reconfigurable cavity-backed slot antenna with frequency, polarization, and radiation pattern agility," *IEEE Transactions on Antennas and Propagation*, vol. 65, no. 5, pp. 2182–2189, 2017.

[125] N. Nguyen-Trong, L. Hall, and C. Fumeaux, "A frequency-and polarization-reconfigurable stub-loaded microstrip patch antenna," *IEEE Transactions on Antennas and Propagation*, vol. 63, no. 11, pp. 5235–5240, 2015.

[126] A. Iftikhar, J. M. Parrow, S. M. Asif, A. Fida, J. Allen, M. Allen, B. D. Braaten, and D. E. Anagnostou, "Characterization of novel structures consisting of micron-sized conductive particles that respond to static magnetic field lines for 4G/5G (Sub-6 GHz) reconfigurable antennas," *Electronics (Switzerland)*, vol. 9, no. 6, p. 908, 2020.

[127] G. Jin, M. Li, D. Liu, and G. Zeng, "A simple planar pattern-reconfigurable antenna based on arc dipoles," *IEEE Antennas and Wireless Propagation Letters*, vol. 17, no. 9, pp. 1664–1668, 2018.

[128] M. S. Alam and A. M. Abbosh, "Beam-steerable planar antenna using circular disc and four PIN-controlled tapered stubs for WiMAX and WLAN applications," *IEEE Antennas and Wireless Propagation Letters*, vol. 15, pp. 980–983, 2016.

[129] F. A. Asadallah, J. Costantine, and Y. Tawk, "A digitally tuned reconfigurable semi-bowtie antenna for IoT devices," *IET Conference Publications*, vol. 2018, no. CP741, pp. 917–918, 2018.

[130] L. H. Trinh, T. N. Le, R. Staraj, F. Ferrero, and L. Lizzi, "A pattern-reconfigurable slot antenna for IoT network concentrators," *Electronics (Switzerland)*, vol. 6, no. 4, pp. 1–7, 2017.

[131] L. Santamaria, F. Ferrero, R. Staraj, and L. Lizzi, "Slot-based pattern reconfigurable ESPAR antenna for IoT applications," *IEEE Transactions on Antennas and Propagation*, no. c, pp. 1–10, 2020.

[132] P. Liu, Y. Li, and Z. Zhang, "Circularly polarized 2 bit reconfigurable beam-steering antenna array," *IEEE Transactions on Antennas and Propagation*, vol. 68, no. 3, pp. 2416–2421, 2020.

[133] H. Li, M. Wu, S. Yuan, and C. Zhou, "Design of off-center fed windmill loop for pattern reconfiguration," *IEEE Antennas and Wireless Propagation Letters*, vol. 18, no. 8, pp. 1626–1630, 2019.

[134] L. Santamaria, F. Ferrero, R. Staraj, and L. Lizzi, "Slot-based pattern reconfigurable ESPAR antenna for IoT applications," *IEEE Transactions on Antennas and Propagation*, no. c, pp. 1–10, 2020.

[135] W. Gao, S. J. Chen, W. Withayachumnankul, and C. Fumeaux, "Horizontally polarized 360° beam-steerable frequency-reconfigurable antenna," *IEEE Transactions on Antennas and Propagation*, vol. 67, no. 8, pp. 5231–5242, 2019.

[136] S. Cheng, E. Öjefors, P. Hallbjörner, and A. Rydberg, "Compact reflective microstrip phase shifter for traveling wave antenna applications," *IEEE Microwave and Wireless Components Letters*, vol. 16, no. 7, pp. 431–433, 2006.

[137] H. Wang, Y. Wang, J. Wu, P. Chen, Z. Wu, C. Y. D. Sim, and G. Yang, "Small-size reconfigurable loop antenna for mobile phone applications," *IEEE Access*, vol. 4, pp. 5179–5186, 2016.

[138] H. Pan, J. T. Bernhard, and V. K. Nair, "Reconfigurable single-armed square spiral microstrip antenna design," *2006 IEEE International Workshop on Antenna Technology, IWAT 2006 - Small Antennas and Novel Metamaterials*, vol. 2006, no. 1, pp. 180–183, 2006.

[139] "A reconfigurable microstrip leaky-wave antenna with a broadly steerable beam," *IEEE Transactions on Antennas and Propagation*, vol. 59, no. 8, pp. 3080–3083, 2011.

[140] J. Hu, Y. Li, and Z. Zhang, "A novel reconfigurable miniaturized phase shifter for 2-d beam steering 2-bit array applications," *IEEE Microwave and Wireless Components Letters*, vol. 31, no. 4, pp. 381–384, 2021.

[141] C. Ding, Y. J. Guo, P. Y. Qin, T. S. Bird, and Y. Yang, "A defected microstrip structure (DMS)-based phase shifter and its application to beamforming antennas," *IEEE Transactions on Antennas and Propagation*, vol. 62, no. 2, pp. 641–651, 2014.

[142] C. Ding, Y. J. Guo, P.-Y. Qin, and Y. Yang, "A compact microstrip phase shifter employing reconfigurable defected microstrip structure (RDMS) for phased array antennas," *IEEE Transactions on Antennas and Propagation*, vol. 63, no. 5, pp. 1985–1996, 2015.

[143] A. Petosa, *Dielectric resonator antenna handbook*. Artech, 2007.

[144] S. Keyrouz and D. Caratelli, "Dielectric resonator antennas: basic concepts, design guidelines, and recent developments at millimeter-wave frequencies," *Int. J. Antennas Propag.*, vol. 2016, 2016.

[145] A. S. Al-Zoubi, A. A. Kishk, and A. W. Glisson, "A linear rectangular dielectric resonator antenna array fed by dielectric image guide with low cross polarization," *IEEE Trans. Antennas Propag.*, vol. 58, no. 3, pp. 697–705, 2009.

[146] X.-Y. Wang, S.-C. Tang, and J.-X. Chen, "Differential-fed pattern-reconfigurable dielectric patch antenna and array with low cross-polarization," *IEEE Trans. Antennas Propag.*, 2021.

[147] J. Huang, S. J. Chen, Z. Xue, W. Withayachumnankul, and C. Fumeaux, "Wideband endfire 3-d-printed dielectric antenna with designable permittivity," *IEEE Antennas and Wireless Propagation Letters*, vol. 17, no. 11, pp. 2085–2089, 2018.

[148] A. Petosa, *Dielectric resonator antenna handbook*. Artech, 2007.

[149] J. Huang, S. J. Chen, Z. Xue, W. Withayachumnankul, and C. Fumeaux, "Impact of infill pattern on 3d printed dielectric resonator antennas," in *2018 IEEE Asia-Pacific Conference on Antennas and Propagation (APCAP)*, 2018, pp. 233–235.

[150] Y.-F. Cheng, X. Ding, W. Shao, and B.-Z. Wang, "Planar wide-angle scanning phased array with pattern-reconfigurable windmill-shaped loop elements," *IEEE Transactions on Antennas and Propagation*, vol. 65, no. 2, pp. 932–936, 2016.

[151] S. Yong and J. T. Bernhard, "Reconfigurable null scanning antenna with three dimensional null steer," *IEEE transactions on antennas and propagation*, vol. 61, no. 3, pp. 1063–1070, 2012.

[152] M. Wang, H. F. Ma, H. C. Zhang, W. X. Tang, X. R. Zhang, and T. J. Cui, "Frequency-fixed beam-scanning leaky-wave antenna using electronically controllable corrugated microstrip line," *IEEE transactions on antennas and propagation*, vol. 66, no. 9, pp. 4449–4457, 2018.

[153] Y. Ji, L. Ge, J. Wang, Q. Chen, W. Wu, and Y. Li, "Reconfigurable phased-array antenna using continuously tunable substrate integrated waveguide phase shifter," *IEEE Transactions on Antennas and Propagation*, vol. 67, no. 11, pp. 6894–6908, 2019.

[154] T. Takahashi, Y. Konishi, S. Makino, H. Ohmine, and H. Nakaguro, "Fast measurement technique for phased array calibration," *IEEE Transactions on Antennas and Propagation*, vol. 56, no. 7, pp. 1888–1899, 2008.

[155] R. Long, J. Ouyang, F. Yang, W. Han, and L. Zhou, "Fast amplitude-only measurement method for phased array calibration," *IEEE transactions on antennas and propagation*, vol. 65, no. 4, pp. 1815–1822, 2016.

[156] J. Geiss, E. Sippel, M. Hehn, and M. Vossiek, "Antenna array calibration using a sparse scene," *IEEE Open Journal of Antennas and Propagation*, vol. 2, pp. 349–361, 2021.

[157] B. M. Fabiani, F. F. Oliveira, J. M. Vieira, E. S. Sakomura, E. S. Silveira, D. C. Nascimento, and D. B. Ferreira, "Closed-loop controlled microwave beamformer," *International Journal of RF and Microwave Computer-Aided Engineering*, vol. 32, no. 3, p. e23020, 2022.

[158] S. Bulja and A. Grebennikov, "Pin diode-based variable directional coupler," *Microwave and Optical Technology Letters*, vol. 54, no. 11, pp. 2643–2646, 2012.

[159] S.-W. Jeong and J. Lee, "Frequency- and bandwidth-tunable bandstop filter containing variable coupling between transmission line and resonator," *IEEE Transactions on Microwave Theory and Techniques*, vol. 66, no. 2, pp. 943–953, 2018.

[160] T. Singh and R. R. Mansour, "Miniaturized reconfigurable 28 GHz PCM-based 4-bit latching variable attenuator for 5G mmwave applications," in *2020 IEEE/MTT-S International Microwave Symposium (IMS)*, 2020, pp. 53–56.

[161] Z. Wang, Z. Li, X. Wang, X. Cheng, Z. Li, and Y. Zhuang, "A 6–18 GHz high dB-linear attenuator based on variable gain amplifier for ultra-wideband phased array systems," *Microwave and Optical Technology Letters*, vol. 64, no. 2, pp. 231–236, 2022.

[162] D. P. Nguyen, B. L. Pham, and A.-V. Pham, "A 1.5–45-GHz high-power 2-D distributed voltage-controlled attenuator," *IEEE Transactions on Microwave Theory and Techniques*, vol. 65, no. 11, pp. 4208–4217, 2017.

[163] B. Aja, E. Artal, E. Villa, L. de la Fuente, and J. P. Pascual, "Microstrip broadband thin-film attenuators without via-hole-ground at millimeter wave frequencies," *AEU-International Journal of Electronics and Communications*, vol. 100, pp. 119–126, 2019.

[164] J. Haidar, A. Vilcot, and M. Bouthinon, "Optically tunable microwave attenuator using a quarter-wave microstrip coupler," *Microwave and Optical Technology Letters*, vol. 10, no. 6, pp. 313–314, 1995.

[165] J. R. Flemish and R. L. Haupt, "Optimization of a photonically controlled microwave switch and attenuator," *IEEE Transactions on Microwave Theory and Techniques*, vol. 58, no. 10, pp. 2582–2588, 2010.

[166] A.-Q. Zhang, W.-B. Lu, Z.-G. Liu, and H. Chen, "A tunable attenuator based on a graphene-loaded coupled microstrip line," *IEEE Transactions on Microwave Theory and Techniques*, vol. 68, no. 3, pp. 939–950, 2020.

[167] W.-T. Kang, I.-S. Chang, and M.-S. Kang, "Reflection-type low-phase-shift attenuator," *IEEE Transactions on Microwave Theory and Techniques*, vol. 46, no. 7, pp. 1019–1021, 1998.

[168] N. K. Khaira, T. Singh, and R. R. Mansour, "Monolithically integrated RF MEMS-based variable attenuator for millimeter-wave applications," *IEEE Transactions on Microwave Theory and Techniques*, vol. 67, no. 8, pp. 3251–3259, 2019.

[169] M.-C. J. Chik and K.-K. M. Cheng, "A novel, varactor-based microwave attenuator with wide tuning ratio and flat insertion loss response," in *2014 IEEE MTT-S International Microwave Symposium (IMS2014)*, 2014, pp. 1–3.

[170] Z. Liu, L. Zhu, and G. Xiao, "A novel microwave attenuator on multilayered substrate integrated waveguide," *IEEE Transactions on Components, Packaging and Manufacturing Technology*, vol. 6, no. 7, pp. 1106–1112, 2016.

[171] L. Pierantoni, D. Mencarelli, M. Bozzi, R. Moro, S. Moscato, L. Perregrini, F. Micciulla, A. Cataldo, and S. Bellucci, "Broadband microwave attenuator based on few layer graphene flakes," *IEEE Transactions on Microwave Theory and Techniques*, vol. 63, no. 8, pp. 2491–2497, 2015.

[172] L. Pierantoni, D. Mencarelli, M. Bozzi, R. Moro, and S. Bellucci, "Graphene-based electronically tunable microstrip attenuator," in *2014 IEEE MTT-S International Microwave Symposium (IMS2014)*, 2014, pp. 1–3.

[173] M. Yasir and P. Savi, "Commercial graphene nanoplatelets-based tunable attenuator," *Electronics Letters*, vol. 56, no. 4, pp. 184–187, 2020.

[174] A.-Q. Zhang, Z.-G. Liu, W.-B. Lu, and H. Chen, "Dynamically tunable attenuator on a graphene-based microstrip line," *IEEE Transactions on Microwave Theory and Techniques*, vol. 67, no. 2, pp. 746–753, 2019.

[175] B. Wu, Y. Zhang, H. Zu, C. Fan, and W. Lu, "Tunable grounded coplanar waveguide attenuator based on graphene nanoplates," *IEEE Microwave and Wireless Components Letters*, vol. 29, no. 5, pp. 330–332, 2019.

[176] A.-Q. Zhang, W.-B. Lu, Z.-G. Liu, H. Chen, and B.-H. Huang, "Dynamically tunable substrate-integrated-waveguide attenuator using graphene," *IEEE Transactions on Microwave Theory and Techniques*, vol. 66, no. 6, pp. 3081–3089, 2018.

[177] A.-Q. Zhang, Z.-G. Liu, L. Wei-Bing, and H. Chen, "Graphene-based dynamically tunable attenuator on a coplanar waveguide or a slotline," *IEEE Transactions on Microwave Theory and Techniques*, vol. 67, no. 1, pp. 70–77, 2019.

[178] M. Yasir, S. Bistarelli, A. Cataldo, M. Bozzi, L. Perregrini, and S. Bellucci, "Enhanced tunable microstrip attenuator based on few layer graphene flakes," *IEEE Microwave and Wireless Components Letters*, vol. 27, no. 4, pp. 332–334, 2017.

[179] ——, "Voltage-controlled and input-matched tunable microstrip attenuators based on few-layer graphene," *IEEE Transactions on Microwave Theory and Techniques*, vol. 68, no. 2, pp. 701–710, 2020.

[180] B. Wu, C. Fan, X. Feng, Y.-T. Zhao, J. Ning, D. Wang, and T. Su, "Dynamically tunable filtering attenuator based on graphene integrated microstrip resonators," *IEEE Transactions on Microwave Theory and Techniques*, vol. 68, no. 12, pp. 5270–5278, 2020.

[181] A. Raeesi, H. Al-Saedi, A. Palizban, A. Taeb, W. M. Abdel-Wahab, S. Gigoyan, and S. Safavi-Naeini, "Low-cost planar RF MEMS-based attenuator," in *2019 IEEE MTT-S International Microwave Symposium (IMS)*, 2019, pp. 869–872.

[182] O. Stukach, "Variable attenuator with low phase shift," in *2006 European Conference on Wireless Technology*, 2006, pp. 241–244.

[183] K. Gupta, R. Garg, and I. Bahl, *Microstrip lines and slotlines (Dedham, MA: Artech House)*. Inc, 1979.

[184] S. J. Chen, D. C. Ranasinghe, and C. Fumeaux, "A robust snap-on button solution for reconfigurable wearable textile antennas," *IEEE Transactions on Antennas and Propagation*, vol. 66, no. 9, pp. 4541–4551, 2018.

[185] L. Gao, T.-W. Lin, and G. M. Rebeiz, "Design of tunable multi-pole multi-zero bandpass filters and diplexer with high selectivity and isolation," *IEEE Transactions on Circuits and Systems I: Regular Papers*, vol. 66, no. 10, pp. 3831–3842, 2019.

[186] F. Teberio, I. Arregui, M. Guglielmi, A. Gomez-Torrent, P. Soto, M. Laso, and V. Boria, "Compact broadband waveguide diplexer for satellite applications," in *2016 IEEE MTT-S International Microwave Symposium (IMS)*, 2016, pp. 1–4.

[187] X. Dai, Q. Yang, W. Xu, C. Guo, and A. Zhang, "Design of diplexer with direct synthesis method for ground penetrating radar," *International Journal of RF and Microwave Computer-Aided Engineering*, vol. 32, no. 12, p. e23542, 2022.

[188] C.-H. Ko and G. M. Rebeiz, "A 1.4–2.3-ghz tunable diplexer based on reconfigurable matching networks," *IEEE Transactions on Microwave Theory and Techniques*, vol. 63, no. 5, pp. 1595–1602, 2015.

[189] J. Xu, "A tunable diplexer based on mixed coupling varactor-tuned stepped-impedance resonators," *Microwave and Optical Technology Letters*, vol. 58, no. 6, pp. 1469–1473, 2016.

[190] W. Feng, Y. Zhang, and W. Che, "Tunable dual-band filter and diplexer based on folded open loop ring resonators," *IEEE Transactions on Circuits and Systems II: Express Briefs*, vol. 64, no. 9, pp. 1047–1051, 2017.

[191] K. Song, Y. Zhou, Y. Chen, A. Mohamed Iman, S. Richard Patience, and Y. Fan, "High-isolation diplexer with high frequency selectivity using substrate integrate waveguide dual-mode resonator," *IEEE Access*, vol. 7, pp. 116 676–116 683, 2019.

[192] A. Kursad Gorur, E. Dogan, C. Karpuz, and A. Gorur, "Design of tunable microstrip diplexer with reconfigurable filtering characteristics based on dual-mode square loop resonators," *IET Microwaves, Antennas & Propagation*, vol. 14, no. 13, pp. 1587–1594, 2020.

[193] X.-Z. Luo, "Design of second-order lumped-element reconfigurable diplexers," *International Journal of RF and Microwave Computer-Aided Engineering*, vol. 29, no. 6, p. e21683, 2019.

[194] T. Yang and G. M. Rebeiz, "A simple and effective method for 1.9–3.4-ghz tunable diplexer with compact size and constant fractional bandwidth," *IEEE Transactions on Microwave Theory and Techniques*, vol. 64, no. 2, pp. 436–449, 2015.

[195] R. Gómez-García, J.-M. Muñoz-Ferreras, L. Yang, and D. Psychogiou, "Contiguous-channel dual-band balanced diplexer," *IEEE Microwave and Wireless Components Letters*, vol. 29, no. 5, pp. 318–320, 2019.

[196] N. C. Pradhan, K. Sholampettai Subramanian, R. K. Barik, and Q. S. Cheng, "Design of a compact siw diplexer with square cavities for c-band applications," in *2020 URSI Regional Conference on Radio Science (URSI-RCRS)*, 2020, pp. 1–4.

[197] R. Gómez-García, L. Yang, J.-M. Muñoz-Ferreras, and D. Psychogiou, "Single/multi-band coupled-multi-line filtering section and its application to rf diplexers, bandpass/bandstop filters, and filtering couplers," *IEEE Transactions on Microwave Theory and Techniques*, vol. 67, no. 10, pp. 3959–3972, 2019.

[198] B. Strassner and K. Chang, "Wide-band low-loss high-isolation microstrip periodic-stub diplexer for multiple-frequency applications," *IEEE Transactions on Microwave Theory and Techniques*, vol. 49, no. 10, pp. 1818–1820, 2001.

[199] J. Konpang, N. Somjit, and I. Hunter, "Two back-to-back three-port microstrip open-loop diplexers," in *2018 15th International Conference on Electrical Engineering/Electronics, Computer, Telecommunications and Information Technology (ECTI-CON)*, 2018, pp. 114–117.

[200] X. Bi, Q. Ma, C. Ning, and Q. Xu, "A compact switchable filtering diplexer based on reused l-shaped resonator," *IEEE Transactions on Circuits and Systems II: Express Briefs*, vol. 65, no. 12, pp. 1934–1938, 2018.

[201] X. Guan, W. Liu, B. Ren, M. Xu, X. Zhang, and Z. Ma, "Synthesized microstrip diplexer with coplanar waveguide feeding based on composite resonators," in *2020 International Conference on Microwave and Millimeter Wave Technology (ICMMT)*. IEEE, 2020, pp. 1–3.

[202] Y.-M. Xue, L. Yang, J.-X. Xu, X.-L. Zhao, and X. Y. Zhang, "Wideband diplexer with narrow channel spacing using hybrid bandpass-bandstop structures," *IEEE Access*, vol. 8, pp. 137 783–137 788, 2020.

[203] A. O. Nwajana, E. A. Ogbodo, and I. I. Imasuen, "Formulation for energy distribution in t-junctions for diplexer design," in *2021 International Conference on Electrical, Communication, and Computer Engineering (ICECCE)*. IEEE, 2021, pp. 1–4.

[204] S.-L. Chen, P.-Y. Qin, W. Lin, and Y. J. Guo, "Pattern-reconfigurable antenna with five switchable beams in elevation plane," *IEEE Antennas and Wireless Propagation Letters*, vol. 17, no. 3, pp. 454–457, 2018.

[205] L. Pazin and Y. Leviatan, "Reconfigurable slot antenna for switchable multiband operation in a wide frequency range," *IEEE Antennas and Wireless Propagation Letters*, vol. 12, pp. 329–332, 2013.

[206] W. Yuan, J. Huang, X. Zhang, K. Cui, W. Wu, and N. Yuan, "Wideband pattern-reconfigurable antenna with switchable monopole and vivaldi modes," *IEEE Antennas and Wireless Propagation Letters*, vol. 22, no. 1, pp. 199–203, 2023.

[207] W. Lin, H. Wong, and R. W. Ziolkowski, "Wideband pattern-reconfigurable antenna with switchable broadside and conical beams," *IEEE Antennas and Wireless Propagation Letters*, vol. 16, pp. 2638–2641, 2017.

[208] Y.-H. Ke, L.-L. Yang, and J.-X. Chen, "Design of switchable dual-balun feeding structure for pattern-reconfigurable endfire antenna," *IEEE Antennas and Wireless Propagation Letters*, vol. 20, no. 8, pp. 1463–1467, 2021.

[209] C.-J. Wang and W.-T. Tsai, "A slot antenna module for switchable radiation patterns," *IEEE Antennas and Wireless Propagation Letters*, vol. 4, pp. 202–204, 2005.

[210]